PROGRESS IN RESEARCH

April 1, 2017 - March 31, 2018

CYCLOTRON INSTITUTE

Texas A&M University

College Station, Texas

PROGRESS IN RESEARCH

APRIL 1, 2017 - MARCH 31, 2018

Prepared By

The Cyclotron Institute Staff

Texas A&M University

College Station, TX 77843-3366

Phone: (979) 845-1411
Fax: (979) 845-1899

Web: http://cyclotron.tamu.edu

June 2018

TABLE OF CONTENTS

**SECTION I: NUCLEAR STRUCTURE, FUNDAMENTAL INTERACTIONS
AND ASTROPHYSICS**

SECTION II: HEAVY ION REACTIONS

SECTION III: NUCLEAR THEORY

SECTION IV: SUPERCONDUCTING CYCLOTRON, INSTRUMENTATION AND RIB UPGRADE

SECTION V: PUBLICATIONS

SECTION VI: APPENDIX

x

Introduction
April 1, 2017 – March 31, 2018

Progress in research and operations at the Texas A&M Cyclotron Institute is summarized in this report for the period April 1, 2017 through March 31, 2018. The format follows that of previous years. Sections I through III contain reports from individual research projects. Operation and technical developments are given in Section IV. Section V lists the publications with Cyclotron Institute authors and outside users and the Appendix gives additional information including talks presented by members of the Institute during the past year. Once again, the full volume of this year's Progress in Research is available only on our web site (http://cyclotron.tamu.edu). *Since most of the contributions presented here are truly reports on progress in research, results and conclusions should not be quoted from the report without the consent of the authors.*

For 50 years scientists at Texas A&M have been exploring the nuclear frontier. The first cyclotron beam was extracted in December 1967 and throughout 2017 we marked the occasion of 50 years of beam. Additionally, we are pleased to celebrate that former TAMU graduate student Zilong Chang (Ph.D., Dec 2016) won the 2017 RHIC & AGS Thesis Award.

The K500 provided an impressive 5,921 hours of beam for both science and radiation effects testing. The K150 cyclotron provided again, a record 4,291 hours of beam on target and continues to be used by external users for radiation effects testing with its proton beams. The growing list of beams from the K150 includes protons (strip extracted), deuterons (strip extracted), ^{4}He, ^{6}Li, ^{7}Li, ^{10}B, ^{12}C, ^{14}N, ^{16}O, ^{18}O, ^{19}F, ^{20}Ne, ^{22}Ne, ^{23}Na, ^{25}Mg, ^{27}Al, ^{28}Si, ^{32}S, ^{40}Ar, ^{63}Cu, and ^{84}Kr. Proton beams from the K150 (strip extracted) are now available from 3 MeV to 49 MeV. We continue to make progress with the light-ion guide (LIG) project: using a ^{114}Cd target, we produced radioactive ^{114}In, which then charge bred and accelerated to 11 MeV/nucleon with the K500 cyclotron. Transporting the accelerated ^{114}Cd/^{114}In beam to MARS, we were able to verify the identity of the beam and that it originated from the LIG gas cell.

As in previous reports, I include here some highlights.

- Published the first ever direct measurement of the ^{19}Ne(p,γ)^{20}Na, significantly reducing uncertainties on the production of fluorine in classical novae.

- Verified the mass separation capabilities of the MDM spectrometer up to A=63 for inverse-kinematics (d,p) reactions, opening the door for future RIB experiments in the A~60 mass region.

- Developed a method of determining the reactor type, burnup, and time since irradiation of used nuclear fuel in collaboration with the Department of Nuclear Engineering.

- Studied the mechanism of extraction of indium and thallium from hydrochloric acid by a variety of organic solvents.

- Demonstrated successful track reconstruction with TexAT for ^{8}B+p and ^{8}Li+p.

- Completed the analysis of the first precise measurement of the superallowed branching ratio for ^{26}Si. With this result, precise *ft* values are now known for the mass-26 pair of $0^+\rightarrow0^+$ superallowed transitions. The result is consistent with the only other measured pair of such transitions (at *A*=38) and together they act to significantly constrain calculations of the isospin-symmetry-breaking corrections, which are required to extract V_{ud}, the upper-left element in the CKM matrix.

- Published the first-ever observation of the Collins effect in pp collisions, enabling tests of universality and factorization of transverse momentum dependent (TMD) fragmentation functions, and the first-ever limits on gluon linear polarization in transversely polarized protons.

- An earlier developed self-consistent many-body approach to the strongly interacting Quark-Gluon Plasma has been deployed to analyze its transport properties. A maximally strongly-coupled solution is necessary to generate a small viscosity-to-entropy ratio and heavy-quark diffusion coefficient as required by phenomenological analyses of light- and heavy-flavor hadron observables in ultrarelativistic heavy-ion collisions.

- Performed a broad investigation with several research groups (with TAMU leadership) within an EMMI rapid reaction task force to scrutinize the theoretical components in the extraction of heavy-flavor transport coefficients in QCD matter from heavy-ion collisions; the leading model uncertainties have been identified and systemic procedures for their improvement established.

- Constructed a new class of hot and dense matter equations of state that simultaneously satisfy constraints from microscopic many-body theory, nuclear experiments, and neutron star observations.

- Computed neutron star tidal deformabilities based on dense matter equations of state constrained by chiral effective field theory and confronted these predictions with observational data from gravitational wave event GW170817.

- Derived an analytical expression which provides a good approximation for the effect of two-body short-range correlations on the one-body matter distributions in nuclei.

- Adopted the thermodynamical approach for the statistical level density in nuclei and carried out calculations within the self-consistent mean-field approach using the extended Thomas-Fermi approximation, which accounts for the liquid drop and the shell models.

- Using 33 commonly employed energy density functionals, we carried out Hartree-Fock based

random phase approximation calculations of the centroid energies of isoscalar and isovetor giant resonances of available experimental data for a wide range of nuclei and studied their sensitivities to properties of nuclear matter and thereby deduced constraints on these properties.

- Suggested and developed a new indirect method in nuclear astrophysics: indirect radiative capture reactions. This method will allow us for the first time in 50 years of hunting to measure the astrophysical factor of the radiative capture $^{12}C(^{4}He,\gamma)^{16}O$ at the most effective astrophysical energy of 300 keV.

- Established a connection between mirror resonance widths which can be used for experiments at the Cyclotron Institute to determine an unknown resonance width through the known ones.

- Reproduced the binding energies of light nuclei in the constrained molecular dynamics model by including the Heisenberg principle and (iso)spin-(iso)spin forces which has application to fusion, fission and fragmentation reactions.

- Performed search for Efimov states in hot nuclei from 3 alpha correlations in $^{70}Zn+^{70}Zn$ at 35MeV/nucleon using the NIMROD 4π detector.

- Measured fusion reactions in strongly compressed plasmas using 8 laser beams (<3ns pulse duration and <20kJ energy) in cylindrical symmetry.

- Commissioned the ParTI Array and measured upper limit of pionic fusion in reaction of $\alpha+^{12}C$.

- Demonstrated ability to do elemental analysis through PIXE and PIGE with K150.

- Demonstrated that the vorticity field produced in non-central heavy ion collisions within the chiral kinetic theory leads to polarizations of quarks and antiquarks and thus of Lambda and anti-Lambda hyperons along its direction as observed in experiments by the STAR Collaboration at the Relativistic Heavy Ion Collider.

- Demonstrated that Including the energy conservation condition in scattering and decay processes in the transport model is necessary for obtaining the correct equilibrium particle distributions and is thus important for extracting the nuclear symmetry energy at high density from the ratio of charged pions produced in high energy heavy ion collisions.

Institute scientists remain active in a number of collaborative research efforts around the world. Major programs include: mass measurements using the Penning Trap at the University of Jyväskylä; continued work with the STAR collaboration at RHIC; measurements of beta decays with the TRINAT

collaboration at TRIUMF; ANASEN at MSU; and participation in the SAMURAI collaboration at RIBF in Tokyo, Japan.

I am indebted to Dr. Y.-W. Lui for assembling this report.

S.J. Yennello
July 1, 2018

50 years of beam celebration

On December 4, 1967, Nobel Prize winners Glenn T. Seaborg and Willard F. Libby helped dedicate the Texas A&M Cyclotron Institute only three days after it had achieved its first external cyclotron-accelerated particle beam. The following are some of the historical milestones of the Cyclotron Institute [1]:

1962 - Proposal to the Atomic Energy Commission for construction and operation of a
      cyclotron at The Agricultural and Mechanical College of Texas.

1964 - Cyclotron Institute created by Board minute order.

1965 - AEC entered contract with TAMU to build a cyclotron:

	(Actual Dollars)	(2015 dollars)
TAMU	$2,000,000	$15,580,000
Welch Foundation	$1,000,000	$ 7,790,000
Atomic Energy Commission	$3,000,000	$23,371,000

1967 - August 8, 4:40 PM Internal beam 88" cyclotron.
      December 1, 12:42 AM External beam 88" cyclotron.

1968 - First experiments and first paper published from Institute.

1969 - First research student to obtain Ph.D. from research at the Institute.
      H.L. Rook - Schweikert

1970 - Enge Split Pole Spectrograph.

1972 - NIH Support - M.D. Anderson neutron therapy cancer project began.
      Treatment of patients 2 days per week.

1977 - Cyclotron Improvement Grant.

1979 - 2 DEC Vax 780 Computer Systems.

1980 - Cancer Therapy program concluded. M.D. Anderson building cyclotron in Houston.
      Consolidate Physics, Chemistry, and Operation funding at Department of Energy.

1982 - Cyclotron Expansion approved by Board of Regents.

1985 - ECR Source and Neutron Ball.

1986 - Proton Spectrometer.

1987 - December 7, Dedication of K500 cyclotron.

1989 - Mars.
      BaF_2 Array.

1991 - Computer System.

1992 - MDM .

1993 - Beam Analysis System.

1995 - ECR Upgrade.
      SEE Line Inaugurated - Boeing.
      FAUST.

1997 - NIMROD.

1999 - MDM Upgrade .
      New ECR.

New Beam Line.

Precision Online Decay facility.

2000 - NIMROD Upgrade.

Beam intensity Upgrade

2005 - Cyclotron Institute Upgrade Project [2].

2010 - H⁻ Souce.

2013 - FAUST-QT

2016 - TAMUTRAP.

TIARA for Texas.

2017 - TexAT

Throughout 2017 the Cyclotron Institute commemorated 50 years of beam with a series of celebratory activities. From April to December 2017, we had the "50 Years of Beam Seminar Series" [3] featuring former students, post-docs, and researchers from the Institute.

An international scientific symposium was held from November 15 – 17, 2017 in the Mitchell Institute auditorium at Texas A&M. The event drew over 100 attendees from leading institutions around the world. Many of the speakers were world-leading experts in their respective fields – a true testament to the status of the Cyclotron Institute on the world stage of nuclear science.

The scientific program of the symposium [4] was arranged to highlight the diverse range of topics studied at the Cyclotron Institute over its 50-year history. These included the nuclear equation of state, nuclear astrophysics, nuclear structure, fundamental symmetries, high-energy nuclear physics, and applications of cyclotron-based nuclear science. In addition to the rich and diverse program of invited and contributed scientific talks, a session focusing on historical talks from Mr. Whit McFarlin and former Institute directors Drs. Dave Youngblood, Joe Natowitz, and Robert Tribble was held on the afternoon of November 16. The focus on history allowed attendees to take a step back and reflect on the development of the Institute, scientific and technical milestones achieved over the years, and to place present and future research projects into the broader historical context. A poster session was also held on the evening of November 15, where the talented group of current Cyclotron Institute graduate students and postdocs presented their research to symposium attendees.

As fitting for a celebration symposium, the program was not entirely focused on talks and poster presentations. A celebration banquet was held on the evening on November 16, with attendees gathering at the TAMU Equine Center to enjoy a catered dinner provided by Napa Flats. At the symposium, the past, present, and future employees of the Institute were recognized, and the current director, Dr. Sherry Yennello, gave a speech highlighting the past accomplishments at the Institute and expressing excitement for the future, as the Institute enters its second 50 years of being a world leader in nuclear science.

In the morning of November 17, a "recognition session" was held [5], where leaders from the Department of Energy, The Robert A. Welch Foundation, State of Texas and Texas A&M University recognized the excellent contributions of the Cyclotron Institute over the past 50 years. Also present was Col. John O. "Jack" Teague (son of Congressman Olin"Tiger" Teague). As fitting for a celebration event in College Station, the attendees were treated to a lunch of Texas Bar-B-Que.

In closing the 50 years of beam celebration in December 2017, we had Dr. Che-Ming Ko remind us about 50 Years of Theoretical Nuclear Physics Research at the Cyclotron Institute, and Drs. Joe Natowitz and Dave Youngblood talked about their 50 years of research at the Cyclotron Institute.

We have been blessed with a group of superb, inventive, and hard working support staff over the past five decades, as D.H. Youngblood said in his historical talk, "The lab would not exist without their effort and contributions". The Cyclotron Institute began as a small laboratory 50 years ago and has turned into a Department of Energy Center of Excellence for Nuclear Physics today, as mentioned in the congratulation letter from Tim Hallman, Associate Director of the Office of Science for Nuclear Physics [6].

It has been fun and we had a great time. Thanks to our wonderful friends, Shana Hutchins, Chris Jarvis and Jennifer Hollein the Dean's office, and our own Julie Anderson, Paula Barton, Haley Forbes, Ruben Gallegos, Sharon Jeske, Victoria Tepe, and Kristina Zimmerhanzel.

Happy 50th anniversary Cyclotron Institute, many more 50 years to come!

[1] D.H. Youngblood, private communication.
[2] Cyclotron Institute Upgrade White Paper.
    https://cyclotron.tamu.edu/wp-content/uploads/facility_upgrade.pdf
[3] 50 Years of Beam Seminar Series, *Progress in Research*, Cyclotron Institute, Texas A&M University (2017-2018), p. VI-13
[4] The scientific program of the 50 Years of Beam Symposium, *Progress in Research*, Cyclotron Institute, Texas A&M University (2017-2018), p. VI-17
[5] Recognition Event Program, *Progress in Research*, Cyclotron Institute, Texas A&M University (2017-2018), p. VI-22
[6] Timothy Hallman, Congratulation letter from the Office of Science for Nuclear Physics, *Progress in Research*, Cyclotron Institute, Texas A&M University (2017-2018), p. VI-23.

G. Christian
Y.-W. Lui
S.J. Yennello

SECTION I

NUCLEAR STRUCTURE, FUNDAMENTAL INTERACTIONS AND ASTROPHYSICS

Study of astrophysically important low-energy resonances in α+^{22}Ne reaction using ^{6}Li(^{22}Ne,^{26}Mg)d alpha transfer with TIARA and MDM spectrometer

S. Ota, G.A. Christian, E.A. Bennett, S. Dede, H. Jayatissa, J. Hooker, C. Hunt,
C. Magana, G. Rogachev, A. Saastamoinen, S. Upadhyayula,
W.N. Catford,[1] S. Hallam,[1] G. Lotay,[1] M. Mouhkaddam,[1] and R. Wilkinson[1]

[1]*University of Surrey, Guildford GU2 5XH, United Kingdom*

In core He burning and C-shell burning of massive stars (> 8 solar mass), the ^{22}Ne(α,n)^{25}Mg reaction is considered to be a dominant neutron source for the weak s-process during which nuclides in the A=60-90 mass range are produced [1]. The reaction also largely contributes to the neutron production for the main s-process in He-low and intermediate mass asymptotic giant branch (AGB) stars during which nuclides in the A~90-209 are produced [1]. Some attempts to experimentally determine the rate for this reaction at the Gamow window corresponding to the *s* process temperatures (T = 0.2-0.3 GK, equivalent to E_α = 400 – 900 keV, where E_α is energy of α particle in the laboratory system, and E_x=10.9-11.5 MeV, where E_x is excitation energy of ^{26}Mg) have been made through direct (^{22}Ne+^{4}He or α+^{22}Ne) measurements [e.g., 2]. However, they have been hindered by the small cross section due to the Coulomb barrier and the resonance at E_α ~ 830 keV (E_x ~ 11.32 MeV in ^{26}Mg excitation energy) is the lowest resonance identified with this method. Although indirect methods such as ^{26}Mg(α,α')^{26}Mg,
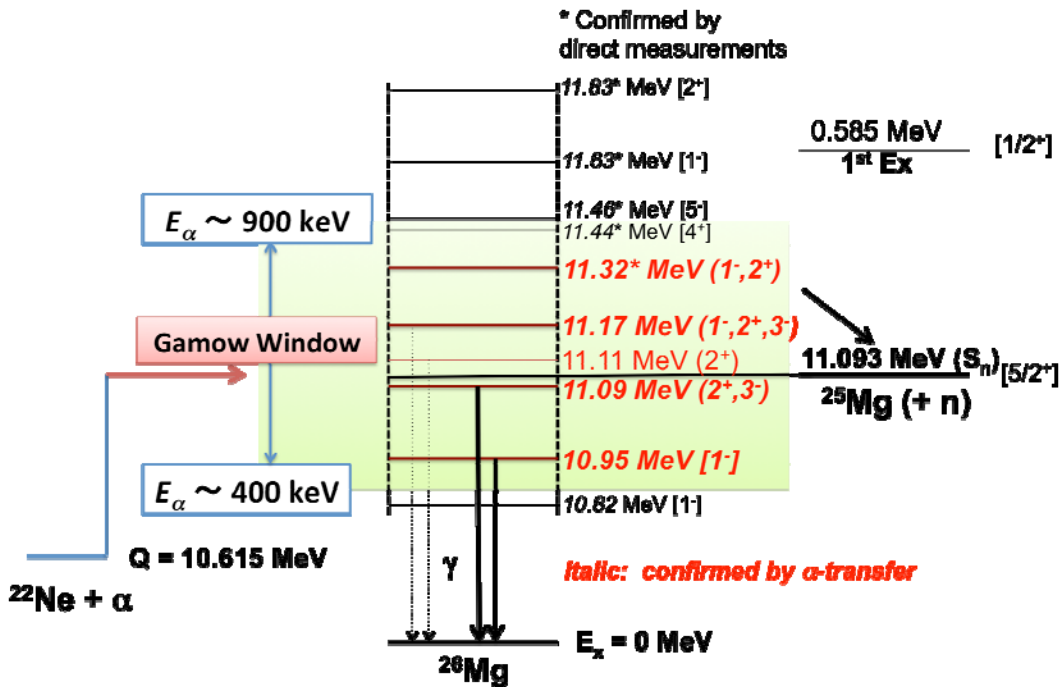
FIG. 1. Level scheme of ^{26}Mg at energy range of our interest. Although the lowest resonance identified by direct measurements is E_x=11.32 MeV (E_α=832 keV), indirect measurements have identified many lower resonances. Previous (^{6}Li,d) measurements in normal kinematics [e.g., 4 and 5] observed four resonances in Gamow window. E_x=11.32 MeV and 11.17 MeV are considered the most important contributors to ^{22}Ne(α,n) reaction for the s-process [e.g., 5].

^{22}Ne(^{6}Li,d)^{26}Mg, ^{25}Mg(n,γ)^{26}Mg, ^{26}Mg(γ,γ')^{26}Mg reactions [e.g., 3-6] have been used to identify lower-energy resonances, there remain many uncertainties in spin-parity (J^π), partial wave widths of respective decay channels (Γ_γ, Γ_n and Γ_α) of these resonances. Since past studies identified particularly two resonances, E_x=11.32 and 11.17 MeV above neutron separation energy (S_n=11.093 MeV), have the largest contribution to the neutron production during the s-process, unambiguously determining J^π, Γ_γ, Γ_n and Γ_α for these resonances is important. Fig. 1 shows the summary of level scheme in ^{26}Mg relevant to the present study.

To determine these resonance parameters, we performed an experiment using the ^{6}Li(^{22}Ne,^{26}Mg)d α-transfer reaction. Because both the α and ^{22}Ne have ground states with J^π=0$^+$, the α-transfer reaction preferentially populates natural parity states in ^{26}Mg. This helps us to enable studies of the resonance parameters of astrophysically relevant natural parity states in ^{26}Mg, and J^π of these resonance states can be determined by measuring the angular distribution of deuterons. Furthermore, the inverse kinematics approach enables us to determine Γ_n / Γ_γ by direct measurements of the ratio of produced ^{25}Mg (^{26}Mg*→^{25}Mg$_{g.s.}$ + n) and ^{26}Mg (^{26}Mg*→^{26}Mg$_{g.s.}$ + γ) ions at the resonance states. Determining Γ_n / Γ_γ is important to understand the neutron yield of these resonances. The ^{22}Ne(α,γ)^{26}Mg reaction can be of considerable strength to compete with the ^{22}Ne(α,n)^{25}Mg reaction at E_x=11.32 and 11.17 MeV resonances and therefore could significantly suppress neutron production for the s-process.

The experiment was performed at Cave 3 using a 7 MeV/u ^{22}Ne beam from the K150 cyclotron. ^{6}Li-enriched (99%) lithium flourite (LiF) targets with the thickness of 30 μg/cm^2 on a graphite backing foil (10 μg/cm^2) were prepared so that the effect of the energy loss of the ^{22}Ne beam and deuterons in those materials on the final energy resolution will be negligibly small. The beam bombarded the target at an intensity of about 3 nA for about 10 days. A large Si detector array, TIARA [8] was used for measuring the energies and angular distribution of light particles (deuterons). The deuteron energies and angles were used to determine excitation energies of ^{26}Mg. TIARA consists of two types of Si detectors, Hyball and Barrel, which cover 145 – 170° and 40-145° in laboratory frame, respectively (see [8]). TIARA was surrounded by four HPGe clover γ-ray detectors, which were used to confirm the populated states of ^{26}Mg. Recoil Mg ions were delivered to the Oxford ionization chamber placed at the back of the MDM spectrometer at 0°with ±2°acceptance [9]. The Oxford chamber consists of four proportional wire counters to determine the trajectories of particles and two MicroMegas detectors to measure the deposited energies in the gas (see details in [10]). The chamber was filled with isobutene gas at 35 torr to stop the Mg ions with the energies of our interests in the region of the second MicroMegas detector. The first and the second MicroMegas detectors thus provide ΔE and E$_{res}$ (residual energy), respectively, and the Mg ions are clearly identified from other elements as shown in [11]. Moreover, ^{26,25}Mg isotopes were identified from each other based on the hit positions on the second wire which is located near the focal plane.

Since the Barrel has insufficient energy resolution to resolve the resonances in ^{26}Mg, it was mostly used to measure elastic scattering. Data from the Hyball is shown in the following analysis. Fig. 2 shows 2D histograms of ^{26}Mg excitation energy and hit positions on the second wire in the Oxford chamber, gated on (a) ^{26}Mg and (b) ^{25}Mg, respectively. It can be seen a blob (inside the circle) increases the excitation energy with the hit position (rigidity) decreased in the Fig. 2(a). This is because the more

highly ^{26}Mg is excited, the lower rigidity (kinetic energy) it has. The background events (outside the circle) are mostly protons, which was confirmed by the E-ΔE plot obtained by the Barrel. In the Fig. 2 (b), the blob ((^{6}Li,d+n)) spreads more widely because an evaporating neutron from ^{26}Mg deposits various momentum to the leftover ^{25}Mg. In the right side of the (^{6}Li,d+n) blob is ^{25}Mg ions produced by ^{22}Ne(^{6}Li,t)^{25}Mg reactions. It is worth noting that the ^{26}Mg (by ^{22}Ne(^{6}Li,d+γ)) disappears in Fig. 2 (a) and ^{25}Mg (^{22}Ne(^{6}Li,d+n)) appears in Fig. 2(b) at nearly S_n=11.09 MeV. This proves that our energy determination is reliable.
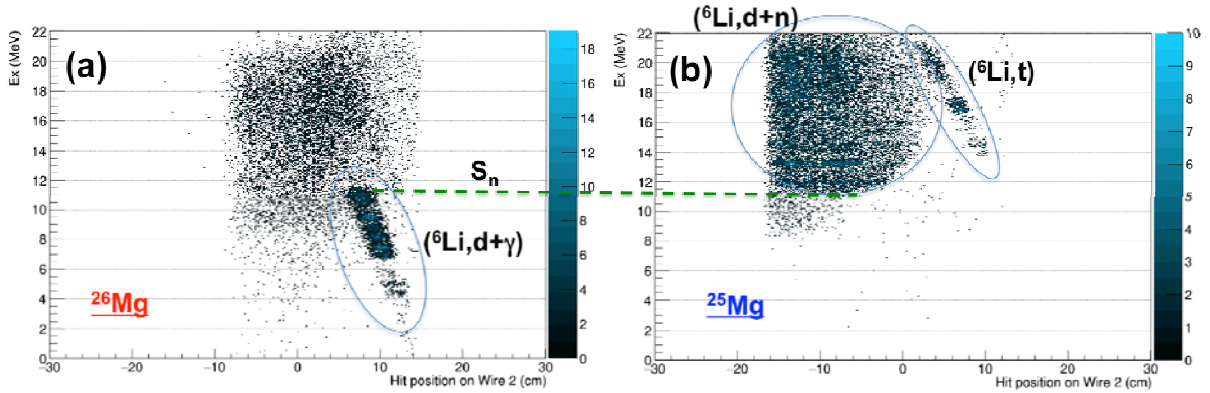
FIG. 2. 2D histograms of E_x (determined by Si detectors) and hit positions of Mg ions on the second wire of the Oxford chamber, (a) ^{26}Mg and (b) ^{25}Mg.

The excitation energy spectrum of ^{26}Mg is shown in Fig. 3. The spectrum covered by red shadow is obtained by gating on ^{26}Mg (the ((^{6}Li,d+γ) blob) and the total spectrum (blue line) was
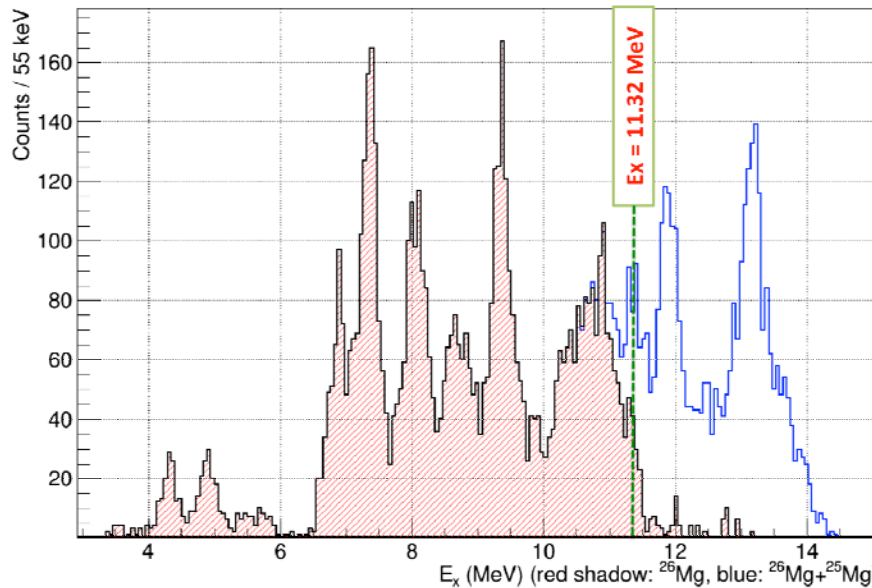
FIG. 3. ^{26}Mg excitation energy spectrum (red shadow: contribution from ^{22}Ne(^{6}Li,d)^{26}Mg, blue: sum of contributions from ^{22}Ne(^{6}Li,d)^{26}Mg and ^{22}Ne(^{6}Li,d+n)^{25}Mg). E_x=11.32 MeV resonance peak is distinct in both spectra.

obtained by gating on both ^{26}Mg and ^{25}Mg (the (^{6}Li,d+n)) blob). It is confirmed that the both spectra (^{26}Mg and ^{25}Mg+^{26}Mg) show a distinct peak at Ex=11.32 MeV. On the other hand, no distinct peak was observed at E_x=11.17 MeV which was clearly observed by [5]. This may be just because the state is not / very weakly populated as reported in [4]. Currently we are making an effort to extract the numbers of events for these resonances with multiple-Gassian fitting assuming various conditions. This will shortly lead to determining J^π and Γ_n / Γ_γ and we will study its influence on the s-process nucleosynthesis.

[1] F. Kappeler, Prog. Part. Nucl. Phys. **43**, 419 (1999).

[2] M. Jaeger *et al.*, Phys. Rev. Let. **87**, 20 (2001).

[3] P. Adsley *et al.*, Phys. Rev. C **96**, 055802 (2017).

[4] U. Giesen *et al.*, Nucl. Phys. **A561**, 95 (1993).

[5] R. Talwar *et al.*, Phys. Rev. C **93**, 055803 (2016).

[6] C. Massimi *et al.*, Phys. Let. B **768**, 1 (2017).

[7] R. Longland *et al.*, Phys. Rev. C **80**, 055803 (2009).

[8] M. Labiche *et al.*, Nucl. Instrum. Methods Phys. Res. **A614**, 439 (2010).

[9] D.M. Pringle *et al.*, Nucl. Instrum. Methods Phys. Res. **A245**, 230 (1986).

[10] A. Spiridon *et al.*, Nucl. Instrum. Methods Phys. Res. **B376**, 364 (2016).

Studying the ^{23}Na(d,p)^{24}Na reaction to constrain the astrophysical ^{23}Mg(p,γ)^{24}Al reaction rate

E.A. Bennett, W.N. Catford,[1] G. Christian, S. Dede, S. Hallam,[1] G. Lotay,[1] S. Ota, A. Saastamoinen,
D. Scriven, and R. Wilkinson[1]

[1] *University of Surrey, Surrey, United Kingdom*

In classical novae, the ^{23}Mg(p,γ)^{24}Al reaction provides an escape from the Ne-Na cycle and is therefore important in understanding nucleosynthesis in the *A>20* mass range. A classical nova provides the increased temperatures necessary for the proton capture reaction on ^{23}Mg to outpace the β decay reaction favored at lower temperatures [1,2]. The ^{24}Al generated by this proton capture reaction quickly decays into ^{24}Mg and allows entrance into the Mg-Al cycle [4].

Several resonances may be of astrophysical interest; however, at nova temperatures, the lowest resonance at ~475 keV appears to be the dominant contributor to the reaction rate [1]. Multiple experiments have investigated the excited states in ^{24}Al that correspond to the resonances of astrophysical interest. A fusion-evaporation experiment at gammasphere found the first resonance energy to be 473 ± 3 keV [3] by performing in-beam γ-ray spectroscopy on the Al nucleus. While this is regarded as the most precise measurement to date, other particle spectroscopy experiments have placed the resonance energy between 456 ± 10 keV and 497 ± 5 keV [4]. Following these experiments, the first direct measurement of 23Mg(p,g)24Al was performed at DRAGON. Using a ^{23}Mg beam a resonance energy of 485.7 keV and a resonant strength of 38 meV [3] were determined. However, an additional resonance strength higher than initially anticipated was noted upstream of the target position. This observation introduces some uncertainty into the veracity of the results produced.

We believe an indirect measurement of the resonant strength will either verify or throw into question the DRAGON measurement. Given the isobaric analogue of ^{24}Al is ^{24}Na, we have made a measurement of the ^{23}Na(d,p)^{24}Na reaction in inverse kinematics to measure the ejected proton and extract the spectroscopic factor. Since the spectroscopic factor for ^{24}Na and ^{24}Al should be the same, we can then use this to calculate the proton width and, utilizing the known gamma width, can extract the resonant strength. The experiment conducted here at the Cyclotron Institute was performed using TIARA, a compact silicon detector array designed to study direct reactions in inverse kinematics [5]. We impinged a 10 AMeV beam of Na on a 500 μg deuterated plastic target mounted in the center of the TIARA chamber. In conjunction with the MDM and Oxford Detector, we are able to look at protons from the ^{23}Na(d,p)^{24}Na reaction in the backward angle silicon array with relatively high precision. HPGe detectors mounted around the target position also allow for gamma-ray spectroscopy.

Significant progress has been made in the analysis of our experimental data. The calibration has been completed for the backward annular silicon detector and work continues towards calibrating the barrel silicon detectors and performing the beam position minimization. This progress has allowed us to generate the first excitation spectrum for our reaction, seen in Fig. 1. You can clearly make out the excited states of the ^{24}Na nucleus and the values for these states fall within expected bounds. Previously, due to an issue we encountered while running, we had thought that few to none of the ^{24}Na nuclei had made it through the MDM and into the Oxford Detector. Recent progress in the analysis has revealed that
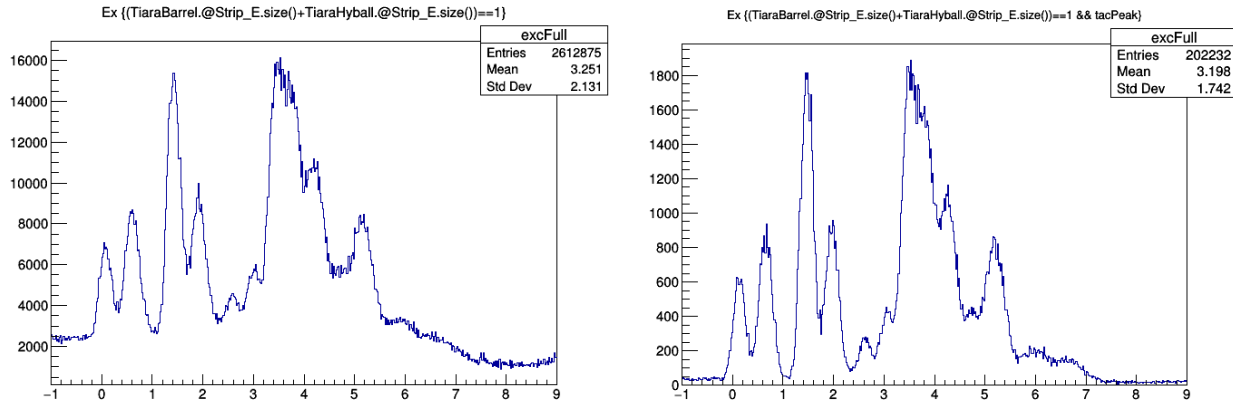
FIG. 1. Current excitation spectrums generated from the 23Na(d,p)24Na experiment. The plot on the left has full statistics and the plot on the right shows only events that made it through to the focal plane.

an appreciable fraction of the beam did in fact make it into the focal plane. Using this data we have managed to almost completely remove the background from our excitation spectrum without too significant a loss in efficiency. Fig. 2 illustrates the most recent particle identification plot generated from this data. More work remains to be done, but these developments mark a meaningful advance towards completing the analysis
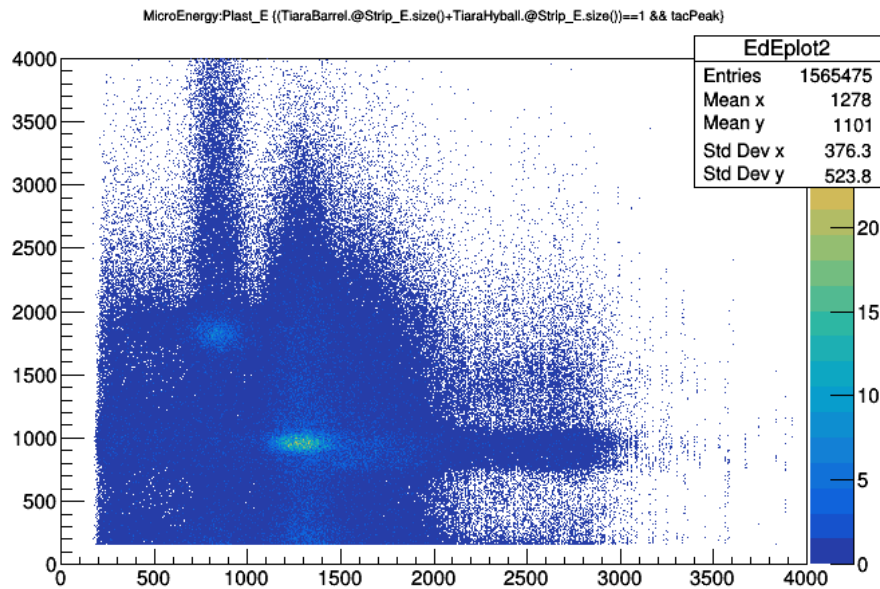
FIG. 2. Particle identification plot generated from events that were accepted into the focal plane. Work is continuing to improve the quality of this data.

In addition, we have been approved to repeat the $^{23}Mg(p,\gamma)^{24}Al$ direct measurement at TRIUMF. This experiment will take advantage of DRAGON's newly upgraded Lanthanum Bromide array, which

will decrease systematic uncertainties relative to the previous experiment. Repeating the direct measurement should remove the aforementioned uncertainty from the previous run and will further constrain the resonant strength of the reaction. We hope to schedule beam time for this experiment at some point in 2019.

[1] H. Herndl, *et al.*, Phys. Rev. C **58**, 1798 (1998).
[2] U. Chowdhury, *et al.*, Phys. Rev. C **92**, 045803 (2015).
[3] L. Erikson, *et al.*, Phys. Rev. C **81**, 045808 (2010).
[4] G. Lotay, *et al.*, Phys. Rev. C **77**, 042802(R) (2008).

High Precision half-life measurement of ^{21}Na

R.S. Behling, B. Fenker, J.C. Hardy, V.E. Iacob, M. Mehlman, D. Melconian, H.I. Park,
P.D. Shidling, and B.T. Roeder

A review of all T=1/2 mirror β decays [1] indicates that ^{21}Na is one of the best candidates from this group for testing the standard model. The total uncertainty in the *ft* value of ^{21}Na was dominated by the half-life. So, half-life measurements were carried out recently by two different groups [2,3] unfortunately with inconsistent results. We have performed a precise half-life measurement for ^{21}Na aimed at resolving this discrepancy.

^{21}Na was produced via the $p(^{22}Ne, 2n)^{21}Na$ reaction in inverse kinematic at a primary beam energy of 25 MeV/u. The Momentum Achromat Recoil Spectrometer (MARS) was used to produce a secondary beam of ^{21}Na with a purity of 99.9%. Fig. 1a shows typical two-dimensional plot of energy-loss vs position as obtained with the 16-strip position-sensitive silicon detector (PSSD) in the MARS focal plane. The secondary beam exited the vacuum system through a Kapton foil and then passed through a thin plastic scintillator, a series of Al degraders and eventually implanted in the center of an Aluminized Mylar tape. In repeated cycles, the fast-tape transport system quickly transported the sample to a well shielded location, placing it in the center of a 4π proportional gas counter where β activity was recorded for about 20 half-lives. The total data set was divided into 21 runs with different settings of the experimental parameters: bias voltage, discriminator threshold and dominant dead-times. Each cycle was dead-time corrected and the cycles from a given run were summed and fit using the Levenberg-Marquardt χ^2 minimization algorithm. The fit function consisted of one exponential corresponding to the decay of ^{21}Na plus a constant background. The decay curve observed with the summed fit overlayed is shown in Fig. 1b.
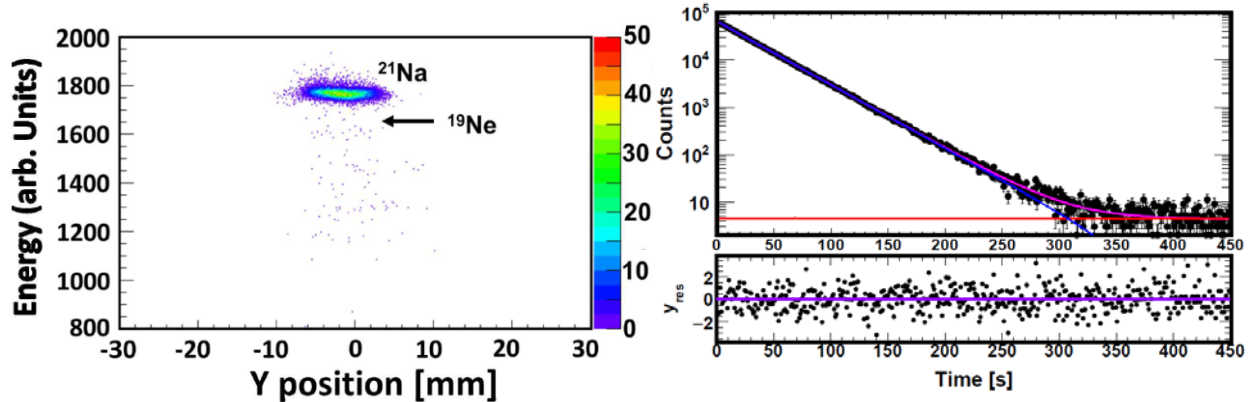
FIG. 1. (a) On the left, two dimensional plot of energy-loss versus position in the PSSD at the MARS focal plane. (b) On the right, typical dead-time corrected summed decay curve obtained from a single run with residuals. The reduced chi-square of the fit is 1.10.

Our final result for the ^{21}Na half-life is $t_{1/2} = 22.4615 \pm 0.0039$ (stat) ± 0.00015 (syst) s [4]. Our result strongly disfavors the half-life measured by Grinyer et al. [2] but does not fully agree with Finlay et

al. [3] either. It should be noted that the uncertainty in our measurement is dominated by statistics, whereas the total uncertainty in the two recent measurements [2,3] is dominated by systematics. In any case, the new world average of the ^{21}Na half-life is increased by 0.0048 s and has an uncetainty reduced by a factor of 1.5. The new *ft* value is now limited in precision by the 95.235(69)% ground state branching ratio. More important still, the uncertainty in V_{ud} is dominated by the ±1% uncertainty associated with the value of ρ, which derives from a correlation measurment [5].

[1] O. Naviliat-Cuncic and N. Severijns, Phys. Rev. Lett. **102**, 142302 (2009).
[2] J. Grinyer *et al.*, Phys. Rev. C **91**, 032501(R) (2015).
[3] P. Finlay *et al.*, Phys. Rev. C **96**, 025501 (2017).
[4] P.D. Shidling *et al.*, Phys. Rev. C (submitted).
[5] P.A. Vetter *et. al.*, Phys. Rev. C **77**, 035502 (2008).

TRINAT result – Precision measurement of the polarization and beta-asymmetry from the β^+ decay of laser-cooled ^{37}K

B. Fenker, D. Melconian, and P.D. Shidling

The TRINAT collaboration is utilizing magneto-optical trapping and optical pumping techniques to cool, confine and highly polarize ^{37}K atoms to provide an ideal source for precision β-decay experiments. Our goal is to measure parameters of the angular distribution to <0.1% which would search for (or help constrain) physics beyond the standard model in a way that is competitive with and complementary to direct searches at high-energy colliders. Recently, we published the results described in Ref [1], representing the best relative accuracy of any β-asymmetry measurement in the nucleus or the neutron [2]. This publication discussed the results which do not depend on the β energy. We are currently analyzing the energy-dependent observables, and in particular the Fierz interference parameter, which is sensitive to scalar and tensor components to the weak interaction. We also expect to place limits on second-class currents.

Our statistical uncertainty is 0.24%, including the 0.09% from the polarization measurement. The two largest sources of systematic uncertainty are a background and the effects of β scattering, which contribute 0.14% and 0.12% respectively to the error budget. Following this, the cloud parameters (trap position, movement and temperature) combine to contribute 0.12%, with all other systematics at or below 0.7%. We believe that with better control of the cloud of trapped atoms and increasing the electric field for collection of the charged daughter particles, we can reduce the backgrounds and uncertainties in the trap characteristics. This, with increased statistics, should reduce our uncertainty by a factor of 2. To reach our goal of 0.1%, we will have to reduce our scattering uncertainty by a factor of 3, which will be our more challenging task. We have a very unique geometry and are considering options on how to reduce this systematic by better calibrating our Monte Carlo simulation of scattering. We are currently developing some ideas on how to benchmark our simulations, using beamtime we have available if necessry.

[1] B. Fenker *et al*., *Progress in Research*, Cyclotron Institute, Texas A&M University (2016-2017) p. I-52.
[2] B. Fenker *et al*., Phys. Rev. Lett. **120**, 062502 (2018).

Superallowed beta decay

J.C. Hardy, V.E. Iacob, H.I. Park, N. Nica, M. Bencomo, T. Eronen, V. Horvat, and L. Chen

Superallowed $0^+ \rightarrow 0^+$ beta decay between T=1 analogue states has been a subject of continuous and often intense study for five decades. The *ft* values of such transitions are nearly independent of nuclear-structure ambiguities and depend uniquely on the vector part of the weak interaction. Their measurement gives us access to clean tests of some of the fundamental precepts of weak-interaction theory, and, over the years, this strong motivation has led to very high precision being achieved both in the experiments and in the theory used to interpret them. We have a major program at the Cyclotron Institute to study superallowed beta decay.

To obtain the *ft* value for any transition, three quantities must be measured: the half-life $t_{1/2}$ of the parent, the Q_{EC} value for the transition of interest, and the branching ratio R for that transition. Our most recent complete survey of world data on these superallowed decays, published in 2015 [1], provides a critical evaluation of all the experimental data and obtains final *ft* values from the averaged results. Radiative and isospin-symmetry-breaking corrections were then applied in order to derive a final set of "corrected ft values", denoted $\mathcal{F}t$ for 14 transitions known to ~0.1% precision. The results from our 2017 update of the survey are shown in Fig. 1. Excellent consistency among the average $\mathcal{F}t$ values for all 14 transitions – an expected consequence of the conservation of vector current (CVC) – confirms the validity of the correction terms; and our recent measurement of ^{38}Ca decay [2,3], which closely compares a pair of mirror superallowed transitions with $A = 38$, further supports that validity.
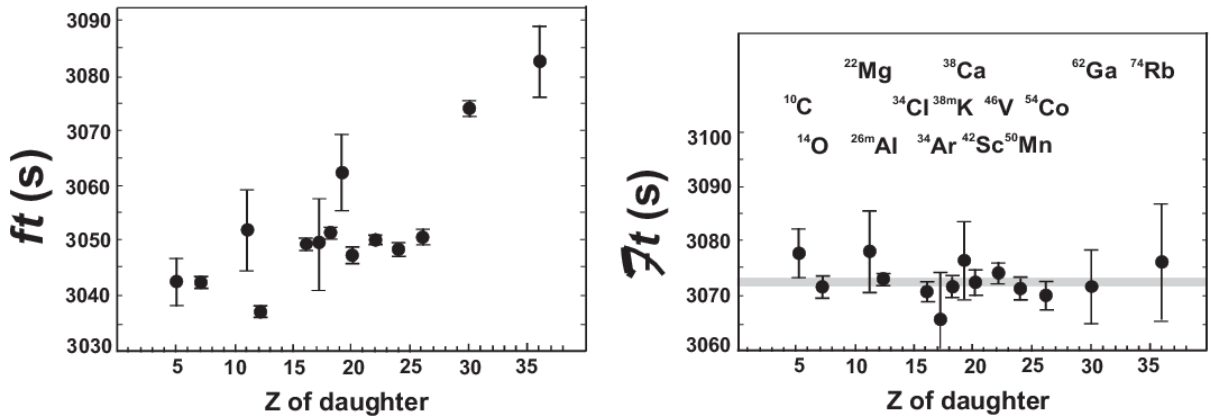
FIG. 1. Results from the 2015 survey [1] updated to 2017: The uncorrected *ft* values for the 14 best known superallowed decays appear on the left; the same results but incorporating the radiative and isospin-symmetry-breaking correction terms are on the right. The grey band in the right panel is the average $\mathcal{F}t$ value and its uncertainty.

The resultant average $\mathcal{F}t$ value, when combined with the muon lifetime, yields the up-down quark-mixing element of the Cabibbo-Kobayashi-Maskawa (CKM) matrix, $V_{ud} = 0.97420(21)$, a result that is consistent with, but more precise than, values we have obtained in previous analyses of superallowed β decay. The unitarity test on the top row of the matrix becomes $|V_{ud}|^2 + |V_{us}|^2 + |V_{ub}|^2 =$

0.99962 (49) if the Particle Data Group recommended value for V_{us} is used. Finally, from the $\mathcal{F}t$ -value data we also set limits on the possible existence of scalar interactions.

This result is not only a significant verification of the standard model but the uncertainty quoted on the sum provides a tight limit on any possible new physics beyond the standard model, such as right-hand currents, extra Z bosons or supersymmetric models. In short, superallowed $0^+ \rightarrow 0^+$ beta decay provides a high-profile application of nuclear-physics measurements to the study of fundamental symmetries, a subject of vital interest to both nuclear and particle physicists. Although much has already been achieved in this field by nuclear physicists, improvements are still possible. Reducing the uncertainty on the unitarity sum – and, with it, the scope for new physics – remains the primary goal of our research program.

Our approach follows from the observation [1] that the second largest contributor to the uncertainty in V_{ud} is the theoretical uncertainty in the nuclear-structure-dependent corrections, δ_{NS} and δ_C, used in the derivation of the $\mathcal{F}t$ values. Though these corrections are only of order 1%, their effect is very significant: The two panels of Fig. 1 show the result of applying the nuclear-structure-dependent corrections, δ_{NS} and δ_C (together with δ'_R, which is nearly independent of Z). Obviously they act very well to remove the considerable "scatter" in ft values apparent in the panel on the left, replacing it with the consistent set of corrected $\mathcal{F}t$ values appearing on the right. Since these corrections were determined [4] completely independently of the superallowed decay data, this consistency in $\mathcal{F}t$ values is already a powerful validation of the calculations, but obviously the remaining uncertainty still influences the final result for V_{ud}.

Even though the 2015 survey [1] included more than 222 individual measurements (and the 2017 update includes at least a dozen more) relating to 14 precisely known ft values, it is still possible for well selected experiments to make real improvements in the validation tests of the nuclear-structure-dependent correction terms. At TAMU we are currently focusing on adding to the ft-value list new superallowed transitions, selected from amongst those with *large* calculated corrections. If the ft values measured for cases with large calculated corrections also turn into corrected $\mathcal{F}t$ values that are consistent with the others, then this must verify the calculations' reliability for the existing cases, which have smaller corrections. We are studying decays from $T_z = -1$ parent nuclei, which consistently have higher predicted structure-dependent correction terms than the well-known $T_z = 0$ cases.

Of particular importance are the four $T_z = -1$ parent nuclei – ^{26}Si, ^{34}Ar, ^{38}Ca and ^{42}Ti – whose decays are mirrors to well-known superallowed decays from $T_z = 0$ parents. Specifically, the mirror-decay pairs are ^{26}Si $\rightarrow$ ^{26m}Al $\rightarrow$ ^{26}Mg, ^{34}Ar $\rightarrow$ ^{34}Cl $\rightarrow$ ^{34}S, ^{38}Ca $\rightarrow$ ^{38m}K $\rightarrow$ ^{38}Ar and ^{42}Ti $\rightarrow$ ^{42}Sc $\rightarrow$ ^{42}Ca. Their importance stems from our observation that the ratio of mirror ft values for such cases is very sensitive to the model used to calculate the small isospin-symmetry-breaking corrections δ_{NS} and δ_C. The details have been described in our report on the first measurement of a mirror pair, with $A = 38$ [2]. Until very recently, none of the $T_z = -1$ parent decays was known precisely enough to provide a statistically significant constraint on the correction terms via the ratio of mirror ft values, but we are now well on our way to rectifying this situation.

After a long period of incremental upgrades to our experimental techniques, we succeeded in pushing our precision in branching ratio measurements close to ±0.1%, our ultimate goal. This is crucial

for the characterization of $T_z = -1$ parent decays, which – unlike $T_Z = 0$ decays – exhibit a number of strong Gamow-Teller branches that compete with the superallowed Fermi branch. A first demonstration of our success in this endeavor was our measurement of the superallowed branching ratio for the decay of ^{38}Ca ($t_{1/2} = 444$ ms) to a precision of $\pm 0.2\%$, where that precision was actually limited by counting statistics, not systematics [3,4]. We have now added another precise branching ratio [5] for a $T_z = -1$ parent nucleus, ^{26}Si ($t_{1/2} = 2.245$s), also with a precision of $\pm 0.2\%$, limited by statistics. To our knowledge, these are the most precise direct branching-ratio measurements ever made for short-lived beta emitters. They also provide the first two mirror pairs of $0^+ \rightarrow 0^+$ superallowed emitters with ft values that are precise enough to distinguish meaningfully between the Saxon-Woods-based radial-overlap correction, δ_{C2}, and the one based on Hartree-Fock radial wave functions. Both favor the former over the latter. We now await results from the remaining pairs at A=34 and A=42.

We are now well embarked on the measurement of the remaining two accessible pairs. We have already completed measurements of the half-life [6] and branching ratio for the superallowed decay of ^{34}Ar. However, the branching-ratio result depends critically on the gamma-branching of the 666-keV level populated by beta decay in the daughter, ^{34}Cl: A possible weak branch from this level has 519 keV, which would be masked in our spectrum by the tail of the strong 511-keV annihilation peak. We are planning a (p, γ) measurement at Notre Dame to determine the relative intensity of this branch before we publish our results. Finally, we have completed a successful measurement of the half-life of ^{42}Ti, which is currently being analyzed [7]. A measurement of the branching ratio is scheduled for late May 2018.

We have now completed and published [8] our measurement of the half-life of another $T_Z = -1$ superallowed emitter, ^{30}S. It is not a member of a mirror pair of decays since its daughter is not a superallowed emitter; however its calculated isospin-symmetry-breaking correction is the second highest among all the superallowed transitions with $A \leq 54$, so it would be a useful case to characterize precisely. So far, the branching ratio is not well known.

With a somewhat different focus, in late 2015 we began a new measurement of the branching ratio for the superallowed decay of ^{10}C. Currently the uncertainty on the branching ratio dominates the uncertainty in the ^{10}C $\mathcal{F}t$ value. However, more interesting than just the precision of the $\mathcal{F}t$ value itself is its relationship to the world average of $\mathcal{F}t$ values for transitions in heavier nuclei, since the ^{10}C transition is the most sensitive to the possible presence of a scalar current. Currently the $\mathcal{F}t$ value for ^{10}C is slightly higher than the world average $\mathcal{F}t$ value, with an error bar that just about touches the world average value's error bar. If a more precise $\mathcal{F}t$ value of ^{10}C were found to deviate with greater statistical significance, it would be a signal for the existence of a scalar current. This work is still in progress [9].

[1] J.C. Hardy and I.S. Towner, Phys. Rev. C **91**, 025501 (2015).
[2] H.I. Park, J.C. Hardy, V.E. Iacob, M. Bencomo, L. Chan, V. Horvat, N. Nica, B.T. Roeder, E. Simmons, R.E. Tribble, and I.S. Towner, Phys. Rev. Lett. **112**, 102502 (2014).
[3] H.I. Park, J.C. Hardy, V.E. Iacob, M. Bencomo, L. Chen, V. Horvat, N. Nica, B.T. Roeder, E. McCleskey, R.E. Tribble, and I.S. Towner, Phys. Rev. C **92**, 015502 (2015).
[4] I.S. Towner and J.C. Hardy, Phys. Rev. C **77**, 025501 (2008).

[5] M. Bencomo *et al*., *Progress in Research,* Cyclotron Institute, Texas A&M University (2017-2018), p. I-17.

[6] V.E. Iacob *et al*., *Progress in Research,* Cyclotron Institute, Texas A&M University (2017-2018), p. I-22.

[7] H.I. Park *et al*., *Progress in Research,* Cyclotron Institute, Texas A&M University (2017-2018), p. I-24.

[8] J.C. Hardy *et al*., *Progress in Research,* Cyclotron Institute, Texas A&M University (2017-2018), p. I-20; and V.E. Iacob *et al*., Phys. Rev. C **97**, 035501 (2018).

[9] T. Eronen *et al*., *Progress in Research,* Cyclotron Institute, Texas A&M University (2017-2018), p. I-15.

Superallowed beta branching-ratio measurement of ^{10}C

T. Eronen, J.C. Hardy, V. Iacob, H.I. Park, M. Bencomo, L. Chen, V. Horvat, N. Nica,
B.T. Roeder, and A. Saastamoinen

Superallowed beta decays yield the most precise value for V_{ud}, the top-left matrix element of the Cabibbo-Kobayashi-Maskawa (CKM) quark-mixing matrix [1,2]. The ^{10}C superallowed β-decay is one of the 14 transitions that are included in the determination. In addition to contributing to the CKM matrix, ^{10}C decay is also sensitive to the possible existence of a scalar current, the existence of which would signal the presence of new physics beyond the Standard Model. A scaler current would manifest itself by causing the comparative half-life, or $\mathcal{F}t$ value, for the ^{10}C superallowed transition to deviate from the world-average value established from the average of the other 13 transitions. Currently, the ^{10}C $\mathcal{F}t$ value is slightly above the average.

The beta decay of ^{10}C is rather simple, as shown in Figure 1. It populates either the 0^+ state at
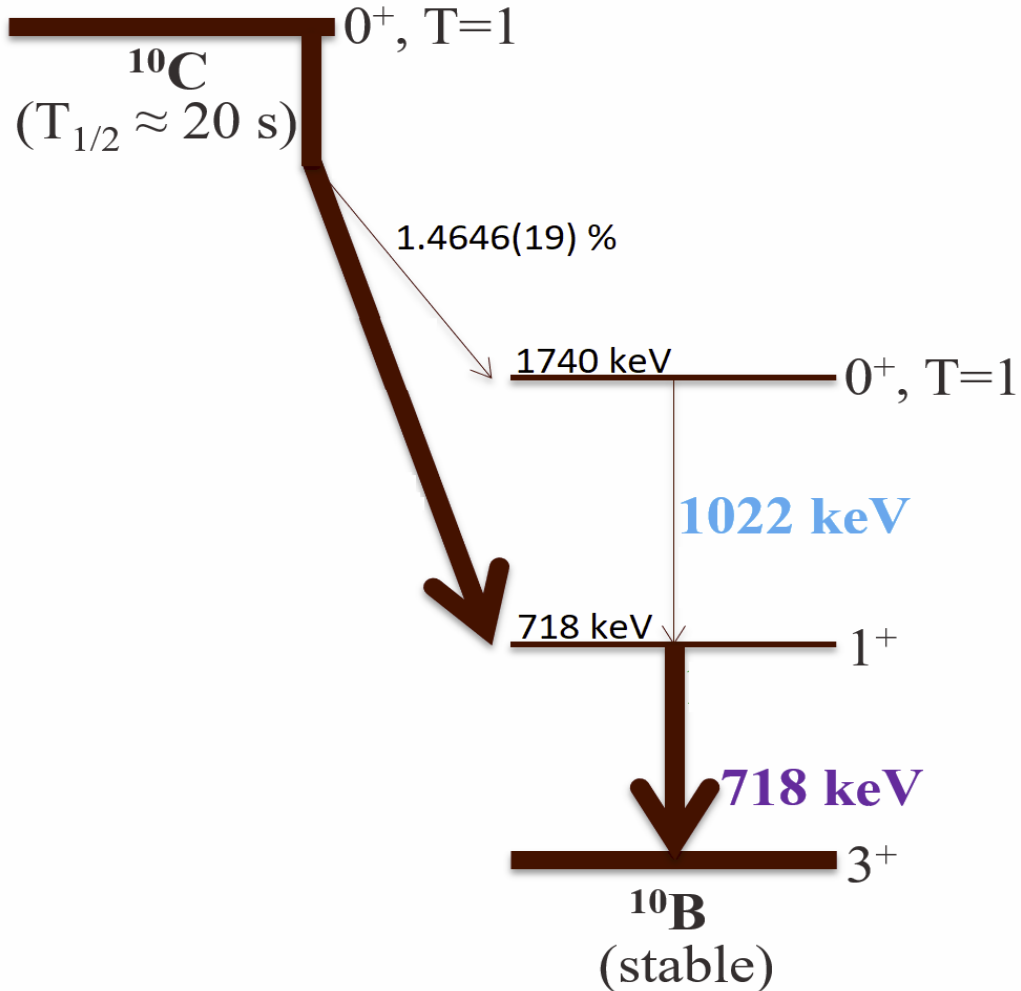
FIG. 1. Beta decay of ^{10}C to states in ^{10}B. The superallowed $0^+ \rightarrow 0^+$ transition is between the ground state of ^{10}C and the state at 1740 keV in ^{10}B.

1740 keV (by the superallowed branch) or the 1^+ state at 718 keV in ^{10}B. Feeding to the 0^+ state is rather weak – the currently adopted value is 1.4646(19)% [2] – rendering the high precision branching ratio determination experimentally challenging. Another difficulty is that the superallowed 0^+ state depopulates by the emission of a 1022 keV gamma-ray, which is exactly twice the energy of annihilation radiation. Since ^{10}C is a positron emitter, there is no lack of annihilation radiation present and, at the high event rate needed to attain sufficient statistics for the branching-ratio measurement, the pile-up of two 511 keV gamma rays must be carefully accounted for.

In September 2017, we had our third run in pursuit of a new measurement of the ^{10}C branching ratio. The earlier two runs took place in 2015 and 2016 [3]. The 2015 experiment utilized a plastic scintillator and the 2016 one, a gas counter for beta detection. The gas counter was chosen in order to get a factor-of-two boost to the beta-detection efficiency but, unfortunately, it also substantially increased the 511+511 keV pile-up as well as Compton scattering. Also, our well-calibrated germanium detector suffered a vacuum failure during the run, though a replacement detector allowed us to continue the run after some delay. In the end, no reliable branching ratio could be obtained from this measurement.

Since the statistics collected during the first experiment in 2015 were rather low, it was decided to run one more time with that configuration (*i.e.* with the plastic scintillator as beta detector). The decay rate of ^{10}C in the September-2017 run was kept just at the maximum tolerable level, which insured that pile-up would not be a limiting effect. Adding the data from both the 2015 and 2017 runs roughly triples our statistics. Analysis is in progress.

[1] J.C. Hardy *et al., Progress in Research,* Cyclotron Institute, Texas A&M University (2017-2018), p. I-11.
[2] J.C. Hardy and I.S. Towner, Phys. Rev. C **91**, 025501 (2015).
[3] T. Eronen *et al.*, *Progress in Research*, Cyclotron Institute, Texas A&M University (2016-2017), p. I-15.

Superallowed β-decay branching ratio measurement of ^{26}Si

M. Bencomo, J.C. Hardy, V.E. Iacob, H.I. Park, L. Chen, V. Horvat, N. Nica, B.T. Roeder,
A. Saastamoinen, and I.S. Towner

We have measured the branching ratios for the superallowed $0^+ \rightarrow 0^+$ β^+ emitter ^{26}Si (Fig. 1). Since the Q_{EC} value[1] and half-life [2] have already been measured, the branching ratio for the superallowed transition allows us to determine the ft value. This completes the second pair of mirror superallowed transitions between T = 1 states, ^{26}Si $\rightarrow$ ^{26m}Al and ^{26m}Al $\rightarrow$ ^{26}Mg. Previous measurements of the A=38 mirror transitions, ^{38}Ca $\rightarrow$ ^{38m}K and ^{38m}K $\rightarrow$ ^{38}Ar, showed that the ratio of mirror ft values is very sensitive to the model used to calculate the small isospin symmetry-breaking corrections required to extract V_{ud}. In calculating this correction both Woods-Saxon (WS) and Hartree-Fock (HF) radial wave functions have been used, with the experimental results from the first pair favoring the Woods-Saxon option [3]. In an effort to determine if this preference can be generalized, we extended our measurements to ^{26}Si.
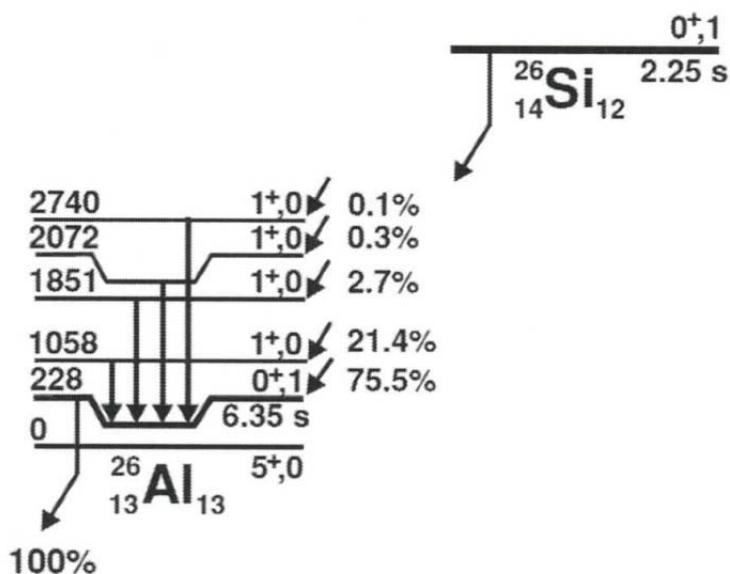
FIG. 1. Decay scheme of ^{26}Si showing only those features of relevance to the superallowed β decay. All energies are in keV. The data are taken from Ref. [4] and show the branching ratios as known before our current work.

Previously, we reported the experimental measurement of ^{26}Si as well as the procedure for analysis and a preliminary result [5]. Most of the experimental corrections needed to determine a branching ratio to the superallowed branch with a precision comparable to those of the half-life and Q_{EC} value were also reported. The analysis for the branching-ratio measurement has now been finalized. The correction for the detection of γ rays in the β detector was the last one to be determined. This correction is

very small, of the order of 0.0012%, and does not have a large impact on the results but it still needs to be taken into account for a high-precision measurement.

We have now checked all corrections using different techniques and have confirmed our previous results. With all these corrections taken into account, the branching ratio to the 1058 keV state of ^{26m}Al, which leads to emission of an 829-keV γ ray, is determined to be 21.28(12)%. Using the relative intensities of the other weaker γ-ray peaks we determine the total of all Gamow-Teller branches to be 24.28(15)%, and consequently establish the superallowed branch to be 75.72(15)%.

Based on the half-life and Q_{EC} values taken from the most recent survey [6], and making use of the relation

$$t = \frac{t_{1/2}}{R}(1 + P_{EC}),$$

we can determine the ft value of ^{26}Si. With the half-life, $t_{1/2} = 2245.3(7)$ ms; the electron-capture fraction, $P_{EC} = 0.0638\%$; the branching ratio, R = 0.7572(15); and $f = 1028.03(12)$; the ft value of ^{26}Si becomes 3050.3(57) s. The ^{26m}Al ft value is known to be 3037.38 ± 0.58 s. Thus the ratio of ft values for the $A=26$ pair is:

$$\frac{ft^a}{ft^b} = \frac{3050.3 \pm 5.7}{3037.38 \pm 0.58} = 1.0043(19)$$

As with the $A=38$ pair, this result can be seen to favor the use of Wood-Saxon radial wave functions (see Fig. 2). The result is similar to the one we reported previously [5] but it has smaller uncertainties.
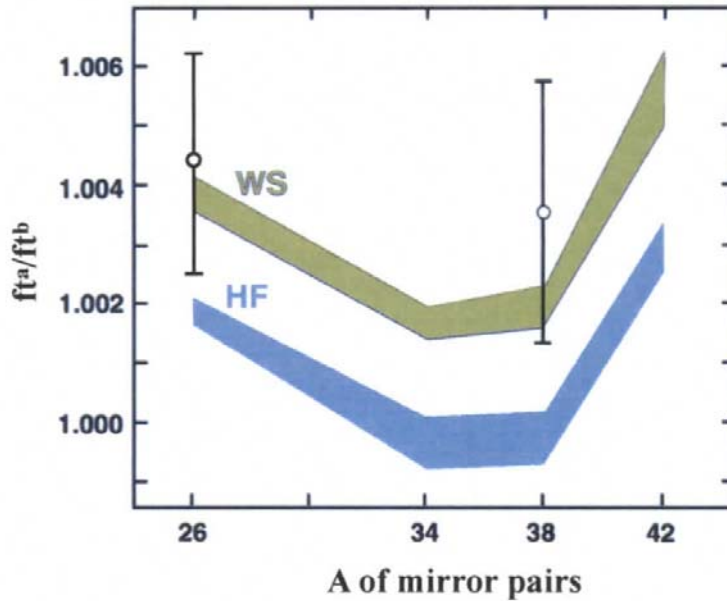
FIG. 2. Result for the ratios of ft values for the A = 26 and 38 pairs, compared to theoretical predictions.

[1] T. Eronen *et al.*, Phys. Rev. C **79**, 032802(R) (2009).

[2] V.E. Iacob, J.C. Hardy, A. Banu, L. Chen, V.V. Golovko, J. Goodwin, V. Horvat, N. Nica, H.I. Park, L. Trache, and R.E. Tribble. Phys. Rev. C **82**, 035502 (2010).

[3] H.I. Park *et al.* , Phys. Rev. Lett. **112**, 102502 (2014).

[4] J.C. Hardy and I.S. Towner, Phys. Rev. C **79**, 055502 (2009).

[5] M. Bencomo *et al.*, *Progress in Research*, Cyclotron Institute, Texas A&M University (2016-2017) p. I-7.

[6] J.C. Hardy and I.S. Towner, Phys. Rev. C **91**, 025501 (2015).

Half-life of the superallowed beta emitter, ^{30}S

J.C. Hardy, I.S. Towner, V. E. Iacob, H.I. Park, N. Nica, M. Bencomo, V. Horvat, and L. Chen

The superallowed $0^+ \rightarrow 0^+$ β-decay branch from ^{30}S is not one of the fourteen $0^+ \rightarrow 0^+$ transitions that have been measured to ±0.1% precision or better. The most recent survey of world data [1] gives ft = 3005(41) s and $\mathcal{F}t$ = 3016(41) s for the ^{30}S transition, a precision of ±1.35%, which is more than a factor of 10 too large for it to contribute to fundamental tests of the weak interaction or of isospin symmetry breaking [2]. The predominant contribution (±1.34%) to the large uncertainty is from the branching ratio, which is based on a single 1963 measurement. Though the half-life is known much more precisely, it is still not adequate since its world-average value [1] is quoted to ±0.14% and that is based on two measurements, only one of which has 0.14% precision. Alone among the three required experimental quantities, the Q_{EC} value can be considered to be measured with sufficient precision: Its contribution to the ft-value uncertainty is merely ±0.03%.

The ^{30}S case is an interesting one because its calculated nuclear-structure-dependent correction term is unusually large: $viz.$ $\delta_C - \delta_{NS}$ = 1.040(32)%. We argue that such a case offers a good test of the correction terms themselves: If the measured ft value for such a transition yields a corrected $\mathcal{F}t$ value that is consistent with the other well-known cases, then this serves to verify the calculations' reliability for the existing cases, which have smaller corrections [2].

We have chosen to begin with a measurement of the half-life of ^{30}S. Quite apart from its ultimate benefit in contributing to a usefully precise ft value, the measurement also offers an excellent opportunity to verify one of the techniques we have used in previous half-life measurements. Unlike most $T_Z = -1$ superallowed β emitters, ^{30}S does not feed a second $0^+ \rightarrow 0^+$ β transition from its daughter. The 0^+, $T=1$ state populated in ^{30}P decays electromagnetically to the ground state, which proceeds by ordinary allowed β decay to ^{30}Si with a half-life of 2.498(4) min. Thus there is a very clean separation between the ^{30}S half-life of 1.18 s and that of its daughter, which is more than a factor of 100 longer. In the $T_Z = -1$ cases we have measured before, the parent and daughter half-lives differ by only a factor of ~2, and because we detect the positrons from both decays together in the same detector, we must use the parent-daughter linkage as input to the fit in order to extract the parent half-life with any precision. This requires us to know the time-dependence of the source deposit rate and also to incorporate the subtle difference between the parent and daughter detection efficiencies for positrons; together, these effects can introduce systematic uncertainties. In the case of ^{30}S, the large difference between parent and daughter half-lives makes it possible to extract a result by treating the two decays as independent components and to compare that half-life result to the one obtained when the linkage between parent and daughter is enforced. This is our first opportunity to make such a comparison.

The experimental details of our measurement were presented in last year's Annual Report [3]. The analysis of the results is now complete and a paper describing them has been published [4]. Our final result for the ^{30}S half-life, obtained with the parent and daughter decays unlinked in the fit, was 1.17992(34) s, a result with ±0.029% precision, which is a factor of 5 better than the most precise previous measurement. If the two decays were treated as being linked, our result became 1.17986(34), in

complete agreement. This convincingly validates the method we have used in the past to determine precise half-lives for $T_Z = -1$ superallowed emitters.

As a byproduct of this measurement, we determined the half-life of the daughter, ^{30}P, to be 2.501(2) min. This agrees with, but is a factor of 2 more precise than, the literature value.

[1] J.C. Hardy and I.S. Towner, Phys. Rev. C **91**, 025501 (2015).
[2] J.C. Hardy *et al.*, *Progress in Research,* Cyclotron Institute, Texas A&M University (2017-2018), p. I-11.
[3] J.C. Hardy *et al.*, *Progress in Research,* Cyclotron Institute, Texas A&M University (2016-2017), p. I-10.
[4] V.E. Iacob *et al.*, Phys. Rev. C **97**, 035501 (2018).

[34]Ar half-life

V.E. Iacob and J.C. Hardy

Our recent work on the half-life of [30]S [1] gave us a unique opportunity to test the data reduction techniques and the corrections we use in parent-daughter decaying systems. In contrast to the[34]Ar-[34]Cl pair with half-lives in a ratio very close to 1:2, the [30]S-[30]P pair has half-lives that differ from one another by 2 orders of magnitude. This allows for fits that treat the combined parent-daughter decays either as two independent components or as a parent-daughter linked system. Making use of this feature, we proved that the use of a small rate-dependent correction makes a small but not negligible improvement in the fit. This prompted us to revisit the half-life analysis of [34]Ar reported in [2].

To understand the origin of the rate-dependent correction, consider how the detection efficiency of our gas proportional counter varies as a function of the applied anode voltage. We measured this before and after the [34]Ar run using a [90]Sr-[90]Y β source. Fig. 1 presents the relevant part of the response function for the three discriminator thresholds used in the experiment: 150 mV, 200 mV and 250 mV. The region where the counting rate is almost constant, the "plateau", is centered on 2600 V and extends for about 150 V above and below this value.
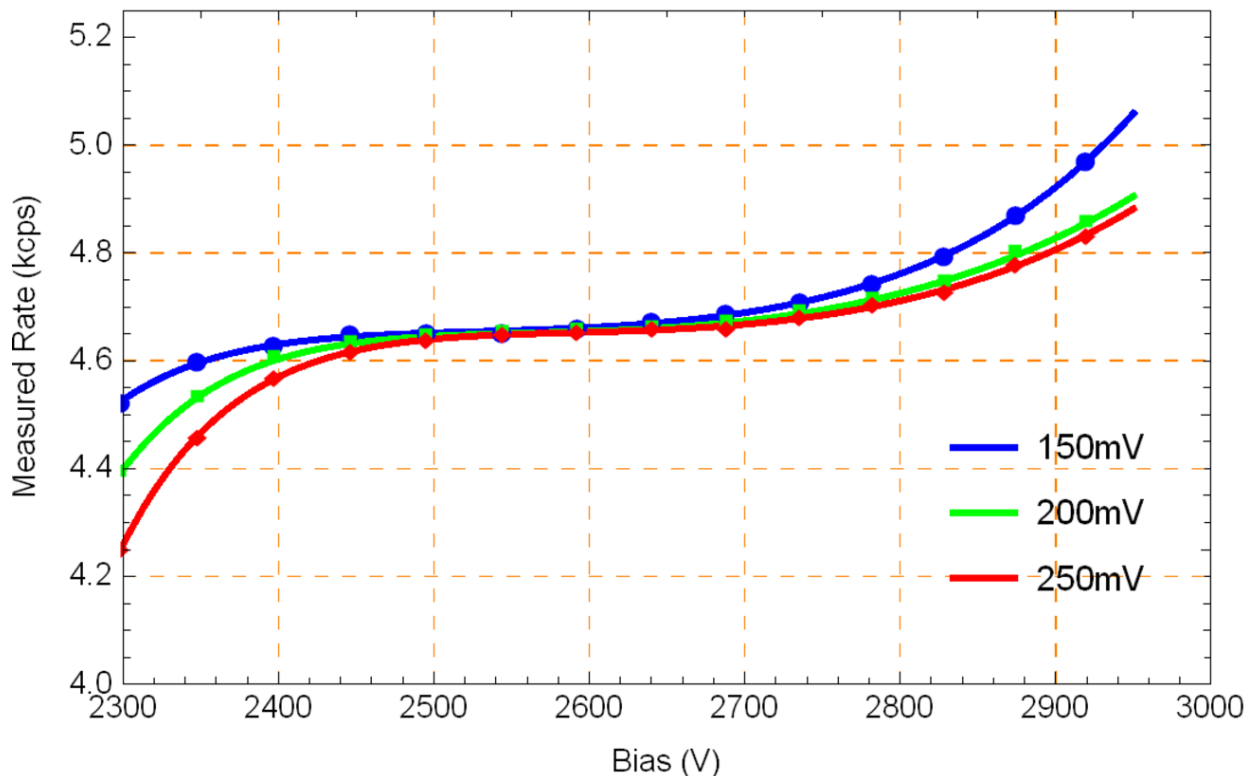
FIG. 1. The "plateau" of the 4π gas counter, for the three discriminator thresholds used in the [34]Ar run.

While the slope of the counting-rate versus anode voltage is small (a change of less than ~0.5% per 100 V), it is not zero. As the counting rate decreases during the decay of the measured sample, the

current through the detector decreases as well. This in turn leads to a decreased voltage across the resistor that biases the anode wires (100 MΩ), leaving a slightly higher voltage on the anode. Thus, as the counting rate decreases, the anode voltage increases, making the detector (slightly) more efficient.

Currently we are re-fitting the ^{34}Ar data with the inclusion of this correction.

[1] J.C. Hardy, I.S. Towner, V. E. Iacob, H.I. Park, N. Nica, M. Bencomo, V. Horvat, and L. Chen, *Progress in Research*, Cyclotron Institute, Texas A&M University (2017-2018) p.I-20; V.E. Iacob *et al.*, Phys. Rev. C **97**, 035501 (2018).
[2] V.E. Iacob, J.C. Hardy, M. Bencomo, L. Chen, V. Horvat, N. Nica, H.I. Park, B.T. Roeder, and A. Saastamoinen, *Progress in Research,* Cyclotron Institute, Texas A&M University (2015-2016) p. I-14.

Precise half-life measurement of ^{42}Ti

H.I. Park, J.C. Hardy, V.E. Iacob, V. Horvat, M. Bencomo, L. Chen, N. Nica, B.T. Roeder,
and A. Saastamoinen

We repeated the half-life measurement of ^{42}Ti after dealing with the problems [1] we encountered in the previous experiment. Again we used the ^{4}He(^{40}Ca, 2n)^{42}Ti reaction in inverse kinematics to produce ^{42}Ti at a primary ^{40}Ca beam energy of 32 MeV/nucleon. With extraction slits on the MARS recoil spectrometer set tight, the ^{42}Ti samples were deposited near the back of the collection tape, thus ensuring that most of the produced impurities passed through the tape without stopping, leaving behind a rather pure ^{42}Ti sample. In addition to acquiring data from the proportional gas counter with our standard analogue electronics, we also ran a TDC-based system in parallel so that we could record the absolute time information event-by-event for the same data. The use of this second data-taking method offers a means to test for possible systematic effects in the measurement, as well as an opportunity to improve our data-acquisition techniques for all half-life measurements.

At the beginning of the experiment, we observed an unphysical structure in the middle of cumulative time-decay spectrum recorded at the lowest discriminator setting. The structure was more pronounced as the tape reel on the take-up deck of the tape-transport system became heavier as more tape wound onto it. This led us to conclude that the cause must be noise pickup arising from the servo-motors that control the tape reels. We assessed the effect of this pickup by measuring a background spectrum, without beam but with the tape-transport system operating normally. Under these conditions we found that for the first 300 cycles the background rate remained at less than 1 count/s, the normal rate with the gas counter in our experimental area; but as the cycles increased beyond 300 the pickup appeared. When we recorded the background spectrum with the 300-cycle restriction, there was no sign of the structure caused by unwanted noise signals from the servomotors. Consequently, throughout the experiment, we rewound the tape manually after every 300 cycles from the beginning of the tape roll, and routinely took 300-cycle cumulative background spectra to ensure the data were free of pickup for the various combinations of detector settings (bias / discriminator level / dead-times) used.

Our current analysis focuses on comparing the ^{42}Ti half-life result determined from two different approaches, one in which the linkage between the parent and daughter activities is enforced and the other in which their activities are treated as two independent decays.

[1] H.I. Park *et al*., *Progress in Research*, Cyclotron Institute, Texas A&M University (2016-2017), p. I-15.

Tests of internal-conversion theory

J.C. Hardy, N. Nica, V.E. Iacob, and M.B. Trzhaskovskaya[1]

[1]*Petersburg Nuclear Physics Institute, Gatchina RU-188300, Russia*

Except for the very lightest nuclei, where internal conversion is weakest, most nuclear decay schemes depend upon calculated internal conversion coefficients (ICCs). Electromagnetic decay intensities are usually determined from gamma-ray measurements combined with calculated ICCs. Consequently, the reliability of the calculations is a matter of some importance, especially where precise decay-scheme data are required, for example in detector calibration. Until quite recently, although various tables of calculated ICCs were readily available, most ICC measurements were relatively imprecise, being aimed only at determining transition multi-polarities. Rarely were they precise enough to distinguish among different calculations or indeed to establish if any of the calculations reproduced reality. We are rectifying this deficiency.

When we began our program of precise measurements in 2004, the then-current survey of world data [1] included barely twenty ICC values measured to ±2% or better, and eighty more with up to 5% precision. They were divided 45-55 between K-shell ICCs (α_K) and total ICCs (α_T), respectively. Based on these data, the authors concluded that all previous tables of ICCs exhibited a 3% systematic bias, but that a table by Band *et al.* [2], which was new at the time, agreed well with the data (within ~1%). This new table was calculated in the framework of the Dirac-Fock method, with the exchange between bound electrons as well as between bound and free electrons treated exactly, an important improvement. Unfortunately, however, the best agreement with the available experimental data was achieved with a version of this calculation in which the final-state electron wave-function was computed in a field that did not include any provision for the atomic vacancy created by the conversion process. Yet the vacancy must be there, since atomic-shell-vacancy lifetimes are known generally to be much longer than the time for a conversion electron to leave the vicinity of the atom. This was an unsatisfactory paradox!

We found ourselves uniquely positioned to potentially resolve the paradox. For our program to measure branching ratios for superallowed β emitters, we had efficiency calibrated an HPGe detector to high precision over a wide range of energies. This would allow us to measure the K x rays and γ rays from a converted transition in the same well-calibrated detector, thus affording access to the transition's α_K value with a minimum of systematic uncertainty. For an isolated electromagnetic transition that converts in the atomic K shell, the observation of a K x ray is a signal that an electron conversion has taken place; whereas a γ ray indicates that no conversion has taken place. If both x rays and γ rays are recorded in a measurement, then the value of α_K is given by

$$\alpha_K \omega_K = \frac{N_K}{N_\gamma} \cdot \frac{\varepsilon_\gamma}{\varepsilon_K} , \tag{1}$$

where ω_K is the K-shell fluorescence yield; N_K and N_γ are the respective peak areas of the K x rays and the γ ray; and ε_K and ε_γ are the respective detector photopeak efficiencies.

Not many nuclei feature a single isolated transition, but a number of cases have small enough interference from other converted transitions that the corrections to Eq. (1) are manageable, allowing the α_K value still to be extracted with percent precision. Since we began this program, we have published α_K values for $E3$ transitions in two nuclei, [111]Cd [3] and [134]Cs [4,5], and $M4$ transitions in six nuclei, [119]Sn [6,7], [125]Te [8], [127]Te [9], [137]Ba [4,5], [193]Ir [10, 11] and [197]Pt [12].

We are currently analyzing the data collected on an $E3$ transition in [103]Rh [13] and have begun to take data on another $M4$ transition, in [93]Nb [14].

The results from our completed measurements appear in Fig. 1, which is taken from a recent publication [15]. In the figure the results are compared with two theoretical models, one that ignores the atomic vacancy and one that includes it. It is immediately evident that the data are completely inconsistent with the no-vacancy theory and in remarkable agreement with the vacancy-inclusive theory. This is consistent with the known vacancy lifetimes, and resolves the earlier paradox.
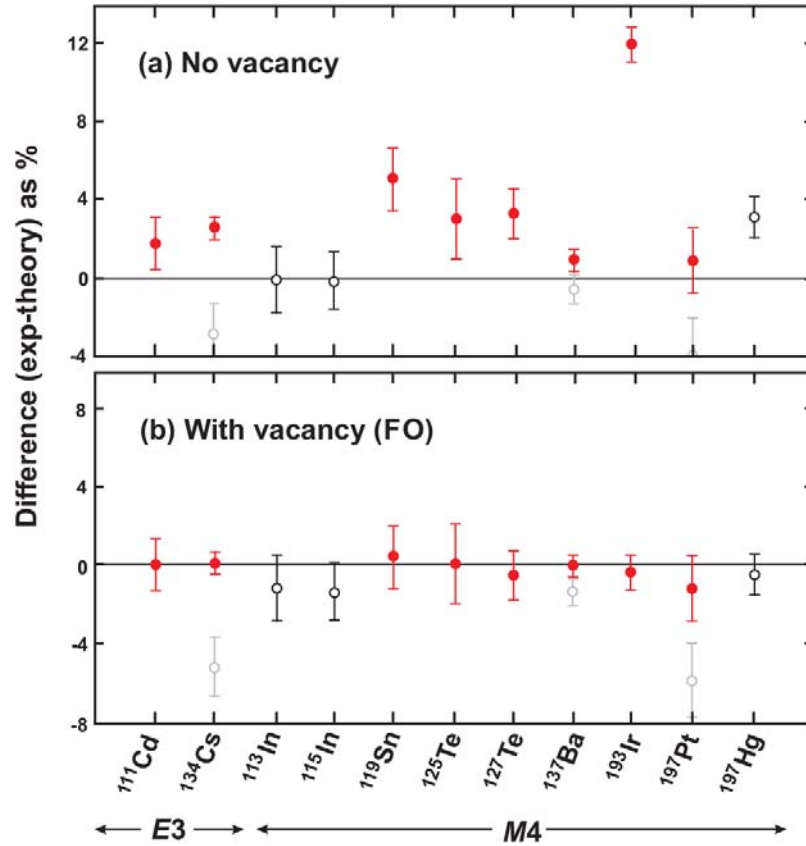
FIG. 1. Percentage differences between the measured and calculated α_K values for the Dirac-Fock calculations with and without provision for the atomic vacancy. Solid (red) circles are our measurements; open circles refer to pre-2002 results, the ones in gray having been replaced. The figure shows all α_K values for high-multiplicity transitions (E3 and above) that are known to ±2% or better.

A few of the cases we measured were chosen not because they were particularly sensitive to the vacancy/no-vacancy choice in the calculations, but because previous results disagreed with *both* types of

calculation. These discrepancies have been removed as well. Note though that among the eleven precisely measured α_K values in Fig. 1, there are eight that statistically distinguish between the vacancy and no-vacancy calculations, and they all present a consistent picture that favors inclusion of the atomic vacancy in ICC calculations. All but one of these cases come from our work.

[1] S. Raman, C.W. Nestor Jr., A. Ichihara, and M.B. Trzhaskovskaya, Phys. Rev. C **66**, 044312 (2002).

[2] I.M. Band, M.B. Trzhaskovskaya, C.W. Nestor Jr., P. Tikkanen, and S. Raman, At. Data Nucl. Data Tables **81**, 1 (2002).

[3] N. Nica, J. C. Hardy, V. E. Iacob, T.A. Werke, C.M. Folden III, L. Pineda, and M. B. Trzhaskovskaya, Phys. Rev. C **93**, 034305 (2016).

[4] N. Nica, J. C. Hardy, V. E. Iacob, W. E. Rockwell, and M. B. Trzhaskovskaya, Phys. Rev. C **75**, 024308 (2007).

[5] N. Nica, J. C. Hardy, V. E. Iacob, C. Balonek, and M. B. Trzhaskovskaya, Phys. Rev. C **77**, 034306 (2008).

[6] N. Nica, J. C. Hardy, V. E. Iacob, M. Bencomo, V. Horvat, H.I. Park, M. Maguire, S. Miller, and M. B. Trzhaskovskaya, Phys. Rev. C **89**, 014303 (2014).

[7] J.C. Hardy, N. Nica, V.E. Iacob, S. Miller, M. Maguire and M.B. Trzhaskovskaya, Appl. Rad and Isot. **87**, 87 (2014).

[8] N. Nica, J.C. Hardy, V.E. Iacob, T.A. Werke, C.M. Folden III, K. Ofodile, and M.B. Trzhaskovskaya, Phys. Rev. C **95**, 064301 (2017).

[9] N. Nica, J. C. Hardy, V. E. Iacob, H. I. Park, K. Brandenburg, and M. B. Trzhaskovskaya, Phys. Rev. C **95**, 034325 (2017); and *Progress in Research*, Cyclotron Institute Texas A&M University (2016-2017) p. I-28.

[10] N. Nica, J. C. Hardy, V. E. Iacob, S. Raman, C. W. Nestor Jr., and M. B. Trzhaskovskaya, Phys. Rev. C **70**, 054305 (2004).

[11] N. Nica, J. C. Hardy, V. E. Iacob, J. R. Montague, and M. B. Trzhaskovskaya, Phys. Rev. C **71**, 054320 (2005).

[12] N. Nica, J.C. Hardy, V.E. Iacob, J. Goodwin, C. Balonek, M. Hernberg, J. Nolan and M.B. Trzhaskovskaya, Phys. Rev. C **80**, 064314 (2009).

[13] N. Nica *et al., Progress in Research*, Cyclotron Institute Texas A&M University (2017-2018) p. I-28.

[14] E.E. Tereshatov *et al., Progress in Research*, Cyclotron Institute Texas A&M University (2017-2018) p. II-30.

[15] J.C. Hardy, N. Nica, V.E. Iacob, and M.B. Tezhaskovskaya, Appl. Rad. Isot. **134**, 406 (2018).

Tests of internal-conversion theory with precise γ- and x-ray spectroscopy:
The case of [103m]Rh studied via [103]Ru β[-] decay

N. Nica, J.C. Hardy, J.B. Bryant, C.M. Folden III, K. Glennon, V. Horvat, V.E. Iacob,
H.I. Park, T. Werke, and M.B. Trzhaskovskaya[1]
[1]*Petersburg Nuclear Physics Institute, Gatchina RU-188300, Russia*

Our program to test internal-conversion theory through precise measurements of K-shell conversion coefficients, α_K, [1] was recently reviewed in Ref. [2]. Eight previously studied transitions, two of *E*3 and six of *M*4 character, showed good agreement with the theory that included the atomic vacancy in the "frozen orbital" approach, while disagreeing strongly with the theory that ignored the vacancy. This conclusion led to the adoption of the "frozen orbital" calculations by the US and international nuclear data networks in the Evaluated Nuclear Structure Data File (ENSDF). The ninth case, described in Ref [2] as still being in progress, is the 39.7-keV, *E*3 transition in [103m]Rh. Its current status is described in this progress report.

The 56-min 39.7-keV isomer in [103m]Rh can be populated either by the 17.0-day [103]Pd electron-capture decay, or by the 39.2-day [103]Ru β[-] decay. Both parents, [103]Pd and [103]Ru, can be obtained conveniently by thermal neutron activation of stable targets; and by measuring both decay channels we gain access to both α_K and α_T for the transition of interest: [103]Pd decay yields the ratio $\alpha_K/(1+ \alpha_T)$ while [103]Ru decay yields α_K. We reported the former in last year's Progress in Research [3]. In this report we describe our progress on the [103]Ru study, which was started one year later.

Two separate runs were done based on different sources. First, we electroplated [nat]RuO$_2$ on thin 25-μm aluminum backing (99.99% pure natural Al, from Goodfellow, USA). We began by dissolving 4.5 mg of RuCl$_3$·xH$_2$O powder (99.98% pure, from Sigma Aldrich, USA) in 185 μL of 0.1 M HNO$_3$ and evaporating the solution to dryness under Ar gas. This step converted the ruthenium chloride into ruthenium nitrate. Each sample was then reconstituted with 5 μL of 0.1 M HNO$_3$ and 12 mL of anhydrous isopropanol. This solution was then transferred to an electrodeposition cell [4], and the ruthenium nitrate was electrochemically deposited using the molecular plating technique [5, 6]. The deposition voltage ranged from 150-500 V and the current density was kept between 2 and 7 mA/cm^2. Deposition times ranged from 4 to 5 hr. After deposition, the targets were baked in atmosphere at 200 °C for 30 min to convert the ruthenium nitrate to ruthenium oxide. The resulting targets had thicknesses between 465 and 545 μg/cm^2 as measured by mass. The plating efficiencies were between 40 and 55%. The [nat]RuO$_2$ targets were characterized using scanning electron microscopy (SEM) to ensure uniformity. An energy-dispersive X-ray spectrometry (EDS) analysis was performed to verify the elemental composition, and the EDS spectra showed that Ru and O were indeed the two main components of the target layer. Although we were unable to verify directly the 1:2 Ru:O ratio, this is the most commonly formed oxide of ruthenium. The targets were black in color, as expected of the RuO$_2$ compound.

One target was activated at the Nuclear Science Center of Texas A&M University at a thermal neutron flux of 7.5×10^{12} n/(cm^{2}s) for 20 h in early May 2017. Preliminary spectra were recorded during May, followed by three different main runs in June, after the shorter lived Ru isotopes had decayed out:

the longest lived was ^{97}Ru with T$_{1/2}$ = 2.9 days. Although we used very pure materials and a very thorough procedure for source preparation, with extreme care taken to prevent any external contamination, we found an unexpectedly prominent impurity, ^{153}Gd (T$_{1/2}$ = 240 day), whose K$_{\alpha1}$ and K$_{\alpha2}$ x-ray peaks at 40.9 and 41.5 keV, respectively, were partially superimposed on the relatively small 39.7-keV γ-ray peak of interest. As a result, the analysis of the 39.7-keV γ ray was compromised.

Consequently, we prepared another target using a different material: a pure metal foil of 0.9-μm ^{nat}Ru on 1.5-μm ^{nat}Cu. The sample was activated for 32 hours under identical conditions to the previous target in September 2017, and was then measured, naturally with the Ru facing the HPGe detector. In this case, an impurity analysis of the γ-ray spectrum revealed a number of heavy metal elements (^{182}Ta, ^{185}Os, ^{191}Os, and ^{192}Ir) but fortunately these did not interfere with the 39.7-keV γ ray or with the Rh *K* x rays of interest.

Although now there were no interfering impurities, the ^{103}Ru β$^-$ decay populates other transitions in ^{103}Rh, which include an internal-conversion component and thus produce rhodium *K* x rays. We carefully determined the strength of this contribution to be 11.3(2)% compared to that of the rhodium K x rays produced by the internal conversion of the 39.7-keV transition γ ray. In addition, some of the γ rays from these competing transitions, especially the strong one at 497.1 keV, were able to excite the x-ray florescence of the ruthenium target material. In the HPGe spectrum, the Rh and Ru K x rays were unresolved so, in order to determine the contribution from these florescence x-rays, we also collected spectra with a small Si(Li) detector, whose energy resolution was sufficient to enable us to separate the two. As a result we concluded that the contribution of the fluorescence x rays was 3.10(5)% [7].

Analysis is not yet complete.

[1] J.C. Hardy *et al.*, *Progress in Research*, Texas A&M University, Cyclotron Institute, 2017-2018, p. I-25.

[2] J.C. Hardy *et al.*, Appl. Radiat. Isot. **134**, 406 (2018).

[3] N. Nica *et al.*, *Progress in Research*, Texas A&M University, Cyclotron Institute, 2016-2017, I-23.

[4] D. A. Mayorov *et al.*, *Progress in Research*, Texas A&M University, Cyclotron Institute 2013, p. II-7.

[5] W. Parker and R. Falk, Nucl. Instrum. Methods **16**, 355 (1962).

[6] W. Parker, H. Bildstein, N. Getoff, H. Fischer-Colbrie, and H. Regal, Nucl. Instrum. Methods **26**, 61 (1964).

[7] V. Horvat *et al.*, *Progress in Research*, Texas A&M University, Cyclotron Institute, 2017-2018, p. IV-50.

Precision γ-ray branching-ratio measurements for long-lived fission products of importance to stockpile stewardship

K. Kolos,[1] A.M. Hennessy,[2] J.A. Clark,[3] J.C. Hardy,[4] V.E. Iacob,[4] G.E. Miller,[2] E. Norman,[5] H.I. Park,[4] G. Savard,[3] N.D. Scielzo,[1] A.J. Shaka,[2] M.A. Stoyer,[1] and A.P. Tonchev[1]

[1]*Lawrence Livermore National Laboratory, Livermore, California*
[2]*University of California at Irvine, Irvine, California*
[3]*Argonne National Laboratory, Argonne, Illinois*
[4]*Cyclotron Institute, Texas A&M University, College Station, Texas*
[5]*University of California at Berkeley, Berkeley, California*

This report describes the progress of our experimental program to precisely measure the β-decay branching ratios of ^{95}Zr, ^{144}Ce, and ^{147}Nd, which began in 2016. More information about the motivation and experimental approach can be found in our previous report [1]. The measurement described in [1] suffered from a β-detector efficiency that was ~15% lower than anticipated due to a high electronic threshold that was discovered after data collection. Therefore, we have repeated these measurements.

As in the previous experiment, high-purity samples of ^{95}Zr (150 Bq) and ^{147}Nd (1600 Bq) were collected on thin (40 μg/cm^2) carbon-foil backings using low-energy mass-separated beams of A=95 and 147 fission products from CARIBU at Argonne National Laboratory. The implanted samples were then shipped to Texas A&M where the decay-counting measurement took place. Because of its long half-life (284.91 d), we were able to reuse a previously-made ^{144}Ce (160 Bq) sample. The γ-ray and β-γ measurements were performed in the same geometry as our previous experiment: The sample was inserted in the middle of a 4π gas proportional counter for β-particle detection and was positioned 15.1 cm from the HPGe detector. We also improved the signal-to-background ratio in the γ-ray spectrum by a factor of 3 by adding a lead-plastic-copper layered shield around the HPGe detector. We performed multiple-day-long measurements with each sample, interleaved with background measurements. The β-γ coincidence spectra are shown on Fig.1.

A thorough analysis of the data is underway. We were able to collect sufficient statistics for a sub-percent uncertainty on all the measured sources: We have collected about 170k, 120k, and 40k β-γ coincidence counts for the most-intense γ-ray peaks in the decays of ^{147}Nd, ^{95}Zr and ^{144}Ce, respectively. We are investigating the systematic uncertainties associated with the measurement. The main challenges are establishing the β-detector and γ-ray detection efficiencies and determining the purity of the samples. The preliminary analysis shows the β detector performed as expected with an efficiency of 96-98% for β transitions with energies in the range, 100-800 keV. The experimental and simulated (GEANT4) efficiencies are in good agreement, as can be seen in Fig. 2. To determine the fraction of observed β-singles counts from the isotope of interest, the contributions from the decay of the daughter isotope and any contaminants must be taken into account. For the ^{95}Zr sample, the grow-in of the daughter ^{95}Nb accounted for about 20% of the activity; for the ^{144}Ce sample, the daughter ^{144}Pr has only a 17.28 minute half-life, so its contribution was 50%; For ^{147}Nd, the daughter ^{147}Pm has a 2.6 year half-life, and so it
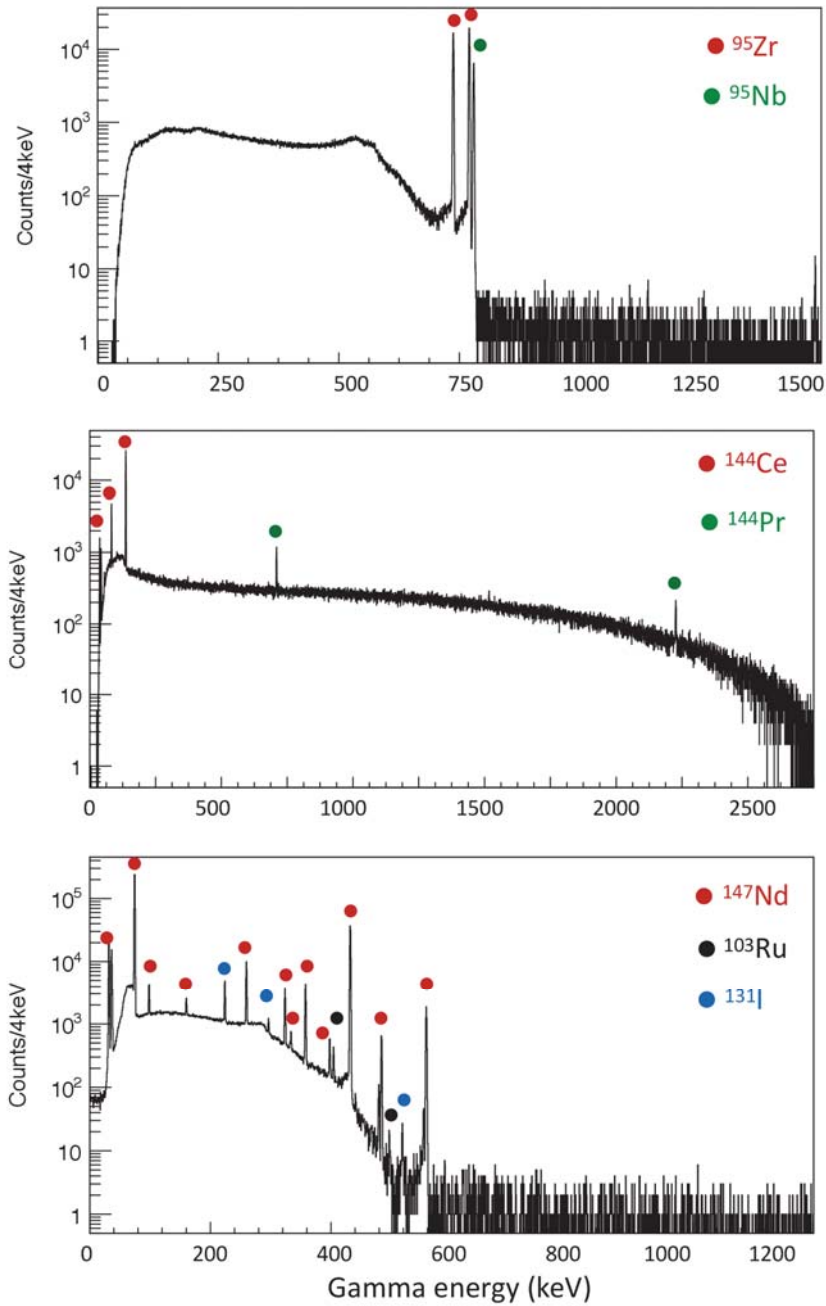
FIG. 1. The γ-ray energy spectra for β-γ coincidences for the ^{95}Zr (top), ^{144}Ce (middle), and ^{147}Nd (bottom) samples.

contributed only about 0.5%. The only additional contaminants observed in any of the samples were in the case of ^{147}Nd, where ~0.3% of the activity was from ^{131}I and ^{103}Ru.
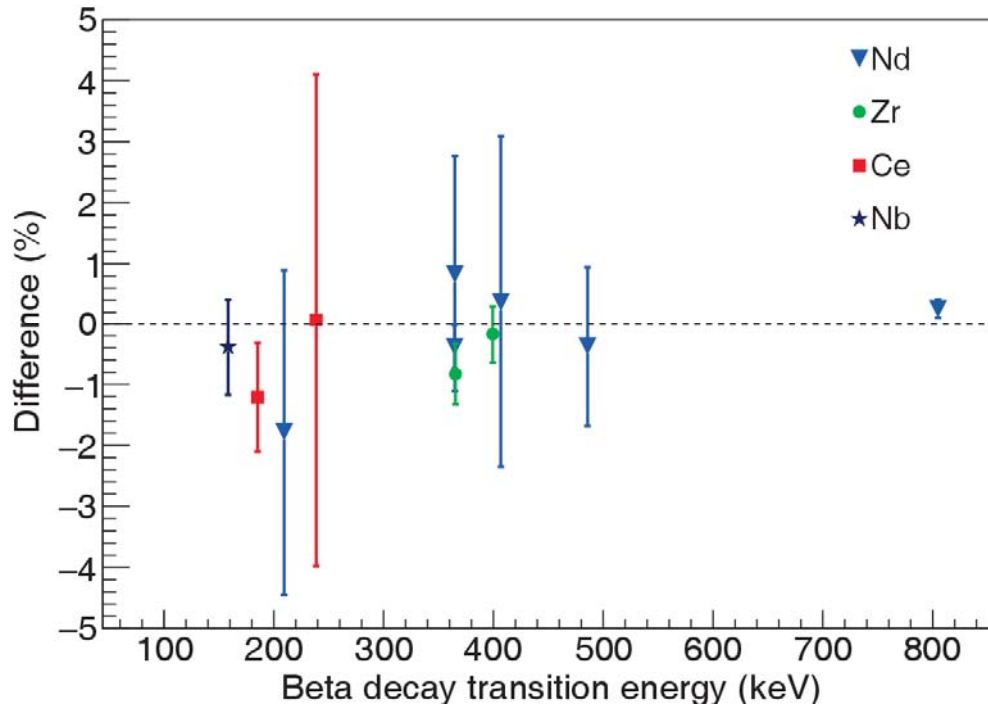
FIG. 2. The efficiency of the 4π gas proportional counter used for β detection compared with GEANT4 simulations. Figure shows the difference between the simulated efficiency and the experimental efficiency for several transitions in ^{95}Zr, ^{144}Ce, and ^{147}Nd.

With this data set we should be able to determine the branching ratios of ^{95}Zr, ^{144}Ce, and ^{147}Nd to 1-2% precision. We intend to complete the analysis by the end of the summer.

[1] K. Kolos *et. al., Progress in Research*, Cyclotron Institute, Texas A&M University (2016-2017), p. I-31.

United States Nuclear Structure Data Program (USNDP) and Evaluated Nuclear Structure Data File (ENSDF) at Texas A&M University ENSDF Data Evaluation Center

N. Nica and J.C. Hardy

Nuclear data evaluation fills a century-long chapter of nuclear science. A search in the *Nuclear Science Reference* (NSR) database maintained at the National Nuclear Data Center (https://www.nndc.bnl.gov/nsr/) on the author "M. Curie" produces a paper titled "*The Radioactive Constants as of 1930*" [1]. The introduction to this paper states that "*the need has arisen for the publication of special Tables of the Radioactive Constants*" and continues, "*This responsibility has been assumed by the International Radium Standards Commission chosen in Brussels in 1910 (...)*". Here we have the origin of what today is known as nuclear data evaluation.

Starting with the first generation of nuclear chemists and physicists, when measurements were already producing diverse and sometimes conflicting data, it became evident that assembling and reconciling the data from all across the published literature was a tedious and difficult task. Nevertheless, only after such a systematic analysis could the community arrive at recommended "practical standards," which could then be updated periodically to reflect the continuous improvements in knowledge and technology. Soon nuclear data evaluation became a specialized branch of research in its own right.

After the Second World War most of this activity was taken across the Atlantic and hosted by the United States Nuclear Structure Data Program (USNDP), which maintains the Evaluated Nuclear Structure Data File (ENSDF) database. While mostly undertaken by U.S. national laboratories, it has expanded to a relatively small number of university research labs, which has included the Texas A&M Cyclotron Institute since 2005. For more than a decade, the Texas A&M effort was financed by a contract with Brookhaven National Laboratory, but in 2017 it started to receive direct financing through the DOE Grant DE-FG03-93ER40773, "Cyclotron-based Nuclear Science"; and since May 2017 Texas A&M Cyclotron Institute has been recognized as an independent ENSDF Data Evaluation Center included within the Nuclear Structure and Decay Data international network.

Since 2005 we have completed and published the following full mass chain evaluations: the superheavy A=252 mass chain [2]; the very data-rich mid-mass chains, A=140 [3], A=141 [4], A=147 [5] and A=148 [6]; the relatively lighter chains, A=97 [7] and A=84 [8], the latter in a large international collaboration. In collaboration with B. Singh and a group of authors from McMaster University, Canada, we also published the A=77 [9], A=37 [10], A=36 [11], and A=34 [12] chains. At the beginning of 2016 another of our big mass chains, A=157, was published in Nuclear Data Sheets [13], followed by A=158 in the 2017 March-April issue of the same journal [14]. Three massive mass chains, A=140, A=155 and A=160 are also in the pipeline for publication.

In Oct 2017 we started a new full evaluation for the mass chain A=153, covering all publications since Jan 2006. The chain consists of the following isobars: Ba, La, Ce, Pr, Nd, Pm, Sm, Eu, Gd, Tb, Dy, Ho, Er, Tm, Yb, Lu, and Hf: in total, 17 nuclei. Our bibliographical search found that, since Jan 2006, 202 papers have been published relating to this mass chain, of which 182 are primary references (most important). In all, 94 are experimental. This work is in progress.

[1] M. Curie, A. Debierne, A.S. Eve, H. Geiger, O. Hahn, S.C. Lind, S. Meyer, E. Rutherford, E. Schweidler, Rev. Mod. Phys. **3**, 427 (1931).

[2] N. Nica, Nucl. Data Sheets **106**, 813 (2005).

[3] N. Nica, Nucl. Data Sheets **108**, 1287 (2007).

[4] N. Nica, Nucl.Data Sheets **122**, 1 (2014).

[5] N. Nica, Nucl. Data Sheets **110**, 749 (2009).

[6] N. Nica, Nucl. Data Sheets **117**, 1 (2014).

[7] N. Nica, Nucl. Data Sheets **111**, 525 (2010).

[8] D. Abriola *et al.*, Nucl. Data Sheets **110**, 2815 (2009).

[9] B. Singh and N. Nica, Nucl. Data Sheets **113**, 1115 (2012).

[10] J. Cameron, J. Chen, B. Singh, and N. Nica, Nucl. Data Sheets **113**, 365 (2012).

[11] N. Nica, J. Cameron, and B. Singh, Nucl. Data Sheets **113**, 1 (2012).

[12] N. Nica and B. Singh, Nucl. Data Sheets **113**, 1563 (2012).

[13] N. Nica, Nucl.Data Sheets **132**, 1 (2016).

[14] N. Nica, Nucl.Data Sheets **142**, 1 (2017).

^{35}K experiments

R. Chyzh, A. Saastamoinen, B. Roeder, R.E. Tribble, A. Spiridon, A. Kankainen,[1] E. Pollacco,[2]
L. Trache,[3] I. Stefanescu,[3] and G. Lotay[4]

[1]*University of Jyvaskyla, Finland*
[2]*IRFU, CEA Saclay, Gif-sur-Yvette, France*
[3]*National Institute for Physics and Nuclear Engineering Horia Hulubei, Bucharest, Romania*
[4]*University of Surrey, United Kingdom*

One the most important questions that nuclear physics is trying to address is the origin and abundance of the elements in the universe. Proton-gamma capture reactions, X(p, γ)Y, play an important role in the creation of elements in processes like X-ray bursts or novae explosions [1-3]. The main focus of this work is one of these reactions, ^{34g,m}Cl(p,γ)^{35}Ar. In novae, production of ^{34}S depends on the amount of ^{34}Cl, which β-decays into ^{34}S with $T_{1/2}$=1.5266 s. Sulfur isotopic ratios can be used for classification of presolar grains, which can be found in the meteorites. One way to destroy ^{34}Cl is the reaction ^{34g,m}Cl(p,γ)^{35}Ar. The rate of this reaction will eventually determine how much ^{34}Cl will be left for the creation of ^{34}S. To be able to accurately predict the reaction rate of ^{34}Cl(p,γ)^{35}Ar, one needs to know the resonances in ^{35}Ar, including their energy, spin-parity, and proton width. We chose to study this reaction by means of an indirect method where we populate states in ^{35}Ar just above the proton threshold, S_p, and observe them decaying into the ground state of ^{34}Cl + proton. The detection of low energy protons becomes the major challenge for the experiment. The AstroBoxII was built to address this problem [4] [6]. To test our system we had an experiment in March, 2017. A beam of ^{36}Ar at 36 MeV/u impinged on an H$_2$ cryogenic gas target in the target chamber of MARS [5]. Through the reaction ^{1}H(^{36}Ar,^{35}K)2n we created a secondary beam of ^{35}K and then implanted it into the AstroBoxII. After gain-matching the AstroBoxII anode pads, we calibrated two HPGe detectors with ^{137}Cs and ^{152}Eu sources. The estimated production rate for ^{35}K was 2.77 event/nC. An Al degrader (13 mil) on a rotary mechanism was used to control the position for the implantation of ^{35}K in the AstroBoxII. Due to a number of technical issues the beam time was very limited with only about 6 hours of data available. This was sufficient to determine that the system was working as expected.

In July, 2017, we had a second experiment with a ^{35}K secondary beam produced through MARS. After initial calibration of the AstroBoxII by the beam of ^{25}Si we switched to a ^{35}K beam. The production rate for ^{35}K was 2.9 event/nC. Along with the AstroBoxII, we used four HpGe Clover detectors that allowed us to measure the coincidences between protons and gamma rays. It was necessary for the setup to be sure that the excited states in ^{35}Ar that were populated by β-decay of ^{35}K were decaying directly to the ground state of ^{34}Cl after emission of a proton. Due to relatively low intensity of the ^{35}K beam it was decided to have a third experiment in October, 2017 to improve our results. The setup was identical to the one we had in July, but with more time and higher beam current we significantly improved the statistics for the low energy proton spectrum, which was the main goal of the experiment.

The analysis of the data from the July and October runs is underway and expected to be finished within next few months as a part of the Ph.D. thesis work for the first author.

[1] J. Jose, C. Iliadis Rep. Prog. **74**, 096901 (2011)

[2] J. Jose, M. Hernanz Eur. Phys. J. A **27**, Supplement 1, 107 (2006)

[3] J. Jose, M. Hernanz, C. Iliadis Nucl. Phys. **A777**, 550 (2006)

[4] A. Saastamoinen *et al.*, Nucl. Instrum. Methods Phys. Res. **A376**, 357 (2016).

[5] R.E. Tribble, R.H. Burch, and C.A. Gagliardi, Nucl. Instrum. Methods Phys. Res. **A285**, 441 (1989).

[6] A. Saastamoinen *et al.*, Progress in Research, Cyclotron Institute, Texas A&M University (2014-2015), p. IV-33.

Structure of ^{9}C via proton resonance scattering

J. Hooker,[1] G.V. Rogachev,[1] E. Koshchiy,[1] E. Ubersede,[1] S. Ahn,[1] E. Aboud,[1] C. Hunt,[1] H. Jayatissa,[1]
S. Upadhyayula,[1] A. Saastamoinen,[1] B. Roeder,[1] and E. Pollacco[2]
[1]Cyclotron Institute, Texas A&M University, College Station, Texas
[2]IRFU, CEA Saclay, Gif-sur-Yvette, France

Light exotic nuclei provide excellent testing grounds for *ab initio* models that can calculate observables such as the energy levels and electromagnetic moments. ^{9}C is an ideal candidate for testing these models because it is the most neutron deficient nucleus (N/Z = 0.5), besides ^{3}He, to be particle bound and lies next to the proton drip line. The ground state, 3/2$^-$, and the first excited state, 1/2$^-$, of ^{9}C were discovered through the transfer reaction ^{12}C (^{3}He, ^{6}He) ^{9}C [1, 2, 3]. The excitation function for p+^{8}B was first measured in [4] using a ^{8}B radioactive beam. R-matrix analysis showed evidence for a broad 5/2$^-$ state at 3.6 MeV and a possible 3/2$^-$ state at 4.1 MeV. The experiment was limited to only one angle and the excitation function was measured up to 4.5 MeV. No positive parity states were observed. The study of ^{9}C was chosen as the first commissioning radioactive beam experiment with the Texas Active Target (TexAT) detector partially because the excitation function at low energies is available, and also because ^{8}B is a very clean and intense radioactive beam at the Cyclotron MARS facility. With this new measurement, we have extend the excitation function for p+^{8}B to higher energies and covered wider range of scattering angles. One of the main physics goals of these measurements was to identify positive parity states in ^{9}C, determining location of the sd-shell.

TexAT is a general purpose active target detector to be used for nuclear reaction measurements with rare isotope beams. This study is part of the first commissioning run of the TexAT detector which consisted of stable beam test with ^{12}C, before switching to ^{8}B and ^{8}Li radioactive beams. TexAT uses a highly segmented Micromegas (Micro-MEsh GAseous Structure) plate of 1024 channels. This consists of 768 pads in the central region with 128 chains (running parallel to the beam axis) and 128 strips (running perpendicular to the beam axis) in the side regions. Each pad fired in the central region along with the measured drift time provides a 3D point of the particle while the chains and strips must be matched together to provide a 3D point. These points allow for accurate track reconstruction of both the beam and scattered light recoils (protons in this case) as well as particle ID using their specific energy loss. A total of 15 Silicon detectors backed by CsI(Tl) scintillators were used, 9 in the forward array and 6 in the left wall array (with respect to the beam direction), to measure the total energy of light recoils protons. Because of the large number of channels used in TexAT, the GET (General Electronics for TPCs) data acquisition system was used. The GET system allows for pre-amplification, shaping and digitization of each signal. More details of the TexAT detector and the electronics used can be found in [5, 6, 7].

One of the largest efforts that has been done for this study is the track reconstruction using the Micromegas detector. Prior the commissioning run, an alpha source was placed in the chamber filled with Methane gas at 50 Torr. We have applied various techniques for track reconstruction and determined that the Hough transform works best. The cumulative plot of the tracks from the alpha source in shown in Fig. 1 for the XY plane. There are 5 distinct bands of tracks going to the forward Si array and 3 towards the

left Si array corresponding the 5 columns of detectors in the front and 3 in the left. All of these tracks converge behind the Micromegas plate (start of the Micromegas is 0 on the Y-axis) roughly to the size of the source ~5 mm.

The study of ^{9}C was performed on the MARS facility at the Cyclotron Institute at Texas A&M University and was the first radioactive beam measurement using TexAT. A primary beam of ^{6}Li was used to create the ^{8}B beam through the two proton pickup reaction (^{3}He,n). The ^{8}B beam had an energy of 7.5 MeV/A with an intensity of 10^3 pps. The chamber was filled with methane at 435 Torr to stop the beam before the last 1/8th section of the Micromegas plate in the central region. Protons were identified by their specific energy loss in the Micromegas.
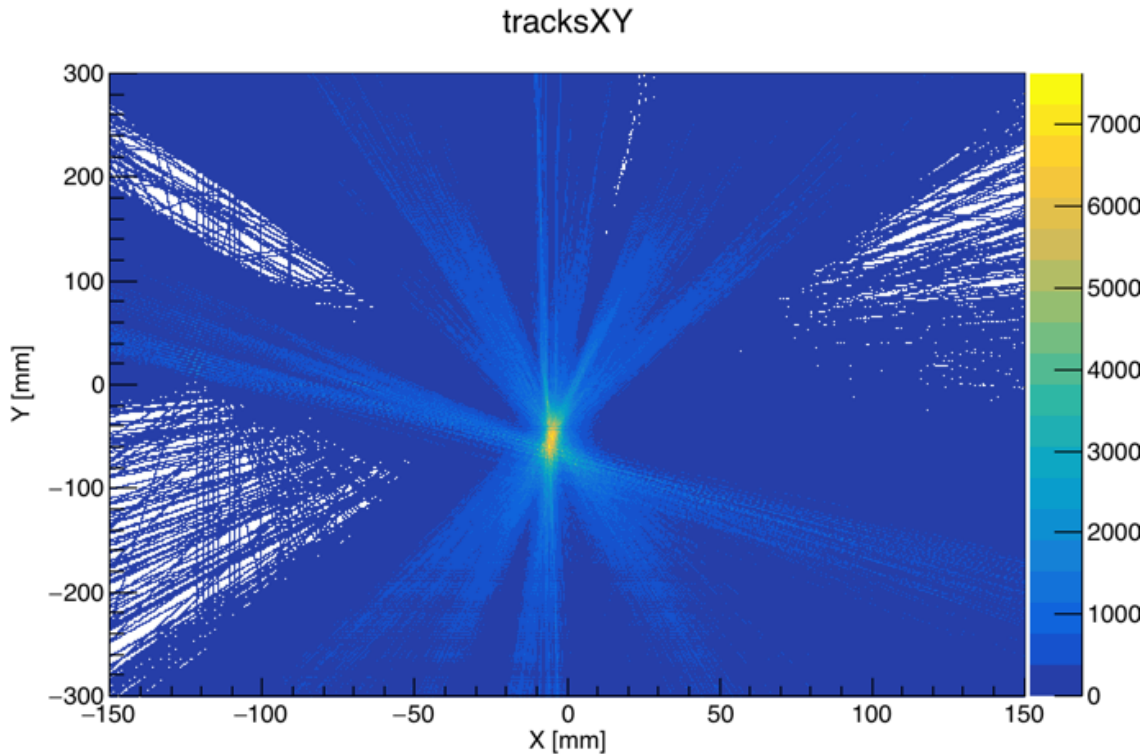
FIG. 1. Cumulative tracks in the XY plane for an α-source in 50 Torr of Methane.

Preliminary partial excitation function for p+^{8}B is shown in Fig. 2. This excitation function is consistent with the excitation function measured in [4]. Analysis is still in progress, but we expect to finalize the project by the end of Summer/beginning of Fall 2018.
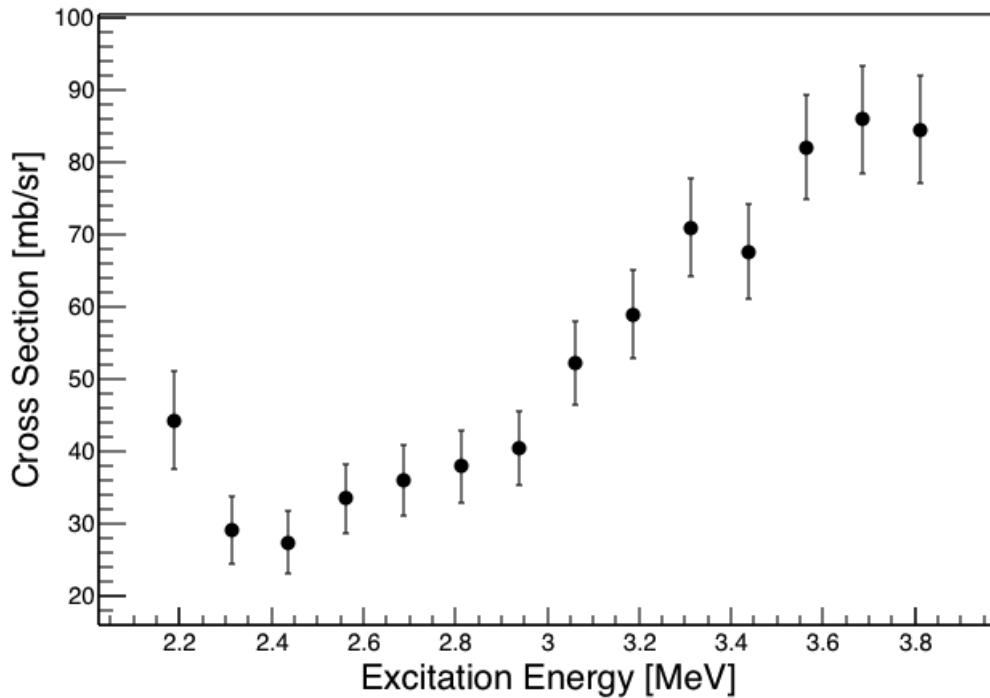
FIG. 2. Preliminary excitation function for one of the central Si detectors.

[1] J. Cerny, R. H. Pehl *et al.*, Phys. Rev. Lett. **13**, 726 (1964).

[2] W. Benenson and E. Kashy, Phys. Rev. C **10**, 2633 (1974).

[3] M.S. Golovkov, V.Z. Goldberg *et al.*, Sov. J. Nucl. Phys. **53**, 550 (1991).

[4] G.V. Rogachev *et al.*, Phys. Rev C **75**, 014603 (2007).

[5] E. Koshchiy, G.V. Rogachev *et al.*, *Progress in Research*, Cyclotron Institute, Texas A&M University (2014-2015) p. IV-42.

[6] E. Uberseder, G.V. Rogachev *et al.*, *Progress in Research*, Cyclotron Institute, Texas A&M University (2014-2015) p. IV-47

[7] E. Uberseder, G.V. Rogachev *et al.*, *Progress in Research*, Cyclotron Institute, Texas A&M University (2014-2015) p. IV-51.

Final results of the study of the astrophysically important ^{22}Ne(α,n)^{25}Mg reaction using indirect techniques at sub-Coulomb energies

H. Jayatissa,[1] G.V. Rogachev,[1] E. Uberseder,[1] E. Koshchiy,[1] O. Trippella,[2] J. Hooker,[1]
S. Upadhyayula,[1] C. Magana,[1] C. Hunt,[1] V.Z. Goldberg,[1] B.T. Roeder,[1]
A. Saastamoinen,[1] A. Spiridon,[1] and M. Dag[1]

[1]*Cyclotron Institute, TexasA&M University, College Station, Texas*
[2]*Department of Physics and Geology, University of Perugia, and Instituto Nationale di Fisica Nucleare,
Section of Perugia, Via A. Pascoli, 06123 Perugia, Italy*

The slow neutron capture process (s-process) that take place in Asymptotic Giant Branch (AGB) stars is responsible for the formation of about half of the elements beyond Iron [1], and the neutrons for this process mainly come from two main neutron source reactions of which one is the ^{22}Ne(α,n)^{25}Mg reaction. Direct experimental measurements for this reaction at astrophysical energies are difficult to carry out due to very low cross section at energies relevant for astrophysics. This reaction was studied using an indirect technique, the ^{22}Ne(^{6}Li,d)^{26}Mg reaction performed at sub-Coulomb energies to study the near alpha-threshold resonances in ^{26}Mg [2]. By using energies close to the Coulomb barrier, the dependence of the extracted partial alpha-widths (Γ_α) on the optical model potentials and the number of nodes in the cluster wave functions can be dramatically reduced.

This reaction was carried out using the Multipole-Dipole-Multipole (MDM) Spectrometer at Texas A&M University. Effective experimental energy resolution of these measurements was about 80 keV. Fig. 1 shows the excitation energy spectrum for the states in ^{26}Mg populated in ^{22}Ne(^{6}Li,d)^{26}Mg reaction covering the entirety of the Gamow energy window for this reaction. The state at 11.3 MeV
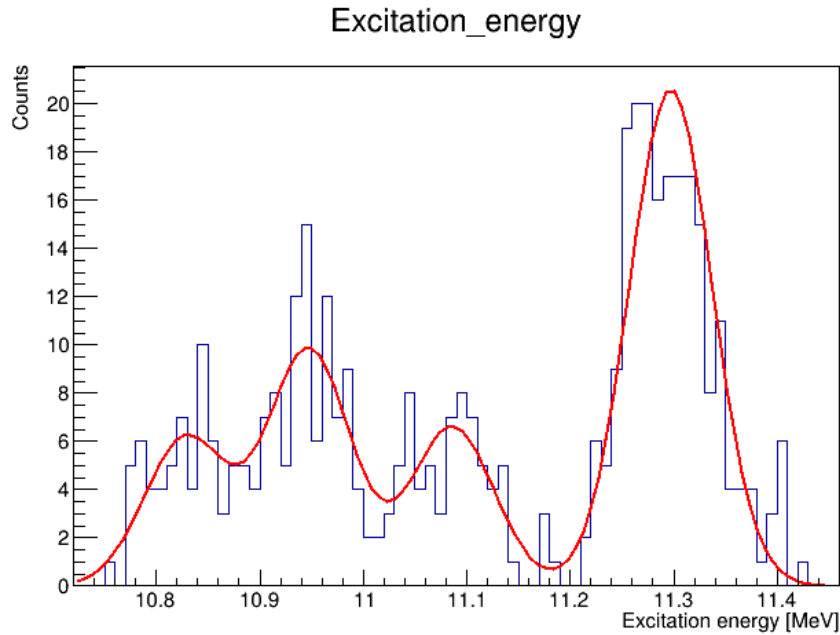
FIG. 1. Spectrum of ^{26}Mg excited states populated in ^{22}Ne(^{6}Li,d)^{26}Mg reaction.

provides the most dominant contribution for the reaction rate of the ^{22}Ne(α,n)^{25}Mg reaction at astrophysical energies and is the lowest excitation energy state that has been observed in direct ^{22}Ne(α,n)^{25}Mg measurements [1].

None of the states observed in this experiment have definitive spin-parity assignment, in spite of the fact that these states have been observed previously [3,4]. Distorted-Wave Born Approximation (DWBA) calculations using the code FRESCO shows that low angular momentum (*L* values of 2 or less) assignments for the transferred alpha particle is preferred for the conditions of the present work. The Γ_α calculated using the experimental cross sections appears not to depend on the form factor potential parameters, and correspondingly the number of nodes of the wave function. However, FRESCO code does not allow calculations of transfer to unbound states. Hence, in order to extract Γ_α of the relevant states in ^{26}Mg which are α-unbound, first the widths were calculated using a bound-state approximation with a maximum uncertainty of ~30% due to the uncertainties of the optical model parameters, and then extrapolated to unbound energies. Additional analysis of α-transfer reactions populating states in ^{26}Mg at higher energies of Li beam (32 MeV [4] and 82 MeV [3]) leads to a conclusion that 1$^-$ is the most likely spin-parity assignment for the dominate state at 11.3 MeV state. The strength of this resonance seems to be a factor of ~2 smaller than the strength established in direct measurements for the ^{22}Ne(α,n)^{25}Mg reaction [3]. This results in significant decrease of the ^{22}Ne(α,n)^{25}Mg reaction rate. Also, the relatively large value of Γ_α for this state (about 15% of single-particle) indicates the importance of α-clustering for this (α,n) reaction.

[1] M. Jaeger *et al.*, Phys. Rev. Lett. **87**, 202501 (2001).
[2] H. Jayatissa *et al.*, *Progress in Research*, Cyclotron Institute, Texas A&M University (2016-2017) p. I-57.
[3] R. Talwar *et al.*, Phys. Rev. C **93**, 055803 (2016).
[4] U. Giesen *et al.*, Nucl. Phys. **A561**, 95 (1993).

Search for the low-lying T=5 states in ^{48}Ca

S. Upadhyayula,[1] A. Hood,[2] C Deibel,[2] C. Hunt,[1] D. Santiago-Gonzalez,[2,3] G. Rogachev,[1]
J. Blackmon,[2] J. Lighthall,[2] J. Hooker,[1] J. Browne,[4] M. Anastasiou,[5] N. Rijal,[5] S. Bedoor,[1]
S. Ahn,[1,4] W. Ong,[4] and Y. Koshichy[1]

[1] *Cyclotron Institute, Texas A&M University, College Station, Texas*
[2] *Louisiana State University, Baton Rouge, Louisiana*
[3] *Argonne National Laboratory, Argonne, Illinois*
[4] *NSCL, Michigan State University, East Lansing, Michigan*
[5] *Florida State University, Tallahassee, Florida*

Particle-hole excitations near closed shells carry information on single-particle energies and on two-body interactions [1,2]. The particle-hole excitations near the doubly magic nuclei are of special interest. Information on the charge-changing particle-hole excitations (T= 5 negative parity states) in ^{48}Ca is not available (Fig. 1). We performed an experiment to establish the level scheme of the low-lying negative parity T=5 states in ^{48}Ca. Excitation functions for the ^{1}H (^{47}K, p) ^{47}K reaction in the c.m. energy range from 1 MeV to 4.5 MeV were measured. The T= 5 states are expected to show up in the p+^{47}K excitation function as narrow resonances.
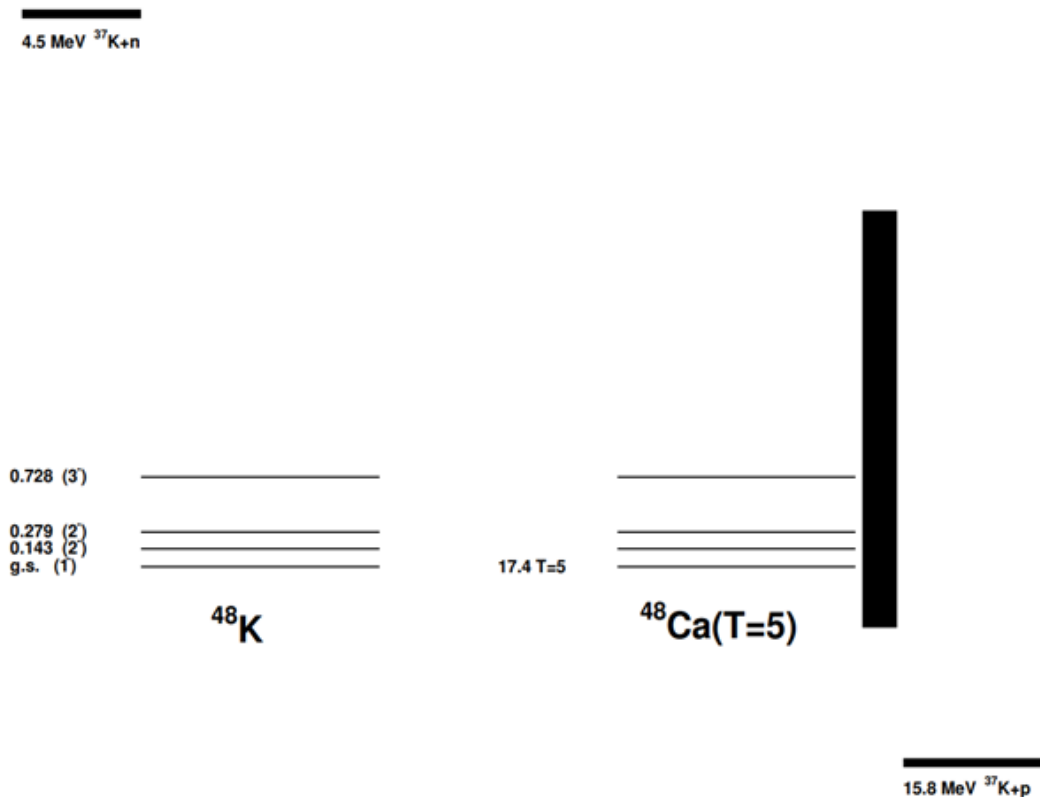
FIG. 1. Level scheme of ^{48}K from [4] and the corresponding (unknown) T=5 isobaric analog states in ^{48}Ca with relevant decay thresholds. Bold vertical line indicates the measured excitation energy range in this experiment.

This experiment was performed at NSCL using the ReA3 beam of ^{47}K at energy of 4.6 MeV/u with an intensity of 10^4 particles per second. The Array for Nuclear Astrophysics and Structure with Exotic Nuclei (ANASEN) [3], set in active target mode, was used for this experiment. Position sensitive silicon barrel and forward annular detector arrays were used along with a cylindrical proportional counter that was installed along the beam axis. Methane gas was used as the active gas volume for the proportional counter wires as well as the target. A 5μm scintillator read out by two PMTs was set up by the entrance of the chamber. There was another thick scintillator that was installed downstream of the beam in the middle of the annular forward detector array. These two scintillators were used in conjunction to allow us to measure the overall beam normalization as well as to identify any beam contaminants. The gas pressure was set to 95 Torr, allowing the beam ions to make it to the downstream scintillator.

The thick target inverse kinematics technique [4], combined with active target capabilities of ANASEN detector allows us to measure entire excitation function for ^{47}K+p without changing the energy of the incident beam. The recoil protons were detected by the silicon array, which provided the main trigger for the data acquisition system. These recoil protons were identified using their energy loss in the proportional counter cells (Fig. 2). The position of the hit in the silicon along with the position detected in
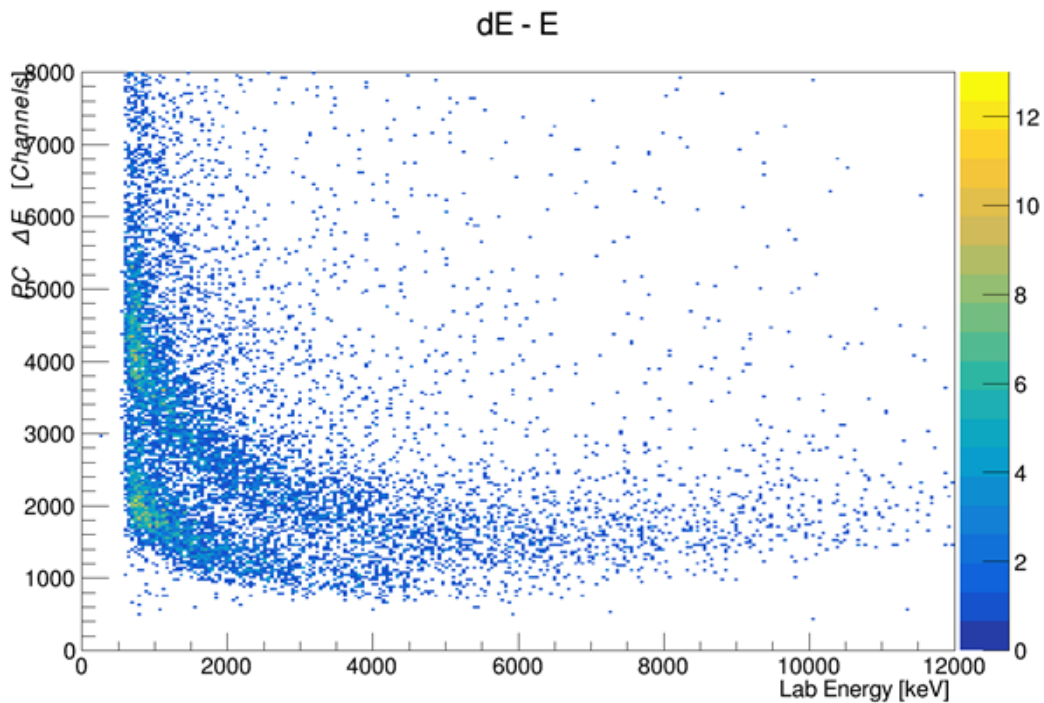
FIG. 2. dE-E plot to identify protons.

the proportional counter allows us to reconstruct the reaction vertex location for event identification (Fig. 3).
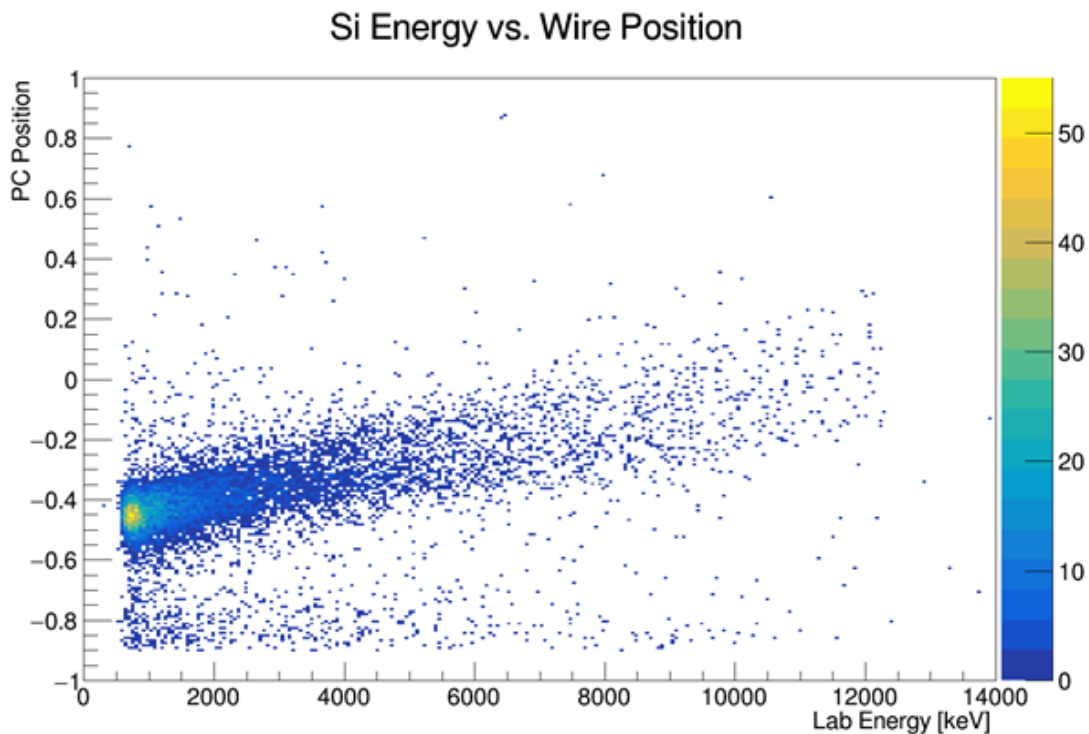
FIG. 3. Uncalibrated position in proportional counter wire.

The main goal of this experiment is to establish the level scheme of the low-lying negative parity T=5 states in ^{48}Ca. These states are expected to show up as relatively narrow resonances between the excitation energy range from 17 MeV to 22 MeV. Preliminary excitation function for ^{47}K+p is shown in Fig. 4 (about 10% of the data). There is an indication of narrow states, but the spectrum is dominated by
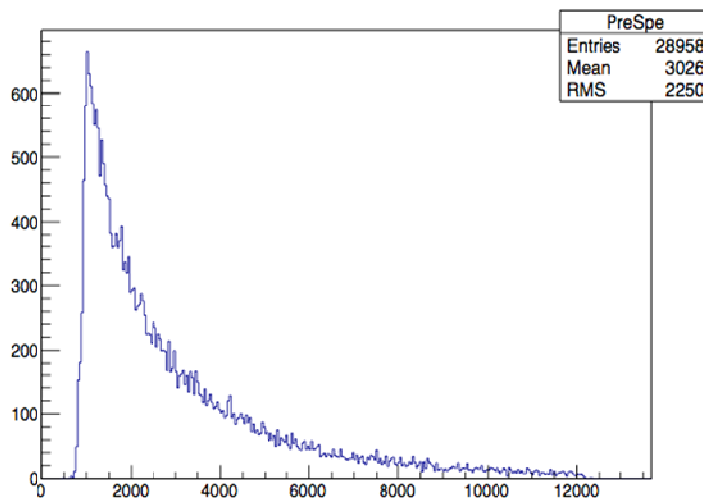
FIG. 4. Preliminary excitation function with about 10% of statistics. We see a peak of interest around 4 MeV.

Rutherford scattering, as expected. Further analysis is needed to confirm existence of the IAS states (with higher statistics) and to extract the excitation function for p+^{47}K elastic scattering. The excitation energies, spin-parities and proton decay widths will be determined using R-Matrix analysis.

[1] T. Otsuka *et al.*, Phys. Rev. Lett. **95**, 232502 (2005).

[2] J. Suhonen, "From Nucleons to Nucleus", Springer-Verlag, ISBN 0172-5998 (2007).

[3] E. Koshchiy *et al.*, Nucl. Instrum. Methods Phys. Res. **A870**, 1 (2017).

[4] K.P. Artemov *et al.*, Sov. J. Nucl. Phys. **52**, 408 (1990).

[5] W. Krolas *et al.*, Phys. Rev. C **84**, 064301 (2011).

Clustering in ^{10}Be

S. Upadhyayula, G.V. Rogachev, E. Koshchiy, E. Uberseder, V.Z. Goldberg, J. Hooker, H, Jayatissa, C. Hunt, and B.T. Roeder

There is a strong experimental evidence that some states in ^{10}Be exhibit molecular-like α:2n:α configuration [1-3]. Theoretically these exotic structures can be explored microscopically in the antisymmetrized molecular dynamics plus Hartree-Fock approach [4] or in Molecular Orbital model [5]. Based on these theoretical studies it appears that the 6.179 MeV 0^+ state in ^{10}Be has a pronounced α:2n:α configuration with an α-α inter-distance of 3.55 fm. This is 1.8 times more than the corresponding value for the ^{10}Be ground state. The 2^+ at 7.542 MeV in ^{10}Be is believed to be the next member of this rotational band [6]. The state at 10.2 MeV was identified as a 4^+ member [1, 3]. The algebraic model [7] predicts that a 6^+ state at around 13 MeV is the next member of this band. It would be of paramount importance to identify this 6^+ state experimentally and to conclusively establish the α:2n:α rotational band. This would become the most striking and well established case of molecular-like configurations in nuclei and an important step towards better understanding of clustering phenomena in atomic nuclei.

We performed an experiment to search for the 6^+ state in ^{10}Be at around 13 MeV excitation energy in the excitation function for ^{6}He+α scattering. The Cyclotron Institute Momentum Achromat Recoil Separator (MARS) facility was used to produce a secondary ^{6}He beam at 7.0 MeV/u from the production reaction of ^{7}Li(d,^{3}He). The sketch of the experimental setup is shown in Fig. 1. Modified thick target inverse kinematics approach [8] was used to measure the ^{6}He+α excitation function. Details of the
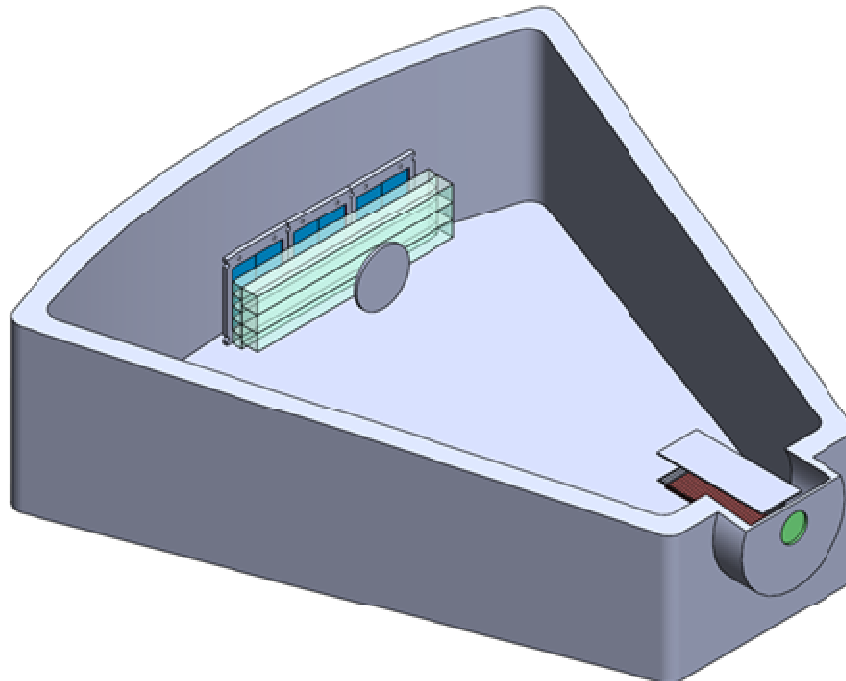
FIG. 1. Sketch of the experimental setup to measure the ^{6}He+α excitation function of ^{10}Be excitation energy.

experimental setup can be found in [9]. The energy of the [6]He beam was reduced down to 22 MeV by the thick scintillator foil located in front of the scattering chamber filled with Helium+CO_2 96:4 gas mixture at pressure of 1700 Torr.

We have observed a distinct peak of α particles that could be a result of resonance in the [6]He+α excitation function which we were looking for. This peak in the α spectrum was verified to be associated with the incoming [6]He beam particles and not the other secondary beam components, the dominant of which is tritium. Given the nature of the set up, we expect the highest energy α particles (between 12 and 15 MeV) to correspond to pure elastic scattering. At lower energies, admixtures from α particles due to inelastic scattering and breakup are possible. Based on the shape of the spectrum compared to Monte Carlo simulations (Fig. 2), the experimental yield and angular dependence of the cross section, we can conclude that the α spectrum is dominated by the breakup of [6]He into α+2n at energies below 8 MeV.
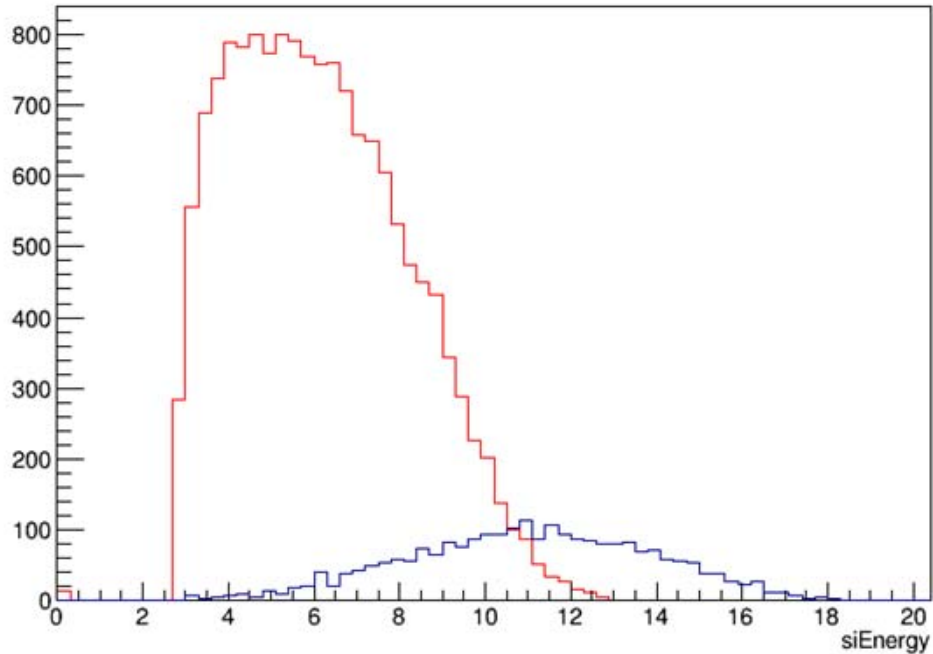
FIG. 2. Monte Carlo simulation of α particles spectrum due to breakup of [6]He. The (red) curve at lower energy shows α particles from [6]He decay. The (blue) curve at higher energy shows α particles due to elastic scattering.

For analysis purposes, we have divided the three different angles in our set up into regions. The detector at the forward angles correspond to Region 1. The other two angles (170° and 162° in the center of mass frame) correspond to Region 2 and Region 3 respectively. The peak in the α spectrum due to the hypothetical 6[+] state at 13.5 MeV [10,11,12] would appear in the vicinity of 8 MeV in the Lab. frame of reference in Region 2 and 6.5 MeV in Region 3 (Fig. 3). There is no indication for a resonance-like structure in our spectrum at that energy at any angle. Since we can't conclusively claim the origins of the α particles in the entire spectrum, we were not able to extract a clean excitation function for [6]He+α
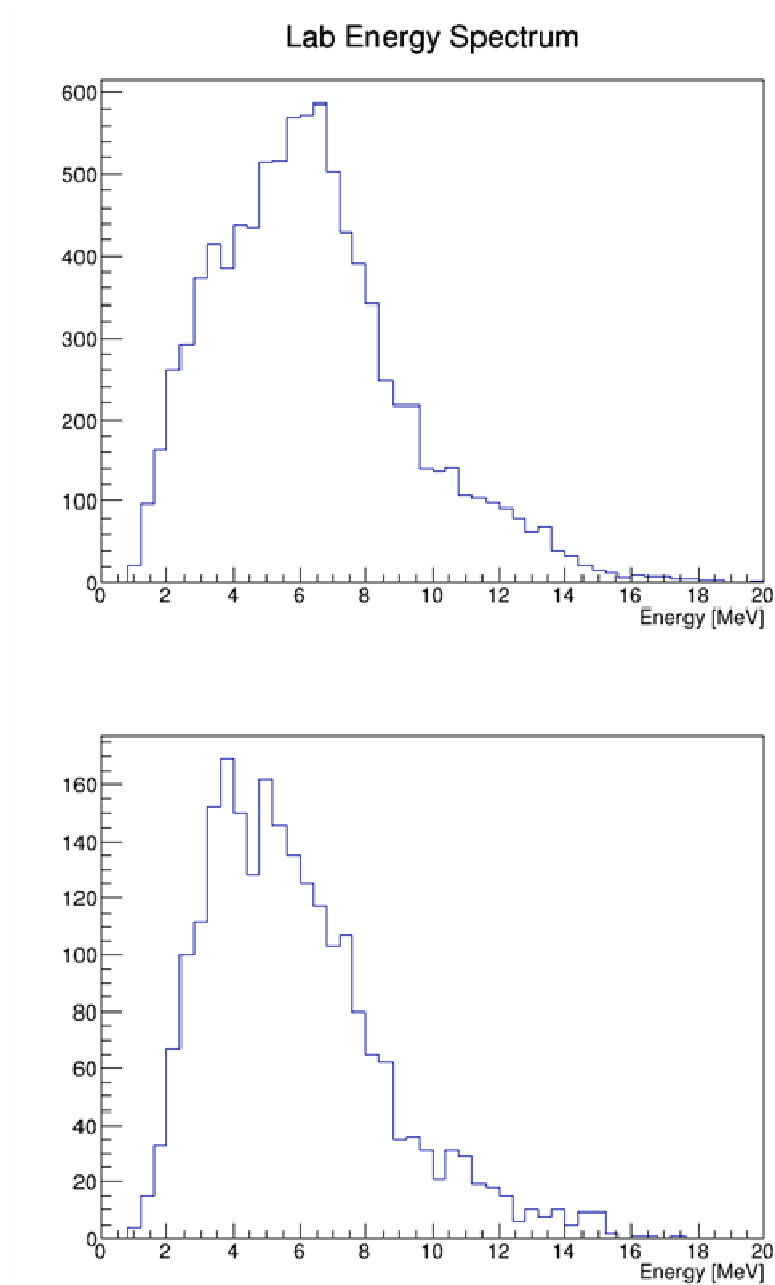
FIG. 3. Spectrum of α particles measured by the off-center Si detectors. The peak at 7 MeV is a result of ^{6}He decay into α + 2n (see text for details).

elastic scattering. However, based on the number of ^{6}He ions accumulated during the run and using 6^+ resonance cross section calculated by AZURE2 R-Matrix software package with R-matrix parameters taken from [12], the effect of the hypothetical cluster 6^+ state can be evaluated. The blue histogram in Fig. 4 demonstrates the expected spectrum of α-particles, compared to the one observed experimentally. There

is no indication of the 6^+ state in both Region 2 and Region 3. In fact, there is no indication for any resonance structures in the excitation function for ^{6}He+α, consistent with conclusions of Ref. [3].
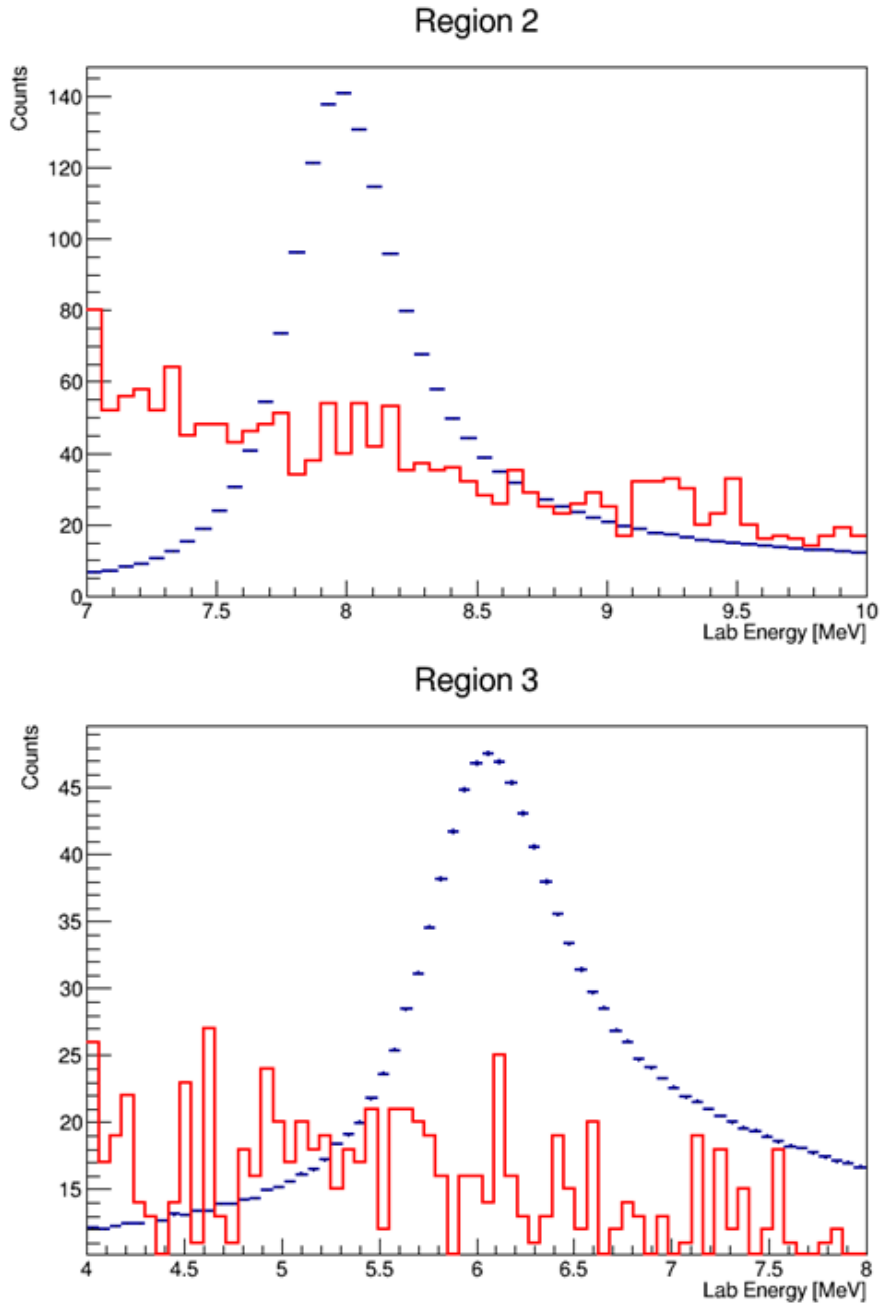
FIG. 4. Blue curve represents the calculated cross section from AZURE2 converted to counts. Red is the alpha spectrum for the respective regions.

In summary, we have performed a search for the lowest 6^+ state in ^{10}Be, which was assumed to be the next member of the molecular α:2n:α rotational band, in the excitation function for ^{6}He+α. No evidence for this state have been observed in the energy range between 11 and 15 MeV (it was expected

at 13 MeV). Either the states does not exist, or it has small coupling to the ^{6}He(g.s.)+α exit channel (small ^{6}He(g.s.)+α dimensionless reduced width). This experimental information provides important constraints on the theoretical models describing clustering in ^{10}Be.

[1] M. Freer *et al.*, Phys. Rev. Lett. **96**, 042501 (2006).

[2] M. Milin *et al.*, Phys. At. Nucl. **69**, 1360 (2006).

[3] D. Suzuki *et al.*, Phys. Rev. C **87**, 054301 (2013).

[4] A. Doté, H. Horiuchi, and Y. Kanada-Enýo, Phys. Rev. C **56**, 1844 (1997).

[5] N. Itagaki and S. Okabe, Phys. Rev. C **61**, 044306 (2000).

[6] A.N. Kuchera *et al.*, Phys. Rev. C **88**, 054615 (2011).

[7] R. Wolsky *et al.*, Phys. At. Nucl. **73**, 1405 (2010).

[8] K. Artemov *et al.*, Sov. J. Nucl. Phys. **52** 408 (1990).

[9] S. Upadhyayula *et al.*, Progress in Research, Cyclotron Institute, Texas A&M University (2016-2017) p. I-54.

[10] D. Dell'Aquila *et al.*, Phys. Rev. C **93** 024611 (2016).

[11] E. Koshchiy *et al.*, Nucl. Instrum. Methods Phys. Res. **A870**, 1 (2017).

[12] A.N. Kuchera, Ph.D. Thesis, Florida State University, 2013.

T=3/2 isobaric analog states in ^{9}Be

C. Hunt, G.V. Rogachev, V.Z. Goldberg, E. Koshchiy, B.T. Roeder, S. Ahn, J. Hooker,
H. Jayatissa, and S. Upadhyayula

Spectroscopy of neutron rich nuclei provides information on evolution of shell structure with an increasing imbalance between protons or neutrons and guides development of modern approaches in nuclei theory [1-4]. Many experimental techniques have been developed during the last two decades to populated states in neutron rich isotopes using radioactive beams, such as transfer, knock-out, charge-exchange and break-up reactions. It has been proposed recently that neutron rich nuclei could also be studied using proton resonance scattering by populating the isobaric analogue states in less exotic nuclei [5]. The main advantage is high cross section and excellent energy resolution (~20 keV). However, the higher isospin states in the analogous nuclei tend to be at high excitation energy, where density of lower isospin states is high. In situations like this one cannot apply the standard R-Matrix approach that is typically used for analysis of resonance scattering data. The R-matrix formulation has to be supplemented with the optical model to describe the featureless background due to the high density of lower isospin states. The A=9, T=3/2 isobaric quartet makes a good test case for the suggested approach. ^{9}Li [6] and ^{9}Be have already been studied with transfer reactions and ^{9}C [7] has been studied using ^{8}B+p resonance scattering. This allows for a direct comparison of T=3/2 states in ^{9}Be, populated in the ^{8}Li+p resonance scattering, to the analogous states in ^{9}Li and ^{9}C.

In August of 2017 we have performed the commissioning run of the new TexAT active target detector using ^{8}B and ^{8}Li radioactive beams produced by MARS. Details of the setup can be found in this annual report [8]. TexAT was filled with 470 Torr Isobutane gas for the ^{8}Li+p measurements. The goal was to measure the ^{8}Li+p excitation function to identify the T=3/2 states in ^{9}Be.

Analysis of this data is still in progress, but major advances have been made in developing automated tracking techniques for the TexAT. One method of determining reaction vertex location involves analysis of the energy deposited in the central region microMegas pads. Since the specific energy loss of the beam ion after elastic scattering is significantly higher than before, the vertex location may be determined using discontinuity in the energy spectrum when plotted as a function of location. The characteristic shape of specific energy loss of ^{8}Li ions for elastic scattering even is shown in Fig. 1. The vertex location can be clearly identified from such plots. The 2D scatter plot of light recoils energy measured by Si detectors versus vertex location along the beam axis is shown in Fig. 2. Events associated with ^{8}Li(p,p) and ^{8}Li(p,d) reactions can be clearly identified. However, the automated procedure for vertex localization still needs improvement, as evidenced by rather "noisy" appearance of the 2D scatter plot. Once reliable tracking algorithm is in place, we will be able to obtain clean data on ^{8}Li+p resonance elastic and inelastic scattering, extract spectroscopic information on the T=3/2 states in ^{9}Be, and compare it to the available experimental data on this and other members of T=3/2 A=9 isospin quartet.
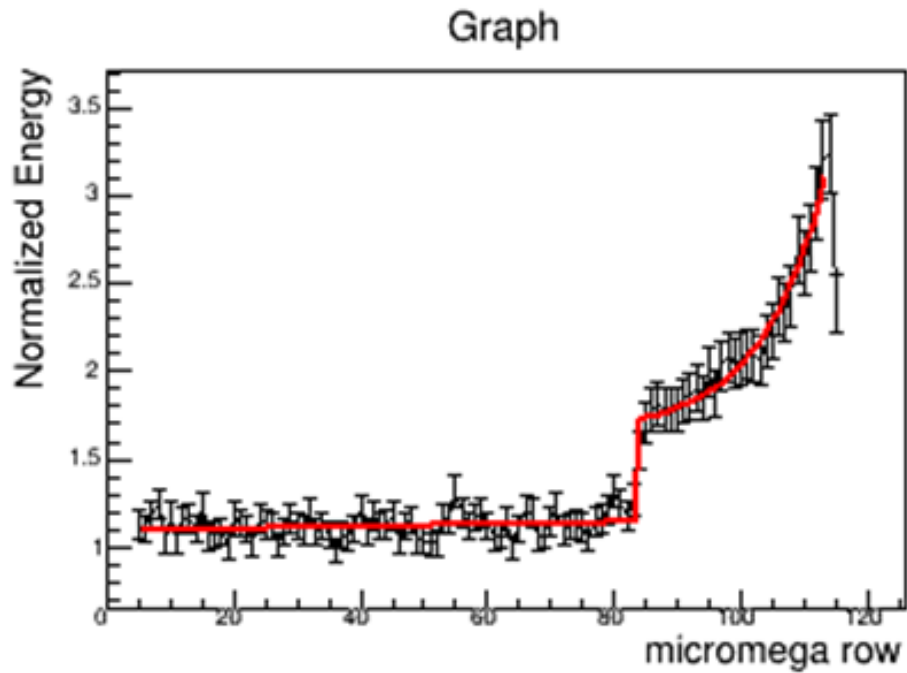
FIG. 1. Normalized Energy deposition of the beam ion (^{8}Li) as a function of location along the beam axis for a single event, showing the discontinuity due to a reaction. Red solid line is a fit that is used to determine the location of the reaction vertex.
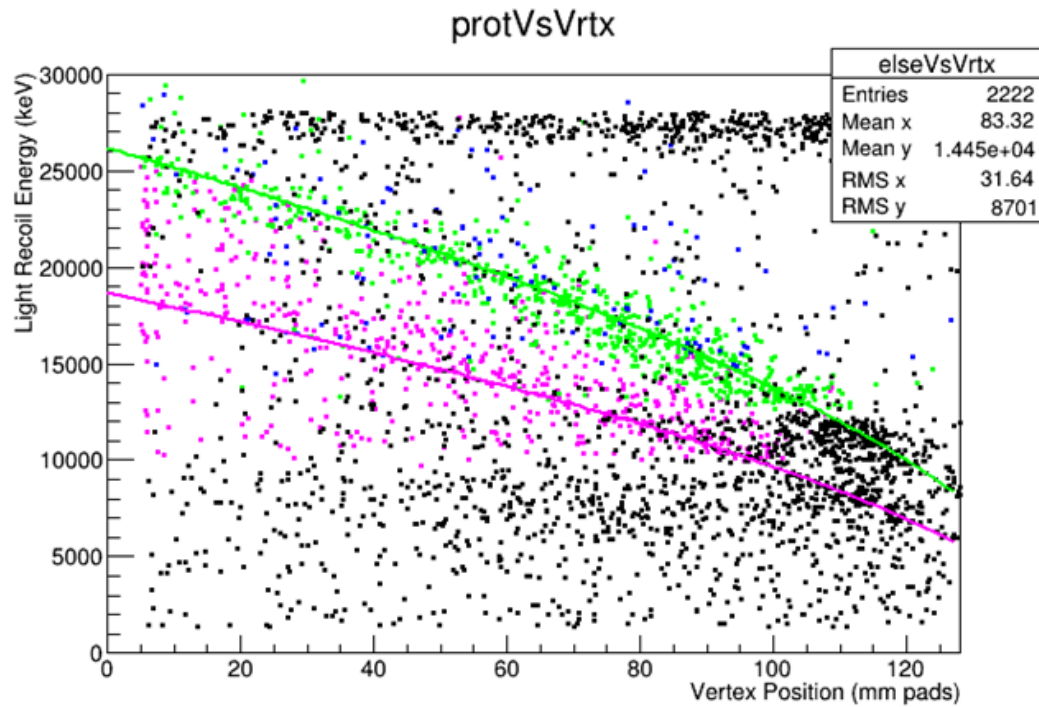
FIG. 2. Light Recoil Energy vs reaction vertex location along the beam axis. Protons identified using ΔE-E approach in Si/CsI(Tl) telescopes are shown in magenta and deuterons are in green. Black points are non Si punch-through events, for which particle ID cannot be performed using ΔE-E approach. The lines shown on top of the points are calculated from kinematics for the ^{8}Li(p,p) and ^{7}Li(p,d)^{8}Li(g.s.) reactions. There is clear separation between the reactions.

[1] I. Tanihata *et al.*, J. Phys. G **22**, 157 (1996).

[2] T. Otsuka *et al.*, Phys. Rev. Lett. **87**, 082502 (2001).

[3] T. Otsuka *et al.*, ArXiv:0910.0132 (2009).

[4] N.A. Smirnova *et al.*, ArXiv:1002.1006 (2010).

[5] V.Z. Goldberg, AIP Conference Proceedings **455**, 319 (1998).

[6] A.H. Wuosmaa *et al.*, Phys. Rev. Lett. **94**, 082502 (2005).

[7] G.V. Rogachev *et al.*, Phys. Rev. C **75**, 014603 (2007).

[8] S. Ahn, G.V. Rogachev, E. Koshchiy, J. Hooker, and S. Upadhiajula, *Progress in Research*, Cyclotron Institute, Texas A&M University (2017-2018), p. IV-81.

Spin physics with STAR at RHIC

C.A. Gagliardi, T. Lin, R.E. Tribble, and the STAR Collaboration

Our group continues to play major roles in STAR investigations of both longitudinal and transverse spin phenomena in polarized pp collisions at RHIC. A major goal of the RHIC spin program is to determine the gluon polarization in the proton over a wide range of momentum fraction x. The longitudinal double-spin asymmetries, A_{LL}, for inclusive jet and di-jet production are ideal tools in this effort because the cross sections are large and dominated by quark-gluon and gluon-gluon scattering processes, both of which have large partonic asymmetries.

As discussed in last year's *Progress in Research*, our former graduate student, Zilong Chang, performed an analysis of A_{LL} for inclusive jet production in 510 GeV pp collisions, using data that STAR collected during 2012. The results will provide new constraints on the gluon polarization in the region x < 0.05 that isn't sampled by mid-rapidity jet production in 200 GeV collisions. A decision was made to combine the 2012 inclusive jet A_{LL} results with the di-jet A_{LL} measurements that are based on the same data set and have been analyzed at University of Kentucky. The last systematic uncertainty estimate for the di-jets is just being completed as this is being written, which has postponed the paper a bit. We now expect that it will be submitted before the end of the current calendar year. In the meantime, Dr. Chang won the 2017 RHIC&AGS Thesis Prize for his dissertation.

Forward rapidity jet production provides an alternative approach to obtain constraints on gluon polarization at low x. The STAR Endcap Electromagnetic Calorimeter (EEMC) measures neutral particles (mostly photons from π^0 decay) over the pseudorapidity range $1.09 < \eta < 2$. In principle, this allows us to extend our jet reconstruction well beyond the $|\eta| < 1$ region that we've investigated to date. However, special care is necessary because the TPC tracking efficiency drops rapidly for charged particles beyond $\eta \sim 1.3$. Our post-doctoral research associate, Dr. Ting Lin, developed novel machine learning techniques to determine the event-by-event jet p_T and mass in this challenging region during his Ph.D. research at Indiana University. He has applied them to measure di-jet A_{LL} with one jet in the range $0.8 < \eta < 1.8$ and the second jet in the range $-0.8 < \eta < 1.8$, using 200 GeV pp data that STAR recorded during 2009. Notably, the events with both jets in $0.8 < \eta < 1.8$ provide sensitivity to gluon polarization down to $x \sim 0.01$. A paper describing Dr. Lin's results will be submitted for publication very soon.

We are also actively investigating transverse spin phenomena at RHIC. Transversity, together with the unpolarized and helicity distributions, are the three leading-twist distributions in the proton. However, much less is known about the transversity distribution because it is chiral odd. The Collins effect convolutes the chiral-odd quark transversity distribution with the chiral-odd Collins fragmentation function, an azimuthal modulation of pion production about the thrust axis of a jet that arises from a transversely polarized quark. It has been observed in semi-inclusive deep-inelastic scattering (SIDIS) by HERMES and COMPASS. The Collins effect is known to be universal in e^+e^- collisions and SIDIS. It has also been argued [1] that the universality of the Collins effect extends to pp collisions if the appropriate jet reconstruction algorithm – $e.g.$, the anti-k_T algorithm – is used.

During the past year, we published the first ever observation of the Collins effect in *pp* collisions [2], based on an analysis of 500 GeV data that STAR recorded during 2011. The measurement samples the region $x \sim 0.15$, with $Q^2 \sim 1000$ GeV^2, as shown in Fig. 1. The latter is two orders of magnitude larger than the Q^2 region than has been sampled in SIDIS.
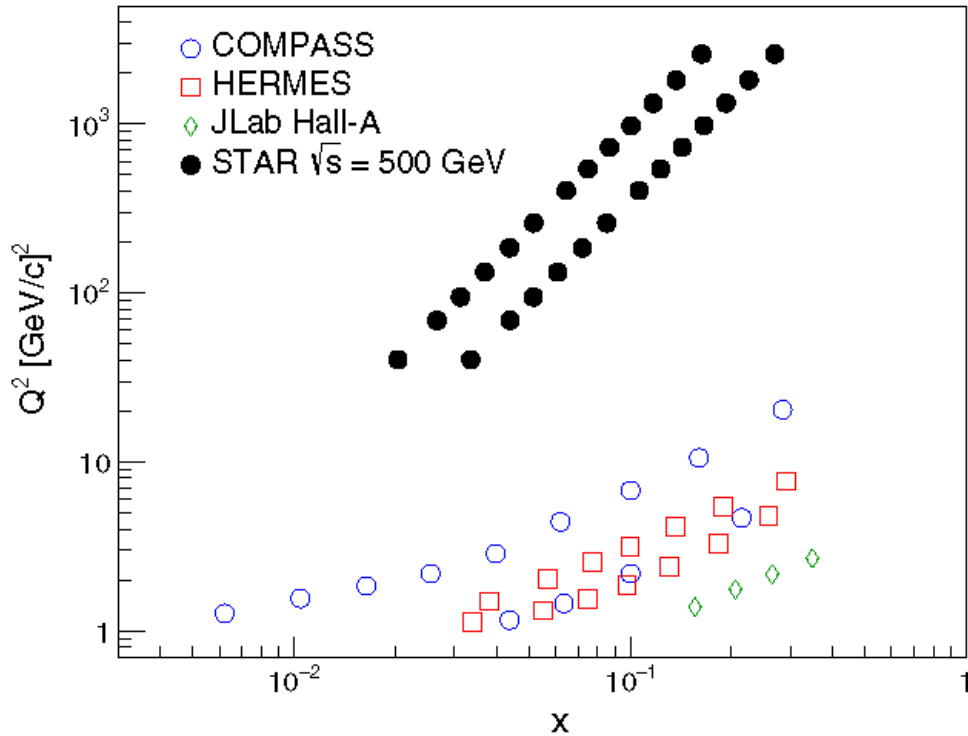
FIG. 1. The *x* vs. Q^2 region sampled by STAR Collins effect measurements with mid-rapidity jets in 500 GeV *pp* collisions [2], compared to that in previous SIDIS measurements.

Figure 2 shows our results for the Collins effect for jets with $0 < \eta < 1$ and $<p_T> = 31$ GeV/c. A difference of >5 sigma is observed between the π^+ and π^- asymmetries. The results are also compared to three predictions [3,4] from recent global analyses of e^+e^- and SIDIS data, one of which includes contributions from TMD evolution. This is the first test of the predicted universality of the Collins fragmentation function. In parallel, we also reported the first ever limits [2] on the "Collins-like" effect, the gluon analog of the Collins effect, which is sensitive to the linear polarization of gluons within a transversely polarized proton, and the first measurement of the transverse single-spin asymmetry A_N for mid-rapidity inclusive jet production in 500 GeV *pp* collisions, which is sensitive to the twist-3 analog of the gluon Sivers function.
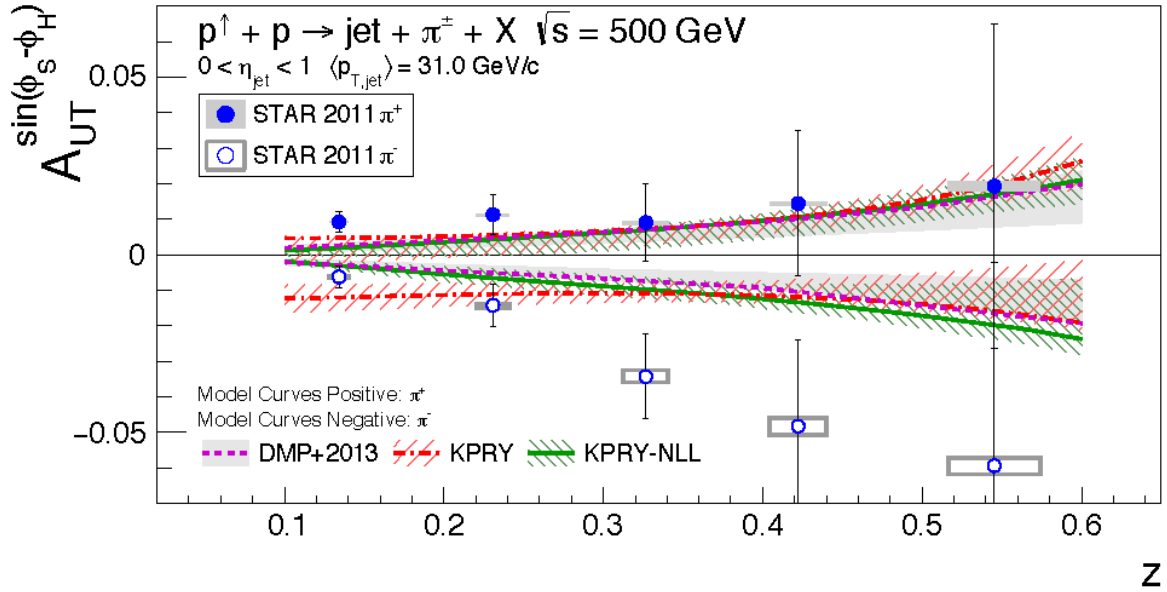
FIG. 2. Collins asymmetries as a function of z [2], compared to predictions from recent global analyses [3,4]. See [2] for details.

We are now investigating the Collins effect and other transverse-spin azimuthal modulations in 200 GeV pp collision data that STAR recorded during 2012 and 2015. The lower energy provides access to higher x, where the transversity distribution peaks in recent global analyses, as well as better statistics in the x region that overlaps between 200 and 500 GeV collisions. Furthermore, the comparison of the two energies will probe non-perturbative TMD evolution effects. Kevin Adkins, a UKy graduate student, has performed the 2012 analysis for his Ph.D. dissertation. The last systematic uncertainties have just recently been finalized, and preparation of the paper and analysis note is starting. The hope is to have the paper into god-parent committee by the end of summer. Meanwhile, Ting Lin began work on the 2015 data after his arrival at Texas A&M. He has completed the run and jet QA steps. The STAR Heavy Flavor Tracker was in place during the 2015 RHIC run, significantly increasing the material budget compared to the 2011 500 GeV and 2012 200 GeV data sets. Thus, the electron contamination is considerably larger, making particle identification more difficult. First studies of the available particle identification variables are now underway. The ultimate plan is to combine them utilizing Dr. Lin's machine learning experience.

Finally, we continue to carry various administrative responsibilities for STAR. Last summer Dr. Gagliardi was named convener of the Cold QCD and Spin Physics Working Group. Dr. Lin is serving as the software coordinator for the EEMC. Drs. Lin and Gagliardi are both serving on the god-parent committee for the 2009 EEMC di-jet A_{LL} paper.

[1] Z.-B. Kang, X. Liu, F. Ringer, and H. Xing, JHEP **11**, 068 (2017).
[2] L. Adamczyk *et al*. (STAR Collaboration), Phys. Rev. D **97**, 032004 (2018).
[3] U. D'Alesio, F. Murgia, and C. Pisano, Phys. Lett. B **773**, 300 (2017).
[4] Z.-B. Kang, A. Prokudin, F. Ringer, and F. Yuan, Phys. Lett. B **774**, 635 (2017).

SECTION II

HEAVY ION REACTIONS

Inclusive production cross sections at 0° from reactions of ^{4}He + ^{12}C

A. Zarrella, J. Gauthier, K. Hagel, A. Jedele, A.B. McIntosh, A. Rodriguez Manso,

A. Wakhle, and S.J. Yennello

An experiment was conducted at the Cyclotron Institute which measured the cross section of the pionic fusion reaction ^{4}He + ^{12}C → ^{16}N + π^+ using a 55 MeV/nucleon ^{4}He beam. The Momentum Achromat Recoil Spectrometer (MARS) [1] was used to separate and collect the ^{16}N fusion residues at a silicon stack located at the spectrometer focal plane. While the search for pionic fusion events was the main goal of the experiment, various reaction products were also being collected. The range of measured magnetic rigidities spans from approximately 0.52 Tm to 0.69 Tm. This range was chosen as it is centered around the rigidity of ^{16}N^{7+} fragments traveling at the center of mass velocity of the colliding system. The cross sections reported in this document are for inclusive production and only consider fragments that are accepted into the spectrometer entrance which has a 9 msr solid angle centered at 0° with respect to the beam axis.

The cross sections have all been calculated using the thin target approximation given in Equation 1 where N is the yield of the detected species, Φ is the total integrated beam flux, ρ_{areal} is the areal density of the carbon target, and σ is the cross section.

$$N = \Phi \rho_{areal} \sigma \qquad (1)$$

The beam current was constantly monitored using the event rate on the silicon stack at the MARS focal plane. This event rate was then calibrated using periodic Faraday cup measurements at the target position. The areal density of the target was determined using the energy lost in the foil by a ^{16}O beam. The particle identification (PID) process for the silicon stack is shown in Fig. 1. Panel (a) shows the first step of the PID where spots are identified in the E_{tot} vs. Y-position PID space. The Y-position is correlated with the mass-to-charge ratio of the species such that each of the clearly separated spots corresponds to particles with a particular mass and charge state. The rectangular PID gates are shown overlaid on this figure with the spot identifications noted. After this stage of identification, however, isobars with the same charge state (^{12}B^{5+} and ^{12}C^{5+}, for instance) are not separated. Panel (b) shows the second stage of PID for events inside the A = 12, Q = 5+ E_{tot} vs Y-position gate. This step uses the energy deposited in the dE component of the silicon stack versus the thickness of the dE silicon at the point where the particle was incident on the detector. This process was necessary because the thickness of the dE silicon was extremely non-uniform. As Fig. 1 (b) shows, this process produces good elemental PID separation between ^{12}B and ^{12}C. The PID gates are also overlaid and labeled.

Once the PID process was established, it is possible to begin considering particle yields. These yields, however, must be modified by various experimental efficiencies. Before the pionic fusion experiment, a beam of ^{16}O^{7+} was used to determine the transport efficiency of MARS for our residues of interest when their rigidity exactly matches the central rigidity of the MARS setting and was found to be 26%. Of course, not all transported particles are exactly at the central rigidity of the spectrometer. This
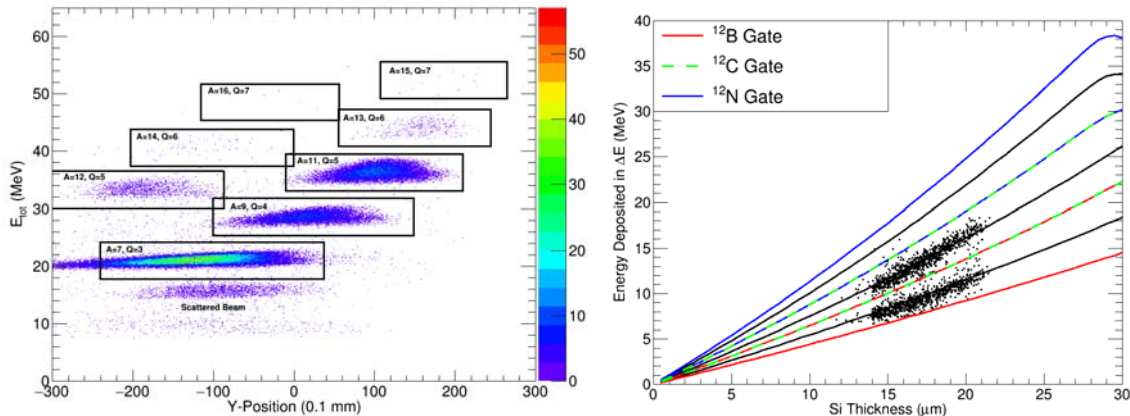
FIG. 1. (a) The Etot vs. Y-position PID plot collected while MARS was tuned for 0.5829 Tm. The vertical axis is the total measured kinetic energy in MeV and the horizontal axis is the Y-position in units of 0.1 mm. Each of the spots corresponds to species with the same mass and charge state and the rectangular PID gates are overlaid with the spot identifications noted. (b) The dE Energy vs. Si Thickness PID figure for the data inside the A = 12, Q = 5 gates from panel (a). The vertical axis is the energy deposited in the dE silicon in MeV and the horizontal axis is the thickness of the dE silicon in microns at the point where the particle hits the silicon stack. The black lines are SRIM predictions for (bottom to top) ^{12}B, ^{12}C and ^{12}N and the colored curves represent the PID gates in this space.

results in a reduction in the transmission efficiency as the particle's rigidity moves away from the central value. This effect, which will be called the Bρ window efficiency was determined using the measured shapes of the energy distributions of the various species. It was determined that this Bρ efficiency is 51%, meaning that around half of the particles with a rigidity inside the tuned MARS window are not transported to the focal plane. The live time of the data acquisition was being measured throughout the experiment and was always above 90%. There is also a detection efficiency associated with the charge state distribution of the residues of interest. Due to the limited width of the MARS Bρ measurement region, the experiment was only sensitive to a single charge state for each residue species. A semi-empirical formula [2] was used to calculate the expected charge state distribution for the residues leaving the ^{12}C target. The yields were then integrated over the charge distributions to produce a charge state integrated cross section.

As a comparison to the measured data, 64 million Gemini deexcitations of ^{16}O compound nuclei were simulated with a flat distribution of spins from 0ℏ to 7ℏ, the critical angular momentum for complete fusion in the reacting system [3]. The cooled fragments were then boosted into the lab frame and passed through a MARS filter which simulates the angular acceptance of the spectrometer and the rigidity selection. In order to translate the simulated particle yields so that they can be compared to the measured data, the number of ^{11}B fragments from the simulation was scaled to the measured cross section of ^{11}B and all of the simulated species were scaled by the same factor. Viewed in this way, the species-to-species trends can be compared to the measured results.

Fig. 2 shows the measured cross sections for all of the identified species in the experiment shown in closed circles and the scaled Gemini results in open circles. Species with the same number of protons, Z, are connected by solid lines in the cases of the data and dashed lines in the cases of the simulation.
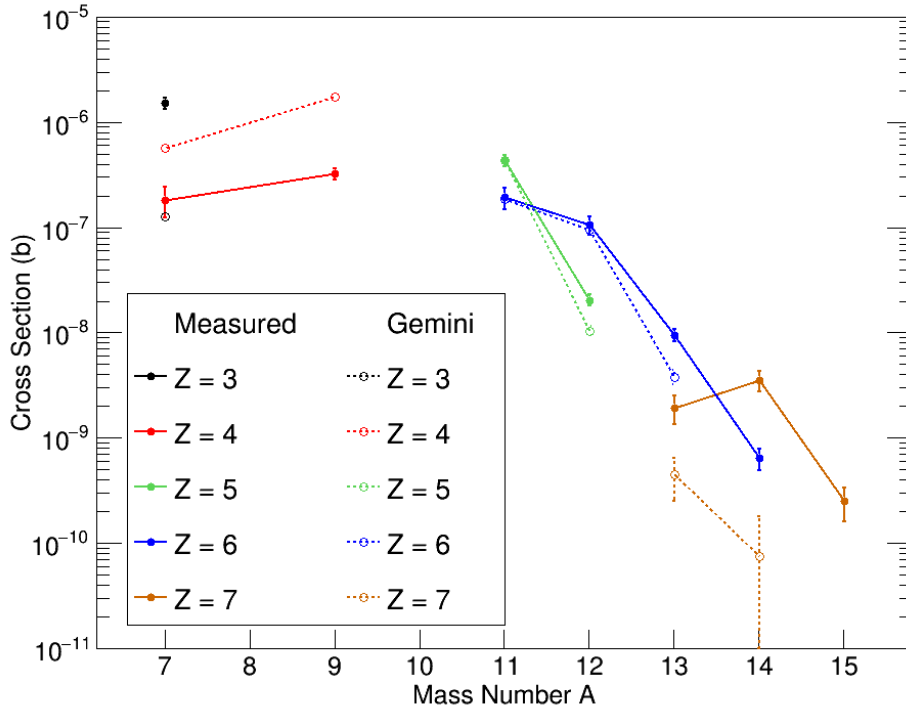
FIG. 2. The Bρ-integrated production cross sections for all species identified at the MARS focal plane during the pionic fusion experiment. The vertical axis is the cross section in barns and the horizontal axis is the particle mass number. The full circles are the measured cross sections and the open circles are the predictions from Gemini deexcitations of the compound nucleus. All species sharing the same proton number are connected with lines, solid for the measured data and dashed for the Gemini results.

The vertical axis is the cross section in barns and the horizontal axis is the species' mass number. The error bars on the measured data are produced by a detailed accounting of the uncertainties associated with the various efficiency corrections, the statistical uncertainties, and the PID uncertainties. The error bars on the Gemini results are produced by the addition in quadrature of the statistical uncertainties and the difference between the species yield at $0\hbar$ spin and at $7\hbar$ spin. This provides a conservative accounting for the non-triangular distribution of spins that were run. However, as is clear from the relative size of the error bars on the Gemini results, the statistical uncertainties dominate in the cases where the error bars are larger than the points. Note that the experimental and simulated values for ^{11}B are identical by definition since it was chosen for the scaling.

The experimental cross sections shown have been integrated over the range of investigated Bρs, 0.52 Tm to 0.69 Tm. The Gemini simulation fairly successfully reproduces the production trends in the mass range from A = 11 to A = 14 to within an order of magnitude in nearly every case. It is not as successful, though, in the A = 7 to A = 9 range. This is likely because the fragments larger than A = 11 are being produced through a similar set of mechanisms with a significant contribution from fusion-evaporation reactions. The lighter species may be resulting from different mechanisms such as pick-up

reactions or incomplete fusion. If this is the case, it is not surprising that the lighter species' productions do not track with the heavier products.

[1] R.E. Tribble *et al*., Nucl. Instrum. Methods Phys. Res. **A285**, 441 (1989).
[2] G. Schiwietz and P.L. Grande, Nucl. Instrum. Methods Phys. Res. **B175-177**, 125 (2001).
[3] W.W. Wilcke, *et al*., Data and Nuclear Data Tables **25**, 389 (1980).

Pionic fusion of ^{4}He + ^{12}C

A. Zarrella, A. Bonasera, J. Gauthier, K. Hagel, A. Jedele, A.B. McIntosh, A. Rodriguez Manso,
A. Wakhle, and S.J. Yennello

Pionic fusion is the process by which two nuclei fuse and then deexcite by the exclusive emission of a pion. The resulting compound nucleus is left in or near its ground state [1]. The process requires that nearly all of the available kinetic and potential energy in the colliding system be concentrated into two degrees of freedom - the rest mass and kinetic energy of the emitted pion. Thus, the energy of the emitted pion is limited by the number of available final states of the fusion residue [2]. The combination of limited available energy and the extreme coherence required in the process ensures that the pionic fusion channel is greatly suppressed. Indeed, the measured pionic fusion cross sections range from hundreds of nanobarns for the lightest systems (He + He) to hundreds of picobarns as one moves to larger systems (A_{tot} = 6 - 24) [2-12].

An experiment was conducted at the Cyclotron Institute to measure the cross section of the pionic fusion reaction ^{4}He + ^{12}C → ^{16}N + π^+ using the Momentum Achromat Recoil Spectrometer (MARS) [13] for detection of the ^{16}N fusion residue and the Partial Truncated Icosahedron (ParTI) phoswich array [14] for the detection of the charged pion. Over the past year, the analysis of the experimental data has nearly been completed. A detailed accounting of the various efficiencies associated with the experimental design and the measurement of the production of ^{16}N fragments detected at the MARS focal plane has been used to produce measured cross sections for the pionic fusion reaction. The Gemini statistical deexcitation code [15] has been used to estimate the ^{16}N background produced in reactions on ^{16}O, the likeliest source of contamination in the ^{12}C target. For those MARS events which were identified as ^{16}N fragments, there were no pions detected in the ParTI array.

Over the course of the pionic fusion experiment, data was collected while MARS was tuned at 6 different central Bρs - 0.5363 Tm, 0.554 Tm, 0.5829 Tm 0.6073 Tm, 0.6304 Tm and 0.6657 Tm. The lowest and highest of these Bρ windows are outside of the allowed energy distribution for ^{16}N residues resulting from the pionic fusion reaction of interest. Thus, any ^{16}N detected with these settings can only be attributable to background. In total, 2 counts of ^{16}N were detected - 1 in the allowable region in the 0.5829 Tm Bρ window and 1 in the background region at 0.6657 Tm. The 1 count in the 0.5829 Tm region corresponds to a cross section of 29.5 ± 29.7 pb and the 1 count in the background region corresponds to 28.9 ± 29.1 pb. The 0.5829 Tm Bρ window covers 42.9% of the total energy distribution of the pionic fusion ^{16}N residues. Scaling by this coverage, therefore, can produce an energy-integrated, gross cross section for pionic fusion of 68.8 ± 69.2 pb.

The level of background in the energy region of interest was estimated using the Gemini statistical deexcitation code. The most abundant contaminant in the ^{12}C target is ^{16}O from adsorbed water on the foil's surface. Gemini was used to deexcite ^{20}Ne fusion residues from reactions on the ^{16}O contamination to predict the energy distribution of the ^{16}N residues created in this background reaction. Figure 1 shows this ^{16}N magnetic rigidity distribution in Tm with the shaded regions indicating the region of interest for pionic fusion (green) and the measured background region (red). Gemini predicts that the

number of ^{16}N residues created in reactions on ^{16}O in the region of interest is 4x higher than the ^{16}N production in measured background region. Since it is not possible for pionic fusion to contribute to the cross section in the 0.6657 Tm background region, and given the reasonable assumption that reactions on ^{16}O are the likely source of the measured background, the expected background cross section in the region of interest would be 4 x 28.9 ± 29.1 pb, or 115.6 ± 116.4 pb.
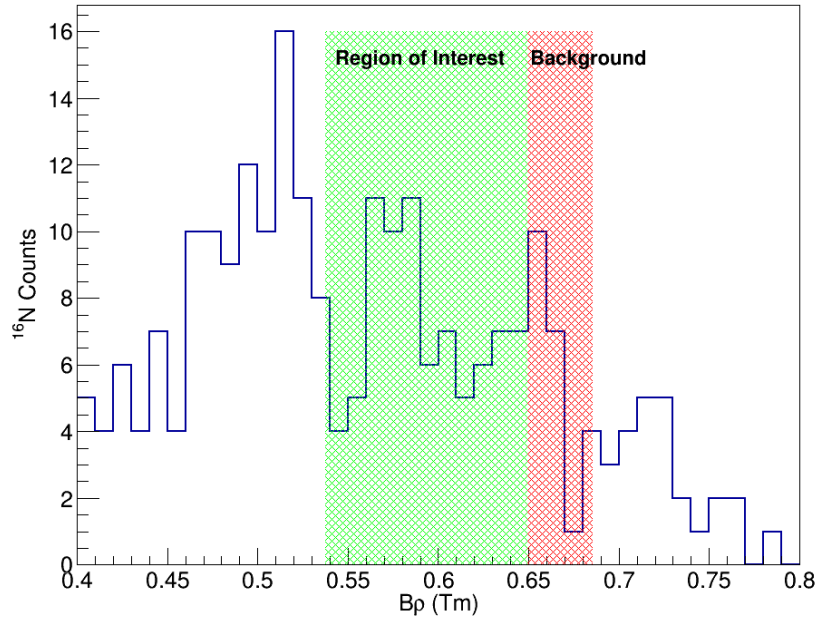
FIG. 1. The ^{16}N Bρ distribution predicted by Gemini deexcitations of ^{20}Ne compound nuclei corresponding to the complete fusion product of ^{4}He + ^{16}O background reactions. The green shaded region is the region of interest for ^{16}N residues of pionic fusion reactions and the red shaded region is the window corresponding to the background measurement around 0.6657 Tm.

The estimated background cross section in the region of interest is consistent with the measured gross cross section in the region of interest. After background subtraction, therefore, the measured pionic fusion cross section measured from the detection of ^{16}N fusion residues is consistent with zero. The upper limit of the cross section is determined by the sensitivity of the cross section measurement. In this case, it is the upper edge of the 1σ error bar on the background measurement - 232 pb. Fig. 2 shows this upper limit for the ^{4}He + ^{12}C → ^{16}N + π^{+} pionic fusion reaction determined in this experiment compared to previous measurements of other pionic fusion reaction cross sections [4]. The horizontal axis is the total mass of the colliding system divided by 2 and the vertical axis is the cross section in nb. When compared with the other pionic fusion results, the measurement from this experiment implies a lower cross section than one would expect given the general trend as a function of colliding system mass. One might reasonably expect that the physics driving the pionic fusion mechanism are more sufficiently complex that a simple accounting for the size of the reacting system is not sufficient to predict cross sections. Such a situation could plausibly explain why this result is seemingly not consistent with the larger trend

produced by previous measurements, none of which used alpha projectiles or the same energy above the pion production threshold (140 MeV center of mass energy). The state of the field of pionic fusion, however, is not such that the question can be answered confidently - highlighting the necessity for further data and theoretical work.
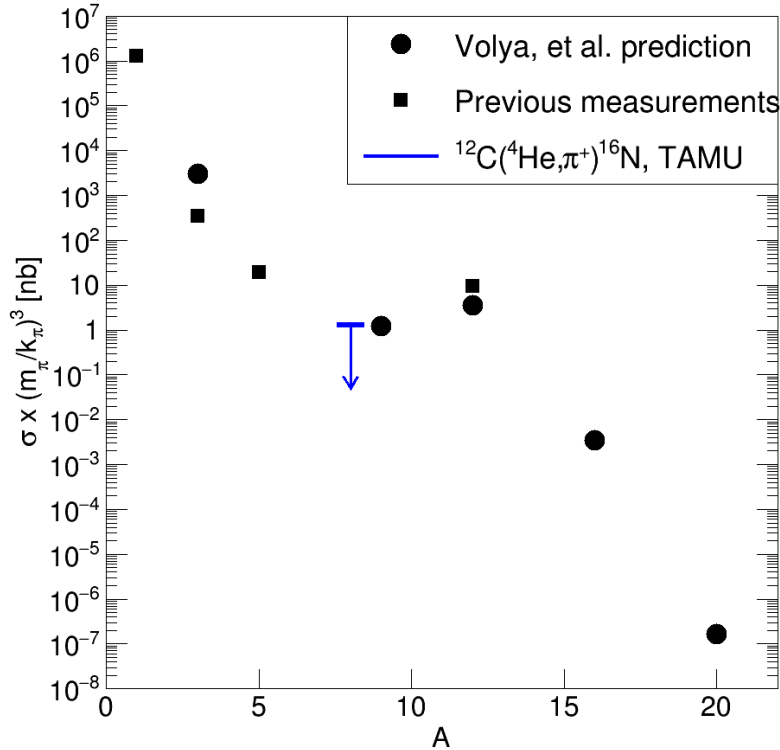
FIG. 2. A comparison of the upper limit for the pionic fusion cross section found in this experiment to previous measurements [4] and predictions [16]. The horizontal axis is the total system mass divided by 2 and the vertical axis is the cross section in nb scaled by the cube of the pion mass divided by the pion kinetic energy corresponding to the energy above the pion production threshold. The blue line is the location of the upper limit measured in this experiment.

The analysis of the ParTI array data from the pionic fusion experiment is still underway. However, it has been confirmed that there are no pion events that come in coincidence with either of the two ^{16}N events in MARS or with any of the other events which were identified as A = 16 particles. We are currently in the process of searching the ParTI array events which were collected without a coincident MARS residue of any kind for any charged pions. At the end of that search, a cross section will be reported based on the detection of charged pions. Because detection of charged pions using the ParTI array is a less sensitive method than detection of the residues using MARS, we expect to report an upper limit on a cross section using this data as well, but with less precision than order 100's pb.

[1] P. Braun-Munzinger and J. Stachel. Ann. Rev. Nucl. Part. Sci. **37**, 97 (1987).

[2] D. Horn *et al*., Phys. Rev. Lett. **77**, 2408 (1996).

[3] Y. Le Bornec *et al*., Phys. Rev. Lett. **47**, 1870 (1981).

[4] L. Joulaeizadeh *et al.*, Phys. Lett. B **694**, 310 (2011).

[5] W. Schott *et al*., Phys. Rev. C **34**, 1406 (1986).

[6] M. Andersson *et al.*, Nucl. Phys. **A779**, 47 (2006).

[7] M. Andersson *et al.*, Phys. Lett. B **481**, 165 (2000).

[8] M. Andersson *et al.*, Phys. Scr. **T104**, 96 (2003).

[9] L. Bimbot *et al.,* Phys. Rev. C **30**, 739 (1984).

[10] L. Bimbot *et al.,* Phys. Lett. B **114**, 311 (1982).

[11] J. Homolka *et al.*, Phys. Rev. C **38**, 2686 (1988).

[12] N. Willis *et al.*, Phys. Lett. B **136**, 334 (1984).

[13] R.E. Tribble *et al*., Nucl. Instrum. Methods Phys. Res. **A285**, 441 (1989).

[14] A. Zarrella *et al*., Physics Procedia. **90**, 463 (20147).

[15] R.J. Charity, Phys. Rev. C. **58**, 10730 (1998).

[16] A. Volya *et al*., Phys. Rev. C **59**, 305(1999).

Neutron-proton equilibration in dynamically deformed nuclear systems: multifragmentation

A. Rodriguez Manso, A.B. McIntosh, K. Hagel, A. Jedele, A. Zarrella, A. Wakhle, and S.J. Yennello

We extend the study of neutron-proton (NZ) equilibration in dynamically deformed nuclear systems presented in [1,2] by investigating further the correlations between the three largest fragments coming from the excited Projectile-Like Fragment (PLF*) produced when beams of ^{70}Zn are accelerated to 35 MeV per nucleon by the K500 Cyclotron at Texas A&M University and focused onto thin foils of ^{70}Zn. Other studies on this topic can be found in [3,4] and the physical idea is depicted in Fig. 1.
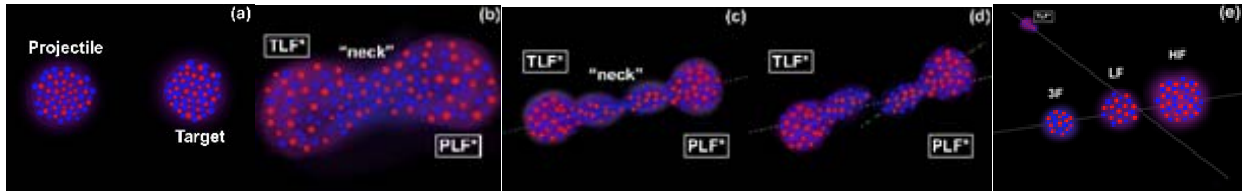
FIG. 1. Cartoon representation of the dynamical deformation and decay following a heavy-ion collision, by [5]. Panel (a): Projectile approaching target. Panel (b): Projectile rotated around target forming a low-density "neck" region. Panel (c): Excited PLF* and target like fragment (TLF*) moved further away from each other and stretched, with the smallest fragments forming out of the neck region. Panel (d): Nuclear system breaks and PLF* separates from TLF*. Panel (e): Subsequent separation of the PLF* into heavy fragment (HF), second heaviest fragment (LF) and third heaviest fragment(3F).

The fragments' velocity distributions in the direction of the beam, shown in Fig. 2, are used to establish the specific fragments that correspond to the PLF* daughters. The figure shows the normalized yield as a function of the velocity distributions of the symmetric ^{70}Zn+^{70}Zn system, for a representative combination of HF (in red), LF (in blue) and 3F (in green), (i.e. ZH = 12, ZL = 7, Z3 = 3). The dashed
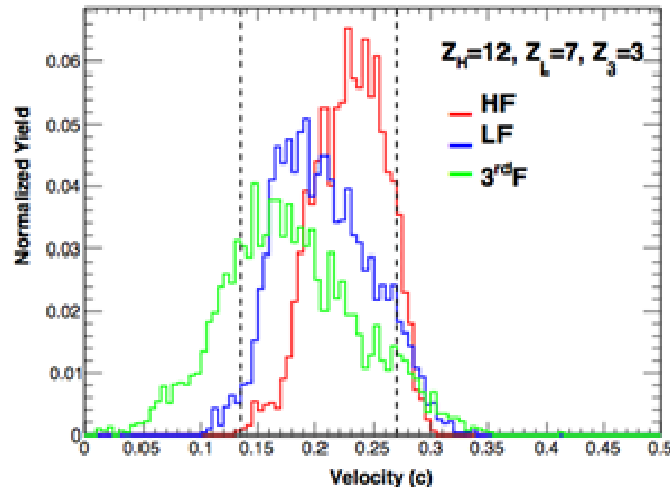
FIG. 2. Normalized velocity distributions for HF, LF and 3F in the direction of the beam.

lines (from right to left) correspond to the beam and half of the beam velocities. HF, LF and 3F are peaked above mid-velocity which indicates that the three of them likely originate from the PLF*. In addition to that, there seems to be a hierarchy in the velocity distributions that is strongly correlated to the charge sorting: the HF is, on average, the fastest one in the beam direction and appears to be forward with respect to the LF and 3F, while the LF is the second fastest fragment in the beam direction and appears to be forward with respect to 3F.

Symmetrized Dalitz plots, like the one shown in Fig. 3, could give information on the three body system's Z correlation. The center of the triangle would correspond to three approximately equal sized fragments. The edges of the triangle, between two vertices, corresponds to one small fragment and two large ones approximately equally sized. Finally, vertices of the triangle filled in hints to large cross sections for very asymmetric breaks. The region where the data in the figure is peaked corresponds to one large and two smaller, equally sized fragments.
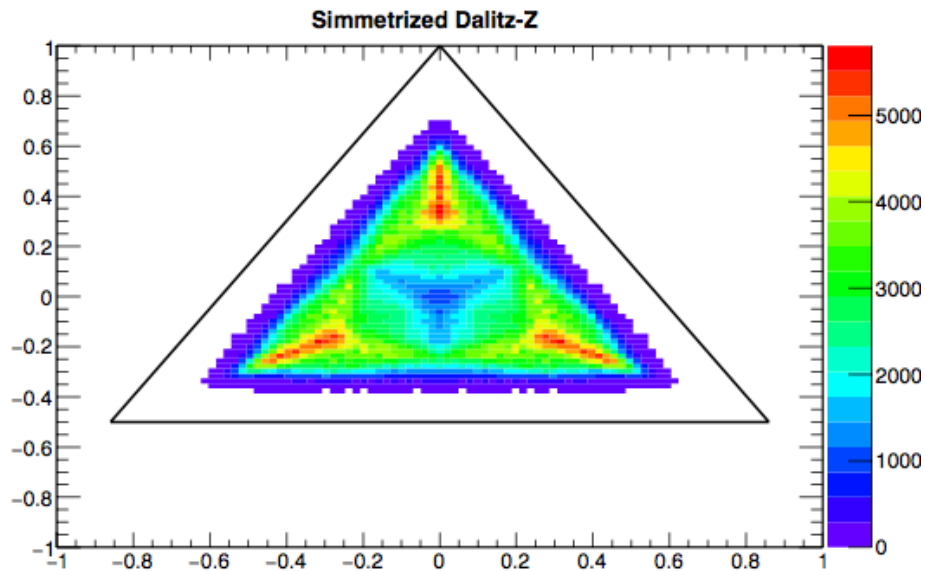
FIG. 3. Z correlation for the HF, LF and 3F studied using symmetrized Dalitz plots.

Two other interesting Dalitz plots one could look at when studying a three body system are shown in Fig. 4. The interpretation of both will be combined shortly. The left panel of the figure illustrates the angular correlation between the projections of the HF, LF and 3F velocities in a plane perpendicular to Vcm, while the right panel depicts the correlations between the angles of the HF, LF and 3F relatives velocities in the plane formed by the three fragments.

Looking at the left panel of the figure, each vertex of the total triangle being filled in would correspond with only one angle being $360°$, that is not possible which is why the vertices of the plot are not filled in. The sides of the triangle being hot, represent two fragments having big angles while another one having a small one, resulting in two fragments seemingly closer to each other and apart from the third one (e.g. majority of events populating combinations of $180°$, $0°$ and $180°$). From the right panel of

Fig. 4 it looks like the three angles are somehow similar with a slight preference to the lower vertices being bigger compared to the top vertex.
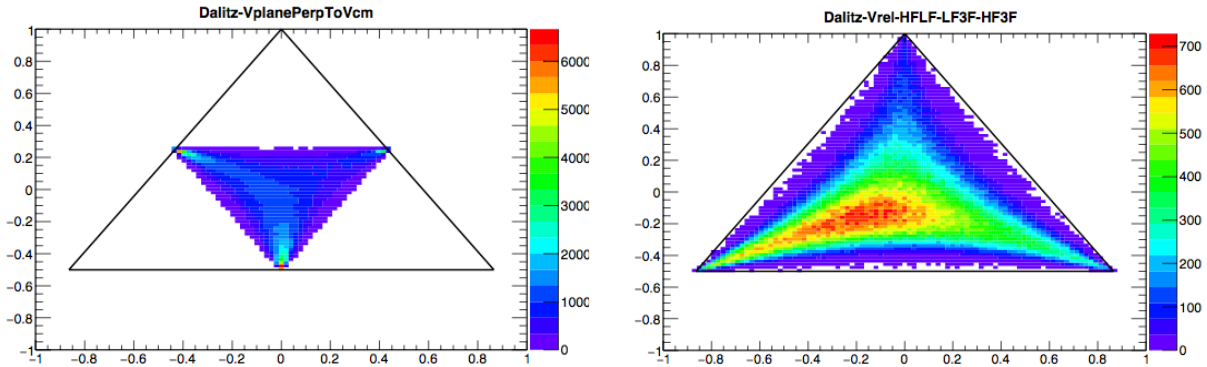
FIG. 4. The left panel illustrates the angular correlation between the projections of the HF, LF and 3F velocities in a plane perpendicular to Vcm, while the right panel depicts the correlations between the angles between the relatives velocities of the HF, LF and 3F in the plane form by the three fragments.

Combining the observations from both panels one could conclude that the physics of the three body system is dominated by the angular momentum, as in [1,2]). The angular momentum seems to be controlling the rupture of the three fragments, because it is occurring in preferential planes. In addition to that, the three fragments don't seem to be aligned.

In Fig. 5 we have a cartoon representation of both the plane perpendicular to V_{cm} and the plane formed by the three fragments. To cause such asymmetric angular projection in the plane perpendicular
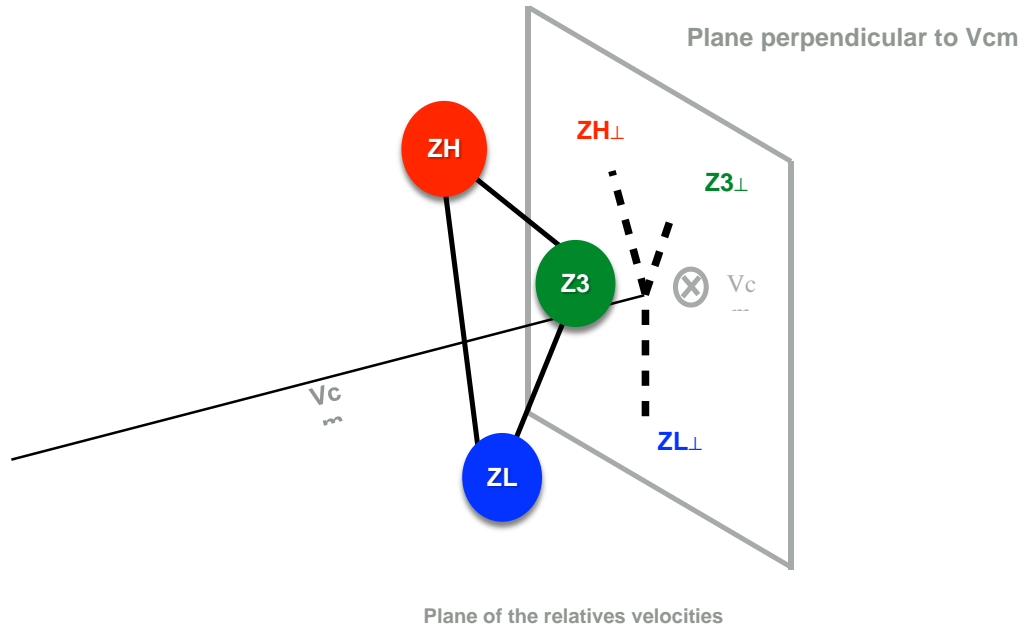
FIG. 5. Cartoon of a plane perpendicular to V_{cm} and a plane form by the three fragments.

to V_{cm}, while having very symmetric angle values for the relatives velocity plane of the three fragments, would mean the latter is oblique to the V_{cm} vector and the three fragments are not aligned.

If one imagines the rupture as being spontaneous (i.e. the three fragments separate simultaneously), we wouldn't have a preference in the direction of the movement. On the other hand, if the system breaks due to rotation and in a double rupture scenario, the plane of the relative velocities is the plane perpendicular to the angular momentum, and almost the same as V_{cm}, or very oblique to V_{cm}. We calculated this angle demonstrating is indeed oblique to V_{cm}, and it is shown in Fig. 6. The three body study is currently ongoing
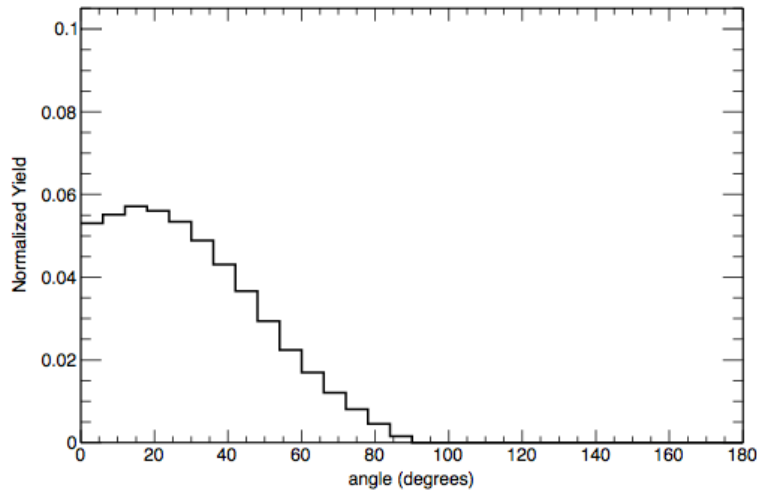
FIG. 6. Oblique angle between the plane that contains the relatives velocities of the three fragments and the V_{cm} vector.

[1] A. Jedele *et al.*, Phys. Rev. Lett. **118**, 062501 (2017).

[2] A. Rodriguez Manso *et al.*, Phys. Rev. C **95**, 044604 (2017).

[3] C. Colin *et al.*, Phys. Rev. C **67**, 064603 (2003).

[4] S. Hudan *et al.*, Phys. Rev. C **80**, 064611 (2009).

[5] A. Poulsen, oxidantshappencomics.wordpress.com, 2016.

Search for an Hoyle state analogous state in ^{16}O using the thick target inverse kinematics technique

M. Barbui,[1] K. Hagel,[1] J. Gauthier,[1] S. Wuenschel,[1] R. Wada,[1] R. T. deSouza,[2] S. Hudan,[2] D. Fang,[3]
X.G. Cao,[1,3] and J.B. Natowitz[1]

[1]*Cyclotron Institute, Texas A&M University, MS3366 College Station, Texas*
[2]*Indiana University, Bloomington, Indiana*
[3]*Shanghai Institute of Applied Physics (SINAP), Chinese Academy of Sciences, Shanghai, China*

Searching for alpha cluster states analogous to the ^{12}C Hoyle state in heavier alpha-conjugate nuclei can provide tests of the existence of alpha condensates in nuclear matter. Such states are predicted for ^{16}O, ^{20}Ne, ^{24}Mg, ^{28}Si etc. at excitation energies slightly above the multi-alpha particle decay threshold [1-3].

The Thick Target Inverse Kinematics (TTIK) [4] technique can be used to study the breakup of excited self-conjugate nuclei into many alpha particles. The reaction ^{20}Ne+α at 12 and 9.7 AMeV was studied at Cyclotron Institute at Texas A&M University. A picture of the experimental setup is shown in Fig. 1. The TTIK method was used to study both single α-particle emission and multiple α-particle decays. The analysis of the three α - particle emission data allowed the identification of the Hoyle state and other ^{12}C excited states decaying into three alpha particles. Some results are reported in ref [5, 6] and compared with other data available in the literature. In this report we update the results of the analysis of the events with alpha multiplicity four. In order to minimize accidentals, only events in which the four
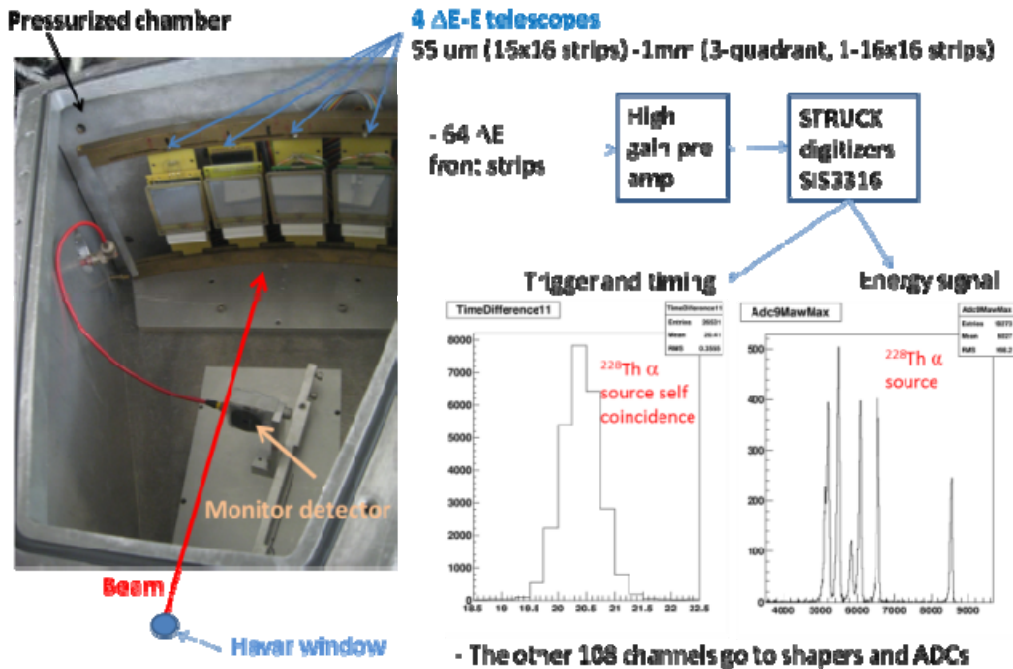
FIG. 1. Experimental setup and scheme of the electronics. Good energy and time resolution are obtained by using the STRUCK digitizers SIS3316.

alpha particles arrive to the detectors in a time window of 30 ns are selected. Due to the very low beam intensity used during this run we estimate one beam particle per beam burst.

The excitation function of [16]O is shown in Fig. 2. The left panel shows the result obtained at maximum beam energy of 12A MeV, the right panel shows the excitation function obtained from the experiment performed at maximum beam energy of 9.7A MeV. The two excitation functions in Fig. 2 show an interesting structure at 15.2 MeV, very close to the energy (15.1 MeV) predicted by Funaki *et al*. [8] for a state in [16]O with the structure of the "Hoyle" state in ^{12}C coupled to an alpha particle.
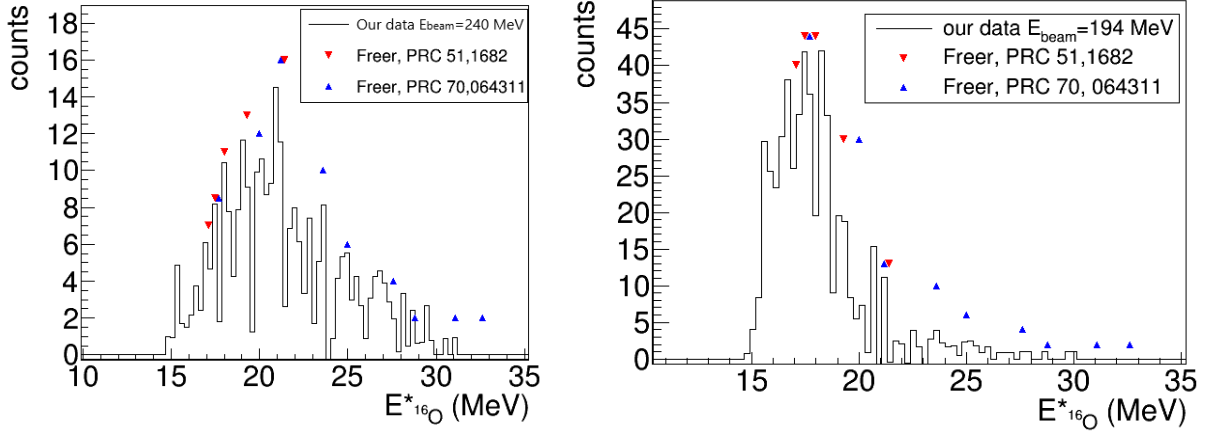
FIG. 2. Left Panel, excitation function at maximum beam energy 240 MeV. Right Panel, excitation function at maximum beam energy 194 MeV. The arrows mark the position of known states in [16]O decaying into alpha particles [7,9].

For some of the peaks in the excitation function including the 15.2 MeV, we determined the amount of events decaying into one alpha particle and one ^{12}C in the Hoyle state or two [8]Be in the ground state. To do this we considered the six possible combinations of two alpha particles (0-1, 2-3; 0-2, 1-3; 0-3, 1-2), the decay proceeded through two [8]Be in the ground state if the relative energies of 0-1 and 2-3 or 0-2 and 1-3 or 0-3 and 1-2 were less than 250 keV.

In the same way we considered the four possible combinations of three alpha particles 0-1-2, 0-1-3, 0-2-3, 1-2-3 and checked if the decay proceeded through the [12]C Hoyle state. In this case the sum of the kinetic energies of the three alpha particles in their center of mass should be less than 500 keV or 600 keV for the events in the higher energy states. The relative partial decay widths R were calculated as:

$$R = \frac{\Gamma(^{8}Be + {}^{8}Be)}{\Gamma(\alpha + {}^{12}C(0_{2}^{+}))} = \frac{Yield(^{8}Be + {}^{8}Be)}{Yield(\alpha + {}^{12}C(0_{2}^{+}))}$$

Monte Carlo simulations showed that the detection efficiency for the two decay modes is the same to within a few percent. The results are shown in Table I and compared with data from Freer et al. [13]. The ratios R for the states at 17, 19 and 21 MeV agree quite well with those measured by Freer et al. The peak at 15.2 MeV shows the same decay probability into two [8]Be ground states or $\alpha + {}^{12}$C Hoyle state.

This might indicate that the state has the same characteristics of the ^{8}Be ground state and ^{12}C Hoyle state. A paper with the final results has been submitted to Physical Review C.

[1] K. Ikeda, N. Takigawa, and H. Horiuchi, Prog. Theor, Phys. Suppl. Extra Number, 464 (1968).

Table I. Relative partial decay widths.

Energy	$\Gamma(Be)/\Gamma(Hoyle)$ this work, max beam energy 240 MeV	$\Gamma(Be)/\Gamma(Hoyle)$ this work, max beam energy 194 MeV	$\Gamma(Be)/\Gamma(Hoyle)$ Freer et al. [13]
15.2±0.2	1±0.7	0.96 ± 0.3	
17.1	0.6±0.3	0.7 ± 0.3	0.65 ± 0.16
17.5		0.6 ± 0.3	0.72± 0.18
19.7	0.43±0.2	0.6 ± 0.5	0.47± 0.15
21.4	5.3±2.8	3 ± 1	>3± 1.1

[2] W. von Oertzen, M. Freer, and Y. Kanada-Enýo, Phys. Rep. **432**, 43 (2006).

[3] C. Beck, J. Phys. Conference Series **436**, 012014 (2013).

[4] K. Artemov *et al.*, Sov. J. Nucl. Phys. **52**, 406 (1990).

[5] M. Barbui *et al.*, Eur. Phys. J. Web of Conferences **66**, 03005 (2014).

[6] M. Barbui *et al.*, Eur. Phys. J. Web of Conferences **117**, 07013 (2016).

[7] M. Freer *et al.*, Phys Rev. C **51**,1682 (1995).

[8] Y. Funaki *et al.*, Phys. Rev. Lett. **101**, 082502 (2008).

[9] M. Freer *et al.*, Phys Rev. C **70**, 064311 (2004).

Progress in the fragment yields analysis in ^{124}Sn+^{112,124}Sn at 26A MeV reaction

J. Gauthier, M. Barbui, X. Cao, K. Hagel, J.B. Natowitz, R. Wada, and S. Wuenschel

As described in reference [1], we are currently using a nucleation time moderated statistical equilibrium model, previously used to reproduce ternary fission isotopic yields, to characterize the neck emission in Sn+Sn collisions at 26A MeV obtained with the NIMDOR detector array [2]. The model description and experimental procedure and selection are detailed in reference [1]. In summary, the model uses the chemical potential and a time limitation to generate cluster formation yields inside a low density nuclear gas. The free parameters are the temperature, the density, the proton fraction, the time limit and the critical cluster size. To select fragments from the mid-rapidity region, we use the relative angle in the center of mass between the largest fragment and the fragment of interest velocity vectors. This angle must be inside the 50$^{\text{o}}$-130$^{\text{o}}$ window in order to reject most of the QP contribution while keeping enough statistics. Fig. 1 shows the corrected yield as a function of N/Z for each detected isotope for this relative angle selection.
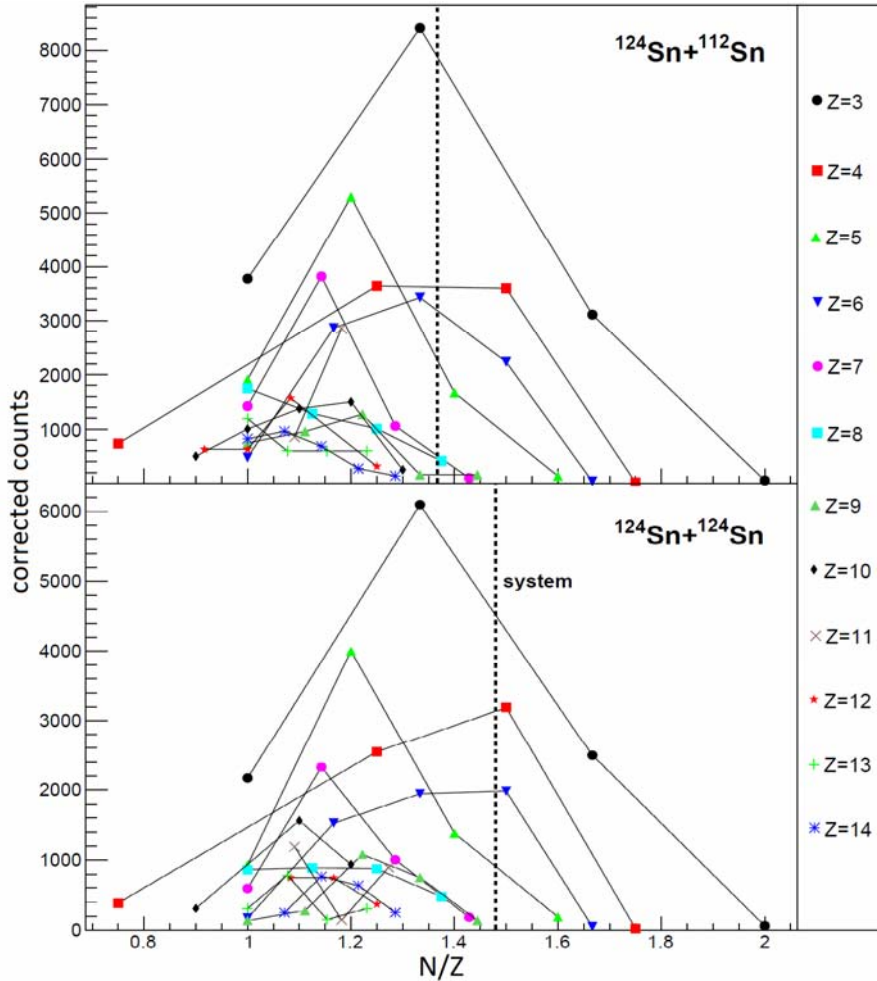
FIG. 1. Corrected yield as a function of N/Z for each isotope and both reactions inside the relative angle selection window.

During the last few months, we improved our minimization technique and extended the fit to isotopes up to Z=14 with a reasonable fit metric. As a reminder, the fit metric is a measure of the average discrepancy and is defined as

$$M^2 = \sum_f \frac{\{ln[Y_{TF}^{exp}(Z_f, A_f) - Y_{PF}(Z_f, A_f)]\}^2}{n} \quad (1)$$

In Fig. 2 we show the results of the best fit we achieved so far and the list of parameter values derived from it is presented in Table I. As we expected, the temperature and density are higher than the
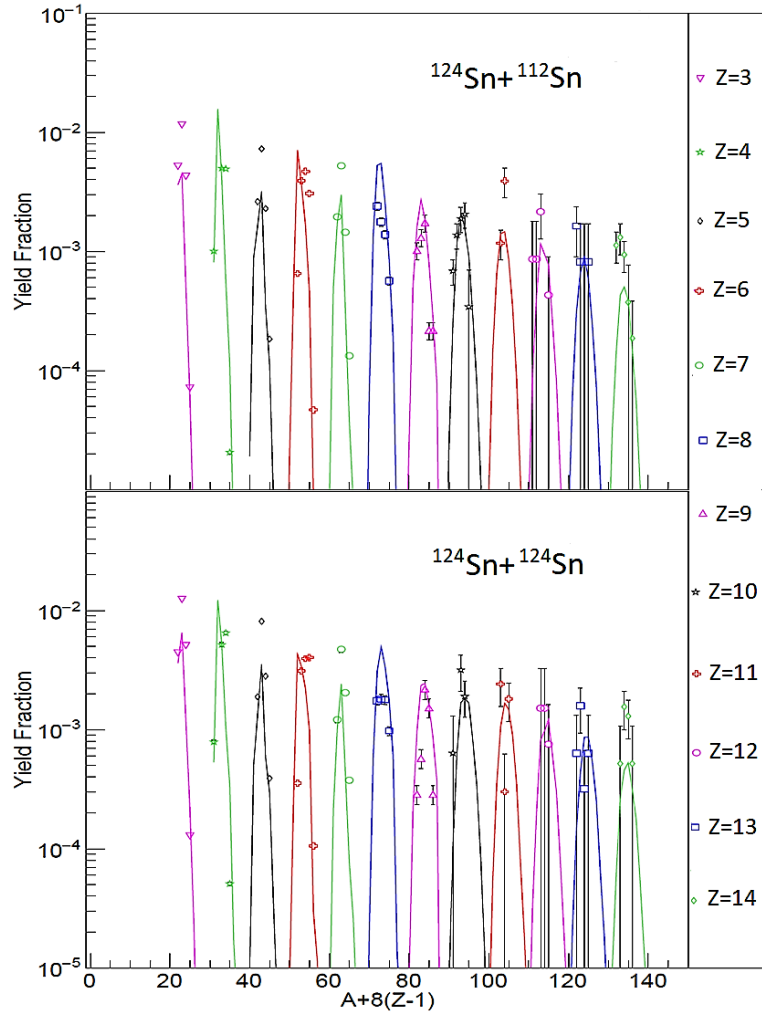
FIG. 2. Normalized fit results for both Sn systems. Lines represent the calculation and symbols are the experimental data.

Table 1. Fit parameter values.

System	^{124}Sn+^{112}Sn	^{124}Sn+^{124}Sn	^{241}Pu
Temperature (MeV)	2.76	2.72	1.4
Density (10^{-4} fm^{-3})	18.67	16.38	4
Time (fm/c)	6000	7300	6400
Critical Cluster Size	15.8	16.1	5.4
Proton Ratio (system)	0.47 (0.42)	0.44 (0.40)	0.34 (0.39

Pu fission ones. To have a comparison point, we calculated the Albergo experimental temperature [3] defined by

$$T_{source} = \frac{14.3}{\ln\left[1.6 \frac{Y(^2H)Y(^4He)}{Y(^3H)Y(^3He)}\right]}, \quad (2)$$

where T is the emission source temperature and Y are the isotope yields. By applying the same relative angle selection to those isotopes, we get 2.74 MeV for ^{112}Sn and 2.88 MeV for ^{124}Sn, which is in very good agreement with the calculation. The time parameters are very similar to the Pu fission and with our 2.7 MeV temperature these times are also in very good agreement with recent fusion-fission time calculations [4]. Another interesting way to test the results and compare with the Pu fission is the equilibrium constant. We know that

$$K = \frac{Y_{product}}{Y_{reactive1} Y_{reactive2}} V = S_0^{\frac{\Delta G^o}{T}} \quad (3)$$

where K is the equilibrium constant, Y is the isotope yield, V is the source volume, S is the reaction spin factor, ΔG^o is the Gibbs free energy and T is the source temperature. By considering a small contribution of the volume difference we write that, for each fragment detected,

$$\frac{K_{Sn}}{K_{Pu}} = \frac{e^{\frac{\Delta G_{Sn}^o}{T_{Sn}}}}{e^{\frac{\Delta G_{Pu}^o}{T_{Pu}}}}. \quad (4)$$

We assume that the fission of Pu leads to fragments in their ground states so we know $\Delta G^o{}_{Pu}$. We also know the temperatures from the calculation and the experimental yields, so we can extract $\Delta G^o{}_{Sn}$ from equation (4). Since the temperature of the mid-rapidity region in the Sn collisions is higher, excited

states must be available to be populated. In Fig. 3, we show $\Delta G^o_{Sn} > \Delta G^o_{Pu}$ for 22 reactions. ΔG^o_{Sn} is in average 33% higher than ΔG^o_{Pu}. A paper draft about those results is being written.
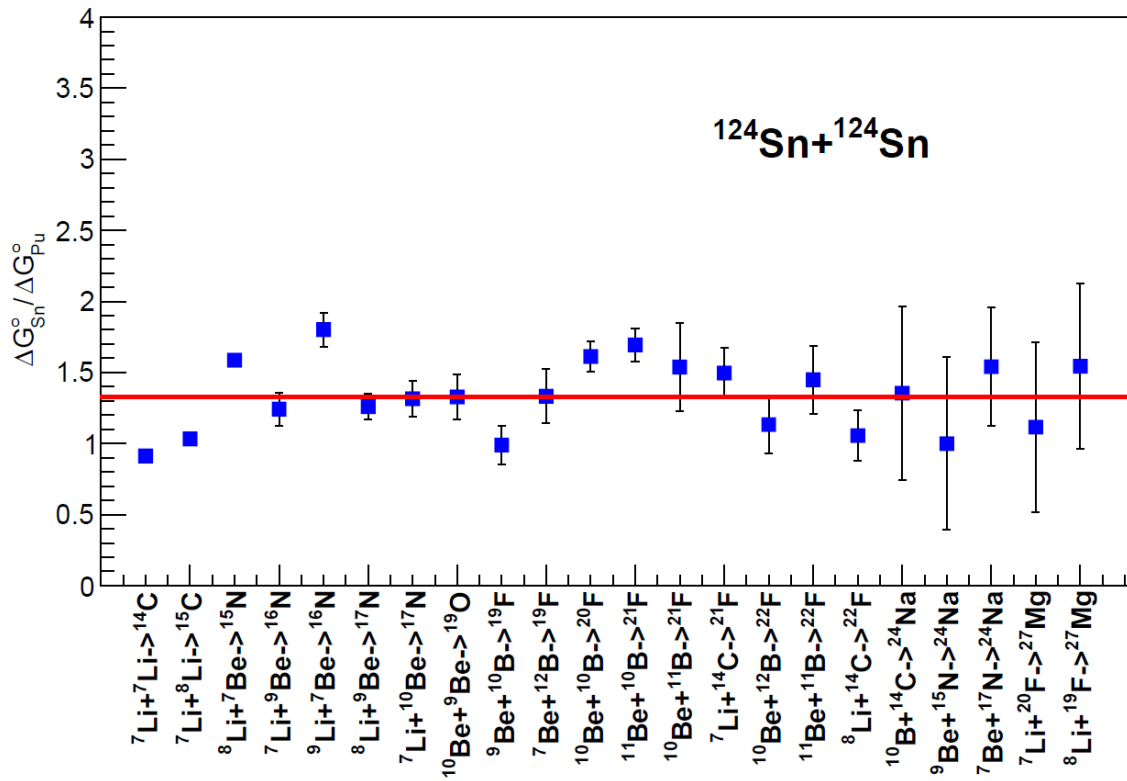
FIG. 3. $^{124}Sn+^{124}Sn$ over ^{241}Pu Gibbs free energy ratio for 22 nuclear reactions. The mean value is 1.33.

[1] J. Gauthier *et al.*, *Progress in Research*, Cyclotron Institute, Texas A&M University (2016-2017), p. II-3.

[2] S. Wuenschel *et al.*, Nucl. Instrum. Methods Phys. Res. **A604**, 578 (2009).

[3] S. Albergo *et al.*, Il Nuovo Cimento, **89 A**, N. 1 (1985).

Searching for toroidal high spin isomer from resonance decay of ^{28}Si

X.G. Cao, K. Schmidt, E.-J. Kim, K. Hagel, M. Barbui, J. Gauthier, R. Wada, S. Wuenschel, M. Huang, G.Q. Zhang, H. Zheng, N. Blando, A. Bonasera, G. Giuliani, M. Rodrigues, C. Botosso, G. Liu, C.Y. Wong, A. Staszczak, Z.X. Ren, Y.K. Wang, S.Q. Zhang, J. Meng, and J.B. Natowitz

Toroidal nuclei were proposed by J. A. Wheeler in 1950s [1]. Then C. W. Wong explored heavy nuclei and light toroidal nuclei and found that large Coulomb energies in heavy mass nuclei and shell effects with sufficiently large angular momentum in light nuclei favor toroidal exotic structure [2-4]. Most recently, various sophisticated Hartree-Fock microscopic methods address this question of light toroidal nuclei [5-7].

Searches for the experimental signal of toroidal high spin isomers (THSI) in collisions of α conjugate nuclei with the NIMROD-ISiS array are still in progress. Partial data analysis progress of the experiments can be found in ref [8][9]. Here we focus on ^{28}Si+^{12}C @35MeV/nucleon since it shows interesting indications and good statistics for possible population and decay of THSI in ^{28}Si*.

It is well verified that the decay of macroscopic tori is dominated by symmetric fragmentations as a result of the development of Plateau-Rayleigh instabilities [10][11][12]. The number of fragments is of the order of the aspect ratio for larger aspect ratio toroids. Nuclear toroid decays might also manifest Plateau-Rayleigh instabilities. However, more factors such as temperature dependent viscosity, Coulomb force and shell effects can largely modify the Plateau-Rayleigh instability. It should be noted that in the Staszczak-Wong, Ichikawa and Meng calculations the minor radius of the toroid is ~1.5fm, essentially the same as the radius of a free α.partice. Ten α in a ring is used as an initial configuration in Ichikawa's cranked Hartree-Fock calculation. Approximately 2/3 of the nuclear saturation density ρ_0 is obtained for the toroidal rings in these calculations. It's already known from theory that quartetting prevails over pairing at $\rho<\rho_0/5$ [13] for symmetric nuclear matter The TAMU data shows evidence that lots of clusters such as α are produced in low densities and moderate temperatures during the heavy-ion collisions at intermediate energy[14]. In addition, α particles can be regarded as quite inert units due to a large binding energy and very high first excitation energy level. Therefore α particles and α conjugate nuclei can offer some possibilities of observing toroidal de-excitations.For ^{28}Si+^{12}C reaction at 35MeV/nucleon, about 3.19×10^5 events with α-like fragment masses summing to 28 were recorded. Among them, about 8200 events are 7α decay events. Fig 1 shows the excitation energy of 7α events. There are three prominent peaks located around 114MeV, 126MeV and 138MeV after the uncorrelated spectrum subtraction. The uncorrelated background is determined in two ways: one is the standard mixed event method using 7α correlated data and the other is 7α excitation spectrum of an AMD+GEMINI simulation. If the 138MeV state corresponds to the predicted 143.18MeV toroidal state by A. Staszczak and C.Y. Wong [5], its angular momentum would be 44$\hbar$. Cranking relativistic density functional calculations [15] predict three toroidal minima in potential energy curves at angular momenta 28$\hbar$, 36$\hbar$ and 44$\hbar$. The associated energies of the three states are within the range suggested by the data although two different interaction parameter sets give slightly different excitation energies.
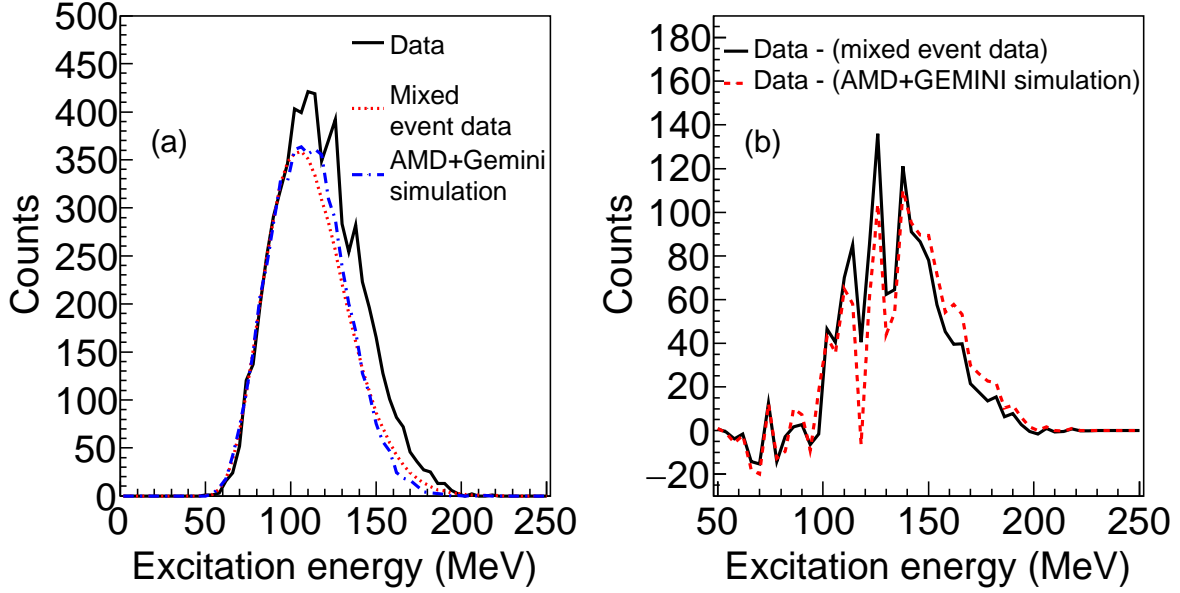
FIG. 1. Excitation function of 7α events, panel (a): experimental correlated spectrum, uncorrelated spectrum derived from event mixing and AMD-Gemini simulation are shown by the solid line, the dashed line, and the dashed and dotted line, respectively. Panel (b): The differences between the experimental spectrum and the other two are shown.

A shape analysis technique [16,17] is used to diagnose the shape of 7α events in momentum space. If the primary fragments are excited or the 7α emission is sequential, the de-excitation process could significantly modify the initial momentum space distribution. GEMINI is used as after burner to simulate the statistical two body decay. The AMD+GEMINI filtered results are similar to the data shown in Fig 2, where most of the events are not in the disk region. The freeze-out momentum distribution @300fm/c predicted by AMD is much more rod to disk like than that observed after de-excitation and filtering. The comparison of data with simulation suggests that 28Si* initially breaks up into larger excited fragments followed by α de-excitation.
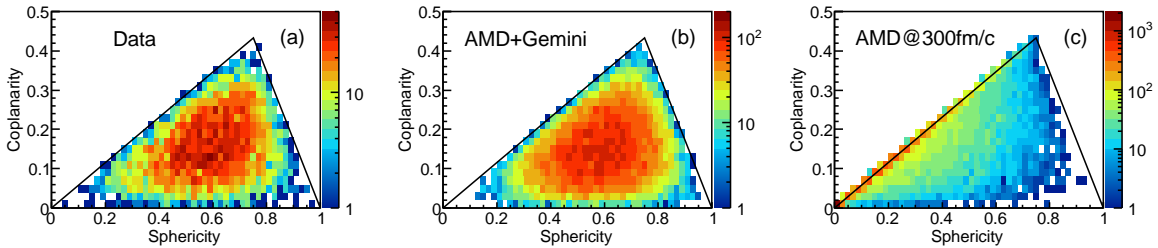
FIG. 2. Shape analysis of 7α exit channels in the de-excitation of 28Si in the 35 MeV/nucleon 28Si + 12C reaction. Panel (a): experimental data. Panel (b): filtered results from AMD+GEMINI simulation. Panel (c): AMD primary fragments at 300 fm/c.

In summary, the 7α resonance structures may indicate the population of high spin toroidal isomers in ^{28}Si+^{12}C @ 35 MeV/nucleon. The several resonance peak energies almost coincide with cranked self-consistent constrained Skyrme–Hartree–Fock and cranked relativistic density functional theory calculations.

[1] J.A. Wheeler, *Nucleonics Notebook*, 1950 (unpublished); G. Gamow, *Biography of Physics*, (Harper & Brothers Publishers, N.Y. 1961) p. 297; Princeton University Graduate Course Physics 576 Take-Home Examination Problem 2, May 22, 1963 (unpublished).

[2] C.Y. Wong, Phys. Lett. B **41**, 446 (1972).

[3] C.Y. Wong, Phys. Rev. C **17**, 331(1978).

[4] C.Y. Wong, Phys. Rev. Lett **55**, 1973 (1985).

[5] A. Staszczak, C.Y. Wong, Phys. Lett. B **738**, 401 (2014).

[6] A.S. Umar *et al.*, Phys. Rev. Lett. **104**, 212503 (2010).

[7] T. Ichikawa *et al.*, Phys. Rev. Lett. **109**, 232503 (2012).

[8] X.G. Cao *et al., Progress in Research*, Cyclotron Institute, Texas A&M University (2014-2015), p. II-16; X.G. Cao *et al.*, *Progress in Research*, Cyclotron Institute, Texas A&M University (2015-2016), p. II-16; X.G. Cao *et al.*, *Progress in Research*, Cyclotron Institute, Texas A&M University (2016-2017), p. II-10.

[9] X.G. Cao *et a*l., arXiv:1801.07366v2

[10] J. Plateau, Annual Report of the Board of Regents of the Smithsonian Institution, 207, (1863); ibid., 286 (1865); ibid., 255 (1866).

[11] Lord Rayleigh, Phil. Mag. **28**, 161 (1914).

[12] E. Pairam and A. Fernández-Nieves, Phys. Rev. Lett. **102**, 234501 (2009).

[13] G. Röpke, A. Schnell, and P. Schuck, Phys. Rev. Lett. **80**, 3177 (1998).

[14] L. Qin *et al.*, Phys. Rev. Lett. **108**, 172701.

[15] J. Meng, J. Peng, S.Q. Zhang, and P.W. Zhao, Front. Phys. **8**, 55 (2013).

[16] G. Fai and J. Randrup, Nucl. Phys. **A404**, 551 (1983).

[17] J.P. Bondorf, C.H. Dasso, R. Donangelo, and G. Pollarolo, Phys. Lett. B **240**, 28 (1990).

Forensic investigations of two irradiated UO$_2$ fuels

K.J. Glennon,[1,2] P.K. Kircher,[1] S.S. Chirayath,[3,4] and C.M. Folden III[1,2]

[1]*Department of Chemistry, Texas A&M University, College Station, Texas 77843*

[2]*Cyclotron Institute, Texas A&M University, College Station, Texas 77843*

[3]*Center for Nuclear Security Science & Policy Initiatives, Texas A&M University, College Station, Texas 77843*

[4]*Department of Nuclear Engineering, Texas A&M University, College Station, Texas 77843*

The detection and prevention of the proliferation of weapons-grade Pu is key to national nuclear security. Pu is produced as a byproduct of UO$_2$ irradiation in a nuclear reactor among other actinides and fission products (FPs). These FPs typically range between 70-170 amu and can be composed of more than 30 different elements. The exact distribution of these FPs within irradiated UO$_2$ depends upon the irradiation history of the fuel; some of the most important parameters are burnup, neutron spectrum, fuel enrichment, and cooling time (time since irradiation). Therefore, by measuring the FP distribution within unseparated irradiated nuclear fuel, modern forensics can attribute these parameters of the fuel's history to learn about the potential origin of unseparated fuel containing weapons-grade Pu. These techniques do not work, however, for separated (chemically purified) Pu. The process used to separate the Pu will decontaminate each FP differently, such that the FP distribution no longer correlates to the fuel's history.

A maximum likelihood technique to determine the most likely irradiation history of separated Pu has recently been developed, which utilizes various FP isotope ratios within the fuel[1]. The use of isotope ratios makes the process agnostic to chemical separation, and therefore applicable to separated or unseparated Pu. This technique has been shown to work for simulated fuel but remains to be tested against real fuel samples. Some of the nuclides necessary for these isotope ratios are stable and need to be measured by mass spectrometry. The most common type of mass spectrometry used in nuclear forensics is inductively coupled plasma mass spectrometry (ICP-MS); although it is a high sensitivity technique capable of detecting some FPs to the part-per-trillion (ppt) level, it is unable to resolve atomic isobars. This presents a challenge since some of the nuclides required for the maximum likelihood technique suffer from isobaric interference. For example, ^{150}Sm in the fuel experiences isobaric interference from ^{150}Nd, which is also present in the fuel. As a result, Sm and Nd must be separated prior to analysis by ICP-MS such that the ^{150}Sm/^{149}Sm isotope ratio may be measured for use with the maximum likelihood technique. The most commonly employed technique to separate lanthanides from each other is cation exchange chromatography utilizing α-hydroxyisobutyric acid (α-HIB) as an eluent.

Two different fuel samples have been separated to determine various Sm isotope ratios for use with the maximum likelihood technique. The first fuel sample was irradiated in the High Flux Isotope Reactor (HFIR) at Oak Ridge National Laboratory, and the second in the University of Missouri Research Reactor (MURR). The HFIR fuel was 12.9 mg of ^{dep}UO$_2$ irradiated in a pseudo-fast spectrum of neutrons to a burnup of 4.4 ± 0.3 GWd/MTU[2], and the MURR fuel was three 16 mg pellets of ^{nat}UO$_2$ irradiated in a thermal spectrum to 0.97 ± 0.03 GWd/MTU[3]. The HFIR fuel was intended to resemble fuel originating from the blanket material of a fast breeder reactor (FBR), and the MURR fuel was

intended to resemble fuel originating from the core of a pressurized heavy-water reactor (PHWR). These reactor types are more commonly found in nations which are not under International Atomic Energy Agency (IAEA) safeguards. Therefore, fuel originating from these reactor types may be more susceptible to proliferation.

Chromatography was performed on the benchtop for each fuel sample using a 300 mm height by 3.1 mm inner diameter column. The stationary phase was a DOWEX 50W X4 200-400 mesh strong cation exchange resin prepared in the NH_4^+ form with a bed height of 200 mm. The fuel samples were loaded onto the column using a 1 M NH_4Cl solution at pH 3.00, then eluted through the column at 0.500 mL/min with 0.4 M α-HIB at pH 3.00. Fractions were collected for each free column volume, corresponding to 550 µL each, and assayed individually by ICP-MS after dilution to 5 mL with 1% HNO_3. The relevant mass bins were swept through the spectrometer 90 times total for each fraction, producing an average and standard deviation for each mass bin of each fraction. Calibration standards were prepared for Cs, Ce, Nd, Sm, Eu, Gd, and U with concentrations ranging between 0.01 to 1 ppb. Preliminary results for the chromatogram of the HFIR fuel is shown in Fig 1.
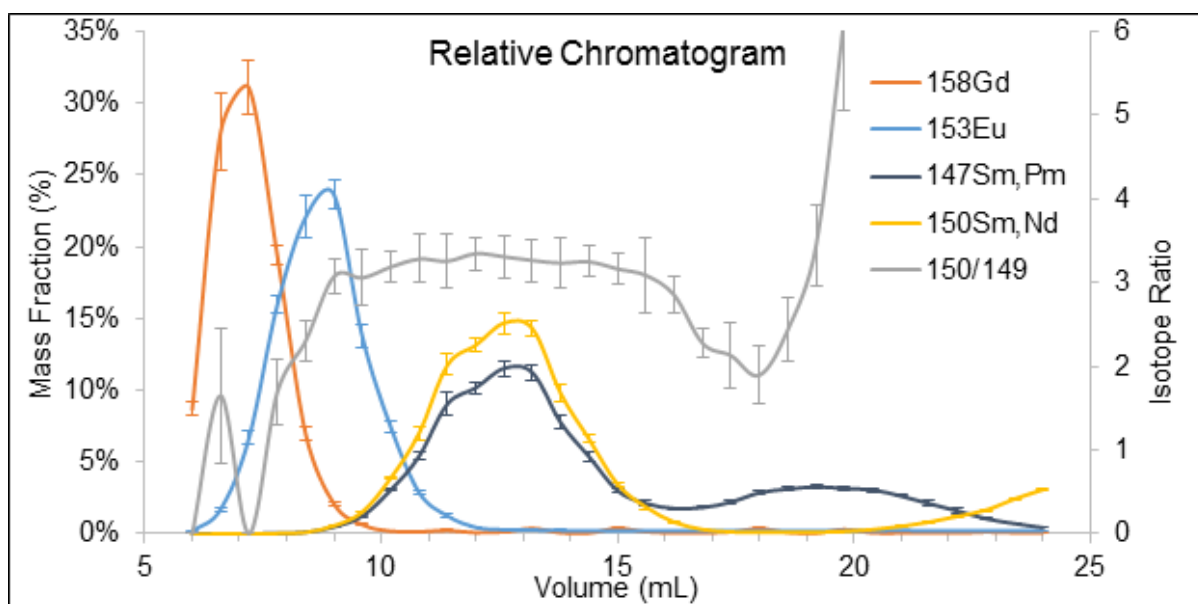
FIG. 1. Chromatogram of the HFIR fuel pellet performed at 0.4 M α-HIB and pH 3.00. The 150/149 (gray) ratio (read from the right-hand axis) is constant in the Sm elution peak.

The lanthanides are shown to elute in the expected order of decreasing atomic number. The 150 mass bin (yellow) shows a distinct elution profile for Sm at 13 mL, while Nd is shown to begin eluting at 21 mL. As Sm and Nd were successfully separated, the $^{150}Sm/^{149}Sm$ isotope ratio was determined using the fractions within the Sm elution peak. The mass bin ratio (gray) is shown to be constant in this region, indicating a constant $^{150}Sm/^{149}Sm$ isotope ratio. Twenty other Sm isotope ratios were determined in this way, as shown in Table I. The relevant $^{150}Sm/^{149}Sm$ and $^{152}Sm/^{149}Sm$ isotope ratios were measured successfully with low experimental error and are to be used with the maximum likelihood method to determine the most likely irradiation history of both fuel samples. These histories will then be compared

to the known history of the samples. The MURR fuel is still being investigated to measure the twenty other Sm isotope ratios.

A second approach to determine the irradiation history of separated Pu by investigating the Plutonium Uranium Redox Extraction (PUREX) process is underway. If the decontamination factor (DF) through the PUREX process were known for every FP element within irradiated fuel, it would be

Table I. Sm isotope ratios measured in the HFIR fuel after separation by cation exchange chromatography with 0.4 M α-HIB at pH 3.00.

Sm Ratio	Measured Value
147/148	12.2 ± 6.8%
147/150	1.31 ± 2.2%
147/151	3.97 ± 2.2%
147/152	1.44 ± 0.91%
147/154	4.43 ± 1.7%
148/152	0.104 ± 3.7%
148/151	0.32 ± 5.5%
148/152	0.117 ± 2.9%
148/154	0.35 ± 7.0%
149/147	0.237 ± 2.4%
149/148	3.0 ± 16%
149/151	0.93 ± 1.7%
149/154	1.03 ± 3.2%
150/149	3.23 ± 2.7%
150/151	3.02 ± 2.1%
150/152	1.112 ± 0.79%
150/154	3.3 ± 5.0%
151/152	0.365 ± 0.82%
151/154	1.12 ± 2.0%
152/149	2.93 ± 1.3%
152/154	3.06 ± 1.4%

possible to reconstruct the original FP distribution within separated Pu. If the original FP distribution were reconstructed, then traditional forensic techniques could be used to determine the burnup, cooling time, neutron spectrum, and enrichment of the fuel. Efforts in this investigation have focused on performing PUREX liquid-liquid extractions in the laboratory based on the industrial PUREX reprocessing scheme as developed at the Barnwell Nuclear Fuel Plant, an American reprocessing facility that was constructed but never operated commercially. Progress so far includes transcribing the industrial 10-stage counter-current flow process for the first PUREX extraction into a series of 15 batch extractions performed in the laboratory. These extractions were performed on the HFIR fuel feed with aqueous phase conditions of 3 M HNO_3 and 0.85 M $UO_2(NO_3)_2$ against an organic stream of n-dodecane containing 30% TBP by volume at 40°C. The phase ratio used for all 15 extractions was 2.3 mL of organic phase to 1 mL of aqueous phase. The DFs measured at the end of these 15 extractions are shown in Table II and represents the DFs of several FP elements through the first step of the PUREX process. Errors may be estimated on the order of 10%. The FP elements listed in this table are those which are readily assayed by

gamma or alpha spectrometry; other FP elements remain to be measured via mass spectrometry. Work will continue by performing the final 7 steps of the PUREX process and measuring the DFs of each FP element at each step. The measured DF at each step will then be multiplied across all steps to determine the overall DF of each FP element throughout the whole process.

Table II. Decontamination factors for the first step of the PUREX process.

Nuclide	Extraction (%)	Decontamination Factor
^{239}Pu	99	-
^{106}Ru	0.506	197.6
^{241}Am	0.67	150
^{144}Ce	0.212	470
^{125}Sb	0.028	3600
^{137}Cs	0.0018	55000
^{154,155}Eu	1.00	100

[1] S.S. Chirayath, J.M. Osborn, T.M. Coles, Science & Global Security **23**, 48 (2015).
[2] M.W. Swinney, C.M. Folden III, R.J. Ellis, S.S. Chirayath, Nucl. Technology **197**, 1 (2017).
[3] J.M. Osborn, K.J. Glennon, E.D. Kitcher, J.D. Burns, C.M. Folden III, S.S. Chirayath, Nucl. Eng. Tech. **(**Accepted 2018).

Mutual solubility of betainium-based ionic liquid and water in the presence of hydrochloric acid and zwitterionic betaine

M.F. Volia,[1, 2] E.E. Tereshatov,[1] M.Yu. Boltoeva,[3, 4] C.M. Folden III[1]

[1]*Cyclotron Institute, Texas A&M University, College Station, Texas 77843 USA*
[2]*Department of Nuclear Engineering, Texas A&M University, College Station, Texas 77843 USA*
[3]*Université de Strasbourg, IPHC, Strasbourg, 67037 France*
[4]*CNRS, Strasbourg, 67037 France*

Ionic liquids (ILs) are salts which have melting temperatures below 100 $^{\circ}$C and many of them are liquid at room temperature.[1] The ILs have been widely used as alternative solvents due their unique physicochemical properties that can be tuned to meet specific needs in various fields. In the past few years our group has been investigating the ability ILs, in particular imidazolium- and pyrrolidinium-based ILs, to extract indium (In) and thallium (Tl), the two lighter homologs of the super-heavy element nihonium, from aqueous acidic media by using the liquid-liquid extraction method.[2-3] From these studies, it was found that the extraction of In and Tl into ILs was initiated by the solubility of the ILs in the aqueous phase. Thus, understanding the solubility of the ILs in the aqueous phase is considered as one of the keys to elucidating the mechanism of metal extraction into the ILs.

Recently, our group studied the extraction of In(III), Tl(I), and Tl(III) into betainium bis(trifluoromethanesulfonyl)imide ([HBet][Tf$_2$N]) from hydrochloric acid media.[4] It was found that In(III) was extracted at low acid concentrations and that the addition of zwitterionic betaine as the extractant improved the extraction efficiency. Tl(III) was also extracted but with lower extraction efficiency compared to that of In(III).

In order to understand the mechanism of In and Tl extraction into this ionic liquid, the mutual solubility of [HBet][Tf$_2$N] and water in the presence of hydrochloric acid was studied. The influence of the presence of zwitterionic betaine in the aqueous phase to the solubility was also investigated. Preliminary results are reported here.

The solubility experiments were carried out by the standard liquid–liquid extraction technique and performed in room temperature. The biphasic system was shaken for 5 min and centrifuged for 1 min, and the two phases were separated for further analysis. The water content in the ionic liquid phase was analyzed by the Karl-Fischer technique. The aqueous phase was analyzed to determine the equilibrium concentration of proton and chloride ions by using NaOH and AgNO$_3$ titrations, respectively. Preliminary results showed the change in the equilibrium concentrations of D$^+$ and Cl$^-$ [in this experiment we used deutero-hydrochloric acid (DCl)] in the aqueous phase compared to the initial ones (Fig. 1). The solid line in the figure represents the reference value when the equilibrium concentrations are equal to the initial ones.
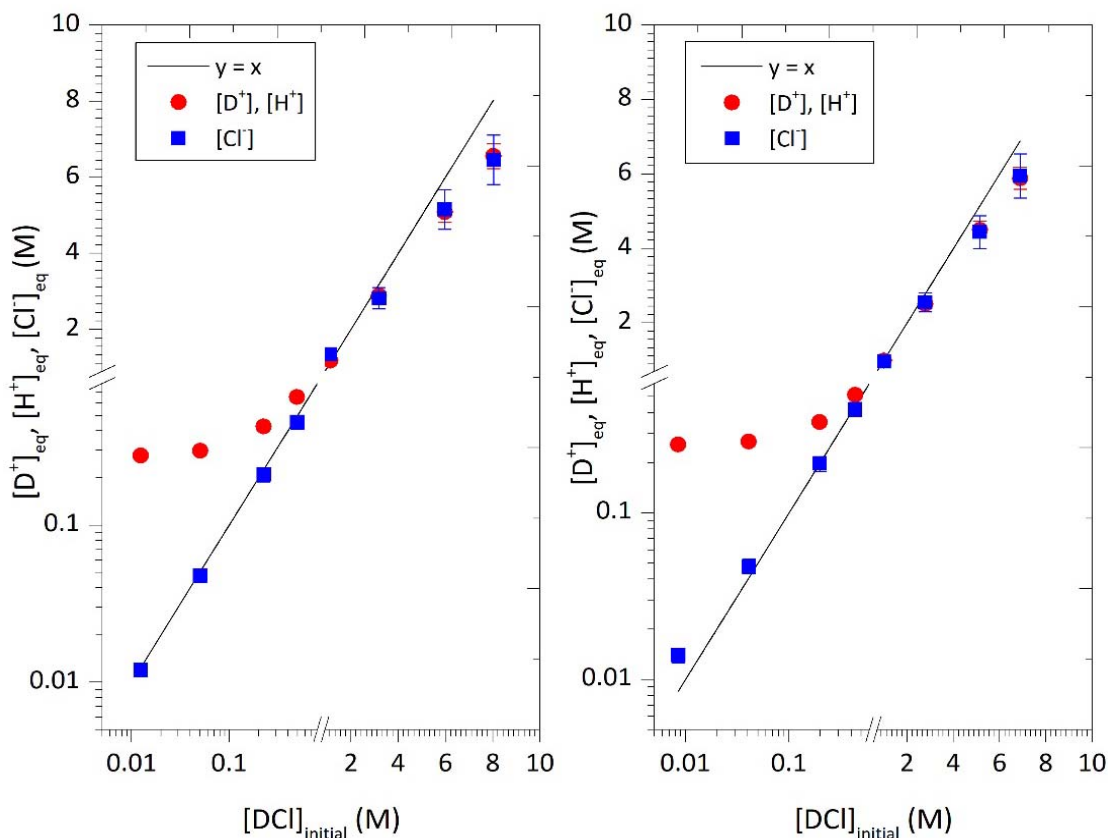
FIG. 1. The equilibrium concentrations of DCl was plotted as the function of the initial DCl concentrations. The solid line indicates the reference value when the equilibrium concentrations are equal to the initial ones. Figure (a) shows the result of $[D^+]$, $[H^+]$, and $[Cl^-]$ equilibrium concentrations without the presence of zwitterionic betaine, and figure (b) shows the result $[D^+]$, $[H^+]$, and $[Cl^-]$ equilibrium concentrations when zwitterionic betaine was added into the aqueous phase. Both figures show a similar trend.

Furthermore, the equilibrium concentrations of $[HBet]^+$ and $[Tf_2N]^-$ in the aqueous phase were assayed by using ^{1}H-NMR and ^{19}F-NMR techniques, respectively. The results showed that $[HBet][Tf_2N]$ is soluble in the aqueous phase and that the equilibrium concentrations of $[HBet]^+_{aq}$ and $[Tf_2N]^-_{aq}$ were dependent on the initial acid concentration and on the presence of zwitterionic betaine (Fig. 2).

Based on the experimental results, these reactions were considered to occur upon dissolution of the ionic liquid into the aqueous phase:

$$[HBet][Tf_2N]_{IL} \leftrightarrow [HBet^+]_{aq} + [Tf_2N^-]_{aq} \tag{1}$$
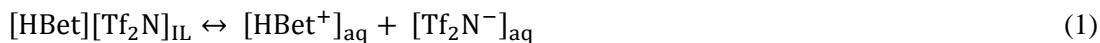
which is followed by an acid-base equilibrium where proton and zwitterionic betaine are formed:

$$[HBet^+]_{aq} \leftrightarrow H^+_{aq} + Bet_{aq} \tag{2}$$

and the protonation of anion [Tf₂N]⁻ in the presence of acidic proton:

$$H^+_{aq} + [Tf_2N^-]_{aq} \leftrightarrow HTf_2N_{aq} \qquad (3)$$

The study of the solubility mechanism is ongoing and this information will be used for further study of mechanism of In and Tl extraction into [HBet][Tf₂N] – HCl system.
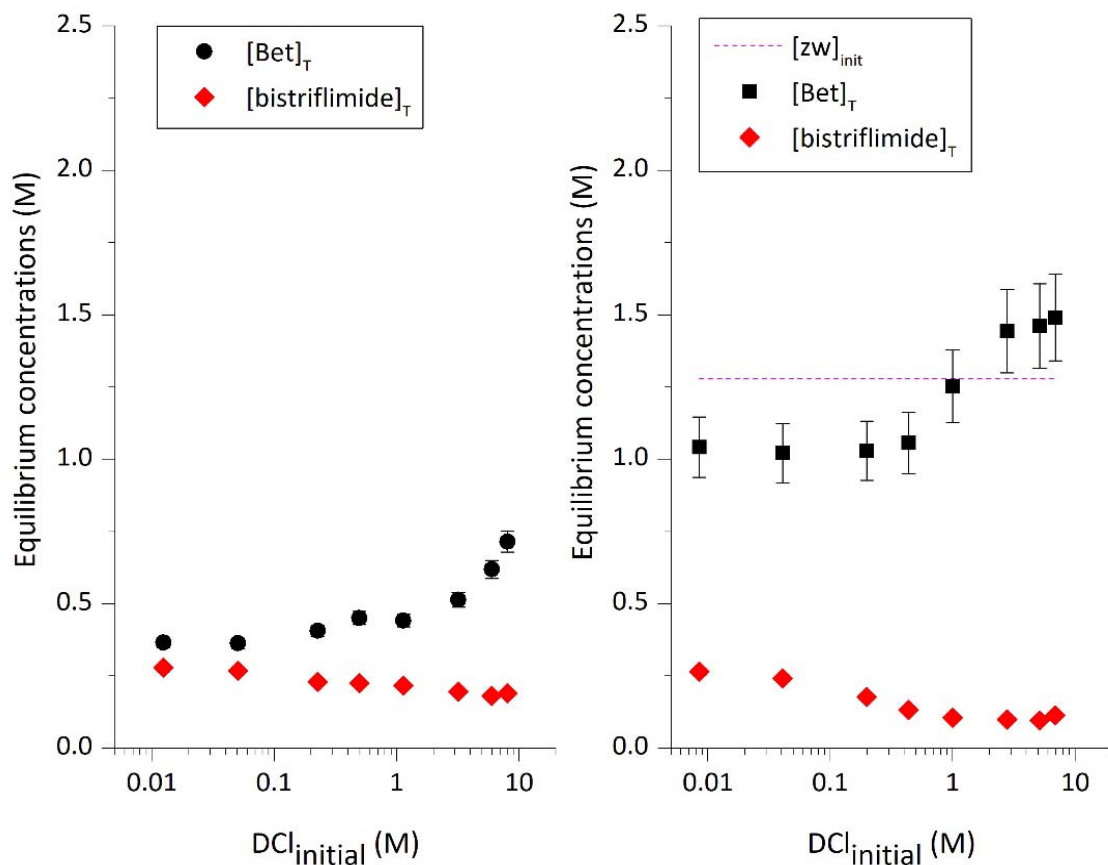
FIG. 2. The results of [HBet]⁺ and [Tf₂N]⁻ solubilities in the aqueous phase measured by ¹H NMR and ¹⁹F NMR methods, respectively. Left: the solubility of [HBet]⁺ and [Tf₂N]⁻ in water containing DCl. Right: the solubility of [HBet]⁺ and [Tf₂N]⁻ in water containing DCl and zwitterionic betaine. The dashed line on the right figure represents the initial concentration of the zwitterionic betaine.

[1] I. Billard, J.C.G. Bünzli, and V.K. Pecharsky; Handbook on the Physics and Chemistry of Rare Earths **43,** 213 (2013).

[2] E.E. Tereshatov, M.Y. Boltoeva, and C.M. Folden III, Solvent Extr. Ion Exc. **33**, 607 (2015).

[3] E.E. Tereshatov, M.Y. Boltoeva, V. Mazan, M.F. Volia, and C.M. Folden III, J. Phys. Chem. B **120** , 2311 (2016).

[4] M.F. Volia, E.E. Tereshatov, M.Y. Boltoeva, and C.M. Folden III, *Progress in Research*, Cyclotron Institute, Texas A&M University (2016-2017) p. II-19. https://cyclotron.tamu.edu/progress-reports/2016-2017/cyclotron_progress_2017pdf.

Preparation and characterization of a Nb-93m target

E.E. Tereshatov, N. Nica, V. Horvat, J.C. Hardy, and C.M. Folden III

We have prepared a thin Nb-93m source using the well-known molecular electroplating technique[1]. To develop the procedure, an aliquot of initial Nb-93m solution in 1 M HNO_3/0.3 M HF was used. The niobium electrodeposition was optimized at a level of 3-5 mA/cm^2 current density. The efficiency of niobium deposition was increased up to 95% for relatively low carrier concentration, the entire procedure taking 2 hours. This was the result of careful purification of isopropanol (the main organic solvent in the target cell) and the aluminum disk (an arbitrary material chosen for the source backing). Apparently, electrochemical removal of water from the solvent, and the oxide layer from the disk (2.275 cm^2) helped to significantly improve the yield of the electrochemical process.

In all, we prepared 5 sources on aluminum backings and subsequently tested each of them by measuring the emitted low energy gammas and X-rays. The source with the highest activity deposited (~4.5 μCi) had an areal density of ~1.3 mg/cm^2. Fig. 1 shows deposition parameters and the gamma-spectrum of the most active source. The electrodeposition method we employed is limited to 1-2 mg/cm^2 of material deposited, so it was decided not to increase the layer thickness to avoid any possible loss of
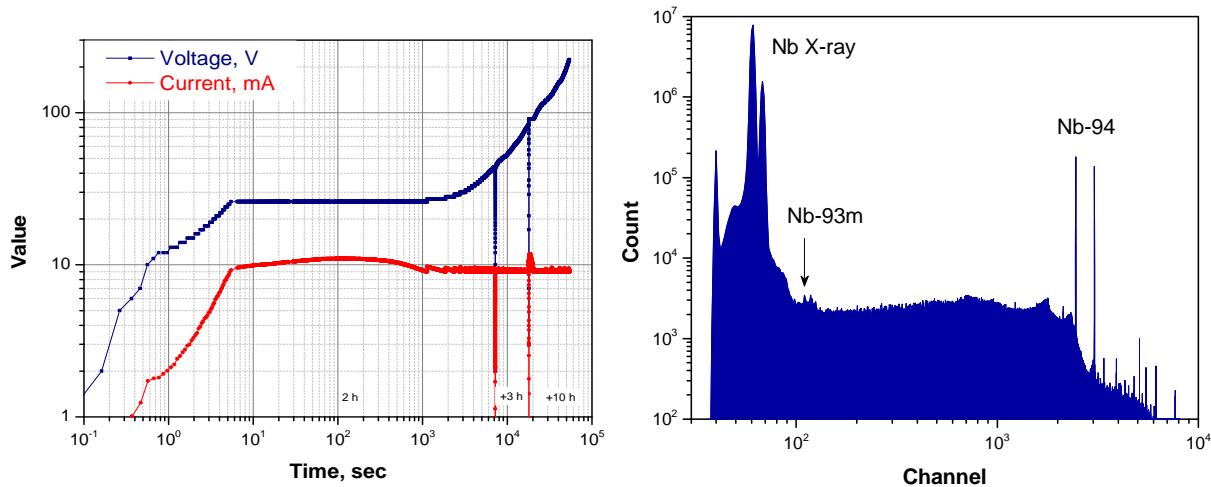
FIG. 1. (Left) Voltage and current parameters during the target preparation. (Right) HPGe-detector spectrum of the target (69 h).

deposited activity from flaking, cracking, and peeling of the thick film. Most likely, a very high concentration of electrolytes affected the procedure and resulted in one source requiring an increased deposition time (15 h) while having a reduced deposition efficiency (~50%). It should be noted that, consistent with our previous studies, energy dispersive spectroscopy (EDS) and X-ray photoelectron spectroscopy (XPS) demonstrated that niobium was deposited in the form of pentoxide Nb_2O_5, despite the presence of nitrates and oxyfluorides in the solution.

This set of targets will be used to determine the effect of self-absorption on low energy X-rays. With this established we will make a long-term decay measurement using the most active source, to make a precise determination of the internal conversion coefficient for the decay transition from Nb-93m.

[1] D.A. Mayorov, E.E. Tereshatov, T.A. Werke, M.M. Frey, C.M. Folden III, Nucl. Instrum. Methods Phys. Res. **B407**, 256 (2017).

Reaction of [44]Ca with Gd targets

C.M. Folden III,[1,2] T.A. Werke,[1*] K.J. Glennon,[1,2] D.A. Mayorov,[3†] E.E. Tereshatov,[1]
M.F. Volia,[1,4] and D.M. Wright[1,5‡]

[1]*Cyclotron Institute, Texas A&M University, College Station, TX 77843-3366*
[2]*Department of Chemistry, Texas A&M University, College Station, TX 77843-3255*
[3]*Los Alamos Neutron Science Center, Los Alamos National Laboratory, Los Alamos, NM 87545*
[4]*Department of Nuclear Engineering, Texas A&M University, College Station, TX 77843-3133*
[5]*Department of Physics, University of Surrey, Guildford, Surrey GU2 7XH United Kingdom*
[*]*Current Address: Rock Island Arsenal, Rock Island, IL 61299*
[†]*Current Address: Institute for Defense Analyses, Alexandria, VA 22311*
[‡]*Next Address: Atomic Weapons Establishment, Aldermaston RG7 4PR United Kingdom*

In a series of publications [1-4], our group has studied the survival of nearly spherical compound nuclei near [208]Pb that are produced in reactions of medium-mass projectiles with lanthanide targets. This work showed that compound nucleus survival is heavily dependent on the difference in the fission barrier and the neutron separation energy of the compound nucleus as well as the influence of collective effects. In the most recent of these publications [2], we studied the reactions of [44]Ca with [158]Gd, [159]Tb, and [162]Dy. These targets all have $N = 94$ or $N = 96$. In the current work, we have expanded our study to include the reactions of [44]Ca with [154, 156, 157, 160]Gd to study the influence of neutron number while also verifying the [158]Gd measurement. We measured excitation functions for production of *xn* evaporation residue products by measuring the known alpha decays of the products, and preliminary results are given here.

Beams were provided by the K500 cyclotron to the MARS spectrometer [5, 6], which acted as a separator. Reaction products were spatially separated from transfer reaction products and unreacted beam using MARS (see [7] for details). A 25 mm x 25 mm 16-strip position-sensitive Si detector was used to detect implantations and subsequent alpha decays, while a microchannel plate detector was mounted upstream of the Si detector to provide discrimination of implantation events. The beam dose was monitored by two collimated Coulomb scattering detectors mounted in the target chamber with an angle of ±30° to the beam axis. The beam energy was varied using a series of Al degraders mounted upstream of the targets.

The primary results for maximum cross sections are shown in Fig. 1 with our previously published data for comparison. Although the general trend of decreasing cross section with decreasing difference in fission barrier and neutron separation energy is maintained, the change is not as pronounced as with other reactions, and the [44]Ca + [157]Gd maximum cross section is surprisingly large. The analysis of these data is ongoing.
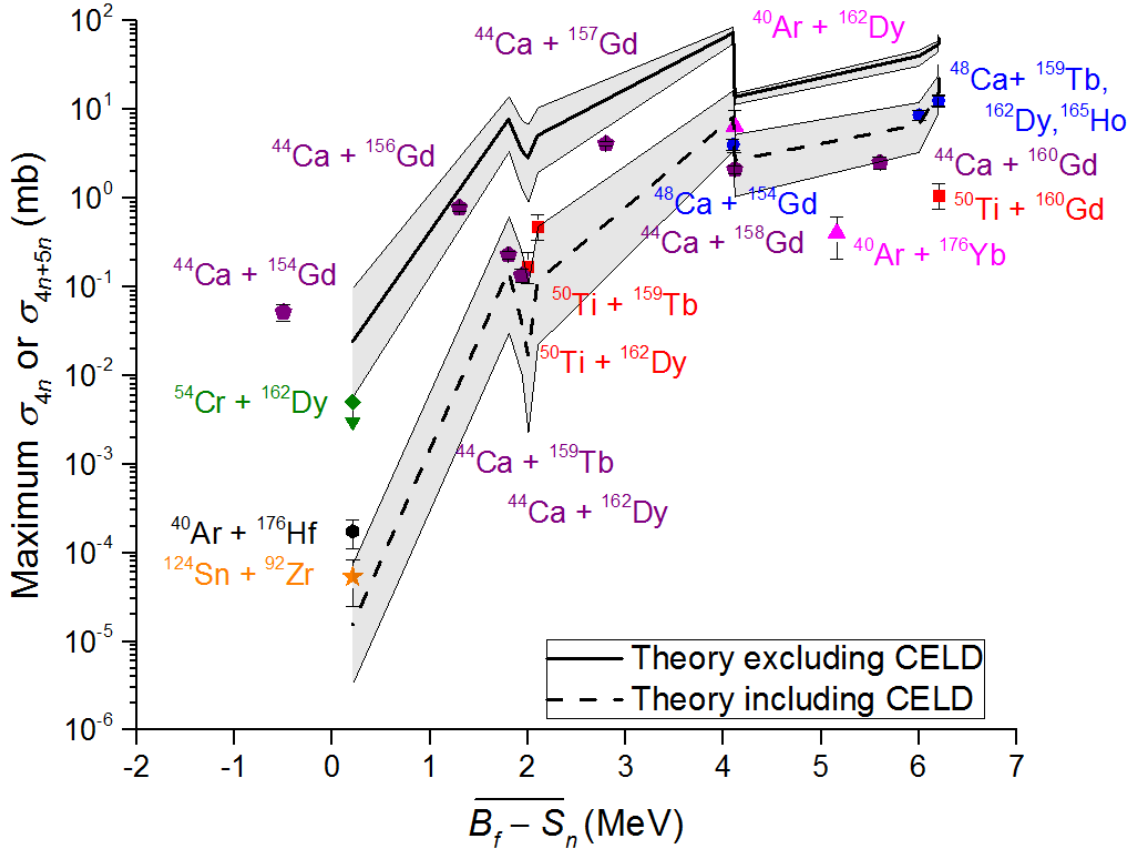
FIG. 1. Maximum measured $4n$ cross sections as a function of average difference in fission barrier and neutron separation energy. Points represented measured values for the indicated reactions, and lines represent theoretical calculations described in [2]. The heavy black line excludes the influence of collective effects, while the dashed line includes these effects. The shaded gray areas indicate the influence of changing the fission barrier by ± 0.5 MeV. The data for ^{40}Ar projectiles are preliminary, as are the data for ^{44}Ca projectiles except ^{158}Gd.

[1] T.A. Werke *et al.*, Phys. Rev. C **92**, 034613 (2015). doi:10.1103/PhysRevC.92.034613

[2] T.A. Werke *et al.*, Phys. Rev. C **92**, 054617 (2015). doi:10.1103/PhysRevC.92.054617

[3] D.A. Mayorov *et al.*, Phys. Rev. C **90**, 024602 (2014). doi:10.1103/PhysRevC.90.024602

[4] D.A. Mayorov *et al.*, Phys. Rev. C **92**, 054601 (2015). doi:10.1103/PhysRevC.92.054601

[5] R.E. Tribble, R.H. Burch, and C.A. Gagliardi, Nucl. Instrum. Methods Phys. Res. **A285**, 441 (1989). doi:10.1016/0168-9002(89)90215-5

[6] R.E. Tribble, C.A. Gagliardi, and W. Liu, Nucl. Instrum. Methods Phys. Res. **B56/57**, 956 (1991). doi:10.1016/0168-583X(91)95070-T

[7] C.M. Folden III *et al.*, Nucl. Instrum. Meth. A **678**, 1 (2012). doi:10.1016/j.nima.2012.02.035

Surface functionalization with ionic liquids

E.E. Tereshatov,[1] M.Yu. Boltoeva,[2,3] D. Krupp,[4] C. Baley,[1] U.W. Scherer,[4] and C.M. Folden III[1]

[1]*Texas A&M University, College Station, Texas 77843 USA*

[2]*Université de Strasbourg, IPHC, Strasbourg, 67037 France*

[3]*CNRS, Strasbourg, 67037 France*

[4]*Hochschule Mannheim, IPRC, Mannheim, 68163 Germany*

It is known that some pure hydrophobic ionic liquids can extract metallic species from aqueous solutions. The unique properties of such organic media allow polymerization techniques to convert a liquid organic phase to a solid one. A pyrrolidinium-based polymerized ionic liquid was used to test radioactive indium and thallium behavior by means of solid-liquid extraction. The results obtained allowed us to consider solid-gas extraction systems for extraction of the metals mentioned above. We used commercially available medical In-111 ($T_{1/2}$ = 2.8 d) and Tl-201 ($T_{1/2}$ = 3.0 d) radionuclides. First, a procedure to coat an inner surface of a round PTFE tube (250 mm length, 4 mm ID) with a solid polymerized layer was developed (Fig. 1). The polymerized ionic liquid was dissolved in acetone and solution obtained was transferred to the PTFE tube. The coating procedure requires a rotary evaporator application in order to remove the volatile solvent from the tube. Second, the polymerized ionic liquid in acetone was added into the PTFE tube filled with glass beads (either 0.5 or 1 mm diameter) to create a pseudo-monolithic column with open pores. The 0.5 mm column was used in experiments with aqueous solution. The solution with radioactive thallium in its +3 oxidation state was loaded into the column and eluted by means of a peristaltic pump. The extraction efficiency was estimated at a level of 50%.
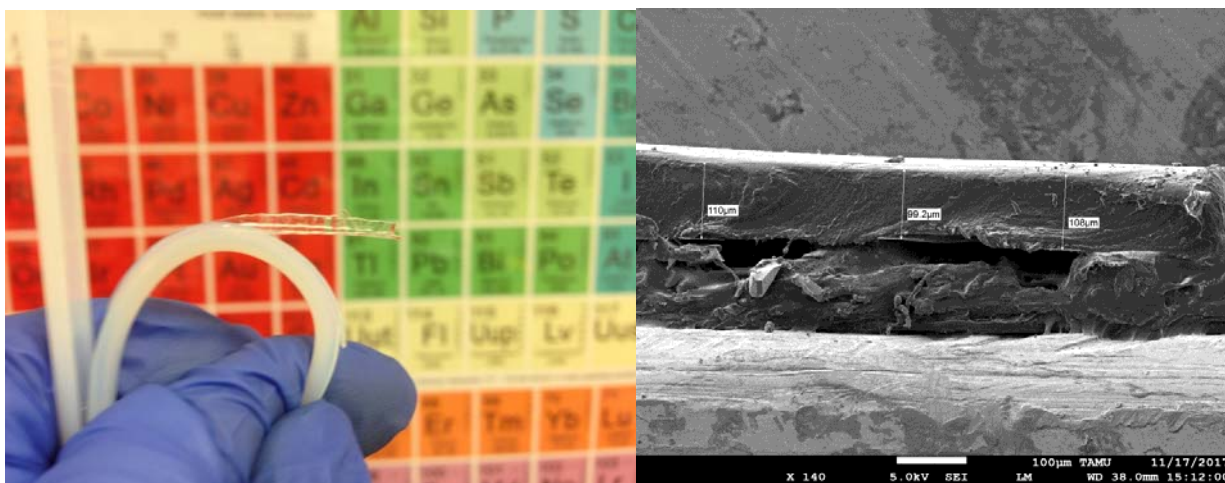
FIG. 1. (Left) The polymer inside the PTFE tube. (Right) SEM thickness measurement of the polymer layer.

In addition, a new step towards advanced Si surface functionalization techniques has been made. Previously developed methods to coat different surfaces with polymerized ionic liquids led to physisorption of the material of interest resulting in a relatively thick layer (~6 mg/cm^2). A new chemisorption technique allows in principle to minimize the layer thickness and to retain chemically

active centers. The first step includes application of alkoxysilane to convert a hydrophilic glass slide surface to hydrophobic one. This chemical step has been substantially optimized and while literature data suggest to perform the silanization for several hours at elevated temperature, our procedure can result in a surface of interest in less than 30 min at room temperature. The functionalized surface quality has been checked by means of contact angle measurements, atomic force microscopy analysis and adsorption of radioactive thallium in its +3 oxidation state. The results obtained indicate that surface coating was uniform, the contact angle between a drop of pure water and a functionalized surface was in agreement with literature data [1] [2], i.e. the surface is hydrophobic now (Fig. 2). Hence, thallium adsorption dropped down by one order of magnitude. The consequent next step of this work is to attach ionic liquids to previously silanized surfaces.
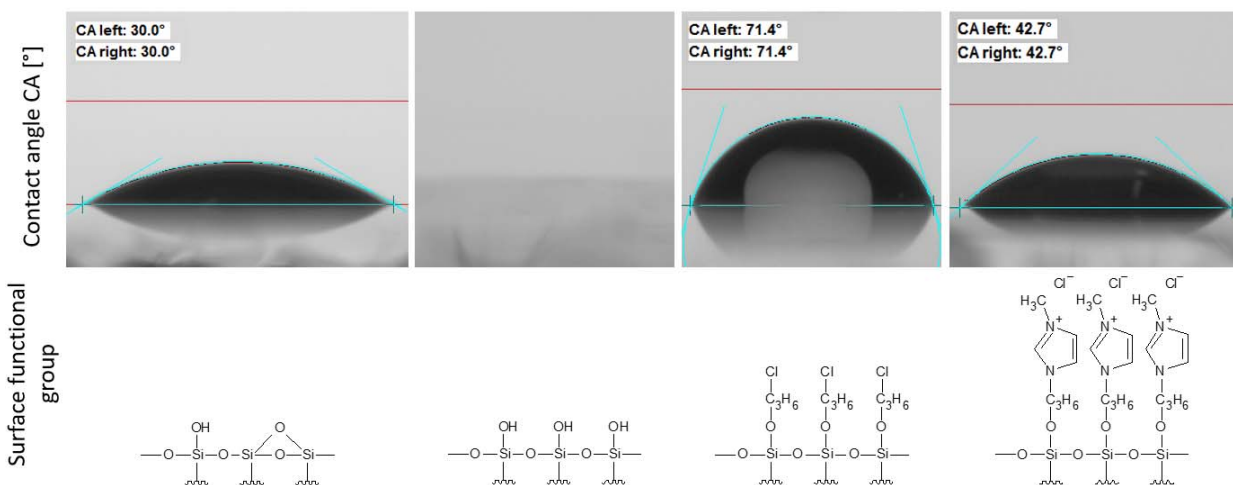
FIG. 2. Contact angle measurements and corresponding functional surface groups. From Left to Right: Untreated surface; cleaned and activated surface; modification with chloro propyl groups; covalently grafted N-methylimidazolium.

[1] R. Gusain, S. Kokufu, P.S. Bakshi, T. Utsunomiya, T. Ichii, H. Sugimura, and O.P. Khatri, Applied Surface Science **364**, 878 (2016).

[2] D.K. Aswal, S. Lenfant, D. Guerin, J.V. Yakhmi, and D. Vuillaume, Analytica Chimica Acta **568**, 84 (2006).

A statistical analysis of experimental multifragmentation events in ^{64}Zn + ^{112}Sn at 40 MeV/nucleon

R. Wada, W. Lin, H. Zheng, X.Liu, and M. Huang

A statistical multifragmentation model (SMM) is applied to the experimentally observed multifragmentation events in an intermediate heavy ion reaction. SMM is applied to the reaction ^{64}Zn + ^{112}Sn at 40 MeV/nucleon, using the experimental temperature and symmetry energy extracted from the isobaric yield ratio (IYR) method based on the modified Fisher model (MFM),

In SMM, the fragmenting system is in the thermal and chemical equilibrium at low density. A Markov chain is generated to represent the whole partition ensemble. In the version used in this study, a symmetry entropy term is added in the symmetry free energy F_{AZ} as,

$$F_{A,Z}^{sym} = E_{A,Z}^{sym} - TS_{sym}.$$

The experimental data from the reconstructed isotopes are compared with SMM simulated events. In our previous works [1,2], the primary isotope yields were experimentally reconstructed in the ^{64}Zn + ^{112}Sn reaction at 40 MeV/nucleon. These yields allow us to compare directly to the SMM primary fragments without an afterburner. The SMM calculations are performed with source size As = 60, charge number Zs = 27, which are extracted from the NN source component of the experimentally observed energy spectra for all particles, including neutrons [3]. The source excitation energy is calculated using the temperature from self-consistent analysis [1, 2] and the fragment multiplicities M_i as

$$E^* = \sum_i (3/2)TM_i - Q.$$

E* = 6.7 MeV/nucleon is obtained from the experimentally extracted temperature value of T = 5.9 MeV. γ = 20.7 MeV from the self-consistent analysis is used. The breakup volume of V= 4, 6, 10 V_0 are examined.

In Fig. 1 (a), mass distribution of the experimentally reconstructed isotopes (solid squares) is compared with the simulations. The results for SMM with and without the symmetry entropy are almost identical (open squares and circles). AMD results from Refs. [1,2] are also plotted (open triangles). All calculated yields are normalized to that of the reconstructed data at A = 15. They reproduce the experimental primary mass distribution for fragments with 10 < A < 30 reasonably well. The experimental mass distribution is compared with those from the SMM events at different breakup volumes in Fig. 1 (b) and at different breakup temperatures in Fig. 1 (c). The SMM mass distribution is not sensitive to the breakup density. On the contrary it is very sensitive to the breakup temperature. The best result is obtained at T = 6 MeV which is consistent to the experimentally determined temperature value of T = 5.9 MeV in Refs. [1, 2].
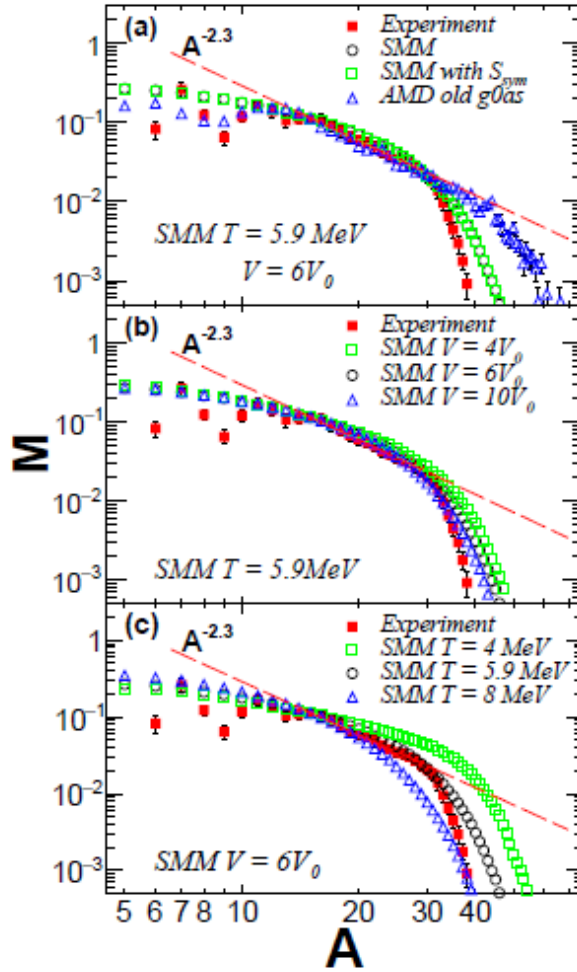
FIG. 1. (a) The experimental mass distribution (solid squares) is compared with that of SMM without (open circles) and with (open squares) the symmetry entropy at T = 5:9 MeV and the breakup volume of $6V_0$. The mass distribution of AMD from Refs. [1.2] is also shown by triangles. The distributions of the simulated results are normalized to the reconstructed data at A = 15. (b) The experimental mass distribution is compared with that of SMM with different breakup volumes at T = 5:9 MeV. (c) The experimental mass distribution is compared with that of SMM with different temperatures at V = $6V_0$.

In Fig. 2 detail comparison of isotope yield distributions are carried out in an absolute scale for Z =3 to 14 between the experimentally reconstructed primary isotopes and the fragments from the SMM events at V = $6V_0$ without (open circles) and with (open squares) the symmetry entropy. AMD results from Ref. [1] are also shown by open triangles. Reasonable agreements are found between the SMM calculations and the reconstructed data, but the widths of the SMM distributions are slightly wider than the experimental ones for all Z values, whereas those of AMD simulations reproduce the widths slightly closer to those of the experimental distributions. The significant differences in the simulated results for Z

= 4 are caused by the fact that ^{8}Be was missing among the final secondary products in the reconstruction, which is crucial for Z = 4 primary fragments.
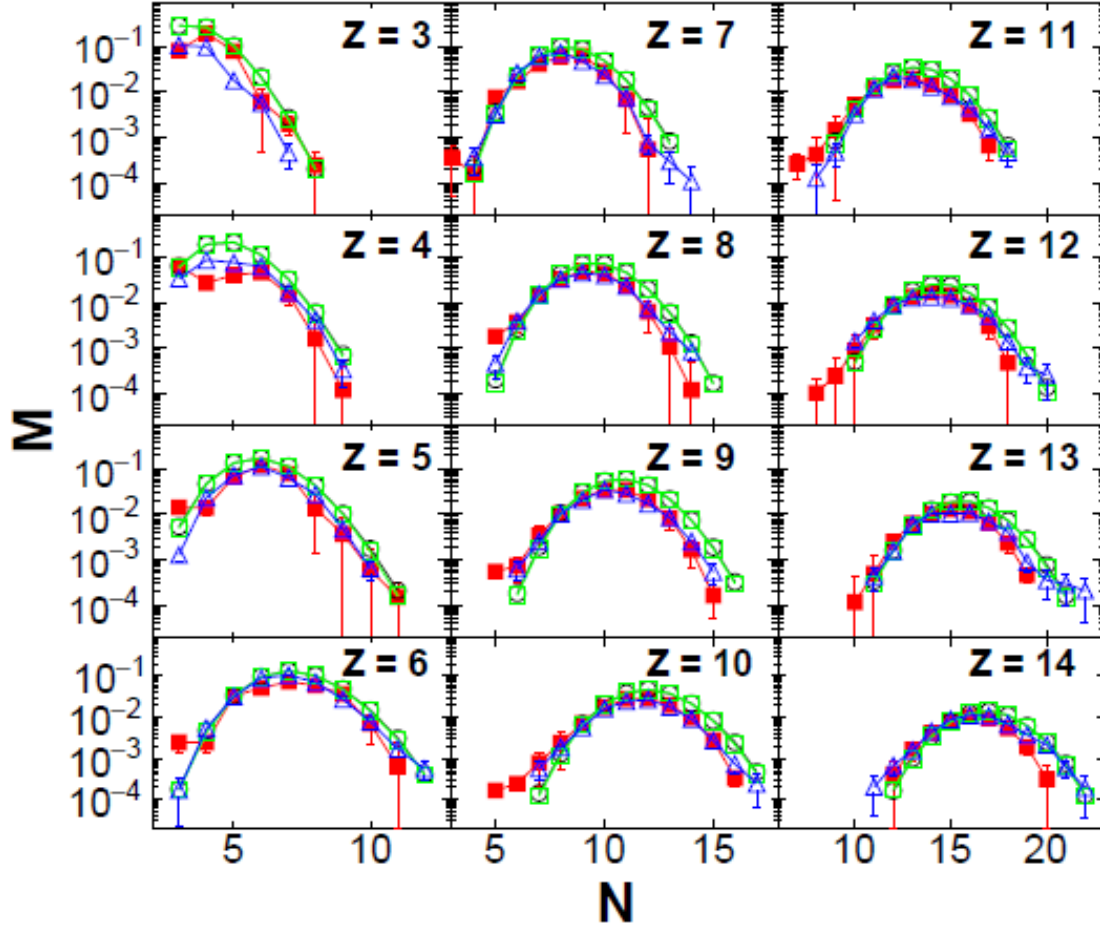
FIG. 2. Isotope distributions of the experimentally reconstructed primary fragments (solid squares) and those from SMM without (open circles) and with (open squares) the symmetry entropy at V = 6V$_0$ are compared for Z = 3 to 14. AMD results from Refs. [1, 2] are also shown by open triangles. All results are plotted in an absolute scale.

This work has been published in Ref.[4].

[1] W. Lin *et al.*, Phys. Rev. C **90**, 044603 (2014).
[2] W. Lin *et al.*, Phys. Rev. C **89**, 021601(R) (2014); W. Lin *et al.*, Phys. Rev. C (Erratum) **95**, 039907 (2017).
[3] R. Wada *et al.*, Nucl. Sci. and Techniq. **23**, 050501 (2013).
[4] W. Lin *et al.*, Phys. Rev. C (in press).

Cluster correlation and fragment emission in ^{12}C + ^{12}C at 95 MeV/nucleon

R. Wada, G. Tian, W. Lin, and A. Ono

Particle production mechanism in intermediate heavy ion collisions is extended to IMFs, using an extended version of antisymmetrized molecular dynamics (AMD) of Ono et al., [1,2]. In the new version, the cluster correlation is taken into account in the final stage of two nucleon (NN) collisions. In a standard AMD, two nucleons N1,N2 collide and end up a final state, N1', N2', same two nucleons, but have different momenta. If the final state is Fermi allowed, the collision is allowed. Otherwise the collision is canceled. In the new version, cluster correlations are taken into account in the final state, that is, other nucleons are within a certain distances, N1' and N2' can be B1, B2, where B1 and B2 can be one of clusters, such as d, t up to A=9. Since the coalescence is examined stochastically at the final state, the dispersion of the wave packet is taken into account. Therefore no quantum branching process, which is used in the version in Ref. [3], are not used in this version.

The program is applied to the experimental data of the 12C + 12C reaction at 95MeV/nucleon [4]. The calculated energy spectra of isotopes with 3≤Z≤6 are shown by blue histograms in Fig.1.
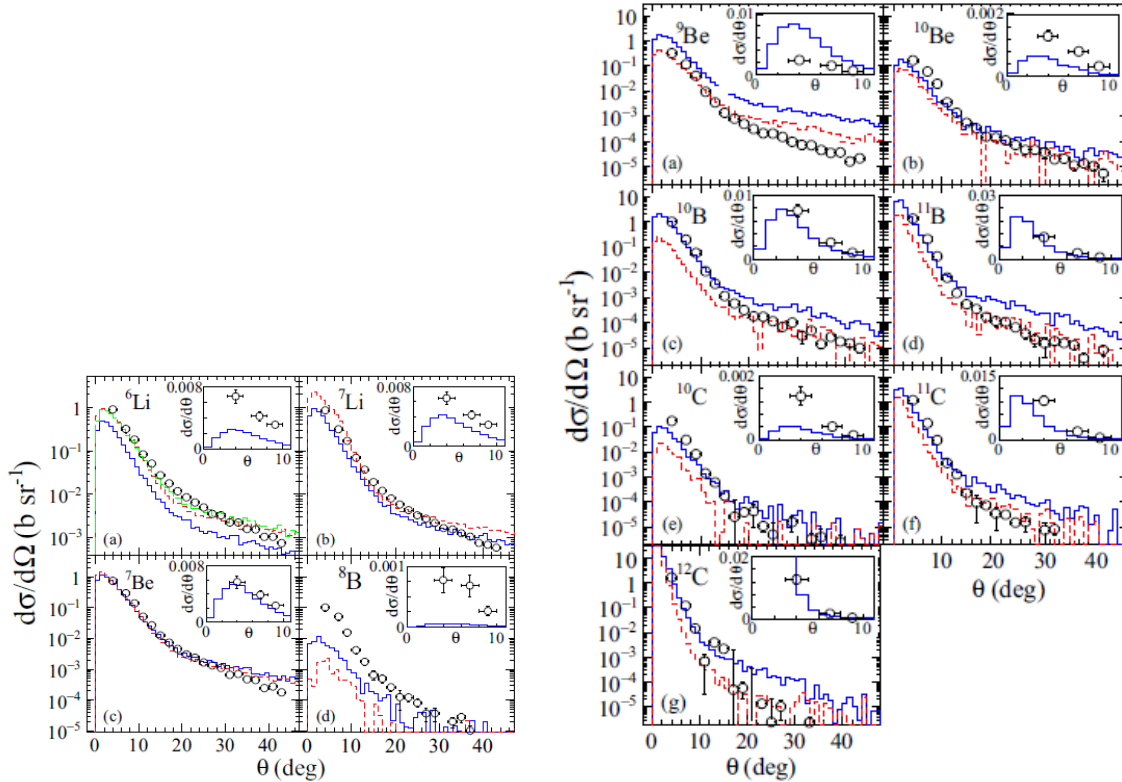
FIG. 1. Calculated energy spectra for isotopes with 3≤Z≤6 (blue by AMD (blue histograms) with the experimental data of 12C+12C at 95 A MeV [4] (circles) . For red dashed lines, see text.

It is clearly noted that the most of the spectra are significantly over-predicted at larger angles, $\theta \geq 20^o$. In contrast to the light particle emission, most of isotopes with $Z \geq 3$ are in an excited state when they are emitted. Therefore the final yield is the result of the two processes, the primary (AMD) and the secondary process. We used Gemini for the secondary process.

In Fig.2, the excitation energy distribution of isotopes are plotted for the primary (red solid) and secondary (blue dashed) when they are emitted at $\theta \geq 20^o$. It is quite surprising that many secondary fragments have the excitation energy, E_X, above their particle-decay energy threshold, E_{pth}. When the secondary isotopes with $Ex > E_{pth}$ are forced to decay, the results are shown in Fig.1 by the red-dashed
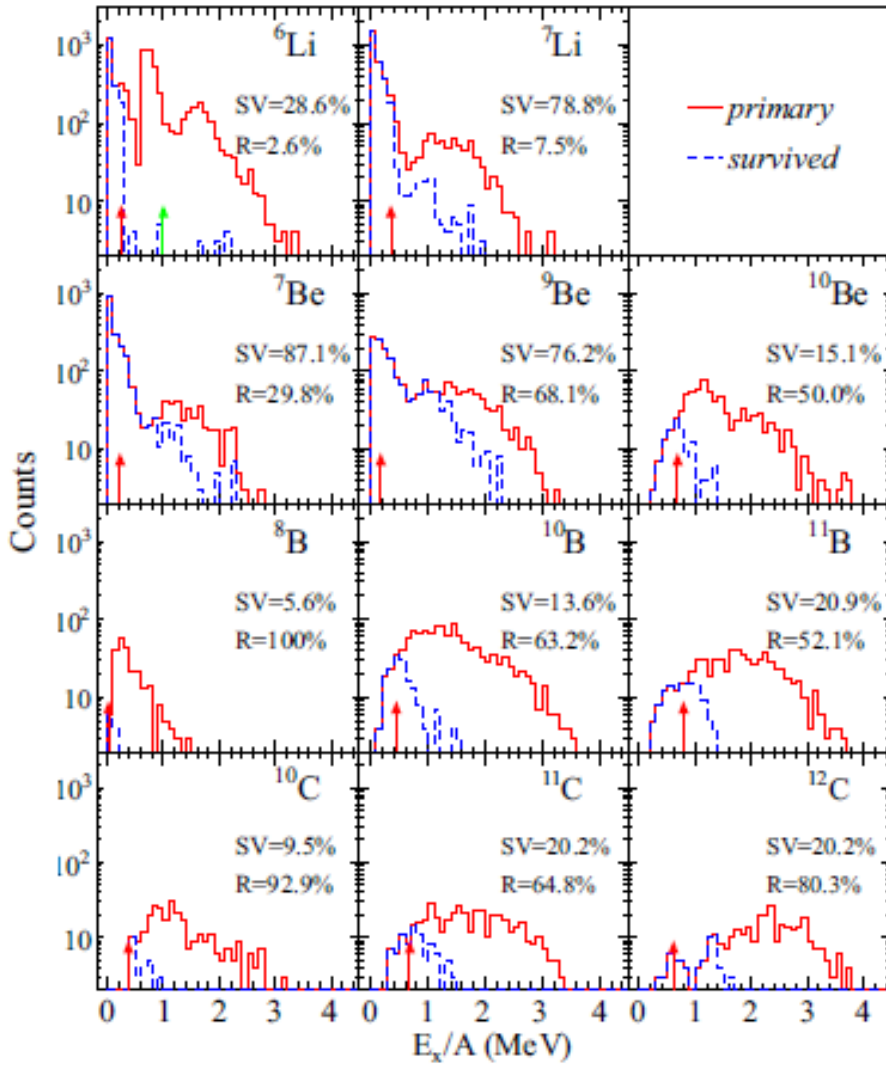
FIG. 2. Excitation energy distributions of each fragment emitted at $\theta \geq 20o$ and with kinetic energies above experimental energy thresholds. Red solid and blue dashed histograms represent those for the excited primary and survived secondary fragments, respectively. The particle decay thresholds are also shown on the X axis by red arrows. SV is given as the ratio of the number of the survived fragments to the total number of the primary fragments for each isotope. R is defined as the ratio between yields with $E_x > E_{pth}$ and the whole, where Epth is the particle decay energy threshold.

histograms. The yields at $\theta \geq 20^o$ are improved significantly for the most of isotopes, but becomes worse at smaller angles, where the PLF component is dominant. We are now currently investing what is the cause of this. A part of this study has been published in Ref. [2].

[1] N. Ikeno, A. Ono, Y. Nara, and A. Ohnishi, Phys. Rev. C **93**, 044612 (2016).
[2] G. Tian *et al.*, Phys. Rev. C **97**, 034610 (2018).
[3] A. Ono and H. Horiuchi, Phys. Rev. C **53**, 2958 (1996).
[4] J. Dudouet *et al.*, Phys. Rev. C **88**, 024606 (2013).

Reexamination of a novel determination of density, temperature, and symmetry energy based on a modified Fisher model

R. Wada, X. Liu, W. Lin, M. Huang, and H. Zheng

In 1967, M.E. Fisher proposed a droplet model of a second order phase transition to describe the power law behavior of the "fragment" mass distribution around the critical point for a liquid-gas phase transition [1]. In the early 1980s, based on the Fisher model, the Purdue group generated a novel classical droplet model, which was the so-called modified Fisher model (MFM), and introduced it into nuclear physics [2–4]. Recently, a series of experimental and theoretical investigations based on the MFM have been carried out to explore the symmetry energy of the nuclear equation of state and the critical behavior of hot fragmenting matter [5-32].

However, the MFM formulation from the pioneering works of the Purdue group contained a mistake which originated from the wrong sign in front of the mixing entropy term and caused some errors. In this study, we address this mistake in their formulation, and quantitative analyses are given for the errors originating from the mistake in typical MFM-related studies.

In MFM, the yield of isotope with (I,A; I=N-Z) can be described as

$$Y(I,A) = Y_0 \, A^{-\tau} \exp\left[\frac{W(I,A) + \mu_n N + \mu_p Z}{T} + S_{\mathrm{mix}}\right].$$

W(I,A) is free energy, μ_n and μ_p are Chemical potential of neutron and proton. S_{mix} is the mixing entropy, which can be described by $S_{\mathrm{mix}}(N,Z) = -[N \ln(N/A) + Z \ln(Z/A)]$ in a classical form. In the original form of Purdue group, S_{mix} is defined as $S_{\mathrm{mix}}(N,Z) = N \ln(N/A) + Z \ln(Z/A)$ and $S_{\mathrm{mix}}(N,Z)$ has a negative value.

The errors from the mistake in the results of the previous MFM-related studies, such as isotopic yield distribution, isobaric yield ratios, isoscaling, m-scaling, self-consistent determination of density, symmetry energy, and temperature, and density and temperature determination related to the IMF freezeout, are quantitatively evaluated. It is found that the errors originating from the mistake in sign of the mixing entropy term are generally small and even have no effect in some cases. The results and conclusions in the original papers are generally valid.

These results have been published in Ref. [33].

[1] M.E. Fisher, Rep. Prog. Phys. **30**, 615 (1967).
[2] R.W. Minich *et al.*, Phys. Lett. B **118**, 458 (1982).
[3] A.S. Hirsch *et al.*, Nucl. Phys. **A418**, 267c (1984).
[4] A. S. Hirsch *et al*., Phys. Rev. C **29**, 508 (1984).
[5] M. Huang *et al.*, Phys. Rev. C **81**, 044620 (2010).
[6] M. Huang *at al.*, Phys. Rev. C **82**, 054602 (2010).
[7] S. Zhang *et al.*, Chinese. Phys. C **41**, 044001 (2017).
[8] M. Huang *et al.*, Nucl. Phys. **A847**, 233 (2010).

[9] Z. Chen *et al.*, Phys. Rev. C **81**, 064613 (2010).

[10] W. Lin *et al.*, Phys. Rev. C **89**, 021601(R) (2014).

[11] W. Lin *et al.*, Phys. Rev. C **90**, 044603 (2014).

[12] X. Liu *et al.*, Phys. Rev. C **90**, 014605 (2014).

[13] X. Liu *et al.*, Nucl. Phys. **A933**, 290 (2015).

[14] X. Liu *et al.*, Phys. Rev. C **92**, 014623 (2015).

[15] A. Bonasera *et al.*, Phys. Rev. Lett. **101**, 122702 (2008).

[16] G. Giuliani *et al.*, Prog. Part. Nucl. Phys. **76**, 116 (2014).

[17] R. Tripathi *et al.*, Phys. Rev. C **83**, 054609 (2011).

[18] P. Marini *et al.*, Phys. Rev. C **85**, 034617 (2012).

[19] J. Mabiala *et al.*, Phys. Rev. C **87**, 017603 (2013).

[20] J. Mabiala *et al.*, Phys. Rev. C **94**, 064617 (2016).

[21] C.W. Ma *et al.*, Phys. Rev. C **83**, 064620 (2011).

[22] C.W.Ma *et al.*, Phys. Rev. C **86**, 054611 (2012).

[23] C.W. Ma *et al.*, Eur. Phys. J. A **48**, 78 (2012).

[24] C.W. Ma *et al.*, Chinese Phys. Lett. **29**, 062101 (2012).

[25] C.W. Ma *et al.*, Phys. Rev. C **88**, 044612 (2013).

[26] C.W. Ma *et al.*, Nucl. Sci. Tech. **24**, 050510 (2013).

[27] C.W. Ma *et al.*, Chinese Phys. Lett. **30**, 052501 (2013).

[28] C.W. Ma *et al.*, Chinese Phys. C **30**, 024102 (2013).

[29] C.W. Ma *et al.*, Commun. Theor. Phys. **64**, 334 (2015).

[30] C.W. Ma *et al.*, Commun. Theor. Phys. **64**, 727 (2015).

[31] C.W. Ma *et al.*, Phys. Rev. C **94**, 024615 (2016).

[32] W. Ma *et al.*, Nucl. Sci. Tech. **27**, 111 (2016).

[33] X. Liu *et al.*, Phys. Rev. C **97**, 014613 (2018).

Sensitivity study of experimental measures for nuclear liquid gas phase transition in statistical multifragmentation model (SMM)

R. Wada, X Liu, W. Lin, M. Huang, and H. Zheng

The experimental measures of the multiplicity derivatives, the moment parameters, the bimodal parameter, the fluctuation of maximum fragment charge number (NVZ), the Fisher exponent (τ) and Z_{ipf}'s law parameter (ξ) [1], are examined to search for the liquid gas phase transition in nuclear multifragmention processes within the framework of the statistical multifragmentation model (SMM).

Y.G. Ma *et al.* in Ref. [1] were examined most of these measures except the multiplicity derivatives, as a function of the excitation energy, using rather light reaction systems of ^{40}Ar+^{27}Al, ^{48}Ti and ^{58}Ni at 47 MeV/nucleon, and showed that all of them show a critical behavior around E/A = 5.6 MeV. However since all values of the measures are plotted as a function of the excitation energy, the signature appears as a broad peak around E/A = 5.6 MeV. Recently the multiplicity derivatives is proposed by S. Mallik et al. [2] for a sensitive probe for the first order phase transition.

SMM calculations are performed with the source mass number As = 100, charge number Zs = 45, the fragmenting volume V = 6V$_0$. The default symmetry energy coefficient = 25 MeV is used. The input source excitation energy (E$_x$) varies from 1 to 15 MeV/nucleon with the energy step of 0.25 MeV/nucleon.

The specific heat capacity has long been considered to be a measure that should provide important information on the postulated nuclear liquid gas phase transition. As one can see from Fig. 1 (a) that a significant plateauing of the caloric curve is found at Ex ~ 4 MeV for the SMM calculations, which reflects a sharp increasing of the C$_v$ as shown in Fig. 1 (b). The sharp maximum of the C$_v$ strongly
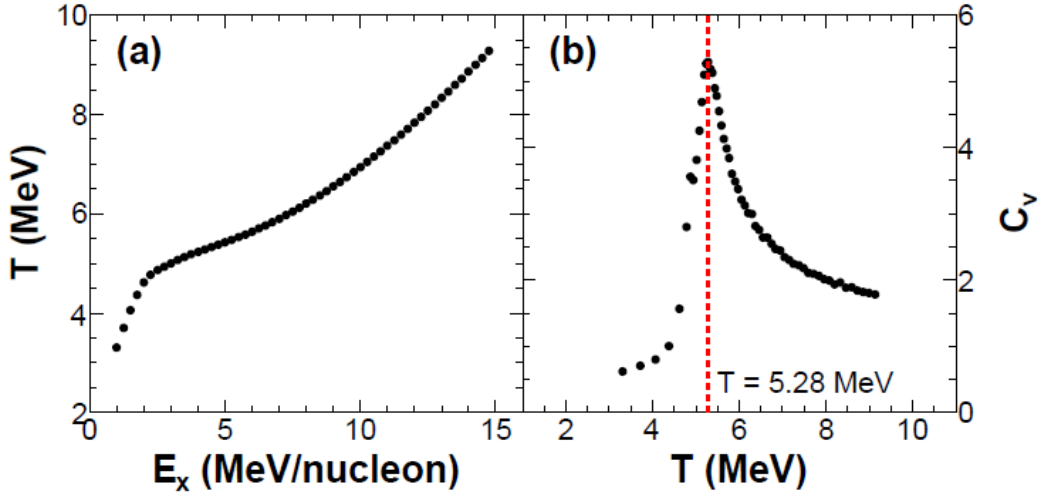
FIG. 1. (Color online) (a) Caloric curve of fragmenting source with As = 100, Zs = 45 of SMM calculations. (b) Specific heat capacity C$_v$ derived from caloric curve as a function of source temperature. The vertical line shows the critical point at T = 5.3 MeV.

obtained. The other measures are also examined and results are shown below. All measures examined above show a critical behavior around T=5.3 MeV.

The sensitivity of these measures are further studied within 5% uncertainties around the peak in each measure. Fig. 2 shows the sensitivities of all these measures except for the bimodal parameter, in which the inflection point is used to obtain the critical point and the sensitivity is unable to be defined.
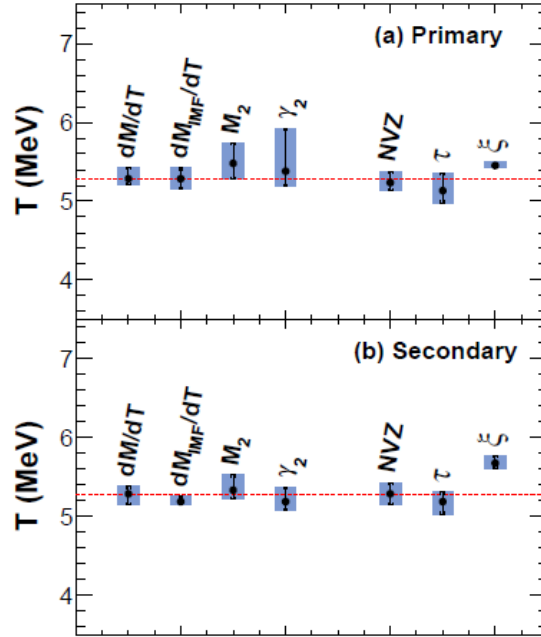
FIG. 2. (Color online) (a) The sensitivities in the critical temperature of primary fragments for all the measures except for bimodal parameter. (b) The same as that in (a) but of secondary fragments. The horizontal lines indicate the critical point at T = 5.3 MeV from Fig. 1 (b). Solid circles correspond to the critical temperature extracted by each measures. The errors indicate the sensitivities in the critical temperature when the critical measures have 5% uncertainties.

From the Fig. 2, we conclude that all measures examined here are sensitive to the first order phase transition, but the total multiplicity derivative and NVZ provide the most accurate measures both for the primary and secondary fragments

[1] Y.G. Ma *et al.*, Phys. Rev. C **71**, 054606 (2005).
[2] S. Mallik *et al.*, Phys. Rev. C **95**, 061601(R) (2017).

Three nucleon interaction in heavy ion collisions at intermediate energies

R. Wada and W. Lin

Two and three nucleon interaction can be written in the Hamiltonian as [1]

$$H = \sum_i -\frac{\hbar^2}{2m_i}\nabla_i^2 + \sum_{i<j} v_{ij} + \sum_{i<j<k} V_{ijk}, \qquad (2.1)$$

The three body interaction, V_{ijk}, can be express as

$$V_{ijk} = V^\pi + V^R$$

V^π is the sum of two and three pion exchange terms and V^R is an empirical medium range repulsive interaction. V^π is long and medium range attractive interaction and slightly decreases the binding energy for light nuclei. V^R is necessary to provide the enough strength of the massive neutron star against collapsing by the gravity.

The binding energy of the ground state and the energy scheme of the excited states provide the bench test of the attractive part of 3NF interaction. For V^R, Furumoto's elastic scattering theory may provide some evidence of the necessity of 3NF, using the diffraction pattern of near and far side scatterings [2].

As the first step, we incorporate 3NF into AMD code as a three nucleon (3N) collision term, which is incorporated into AMD-FM[3]. The new version is referred as AMD-FM (3N). The 3N collision
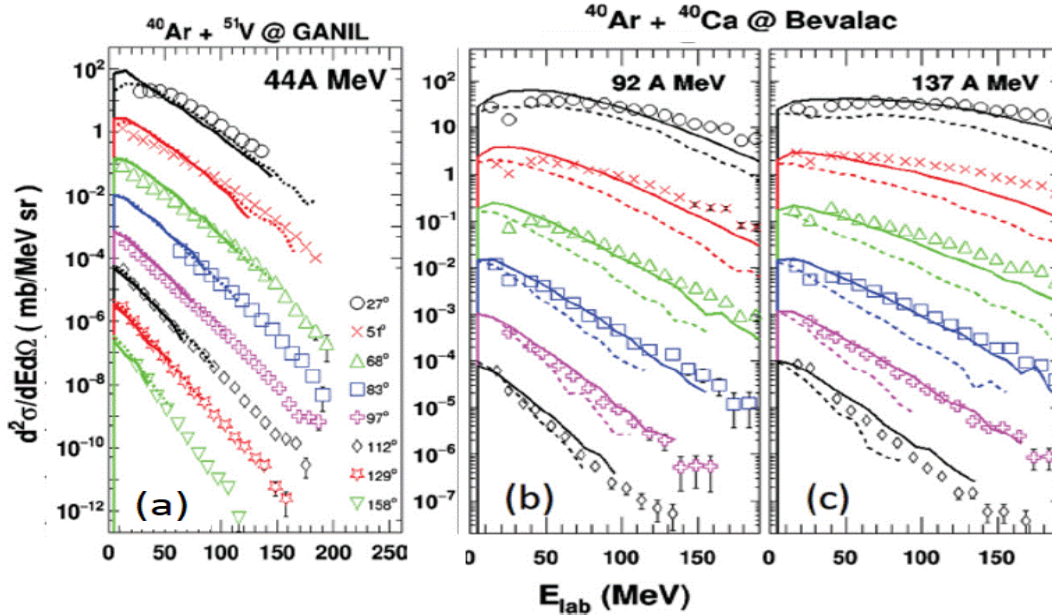
FIG. 1. Simulated results of proton energy spectra for the reactions ^{40}Ar+^{51}V reaction at 44AMeV 44 (a), at ^{40}Ar+^{40}Ca reaction at 92 A MeV (b), and 137A MeV (c). Data in (a) are taken from Ref. [5] and (b) and(c) are from Ref. [6]. Solid curves are for the results of AMD-FM(3N) and dashed curves are for those of AMD-FM. Data and results are plotted in an absolute scale. All results are multiplied by a factor of 10^{-n} from top to bottom for clarity.

is simply calculated by a succession of three binary collisions where one pair of nucleons interacts twice when three nucleons are within the collision distance each other. Pauli blocking is only examined at the final state. When the final state for the three nucleons are occupied, then the collision is canceled. A constant in-medium 3N collision cross section of 40mb is used.

AMD-FM(3N) is applied to the high energy proton energy spectra. The calculated results are compared with the available experimental data in Fig.1. Solid curves correspond to the results from AMD-FM(3N) and dashed ones from AMD-FM without 3N collisions. One can clearly see the role of the 3N collision term in the high energy slops and their angular distribution [4].

The calculations are further extended to a higher incident energy. In Fig.2, the calculations are compared with the high energy neutron data from a Bevalac experiment. As one can see, the experimental data are poorly reproduced by both calculations, except those at θ=60$^{\text{o}}$.

FIG. 2. Neutron energy spectra for ^{20}Ne+^{27}Al at 337 A MeV are compared in those between the AMD-FM(3N) and experiments [6]. Calculations are made with a standard Gogny interaction (K=228 MeV), g0, (black solid curve) and a modified version with K=380 MeV, d1g3,(red dashed one). Experimental data are shown by symbols, circles at 30$^{\text{o}}$, crosses at 45$^{\text{o}}$, triangles at 60$^{\text{o}}$ and squares at 90$^{\text{o}}$.

Neutron energy spectra for ^{20}Ne+^{27}Al at 337 A MeV are compared in those between the AMD-FM(3N) and experiments [6]. Calculations are made with a standard Gogny interaction (K=228 MeV),

g0, (black solid curve) and a modified version with K=380 MeV, d1g3,(red dashed one). Experimental data are shown by symbols, circles at 30°, crosses at 45°, triangles at 60° and squares at 90°.

[1] S.C. Pieper *et al.*, Phys. Rev. C **64**, 014001 (2001).
[2] T. Furumoto *et al.*, Phys. Rev. C **82**, 044612 (2010).
[3] W. Lin *et al.*, Phys. Rev. C **94**, 064609 (2016).
[4] R. Wada, Phys. Rev. C **96**, 031601(R) (2017).
[5] M. Germain *et al.*, Nucl. Phys. **A620**, 81 (1997).
[6] H. Kruse *et al.*, Phys. Rev. C **31**, 1770 (1985).
[7] R.A. Cecil *et al*., Phys. Rev. C **24**, 2013 (1981).
[8] Z. Zhang *et al.*, Phys. Rev. C **94**, 064326 (2016).

Toward understanding relativistic heavy-ion collisions with the STAR detector at RHIC

D.M. Anderson, Y. Liu, S. Mioduszewski, N.Sahoo, and the STAR Collaboration

This project is a study of high-energy heavy-ion collisions at the Relativistic Heavy Ion Collider (RHIC). The focus of the study is on two probes of the dense, partonic matter created in these collisions: 1) direct-photon-triggered jets (and their correlations) and 2) heavy-quarkonium production and suppression.

1 Investigating Energy Loss through Photon-Triggered Jet Measurements

The hard production of a direct photon back-to-back with a jet (γ-jet) is a probe of the parton energy loss in heavy-ion collisions [1]. In the "γ-jet" coincidence measurement, the measured energy of the trigger particle (the photon) serves as a calibrated baseline for the total energy of the jet particles on the recoil side (i.e. opposite in azimuth) of the trigger. The mean-free path of the γ in the medium is large enough so that its momentum is preserved, regardless of the position of the initial scattering vertex. Thus it does not suffer from the geometric biases, i.e. the non-uniform spatial sampling of hadron triggers due to energy loss in the medium, of e.g. π^0 triggers. Because of the difference in path length traversed, on average, between a direct-γ and a π^0 trigger, comparisons of γ-jet to hadron(π^0)-jet measurements can provide insight into the path-length dependence of the energy loss.

As the dominant background to direct photons are π^0 (decaying to two photons), the Barrel Shower Maximum Detector (BSMD) has provided the capability of distinguishing direct photons from neutral pions via the transverse shower shape. Our group has used this method in the measurement of direct photon+hadron correlations [2]. The γ-hadron correlation studies are currently being extended to studies of γ-triggered jet reconstruction measurements (as has been done at the LHC [3, 4]). The away-side jet will then be reconstructed in coincidence with triggers selected as direct photon candidates or (for p_T<20 GeV using the shower shape with the BSMD) identified π^0 triggers. The advantage of this should be the ability to reach lower energy fragments in the jet to study jet-shape modification and the medium response.

The Run-14 "L2Gamma" triggers in Au+Au collisions have been fully analyzed for charged jets recoiling from a high-energy neutral (π^0 or γ) trigger [5]. Fig. 1 shows the charged-jet spectra for a sample of triggers (γ_{rich}) enriched to be direct photons, using cuts on the transverse shower profile as measured by the Barrel Shower Maximum Detector, for increasing cuts on the trigger transverse momentum. In this figure, the result has not been corrected for instrumental effects, but clearly shows the growing signal of "true" jets over combinatorial jets, as estimated by a mixed-event technique [6].

In addition to the reconstruction of jets with charged particles, we are working to include the calorimeter hits in the jet reconstruction, extending the photon- or π^0-triggered charged-jet measurement to a full-jet measurement. Since this is quite challenging, we are concentrating on the p+p data set for now.
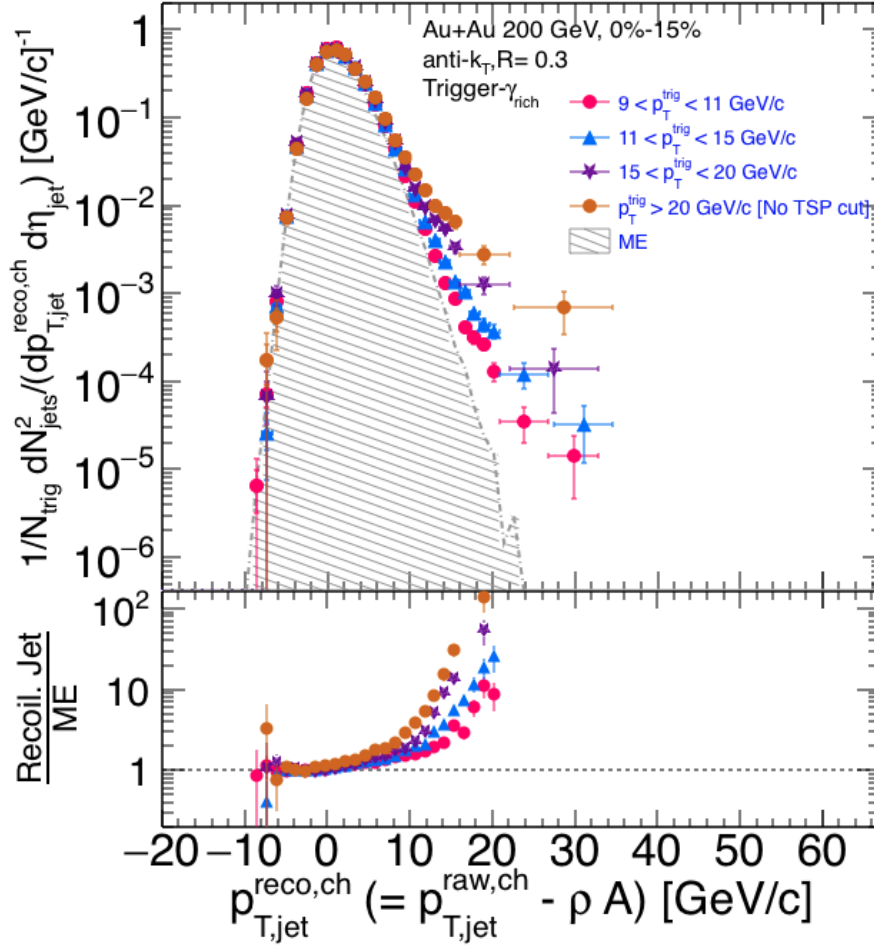
FIG. 1. Reconstructed charged-jet transverse-momentum spectrum recoiling from photon-rich triggers with different cuts on transverse momentum (p_T), using the high-statistics Run-14 Au+Au data set. The hatched histogram shows the estimated combinatorial jets from mixed events (ME). The bottom panel shows the ratio of the measured spectrum in real events to the spectrum from mixed events. The signal (yields greater than 1) increases for increasing trigger p_T.

Fig.2 shows the charged-jet (upper panels) vs. full-jet (lower panels) spectra recoiling from π^0 vs. γ_{rich} triggers in p+p collisions, for three trigger energy ranges (E_T = 9-20 GeV, E_T = 9-11 GeV, and E_T = 11-15 GeV). The full jets show more of a pronounced structure in the p_T range corresponding to the trigger energy, presumably because all of the energy is measured, while some of the energy is missing when reconstructing jets from only the charged particles. Also shown for each case is a ratio of the spectrum recoiling from π^0 triggers to that recoiling from γ_{rich} triggers. The difference in the spectra is expected because π^0 triggers are from a parton fragmentation, for which the parent parton (and therefore the recoiling jet) has a higher energy than the trigger particle, while direct photons carry the full energy

corresponding to the recoil jet. The ratio has been compared to PYTHIA, and agrees when including the estimated purity of our γ_{rich}-trigger sample.
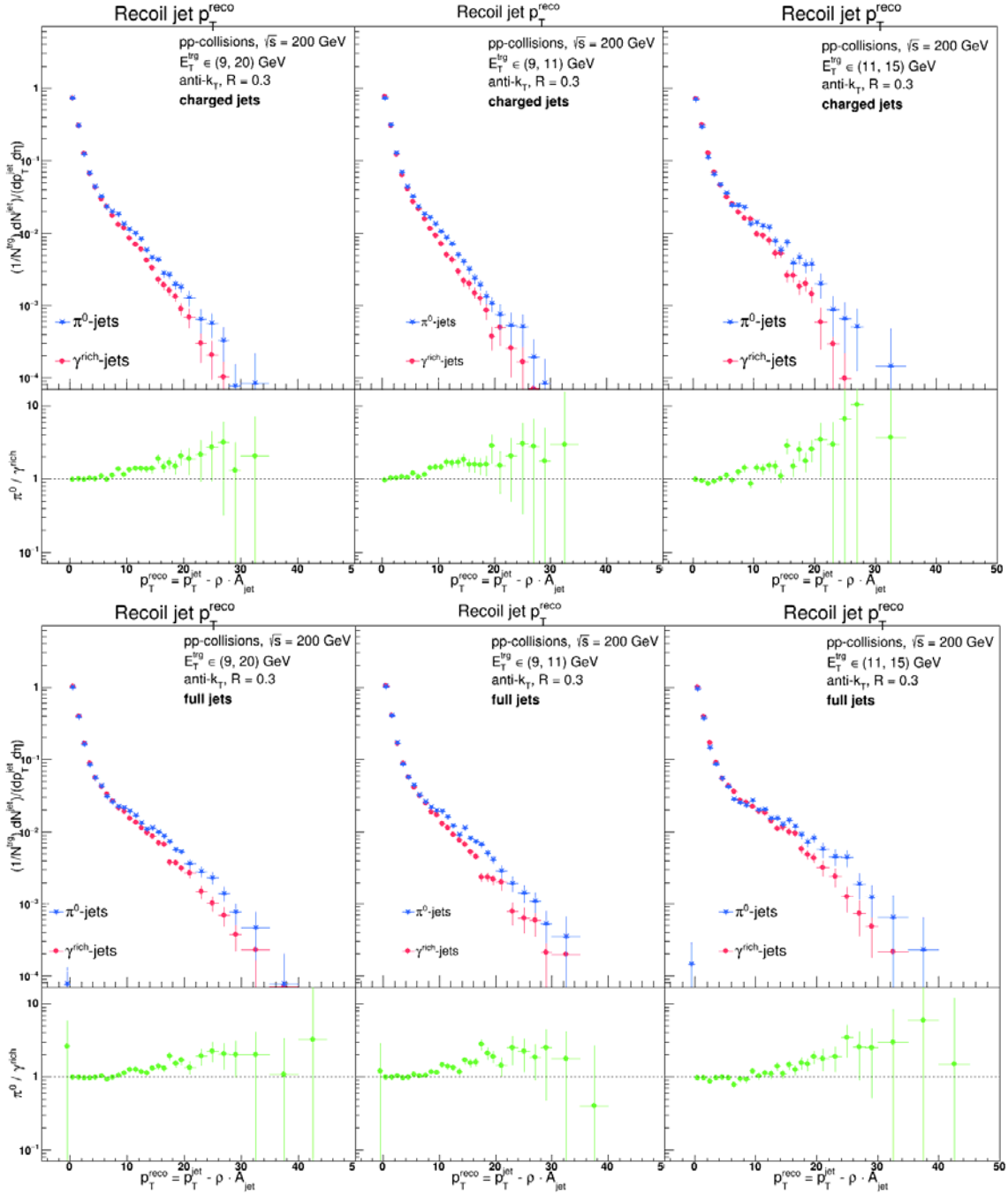
FIG. 2. Fully reconstructed jets (upper 3 panels) vs. charged jets (lower 3 panels) recoiling from a π^0 (blue) vs. γ_{rich} (red) triggers, for three different trigger energy ranges: 9-20 GeV (left), 9-11 GeV (middle), 11-15 GeV (right). Also shown in green is the ratio of the spectrum recoiling from a π^0 trigger to that recoiling from a γ_{rich} trigger, for each case.

2 Unraveling Cold Nuclear Matter Effects in J/Ψ Suppression

The J/ψ has long been considered one of the most promising direct probes of deconfinement. According to theoretical predictions in 1986 [7], the produced $c\bar{c}$ pair will not be able to form a J/ψ bound state in the QGP, if a sufficiently high temperature is reached where the screening radius is smaller than the binding radius of the J/ψ resonant state. The "Debye" screening radius is the distance at which the color charges of two quarks are screened from one another, so that the confinement force is not able to hold the quarks together. A suppression in the yield of J/ψ was first observed in Pb+Pb collisions by the NA50 experiment at the CERN SPS (see, for example, [8]).

At RHIC, the predicted suppression of J/ψ due to screening in the QGP is much larger than the suppression observed at SPS due to the higher initial density of the produced medium [9]. The RHIC measurements, however, show a level of suppression similar to NA50 at mid-rapidity [10], which is significantly smaller than expectations due to color screening effects alone. This can be understood in a scenario where charmonium is regenerated due to the large initial production of charm + anti-charm quarks at $\sqrt{s_{NN}}$= 200 GeV, in conjunction with their possible thermalization in the created medium [11]. If charm quarks (partially) thermalize in RHIC collisions, then the coalescence of $c\bar{c}$ could lead to a smaller than expected suppression [12].

With counteracting effects, it is a challenge to disentangle the suppression from the regeneration. Further complicating this task is that the J/ψ-particle yields that are measured are not all primordial; some ~40% are feed-down from χ_c (approximately 30%) and ψ′ (approximately 10%) decays. Since the survival rate of different charmonium states may be different, due to the different sizes, it is important to know these feed-down fractions precisely. In addition, there are cold nuclear matter effects [13], including modification of the parton distribution functions ("shadowing") and partonic multiple scattering, that also lead to suppression of heavy quarkonium and need to be disentangled from QGP suppression. In order to quantify effects of deconfinement, cold nuclear matter effects (via p+A collisions) must be measured and disentangled.
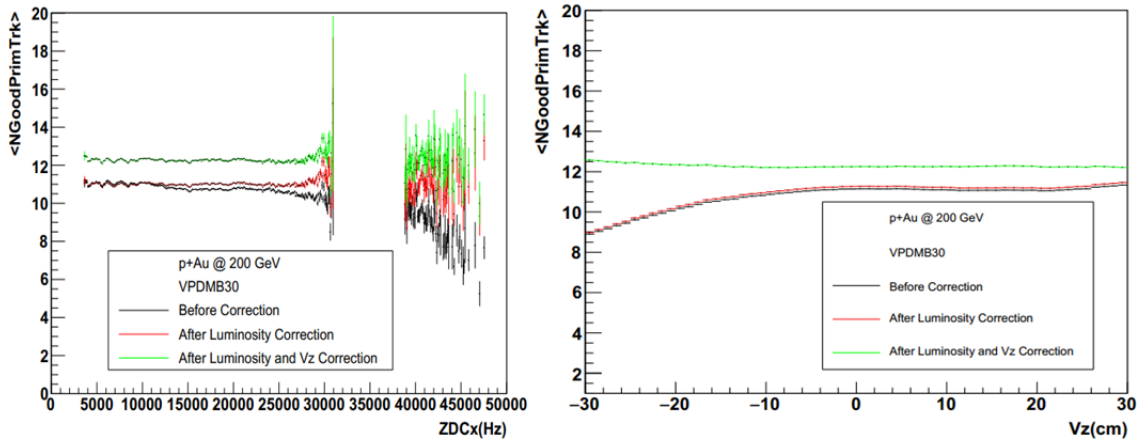
FIG. 3 Average number of good primary tracks, before (black) and after (green) correcting the vertex and luminosity dependence, (Left) as a function of ZDC interaction rate and (Right) as a function of vertex z-position.

We have worked on the quality assurance and a centrality determination for the 2015 p+Au data set. In the previous reporting period, we performed a centrality determination for p+Au collisions, based on the number of good primary tracks in an event. In the current reporting period, we calculated corrections for the centrality determination, including trigger bias, vertex dependence, and luminosity dependence. Fig. 3 shows the effect of the corrections on the average number of good primary tracks in an event.

For the studies of charmonium production in p+A collisions, we have started working on extracting J/Ψ yields, as a function of p_T and centrality. Fig. 4 shows the mass distribution of muon pairs (unlike-sign in black and like-sign in blue) that were has obtained as a function of p_T. The next step will be to extract the yields as a function of centrality and perform efficiency corrections.
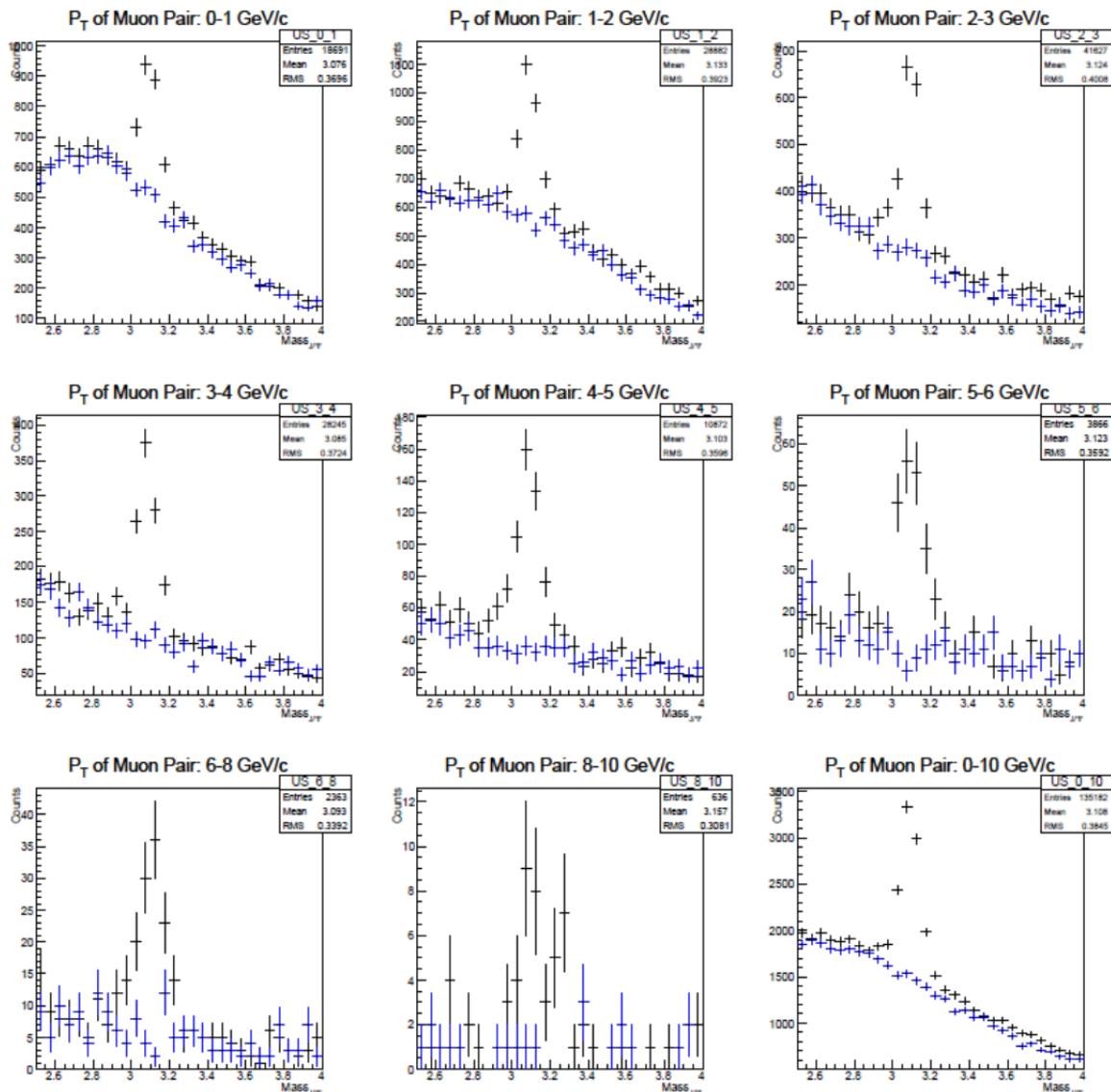
FIG. 4 Mass distributions for muon pairs: unlike-sign pairs in black and like-sign pairs (background) in blue, with each panel showing a different range of pair p_T. There is a clear signal of J/Ψ at the mass ~ 3.1 GeV/c^2.

[1] X.N. Wang, Z. Huang, and I. Sarcevic, Phys. Rev. Lett. **77**, 231 (1996).

[2] L. Adamczyk *et al.* [STAR Collaboration], Phys. Lett. B **760**, 689 (2016).

[3] S. Chatrchyan *et al.* [CMS Collaboration], Phys. Lett. B **718**, 773 (2013).

[4] [ATLAS Collaboration], ATLAS-CONF-2012-121.

[5] N.R. Sahoo *et al.* [STAR Collaboration], arXiv:1704.04814 [nucl-ex].

[6] L. Adamczyk *et al.* [STAR Collaboration], arXiv:1702.01108v1 [nucl-ex].

[7] T. Matsui and H. Satz, Phys. Lett. B **178**, 416 (1986).

[8] M.C. Abreu *et al.* [NA50 Collaboration], Eur. Phys. J. C **39**, 335 (2005).

[9] L. Grandchamp, R. Rapp, and G.E. Brown, Phys. Rev. Lett. **92**, 212301 (2004); A. Capella and E.G. Ferreiro, Eur. Phys. J. C **42**, 419 (2005).

[10] A. Adare *et al.*, [PHENIX Collaboration], Phys. Rev. Lett. **98**, 232301 (2007).

[11] P. Braun-Munzinger and J. Stachel, Phys. Lett. B **490**, 196 (2000).

[12] L. Grandchamp and R. Rapp, Phys. Lett. B **523**, 60 (2001).

[13] R. Vogt, Phys. Rev. C **71**, 054902 (2005).

SECTION III

NUCLEAR THEORY

Neutron-rich matter from chiral effective field theory

J.W. Holt

Nuclear thermodynamic equation of state

The equation of state of neutron-rich matter from sub- to supra-nuclear densities directly influences neutron star structure and evolution, the dynamics of core-collapse supernovae, r-process nucleosynthesis, as well as features of gravitational waves produced during the late inspiral and post-merger phases of binary neutron star coalescence. The major challenge is to model the free energy $F(n, T, Y_p)$ of baryonic matter over approximately eight orders of magnitude in density ($n \sim 10^8 - 10^{15}$ g/cm^3), temperatures up to $T \sim 5 \times 10^{11} \, K$, and proton fractions $Y_p \leq 0.6$. Under this range of conditions (well below the chiral symmetry breaking scale of $\Lambda_\chi \approx 1$ GeV) effective field theory methods [1-3] are expected to provide a suitable framework for the description of strongly interacting matter. In anticipation of new observational campaigns of neutron stars (e.g., NICER) and additional discoveries from gravitational wave observations of binary neutron star mergers (Advanced LIGO), present efforts in our research group are focused on reducing theoretical uncertainties in the nuclear thermodynamic equation of state and refining phenomenological energy density functionals by imposing microscopic constraints from chiral effective field theory (chiral EFT).

Microscopic many-body calculations based on chiral EFT are now able to provide reliable predictions for the homogeneous matter equation of state through a multi-channel analysis of theoretical uncertainties. In the past year we constructed a class [4] of equations of state for homogeneous matter at finite temperature that simultaneously satisfy constraints from microscopic many-body theory [5-7], nuclear experiments, the model-independent virial expansion, and observed neutron star radii. The different regimes are smoothly joined, resulting in a thermodynamically stable hot and dense matter equation of state. In the upcoming year we will work toward full supernova equation of state tables that include the inhomogeneous mixed phase at low temperatures and densities.

Neutron star tidal deformabilities constrained by chiral effective field theory

Gravitational wave and electromagnetic signals from binary neutron star mergers offer a unique probe for studying the properties of ultra-dense matter. The recent observation of gravitational wave event GW170817 [8] and the associated electromagnetic counterpart [9] suggest the source to be a merger of two neutron stars with combined mass $M_{\text{total}} = 2.74^{+0.04}_{-0.01} \, M_\odot$ that left behind a relatively long-lived hypermassive neutron star remnant.

Measurement of the late inspiral gravitational waveform from GW170817 was sufficient to place a conservative upper bound of $\Lambda < 800$ on the tidal deformability of a 1.4 $M_\odot$ neutron star, competitive with bounds [10] deduced from current neutron star mass and radius measurements. In a recent work [11] we constructed a large class of over 72,000 energy density functionals constrained by the neutron matter equation of state from chiral effective field theory and the known saturation properties of homogeneous nuclear matter in order to place theoretical constraints on the neutron star tidal deformability, shown in Fig. 1. We found that the tidal deformability of a 1.4 $M_\odot$ neutron star lies in the range $350 < \Lambda < 540$,
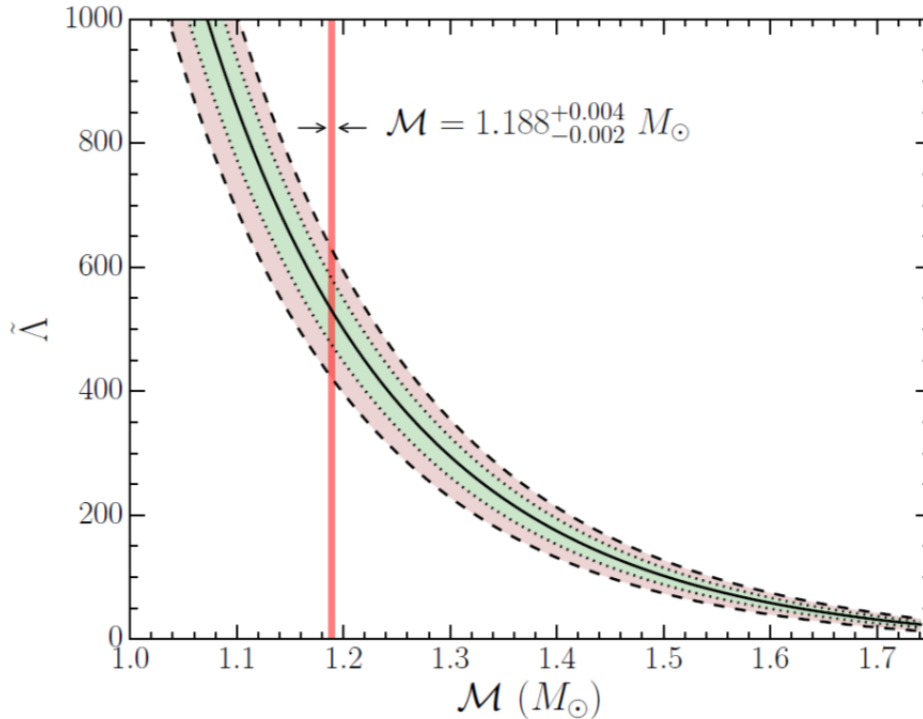
FIG. 1. Neutron star chirp tidal deformability as a function of chirp mass from chiral nuclear forces.

which is consistent with the upper bound from the observed neutron star merger event. We also examined the neutron star mass-radius relation and determined the radius of a $1.4\,M_\odot$ neutron star to lie in the range $11.6\,\text{km} < \text{R} < 12.9\,\text{km}$. As future neutron star merger events are observed, the framework developed in [11] will enable stronger constraints on the equation of state and nuclear force

Tensor Fermi liquid parameters in nuclear matter from chiral EFT

Fermi liquid theory is widely used to describe the transport, response, and dynamical properties of nuclear and neutron matter in terms of interacting quasiparticles. In recent work [12] we have calculated for the first time the full decomposition of the quasiparticle interaction in symmetric nuclear matter into its central, relative tensor, center-of-mass tensor, and cross-vector interaction components. Realistic two- and three-body forces derived within the framework of chiral effective field theory were employed, and we estimated theoretical uncertainties by varying the resolution scale and order in the chiral expansion. The work is expected to provide microscopic guidance for the tensor forces employed in modern mean field effective interactions and nuclear energy density functionals. Work to derive the quasiparticle interaction in asymmetric nuclear matter with applications to neutrino diffusion in proto-neutron stars is underway.

Proton pairing in neutron stars from chiral effective field theory

Neutron superfluidity and proton superconductivity play an important role in the thermal evolution of neutron stars and the large-scale dynamical phenomenon of pulsar glitches. In a recent work [13] we studied the 1S0 proton pairing gap Δ as a function of density in beta-equilibrated neutron star

matter within the BCS approximation starting from realistic two- and three-body chiral nuclear forces. We find that three-body forces suppress proton pairing and lead to a transition to the normal state at a density around twice that of saturated nuclear matter. The peak in the proton pairing gap occurs close to the crust-core interface where the density is about one-half that of saturated nuclear matter. We estimate the critical temperature for the onset of proton superconductivity to be $T_c = (3.7 - 6.0) \times 10^9 K$, which is consistent with previous theoretical results in the literature and marginally within the range deduced from a recent Bayesian analysis [14] of neutron star cooling observations.
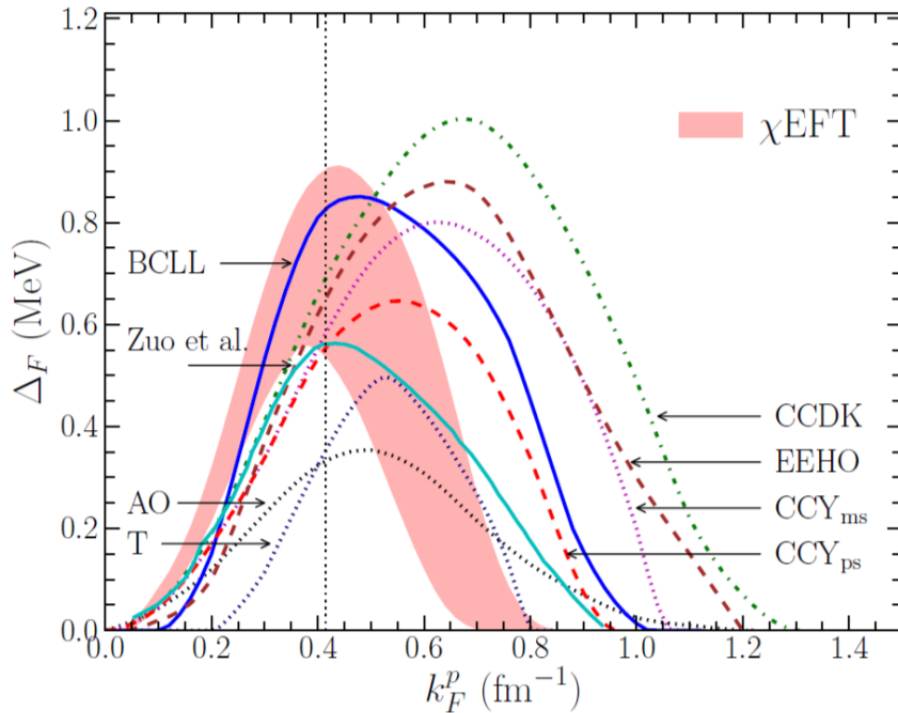
FIG. 2. Proton pairing gap as a function of the proton Fermi momentum in beta-equilibrated neutron star matter.

[1] S. Weinberg, Physica A **96**, 327 (1979).

[2] E. Epelbaum, H.-W. Hammer, and U.-G. Meissner, Rev. Mod. Phys. **81**, 1773 (2009).

[3] R. Machleidt and D.R. Entem, Phys. Rep. **503**, 1 (2011).

[4] X. Du, A.W. Steiner, and J.W. Holt, arXiv:1802.09710.

[5] C. Wellenhofer, J.W. Holt, N. Kaiser, and W. Weise, Phys. Rev. C **89**, 064009 (2014).

[6] C. Wellenhofer, J.W. Holt, and N. Kaiser, Phys. Rev. C **92**, 015801 (2015).

[7] C. Wellenhofer, J.W. Holt, and N. Kaiser, Phys. Rev. C **93**, 055802 (2016).

[8] B.P. *Abbot et al.* (LIGO Scientific Collaboration and Virgo Collaboration), Phys. Rev. Lett. **119**, 161101 (2017).

[9] B.P. Abbot *et al.*, Astrophys. J. **848**, L12 (2017).

[10] A.W. Steiner, S. Gandolfi, F.J. Fattoyev, and W.G. Newton, Phys. Rev. C **91**, 015804 (2015).

[11] Y. Lim and J.W. Holt, arXiv:1803.02803.

[12] J.W. Holt, N. Kaiser, and T. R. Whitehead, Phys. Rev. C **97**, 054325 (2018).

[13] Y. Lim and J.W. Holt, arXiv:1709.08793.

[14] S. Beloin, S. Han, A.W. Steiner, and D. Page, Phys. Rev. C **9**7, 015804 (2018).

Analysis of pairing correlations in neutron transfer reactions and comparison to the constrained molecular dynamics model

C. Agodi,[1] G. Giuliani,[2] F. Cappuzzello,[1,2] A. Bonasera,[1,5] D. Carbone,[1] M. Cavallaro,[1]
A. Foti,[2,4] R. Linares,[3] and G. Santagati[1]

[1]INFN - Laboratori Nazionali del Sud, Catania, Italy
[2]Dipartimento di Fisica e Astronomia, Università di Catania, Catania, Italy
[3]Instituto de Física, Universidade Federal Fluminense, Niteroi, Rio de Janeiro, Brazil
[4]INFN, Sezione di Catania, Catania, Italy
[5]Cyclotron Institute, Texas A&M University, College Station, Texas 77843

The transfer yields mass spectra were measured in ^{11}B, ^{12,13}C, ^{28}Si(^{18}O,^{17}O) and ^{11}B, ^{12,13}C, ^{28}Si(^{18}O,^{16}O) reactions at 84 MeV. The two-neutron transfer (2NT) and the one-neutron transfer (1NT) cross sections were extracted for all the systems. The 2NT cross section is found comparable to the 1NT one and remarkably larger than that predicted assuming no correlations among the two transferred nucleons and only natural parity states are populated via the (^{18}O,^{16}O) two-neutron transfer reaction. Calculations based on the constrained molecular dynamics model show that such behavior is uniquely a consequence of neutron pairing correlations in the ^{18}O ground state [1].

[1] C. Agodi *et al.* ,Phys. Rev. C **97**, 034616 (2018).

Decay modes of the Hoyle state in ^{12}C

H. Zheng,[1] A.Bonasera,[1,2] M. Huang,[3] and S. Zhang[3]

[1]*Laboratori Nazionali del Sud, INFN, via Santa Sofia, 62, 95123, Catania, Italy*

[2]*Cyclotron Institute, Texas A&M University, College Station, TX 77843, USA*

[3]*College of Physics and Electronics Information, Inner Mongolia University for Nationalities, Tongliao, 028000, China*

Recent experimental results give an upper limit to the direct decay of the Hoyle state into 3α of equal energy respect to the sequential decay into ^{8}Be+α less than 0.043% (95% C.L.). We performed one and two-dimensional tunneling calculations to estimate such a ratio and found it to be more than one order of magnitude smaller than experiment depending on the strength of the nuclear force [1]. This is within high statistics experimental capabilities. Our results can also be tested by measuring the high excitation energy states of ^{12}C decay modes where the ratio of direct to sequential decay might reach 10% at $E^{*}(^{12}C)$=10.3MeV. The link between a Bose Einstein Condensate (BEC) and the direct decay of the Hoyle state is also addressed. We discuss a hypothetical 'Efimov state' at $E^{*}(^{12}C)$=7.458MeV, which would mainly *sequentially* decay with 3α of equal energies: a counterintuitive result of tunneling. Such a state, if it would exist, is at least 3 orders of magnitude less probable than the Hoyle's, thus below the sensitivity of recent and past experiments.

[1] H. Zheng *et a*l., Phys. Lett. B **779**, 460 (2018).

Mean free path and shear viscosity in central ^{129}Xe+^{119}Sn collisions below 100 MeV/nucleon

H.L. Liu,[1,2,3] Y.G. Ma,[1,3] A. Bonasera,[4,5] X.G. Deng,[1,2] O. Lopez,[6] and M. Veselsky[7]

[1]*Shanghai Institute of Applied Physics, Chinese Academy of Sciences, Shanghai 201800, China*
[2]*University of the Chinese Academy of Sciences, Beijing 100080, China*
[3]*School of Physical Science and Technology, ShanghaiTech University, Shanghai 201203, China*
[4]*Cyclotron Laboratory, Texas A & M University, College Station, TX, USA*
[5]*INFN, Laboratori Nazionali del Sud, Catania, Italy*
[6]*Laboratoire de Physique Corpusculaire, ENSICAEN, Universite de Caen Basse Normandie, CNRS/IN2P3, F-14050 Caen Cedex, France*
[7]*Institute of Physics, Slovak Academy of Sciences, Dubravsk´a cesta 9,84511 Bratislava, Slovakia*

Thermal and transport properties of hot nuclear matter formed in central ^{129}Xe + ^{119}Sn collisions at the Fermi energy are investigated using the isospin-dependent quantum molecular dynamical (IQMD) model [1]. Temperature (T), average density (ρ), chemical potential (μ), mean momentum (P), shear viscosity (η) and entropy density (s) are obtained from the phase-space information. The mean free path (σ_{nn}) and the in-medium nucleon-nucleon cross-section (λ_{nn}) in the largest compressible stage at different incident energy are deduced and compared with the experimental results from Phys. Rev. C 90,064602 (2014). The result shows that λ_{nn} and σ_{nn} have the same trend and similar values as the experimental results when the beam energy is greater than 40 MeV/nucleon at maximum compressed state. Furthermore, the derived shear viscosity over entropy density (η/s) shows a decreasing behaviour to a saturated value around $\frac{3}{4}\pi$ as a function of incident energy.

[1] H.L. Liu *et al.*, Phys. Rev. C **96**, 064604 (2017).

Advancing low-energy nuclear reaction theory and indirect methods in nuclear astrophysics

Akram Mukhamedzhanov

Indirect radiative capture reactions

Advancing the theory of the indirect methods, like ANC and Trojan Horse in the era of higher intensity radioactive beams.

The main stress is on the indirect radiative capture reactions with stable and exotic beams. Among the most important application of the developed theory is the famous $^{12}C(\alpha,\gamma)^{16}O$ reaction. For more than 30 years there were numerous unsuccessful attempts to come close to the energy of 1 MeV while we need to reach the most effective astrophysical energy of 300 keV. New facilities, like underground labs in South Dakota, USA, and at IMP, China, new gamma-ray facilities in USA and Romania, are aimed to come closer to 1 MeV energy, which is still far away from the desired 300 keV. Meantime I and Prof. G. Rogachev suggested a new method to reach 300 keV energy by using the indirect radiative capture reaction $^{12}C(^{6}Li,d,\gamma)^{16}O$ to get information about the $^{12}C(\alpha,\gamma)^{16}O$ reaction.

Measurements of this reaction would constitute a main breakthrough in nuclear astrophysics, what is exactly in the FRIB agenda. The proposed experiment is very difficult but doable. I hope Prof. Rogachev's group will add devices they needs to do this experiment.

Generalization of the theory of the indirect Trojan Horse method for three charged particles in the final state

Higher intensity radioactive beams allow one to use FRIB to conduct measurements of many astrophysical reactions using the Trojan Horse method for resonant rearrangement reactions and indirect radiative capture processes. Until now low triple differential cross sections of the Trojan Horse reactions forced experimentalists to measure only energy dependence of the Trojan Horse cross sections. Their absolute values were determined by normalization of the Trojan Horse cross sections to the available direct measurements at higher energies. When higher intensity stable and unstable beams are available the indirect Trojan Horse experiments would allow one to measure both energy dependence and absolute values of the experimental cross sections. Until now, because the absolute cross sections were not measured, I developed the theory of the indirect Trojan Horse method for resonant rearrangement and radiative capture reactions using only the plane wave approximation.

Now, taking into account a possibility to conduct absolute measurements of the indirect cross sections, I am planning to develop a theory, which includes the distorted waves, especially the final-state three-body Coulomb interactions to analyze the Trojan Horse reactions with three charged particles.

Generalization of the Faddeev equations for peripheral reactions

I will be working on the generalization of the three-body Faddeev integral equations in the two-particle Alt-Grassberger-Sandhas (AGS) form to analyze both sub-Coulomb and above the Coulomb barrier reactions. The AGS equations will be modified by rewriting the effective potentials in the form of the distorted-wave-Born-approximation.

Investigating the dependence of the value of the isovector giant octupole resonance in select spherical nuclei on the symmetry energy and on the energy weighted sum rule enhancement coefficient for the IVGDR

G. Bonasera, M.R. Anders, and S. Shlomo

We have performed fully self-consistent Hartree-Fock (HF)-based random phase approximation (RPA) calculations of the centroid energies for the isovector resonances up to L=3 multi-polarity for several ^{40,48}Ca, ^{68}Ni, ^{90}Zr, ^{116}Sn, ^{144}Sm and ^{208}Pb. The calculations were done using 33 different Skyrme-type effective nucleon-nucleon interaction commonly adopted in the literature.

The Pearson linear correlation coefficient (C) is calculated for every nuclear matter (NM) property in an effort to make constraints on NM property when the correlation is high. In Fig. 1 we study the centroid energy of the isovector giant octupole resonance (IVGOR), calculated within the HF-RPA framework with the 33 Skyrme interactions, as a function of the symmetry energy J. Each nucleus has its own panel. We don't have any available experimental data for the IVGOR. We do not find any correlation between the calculated E_{CEN} and J (C ~ -0.32) for all nuclei considered. Similar results were found for the first derivative of the symmetry energy, L (C ~ 0.19) and for the second derivitative of J, K_{Sym} (C ~ 0.02). On the other hand, we find a strong correlation between the E_{CEN} of the IVGOR and the energy weighted sum rule enhancement coefficient κ for the isovector giant dipole resonance (Pearson linear correlation coefficient C ~ 0.81), as can be seen in Fig. 2. Similar calculations were carried out for both the isoscalar and the isovector resonances of multipolarity L = 1, 2 and 3. Analysis was also performed for all the resonances of these nuclei [1] and other nuclear matter quantities. These results will be used to determine the next generation nuclear energy density functional with improved predictive power for properties of nuclei and nuclear matter.
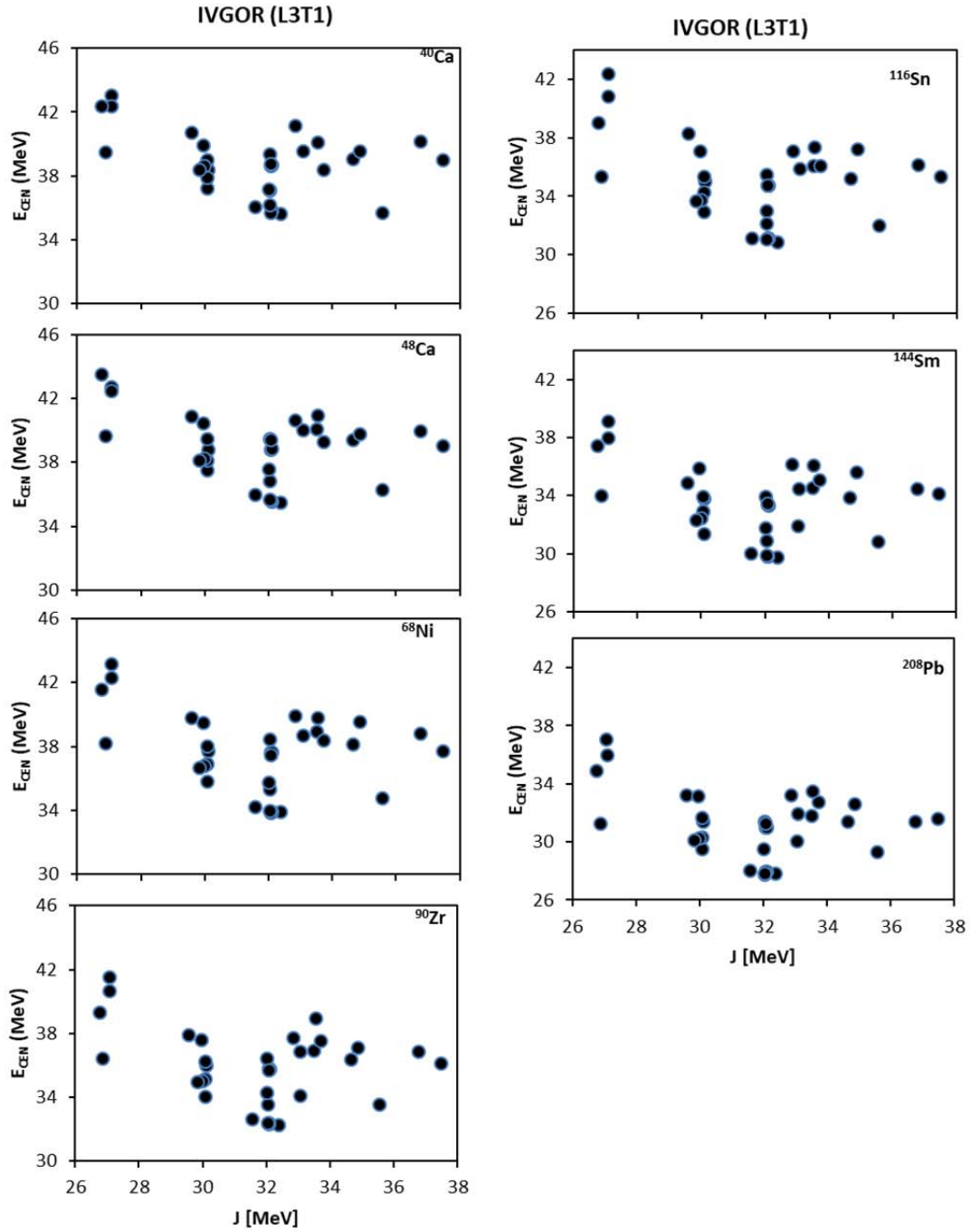
FIG. 1. Calculated centroid energies, E_{CEN}, in MeV (full circle) of the isovector giant octupole resonance (IVGOR), for different interactions, as a function of the symmetry energy coefficient J. We don't find any correlation between this isovector property and the value of the E_{CEN} with a Pearson linear correlation coefficient of $C \sim -0.32$.
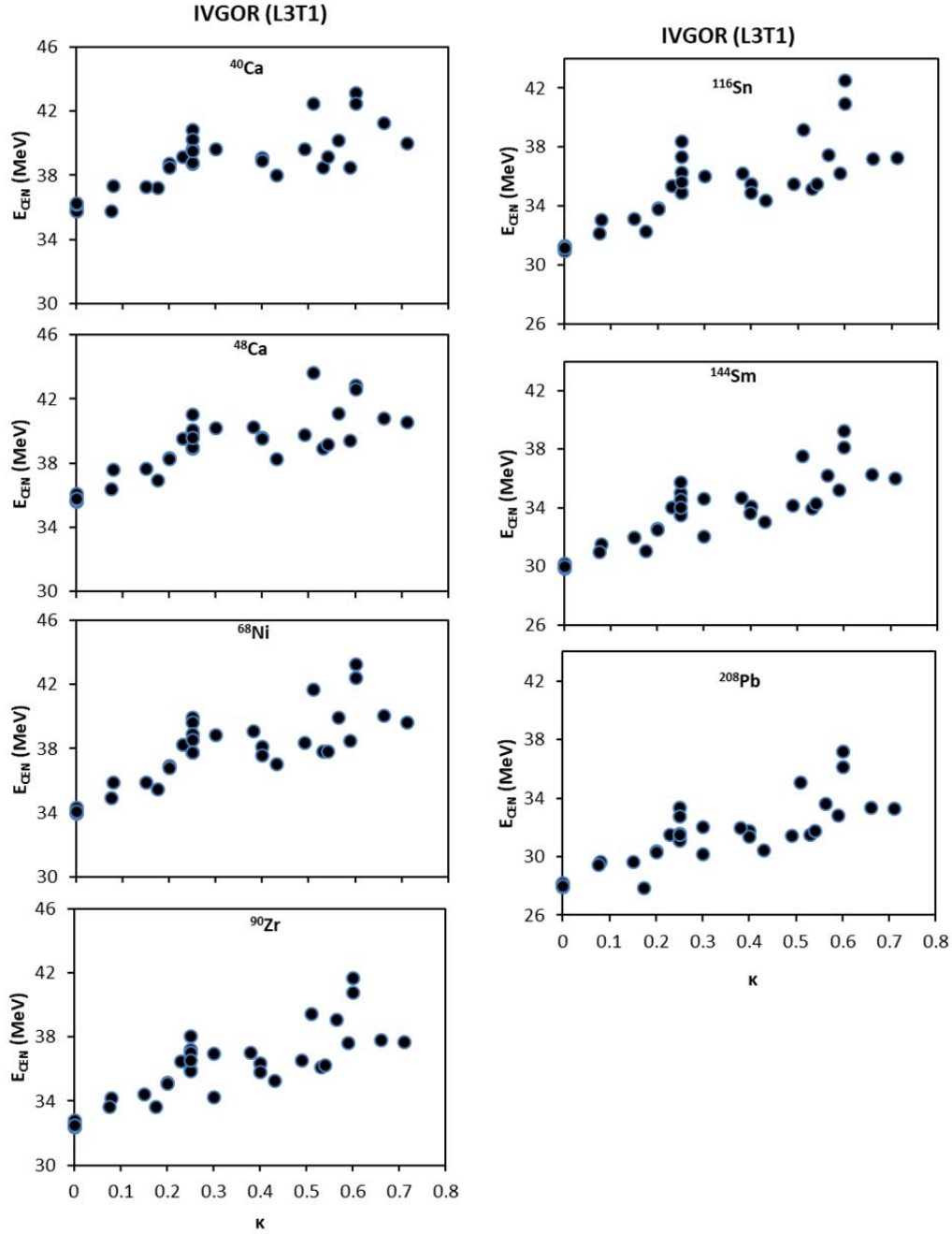
FIG. 2. Calculated centroid energies, E_{CEN}, in MeV (full circle) of the isovector giant octupole resonance (IVOGR), for the different interactions, plotted against the energy weighted sum rule enhancement coefficient for the isovector giant dipole resonance. We find a strong correlation between this NM property and the calculated E_{CEN} with a Pearson linear correlation coefficient close to C = 0.81 for all isotopes considered.

[1] G. Bonasera *et al.*, in preparation for publication.

Isovector giant dipole resonances in ^{92,94,96,98,100}Mo and ^{90,92,94}Zr and the energy weighted sum rule enhancement coefficient

G. Bonasera and S. Shlomo

We have performed fully self-consistent Hartree-Fock (HF)-based random phase approximation (RPA) calculations of the centroid energies for the isovector resonances up to L=3 multi-polarity for the isotopes of ^{92,94,96,98,100}Mo and ^{90,92,94}Zr. The calculations were done using 33 different Skyrme-type effective nucleon-nucleon interaction commonly adopted in the literature. The interactions considered cover a wide range of values of nuclear matter properties. We use the occupation number approximation for the single particle orbits of the open shell nuclei to carry out spherical HF and RPA calculations.

The Pearson linear correlation coefficient is calculated for every nuclear matter (NM) property. We then compare our theoretical calculation to the available experimental data and in the cases where we have high correlation we can set limiting values on the NM properties. Here we report on a strong correlation between the centroid energies, E_{CEN}, of the isovector giant dipole resonances (ISGDR) and the energy weighted sum rule coefficient factor κ. In Fig. 1 we show that the centroid energies, of the isovector giant dipole resonance associated with each Skyrme interaction as a function of κ, have a strong Pearson linear correlation coefficient for all nuclei shown. Similar results were found for the isovector resonance with L= 2 and 3. With the available experimental data, we can limit the value of κ to be between 0.25 and 0.65. Analysis was performed for all the resonances and nuclei [1] and other nuclear matter quantities.

These results, together with a similar analysis done for a wide mass range of spherical nuclei [2], will be used to set constrains on NM properties and determine the next generation nuclear energy density functional with improved predictive power for properties of nuclei and nuclear matter.
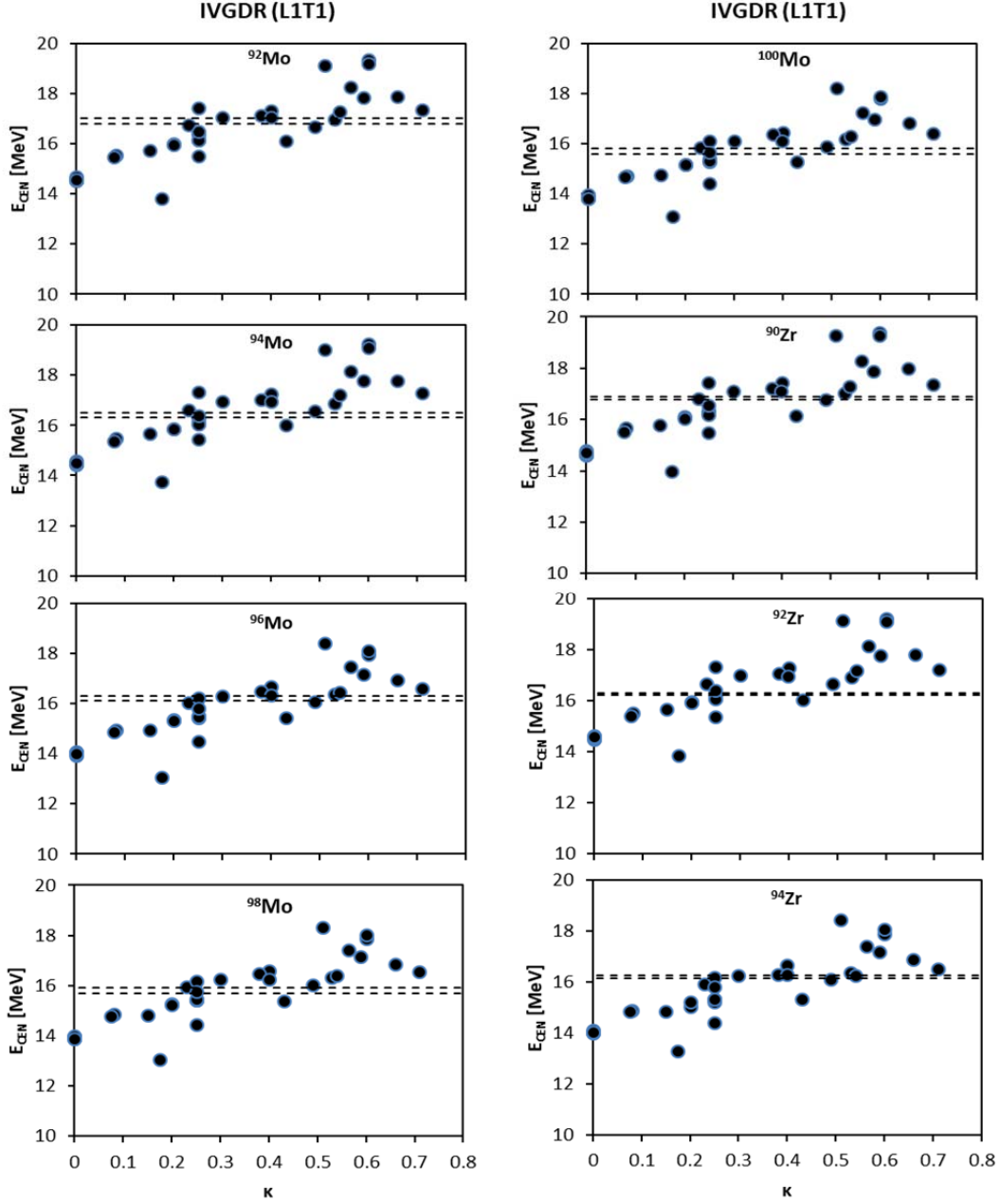
FIG. 1. Calculated centroid energies, E_{CEN}, in MeV (full circle) of the isovector giant dipole resonance (ISGDR), for Skyrme interactions, as a function the isovector enhancement coefficient κ. Each nucleus has its own panel and the experimental uncertainties are contained by the dashed lines. We find strong correlation between this NM property and the calculated E_{CEN} with a Pearson linear correlation coefficient C = .85 for all isotopes considered.

[1] G. Bonasera *et al.*, in preparation for publication.
[2] G. Bonasera *et al.*, in preparation for publication.

Self-consistent mean-field approach to the statistical level density in spherical nuclei

V.M. Kolomietz,[1] A.I. Sanzhur,[1] and S. Shlomo[2,3]

[1]*Institute for Nuclear Research, 03680 Kiev, Ukraine*
[2]*Cyclotron Institute, Texas A&M University, College Station, Texas 77843, USA*
[3]*Department of Particles and Astrophysics, the Weizmann Institute of Science, Rehovot 76100, Israel*

We have applied the thermodynamical approach to a study of the statistical level density, $\rho(E_{\text{ex}})$, of a nucleus. The approach is based on the extended Thomas-Fermi approximation (ETF) with Skyrme forces. The adopted approach describes successfully the basic nuclear liquid-drop properties as well as the single particle characteristics related to the nuclear mean field. The ETF approximation employed with Skyrme forces can be considered as a unification of both fundamental nuclear models: the liquid drop model and the shell model. In a practical sense, this approach allows us to evaluate the quantum single-particle corrections to the bulk liquid drop characteristics, in particular, the shell corrections to the mass formula and the deformation energy. An advantage of this approach is that the nuclear mean field is consistent with the nuclear liquid drop because both of them are generated by the common Skyrme forces.

To evaluate the statistical level density $\rho(E_{\text{ex}})$ we need to know the excitation energy E_{ex} which is a complicate problem for a system of strongly interacting particles like a nucleus. We pointed out that a significant progress is achieved by use of the Landau's conception of quasiparticles where the excitation energy E_{ex} is derived within a Fermi-gas system of noninteracting quasiparticles and thereby depends on the mean field $V(\boldsymbol{r})$ and the effective mass m^* of the quasiparticle. In our consideration, the nuclear mean field $V(\boldsymbol{r})$ and the single-particle level density $g(\epsilon)$ are derived within the ETF using the effective SkM* and KDE0v1 Skyrme interactions. Using the Wigner distribution function in phase space $f(\boldsymbol{r}, \boldsymbol{p})$, we have presented a semiclassical derivation of the single-particle level density $g(\epsilon)$ and the number of states $N(\epsilon)$ embedded in potential well $V(\boldsymbol{r})$ with energy below ϵ. Analyzing the value of $N(\epsilon)$, we have shown that the $\hbar^2$-corrections to $N(\epsilon)$ play only a minor role.

Applying the Landau's conception of quasiparticles, we have evaluated the excitation energy E_{ex} and the statistical inverse level density parameter K of the nucleus. The evaluation of the excitation energy E_{ex} needs the single particle states near Fermi energy only. This fact confirms the Landau's conception of quasiparticles and allows one to use the Fermi-gas approach to evaluate the nuclear excitation energy. Involving the effective mass $m^*(r)$ of quasiparticles, we took into consideration both contributions to $m^*(r)$ caused by the non-locality of the nucleon-nucleus interaction (k-mass $m_k^*(r)$) which is generated by the Skyrme interaction and the correlation correction (frequency dependent ω-mass $m_\omega^*(r)$) which arises from the scattering of nucleons from low-lying surface vibrations of the nucleus. We have shown that the presence of the frequency dependent ω-mass $m_\omega^*(r)$ distorts significantly the selfconsistent mean field and leads to an enhancement of the single particle level density near the Fermi surface. We have shown (see Fig. 1) that the ETF approximation with Skyrme interaction provides a quite satisfactory description of average A-dependence of the statistical inverse level density parameter K.
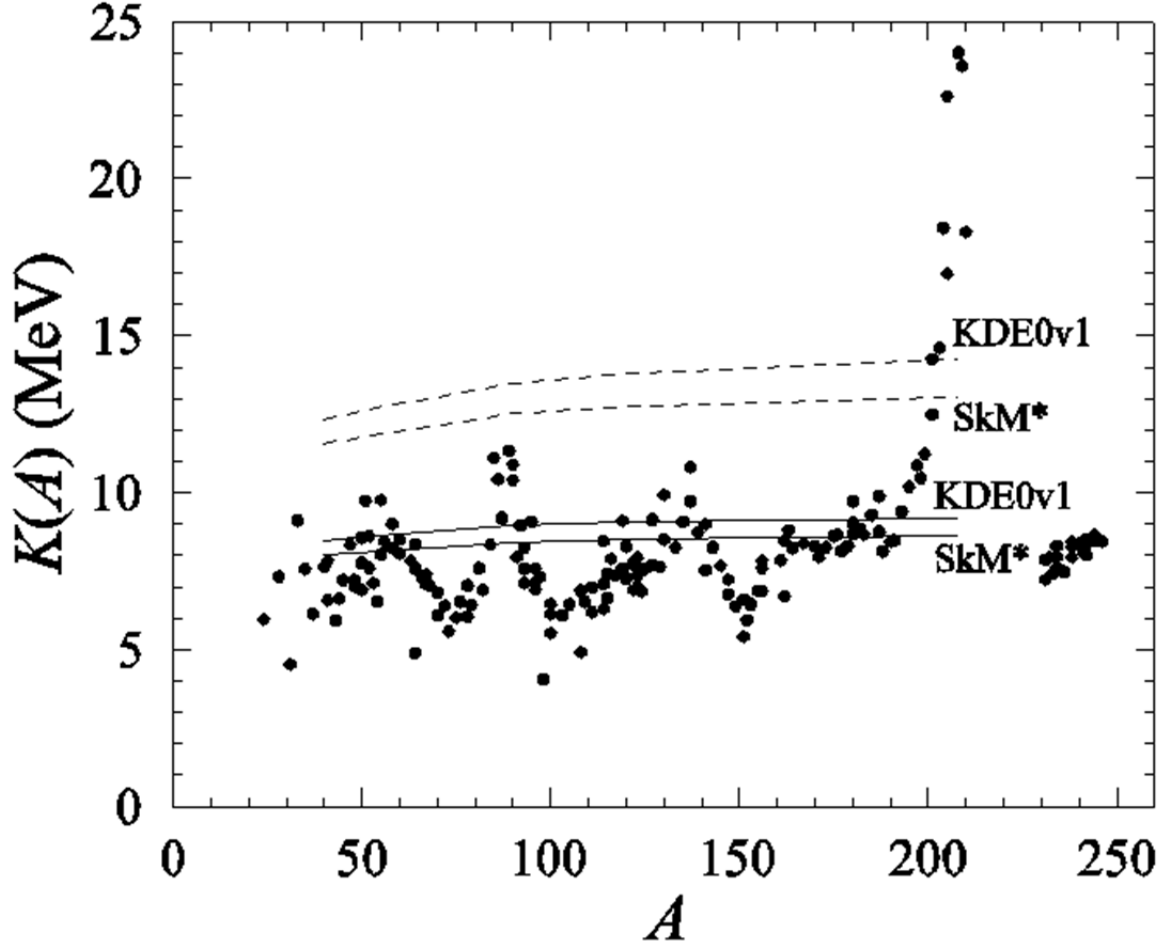
FIG. 1. Experimental values of K for even-even nuclei (solid points). The solid lines represent the ETF calculations with Skyrme interactions SkM* and KDE0v1 with effective mass $m_{q,\omega}^*(r)$. The dashed lines are for he case $m_{q,\omega}^*(r) = m$. See Ref. [1] for details of the calculations

Using the ETF finite-depth potential $V(r)$, we have paid a special attention to the accuracy of the derivation of the level density $g(\epsilon)$ in continuum at $\epsilon > 0$. The subtraction of the free space contribution from $g(\epsilon)$ allows one to prevent a spurious contribution to the excitation energy E_{ex}. A spurious contribution to E_{ex} occur due to the free space states which are not associated with the potential well $V(r)$. Our numerical calculations for the Skyrme ETF potential show that the correct subtraction of the free-state contribution from the continuum states reduces strongly the result for the excitation energy E_{ex} and thereby increases the result for K in the case of high enough temperatures, see Fig. 2.
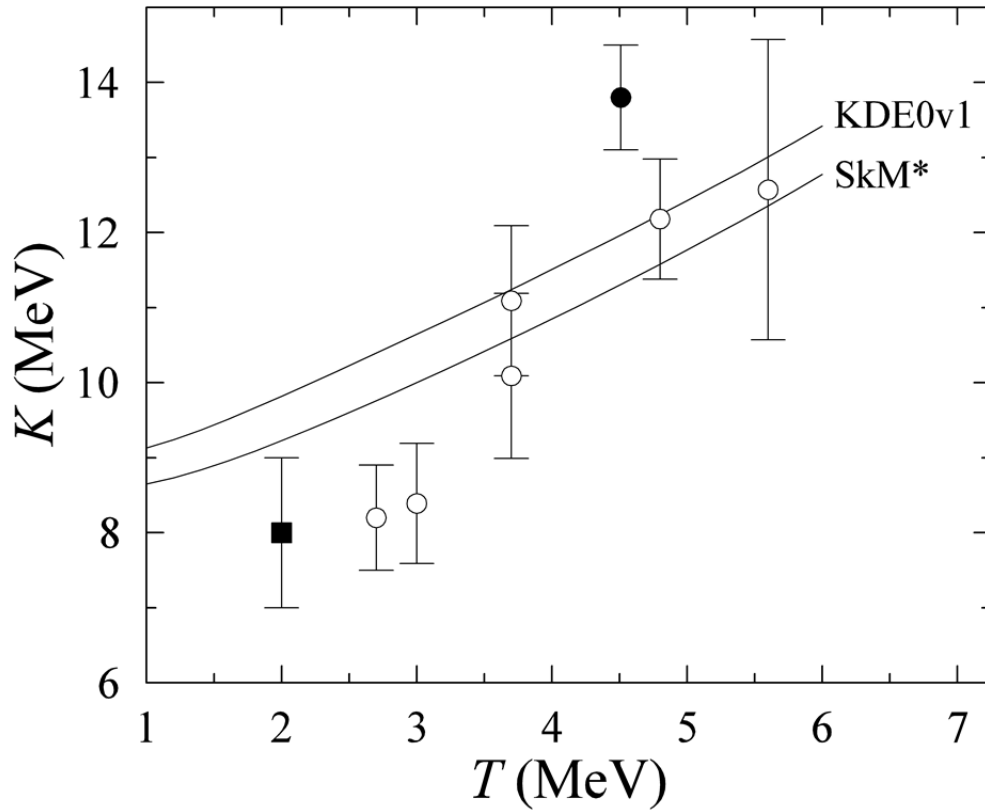
FIG. 2. The calculated temperature dependence of the inverse statistical level-density parameter $K(T)$ for the nucleus with $Z = 60$ and $A = 160$ for Skyrme interactions SkM* and KDE0v1 (solid lines), is compared with the experimental data. See Ref. [1] for details

[1] V.M. Kolomietz, A.I. Sanzhur, and S. Shlomo, Phys. Rev. C **97**, 064302 (2018).

The Equation of state of hot nuclear matter

V.M. Kolomietz,[1] and S. Shlomo[2,3]

[1]*Institute for Nuclear Research, 03680 Kiev, Ukraine*
[2]*Cyclotron Institute, Texas A&M University, College Station, Texas 77843, USA*
[3]*Department of Elementary Particles and Astrophysics, the Weizmann Institute of Science, Rehovot 76100, Israel*

We have carried out calculations of the equation of state (EOS) of hot nuclear matter, using the semi classical extended Thomas-Fermi approximation for the internal kinetic energy of nucleons and the potential energy due to the Skyrme effective nucleon-nucleon interaction. We have paid special attention to the derivation of the stiffness coefficients, such as the incompressibility coefficient $K(\rho_0)$ and the isospin symmetry coefficient $C_{\text{sym}}(\rho_0)$. We point out that the use of the Skyrme interaction with parameters adjusted to reproduce the ground state properties of nuclei within the mean-field model is a reasonable approximation for our purposes. In fact, the effective interaction is modified only slightly (by a few percent) in a wide temperature range, $T = 0 \div 20$ MeV. Here, we present results of numerical calculations of the incompressibility coefficient $K(\rho_0)$ and the symmetry energy coefficient $C_{\text{sym}}(\rho_0)$ for the SkM[*], Sly203b and the more modern KDE0v1 Skyrme interactions.

In Table I we give the values of the Skyrme parameters for the SkM[*], KDE0v1 and Sly230b interactions and the corresponding physical quantities of symmetric nuclear matter at saturation density, ρ_{eq}. Note that, in general, the transport coefficients K, and C_{sym}, are temperature dependent. This can be seen, in a transparent way, by normalizing the density ρ_0 to the equilibrium density $\rho_{\text{eq}}(T)$ and using the dimensionless ratio $\rho_0/\rho_{\text{eq}}(T)$ as a variable. To avoid any misunderstanding, we point out that the particle density ρ_0 is an independent variable which is fixed by the Lagrange multiplier ξ in the variational Euler-Lagrange equation. In the case of $\xi = 0$ and zero temperature $T = 0$, the variational equation provides the actual equilibrium state with the saturation density $\rho_0 = \rho_{\text{eq}}(T = 0)$. In a heated system at $T \neq 0$ and below the phase separation point, the equilibrium density $\rho_{\text{eq}}(T)$ is derived by the equilibrium condition for the pressure $P(\rho, T) = 0$, where $P(\rho, T) = \rho^2 \partial F(\rho, T)/\partial \rho$ and $F(\rho, T)$ is the free energy. For higher temperatures above the point of the phase separation, the value of $\rho_{\text{eq}}(T)$ is obtained from the interphase equilibrium condition. The temperature dependence of the equilibrium density $\rho_{\text{eq}}(T)$ can be approximated as $\rho_{\text{eq}}(T) = \rho_{\text{eq}}(T = 0)(1 - 1.6 \cdot 10^{-3} T^2)$, where the temperature T is taken in MeV. In Figs. 1 and 2, we show the density dependence of the incompressibility, K, and the symmetry energy coefficient, C_{sym}, respectively, for different temperatures T for three sets of Skyrme forces, SkM[*], KDE0v1 and Sly230b.

As seen from Fig.1, the instability regime where $K < 0$ is shifted to higher values of the ratio $\rho_0/\rho_{\text{eq}}(T)$ with increasing temperature T. The stable mode disappears at the critical temperature $T_{\text{crit}} = 14 \div 15$ MeV, where $K = 0$ at $\rho_0/\rho_{\text{eq}}(T) = 1$, see Table I.
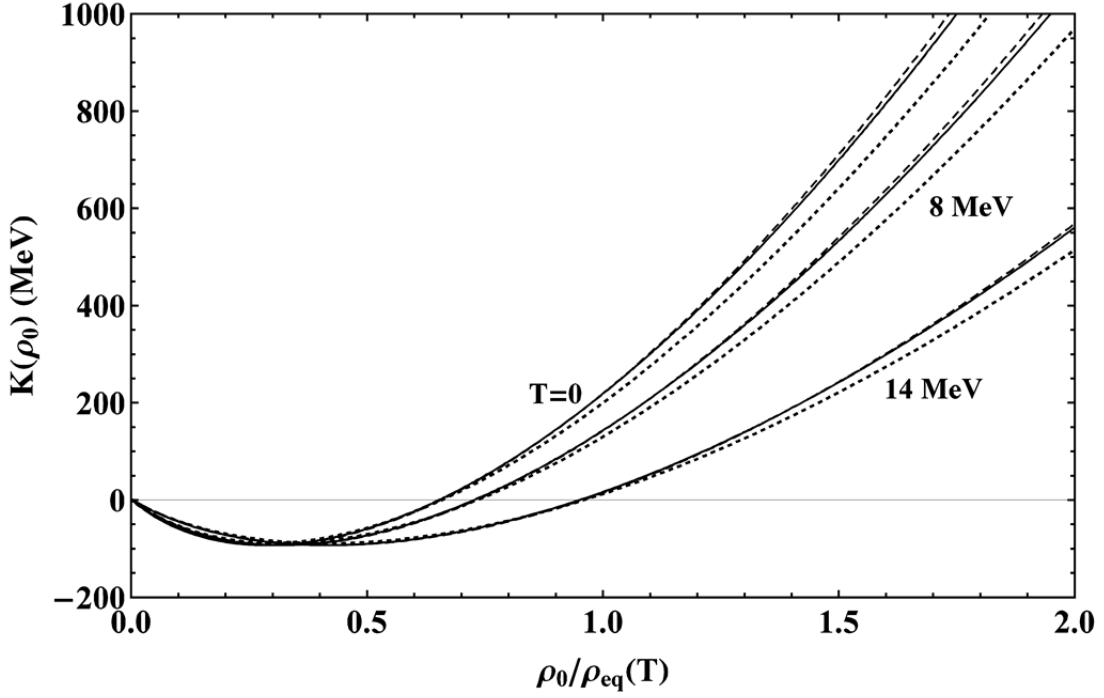
FIG. 1. The density dependence of the incompressibility coefficient $K(\rho_0)$ for different temperatures $T = 0$, **8** and **14** MeV (shown) calculated for Skyrme interactions SkM* (dotted lines), KDE0v1 (solid lines) and SLy230b (dashed lines).

Table 1. Values of the Skyrme parameters and the corresponding physical quantities of nuclear matter for the SkM*, KDE0v1 and Sly230b interactions.

Parameters	SkM^*	$KDE0v1$	$Sly230b$
$t_0 \ (MeV \cdot fm^3)$	-2645.00	-2553.0843	-2488.91
$t_1 \ (MeV \cdot fm^5)$	410.00	411.6963	486.82
$t_2 \ (MeV \cdot fm^5)$	-135.00	-419.8712	-546.39
$t_3 \ (MeV \cdot fm^{3(1+\nu)})$	15595.00	14603.6069	13777.0
x_0	0.0900	0.6483	0.8340
x_1	0.0000	-0.3472	-0.3438
x_2	0.0000	-0.9268	-1.0
x_3	0.0000	0.9475	1.3539
$W_0 \ (MeV \cdot fm^5)$	130.00	124.4100	122.69
ν	0.16667	0.1673	0.166667
E/A	15.78	16.23	15.972
$K \ (MeV)$	216.7	227.54	229.90
$\rho_{eq}(fm^{-3})$	0.160	0.165	0.160
m^*/m	0.79	0.74	0.695
$C_{sym}(MeV)$	30.03	34.58	32.01
$L(MeV)$	45.78	54.69	45.97
κ	0.53	0.23	0.25
$T_{crit}(MeV)$	14.62	14.74	14.67

Fig. 2 shows that the dependence of symmetry energy coefficient, $C_{sym}(\rho_0)$, on the particle density ρ_0 is strongly sensitive to the choice of the Skyrme interactions. In contrast to the behavior of the incompressibility coefficient $K(\rho_0)$ in Fig. 1, the ρ-dependence of the symmetry energy coefficient $C_{sym}(\rho_0)$ is completely different for the SkM* than for KDE0v1 and the Sly230b interactions. In the case of SkM* interaction, the symmetry energy coefficient $C_{sym}(\rho_0)$ is a non-monotonic function of the density and it becomes negative in a superdense nuclear matter. In this case, the symmetry energy coefficient $C_{sym}(T)$ and thereby the isospin stability of Fermi liquid decreases with temperature for the dilute regime at $\rho_0/\rho_{eq}(T) \lesssim 1$. This behavior is reversed for the super dense regime at $\rho_0/\rho_{eq}(T) \gtrsim 2$. For the KDE0v1 and Sly230b interactions, the symmetry energy coefficient $C_{sym}(\rho_0)$ is an increasing function of particle density and the nuclear matter does not reach the instability regime. Thus, the density dependence of the symmetry energy coefficient $C_{sym}(\rho_0)$ and the occurrence of the isospin instability are sensitive to the Skyrme interaction parametrization.
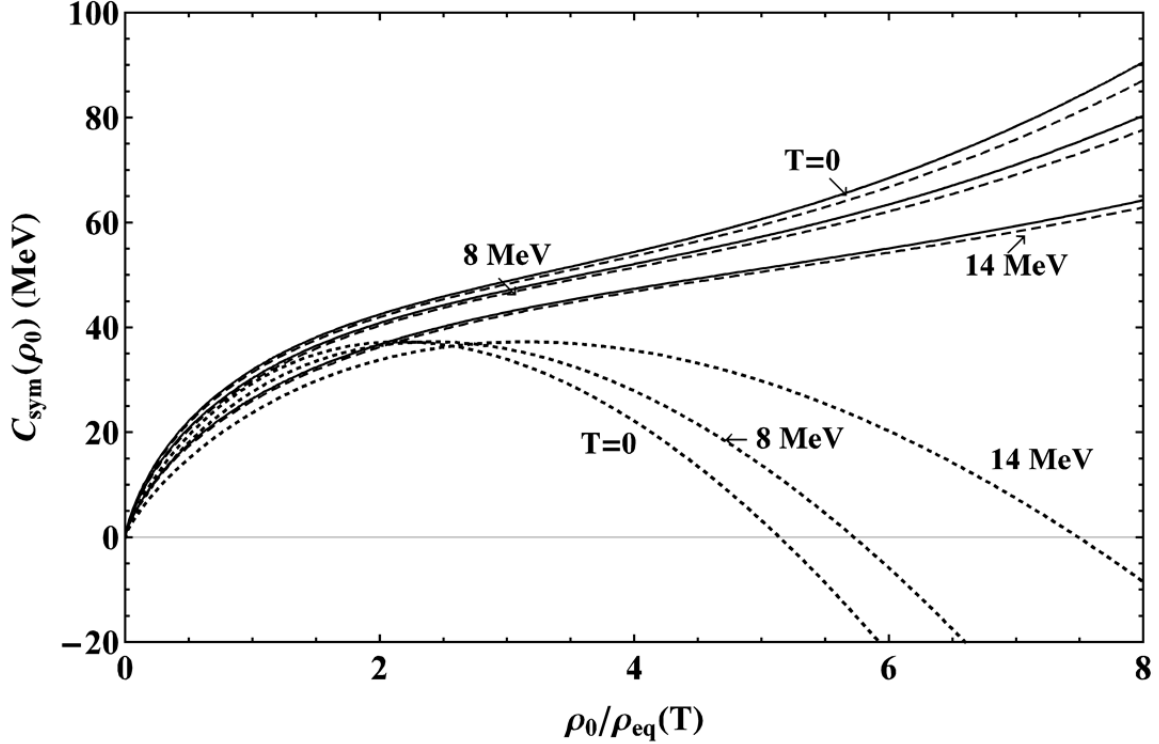
FIG. 2. The same as in Fig. 1, but for symmetry energy coefficient C_{sym}.

[1] V.M. Kolomietz and S. Shlomo, Phys. Rev. C **95**, 054614 (2017).

Chiral kinetic approach to chiral magnetic effect in isobaric collisions

Y. Sun and C.M. Ko

Based on the chiral kinetic approach using quarks and antiquarks from a multiphase transport model [1] as initial conditions, we have studied the chiral magnetic effect, i.e., the magnetic field induced separation of charged particles in the transverse plane, in non-central isobaric collisions of Zr+Zr and Ru+Ru, which have the same atomic number but different proton numbers [2]. For the observable $\gamma^{OS} - \gamma^{SS}$ related to the difference between the correlations of particles of opposite charges and of same charges, we find a difference between the two collision systems if the magnetic field has a long lifetime of 0.6 fm/c and the observable is evaluated using the initial reaction plane. This signal of the chiral magnetic effect becomes smaller and comparable to the background contributions from elliptic flow if the event plane determined from particle emission angles is used. For the other observable given by the $R(\Delta S)$ correlator related to the distribution of average charge separation in a collision, it depends less on whether the reaction or event plane is used in the analysis, making it a plausible observable for identifying the chiral magnetic effect from its difference in the two isobaric collision systems.
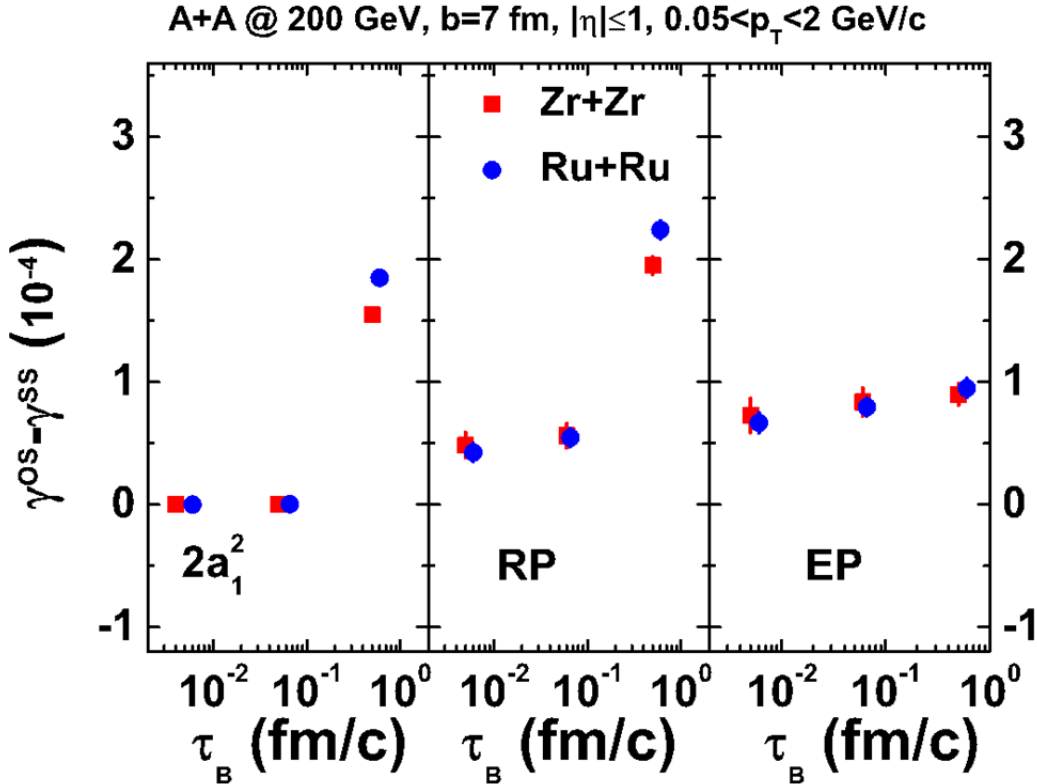
FIG. 1. Magnetic field lifetime dependence of the $\gamma^{OS} - \gamma^{SS}$ correlator of mid-pseudorapidity ($|\eta| \leq 1$) light quarks in Ru+Ru and Zr+Zr collisions at $\sqrt{s_{NN}} = 200$ GeV and impact parameter b = 7 fm for transverse momenta in the range $0.05 \leq p_T \leq 2$ GeV/c and using different calculation methods. The error bars denote the statistical errors due to the finite number of events used in the study.
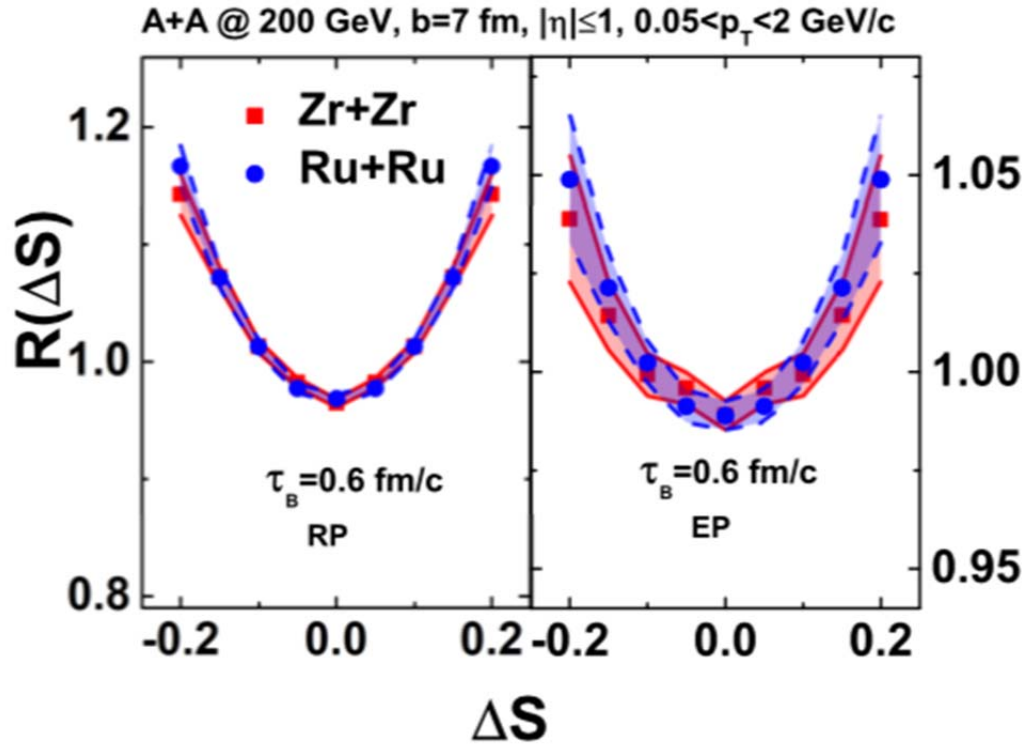
FIG. 2. Same as Fig. 1 for **ΔS** dependence of the **R(ΔS)** correlator.

[1] Z.-W. Lin, C.M. Ko, B.-A. Li, B. Zhang, and S. Pal, Phys. Rev. C **72**, 064901 (2005).
[2] Y. Sun and C.M. Ko, arXiv:1803.06043 [nucl-th].

Effects of energy conservation on equilibrium properties of hot asymmetric nuclear matter

Z. Zhang and C.M. Ko

We have employed the relativistic Vlasov-Uheling-Uhlenbeck (RVUU) transport model [1] to study a thermalized nucleon-Delta-pion system in a box with periodic boundary conditions [2]. We have found that with the inclusion of both baryon scalar and vector potentials in the energy conservation condition for particle production or absorption in scattering and decay processes, our results can well reproduce the equilibrium numbers of particles obtained in thermal model calculations, shown by open circles in Fig. 1, which verifies the reliability of the RVUU model. Omitting the vector potentials of baryons in the energy conservation conditions for scattering and decay processes reduces slightly the number of pion-like particles by about 3.3%, but significantly the effective charged pion ratio by about 26.7%. Neglecting also the scalar potential further reduces the pion-like particle number by a factor of about 2 and increases the effective charged pion ratio by about 9%. Our results thus indicate that the correct treatment of the energy conservation condition in scattering and decay processes in transport
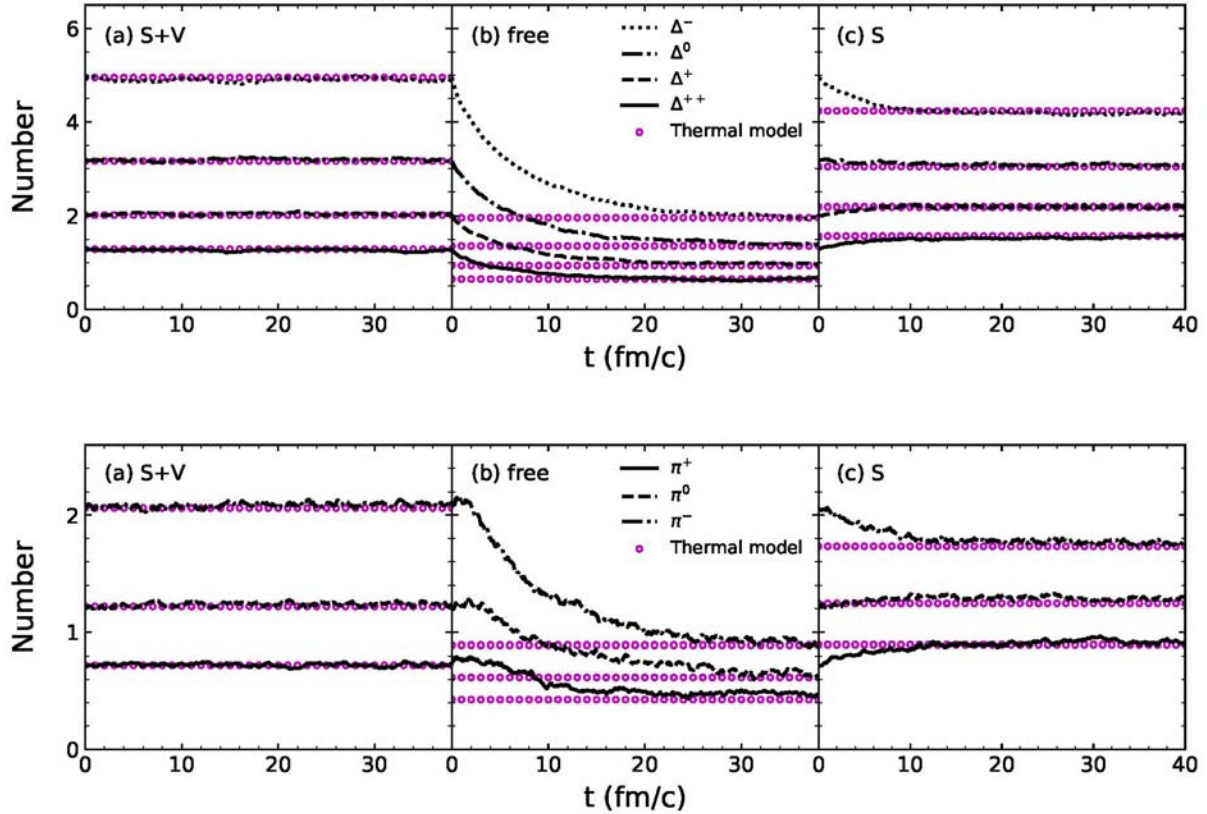
FIG. 1. Time evolutions of Delta (upper window) and pion (lower window) numbers in a box with periodic boundary conditions for the three cases of mean-field potentials. For comparison, the thermal model results are shown as open circles.

models, which have not been included in most transport models, is very important for studying pion production in heavy ion collisions at intermediate energies, particularly for extracting the nuclear symmetry energy at high density from the ratio of charged pions [3].

[1] C.M. Ko, Q. Li, and R. Wang, Phys. Rev. Lett. **59**, 1084 (1987); C.M. Ko and Q. Li, Phys. Rev. C **37**, 2270 (1988); C.M. Ko and G. Q. Li, J. Phys. G **22**, 1673 (1996).

[2] Z. Zhang and C.M. Ko, Phys. Rev. C **97**, 014610 (2018).

[3] Z. Zhang and C.M. Ko, Phys. Rev. C **95**, 064604 (2017).

Hypertriton production in relativistic heavy ion collisions

Z. Zhang and C.M. Ko

Using the coalescence model based on the phase-space distributions of kinetically freeze-out nucleons and Lambda hyperons from a blast-wave model, we have studied [1] in a coalescence model the production of hypertriton, which has a very small binding energy of about 130 keV [2] and large root-mean-square radius of about 4.9 fm [3], in relativistic heavy ion collisions. Including not only the coalescence process $p + n + \Lambda \rightarrow {}^3_\Lambda H$ but also the coalescence process $d + \Lambda \rightarrow {}^3_\Lambda H$ as the hypertriton can be considered as a loosely bound state of deuteron and Lambda, we have studied the dependence of the hypertriton yield on its freeze-out time by letting nucleons, Lambda hyperons, and deuterons to stream freely after they have frozen out from the initial fireball, and then carrying out the coalescence calculations for different free streaming times. We have found that the hypertriton yield, which reproduces the experimental data from central Pb+Pb collisions at $\sqrt{s_{NN}}$ = 2.76 TeV at the LHC with the two coalescence processes giving similar contributions, decreases slowly with the free expansion of the fireball as shown in Fig. 1, especially for those produced from the $d + \Lambda$ coalescence. Our result thus indicates that the yield of hypertritons in relativistic heavy ion collisions is essentially determined when nucleons and Lambda hyperons freeze out kinetically, although they still undergo scattering with the freeze-out pions.
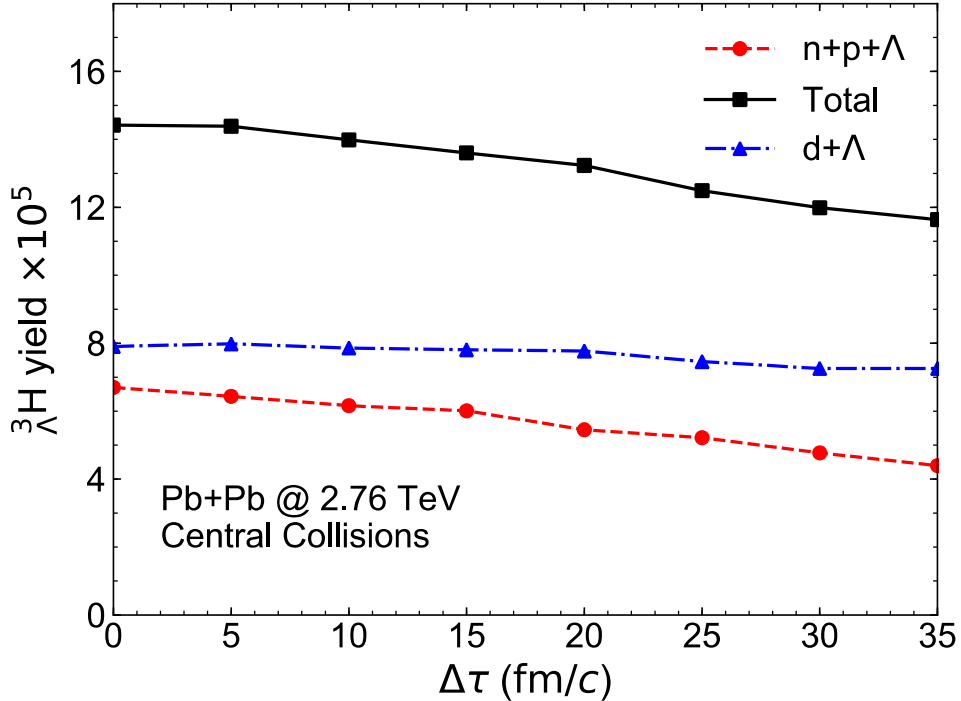
FIG. 1. Hypertriton yields from $n + p + \Lambda$ and $d + \Lambda$ coalescence together with the total yield as functions of the free streaming time $\Delta\tau$.

[1] Z. Zhang and C.M. Ko, Phys. Lett. B **780**, 191 (2018).

[2] M. Juric, G. Bohm, J. Klabuhn, U. Krecker, F. Wysotzki, G. Coremans-Bertrand, J. Sacton, G. Wilquet, T. Cantwell, F. Esmael *et al.*, Nucl. Phys. **B52**, 1 (1973).

[3] H. Nemura, Y. Suzuki, Y. Fujiwara, and C. Nakamoto, Prog. Theor. Phys. **103**, 929 (2000).

Lambda hyperon polarization in relativistic heavy ion collisions from a chiral kinetic approach

Y. Sun and C.M. Ko

Based on the chiral kinetic approach, which includes the propagation of massless quarks with definite helicity and their modified scattering in magnetic and vorticity fields [1,2], we have studied the spin polarizations of quarks and antiquarks in non-central heavy ion collisions at the Relativistic Heavy Ion Collider [3]. Using initial conditions from a multiphase transport model [4] and with the vorticity field calculated self-consistently from the velocity field of quarks and antiquarks in these collisions, we have found that quarks and antiquarks acquire appreciable spin polarizations in the direction perpendicular to the reaction plane of the collisions. Converting quarks and antiquarks to hadrons via the coalescence model, we have further calculated the spin polarizations of Lambda and anti-Lambda hyperons and found their values comparable to those measured in experiments by the STAR Collaboration [5] as shown in Fig. 1.
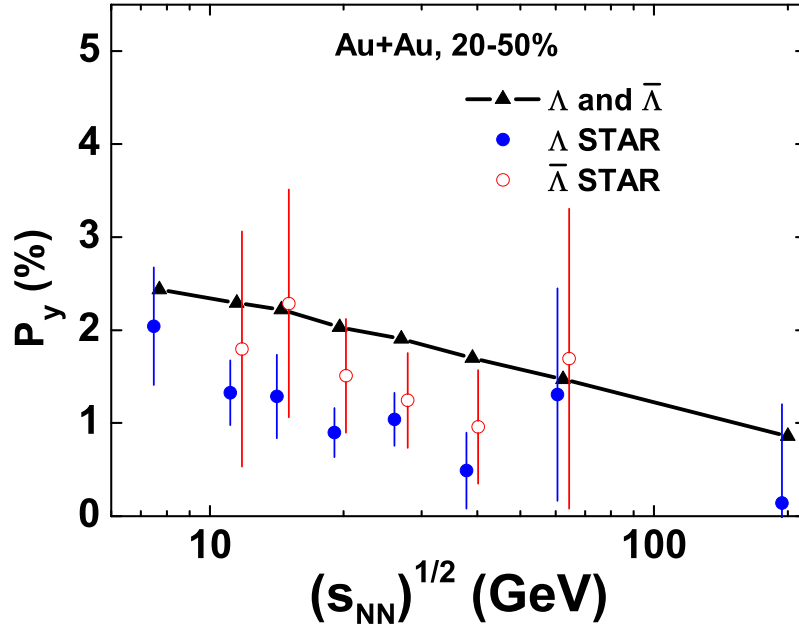
FIG. 1. Energy dependence of the spin polarization of midrapidity ($|y| \leq 1$) lambda and antilambda hyperons in Au+Au collisions at energies from 7.7 GeV to 200 GeV. Data with error bars are from the STAR Collaboration [5].

[1] Y. Sun, C.M. Ko, and F. Li, Phys. Rev. C **94**, 045204 (2016).

[2] Y. Sun and C.M. Ko, Phys. Rev. C **95**, 034909 (2017).

[3] Y. Sun and C.M. Ko, Phys. Rev. C **96**, 024906 (2017).

[4] Z.-W. Lin, C.M. Ko, B.-A. Li, B. Zhang, and S. Pal, Phys. Rev. C **72**, 064901 (2005).

[5] L. Adamczyk *et al.* [STAR Collaboration] (2017), arXiv:1701.06657 [nucl-ex].

Light nuclei production in Pb+Pb collisions at $\sqrt{s_{NN}}$ = 2.76 TeV

L. L. Zhu,[1] H. Zheng,[2] C.M. Ko, and Y. Sun

[1]*Department of Physics, Sichuan University, Chengdu 610064, China*
[2]*Laboratori Nazionali del Sud, INFN, via Santa Sofia, 62, 95123 Catania, Italy*

Based on an extended blast-wave model, which includes a space-momentum correlation in the phase-space distribution of high momentum nucleons and has its parameters fitted to the measured proton transverse momentum spectrum [1] and elliptic flow [2] from Pb+Pb collisions at $\sqrt{s}$=2.76 TeV for the two centralities of 10-20% and 30-40%, we have used the coalescence model to calculate the transverse momentum spectra and elliptic flows of deuteron and helium-3 [3]. As shown in Fig. 1, our results for deuterons agree with the experimental data from the ALICE Collaboration [4,5]. Although the deuteron elliptic flow obtained from the blast-wave model by using the deuteron mass is roughly consistent with
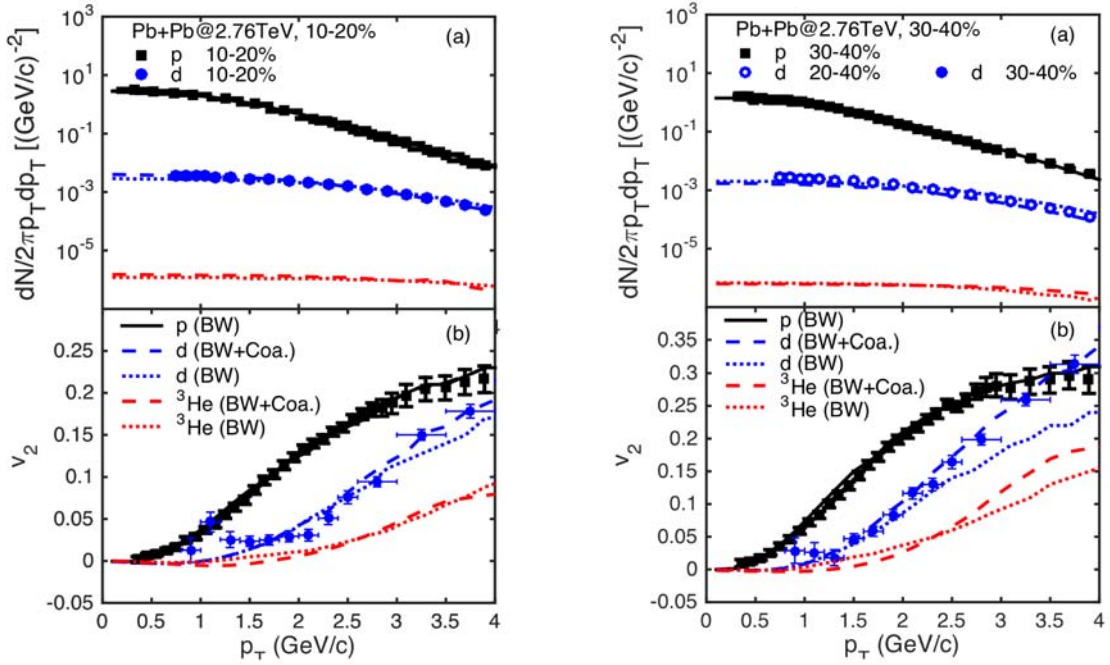
FIG. 1. Transverse momentum spectra and elliptic flows of midrapidity proton (p), deuteron (d) and helium-3 (^{3}He) from the blast-wave model (BW) and the coalescence model (BW+Coa.) for Pb+Pb collisions at $\sqrt{s_{NN}}$ = 2.76 TeV and centrality of 10-20% (left window) and 30-40% (right window). Data shown by black solid squares and blue solid circles for proton and deuteron, respectively, are taken from Ref. [1] and Ref. [4] for their respective transverse momentum spectra, and from Ref. [2] and Ref. [5] for their respective elliptic flows.

the data within their systematic errors for the centrality of 10-20%, it fails to describe the data at large transverse momentum for collisions at the centrality of 30-40%. A similar difference is found between the helium-3 elliptic flows at large transverse momentum obtained from the coalescence model and the

blast-wave model using the helium-3 mass. These results are similar to those shown previously for the elliptic flows of deuteron and helium-3 in Au+Au collisions at RHIC [6]. Our studies thus demonstrate that light nuclei production can provide the possibility to probe the properties of the emission source of nucleons in relativistic heavy ion collisions, complimenting the study based on the Hanbury-Brown-Twiss (HBT) interferometry of identical particles emitted at freeze-out [7,8] as originally pointed out in Refs. [9,10].

[1] J. Adam *et al.* [ALICE Collaboration], Phys. Rev. C **93**, 034913 (2016).
[2] B.B. Abelev *et al.* [ALICE Collaboration], JHEP **06**, 190 (2015).
[3] L.L. Zhu, H. Zheng, C.M. Ko, and Y. Sun, arXiv:1710.05319 [nucl-th].
[4] J. Adam *et al.* [ALICE Collaboration], Phys. Rev. C **93**, 024917 (2016).
[5] S. Acharya *et al.* [ALICE Collaboration] (2017), arXiv:1707.07304 [nucl- ex].
[6] X. Yin, C.M. Ko, Y. Sun, and L. Zhu, Phys. Rev. C **95**, 054913 (2017).
[7] G. Bertsch, M. Gong, and M. Tohyama, Phys. Rev. C **37**, 1896 (1988).
[8] S. Pratt, T. Csorgo, and J. Zimanyi, Phys. Rev. C **42**, 2646 (1990).
[9] S. Mrowczynski, Phys. Lett. B **277**, 43 (1992).
[10] R. Scheibl and U. W. Heinz, Phys. Rev. C **59**, 1585 (1999).

Probing QCD critical fluctuation from light nuclei production

K.J. Sun,[1] L.W. Chen,[1] C.M. Ko, and Z. Xu[2,3]

[1]*School of Physics and Astronomy and Shanghai Key Laboratory for Particle Physics and Cosmology,*
Shanghai Jiao Tong University, Shanghai 200240, China
[2]*Brookhaven National Laboratory, Upton, NY 11973, USA*
[3]*School of Physics & Key Laboratory of Particle Physics and Particle Irradiation (MOE), Shandong*
University, Jinan, Shandong 250100, China

Based on the coalescence model for light nuclei production, we have found that the yield ratio $O_{p-d-t} = N_t N_d^2 / N_p$ of p, d, and ^{3}H (t) in heavy-ion collisions is sensitive to the neutron relative density fluctuation $\Delta n = \langle (\delta n)^2 \rangle / \langle n \rangle^2$ at kinetic freeze-out [1]. From recent experimental data in central Pb+Pb collisions at $\sqrt{s_{NN}}$ = 6.3 GeV, 7.6 GeV, 8.8 GeV, 12.3 GeV and 17.3 GeV measured by the NA49 Collaboration at the CERN Super Proton Synchrotron (SPS) [2], we find a possible non-monotonic behavior of Δn as a function of the collision energy with a peak at $\sqrt{s_{NN}}$ = 8.8 GeV, as shown in Fig. 1 for various values of the correlation α between the neutron and proton density fluctuations defined by
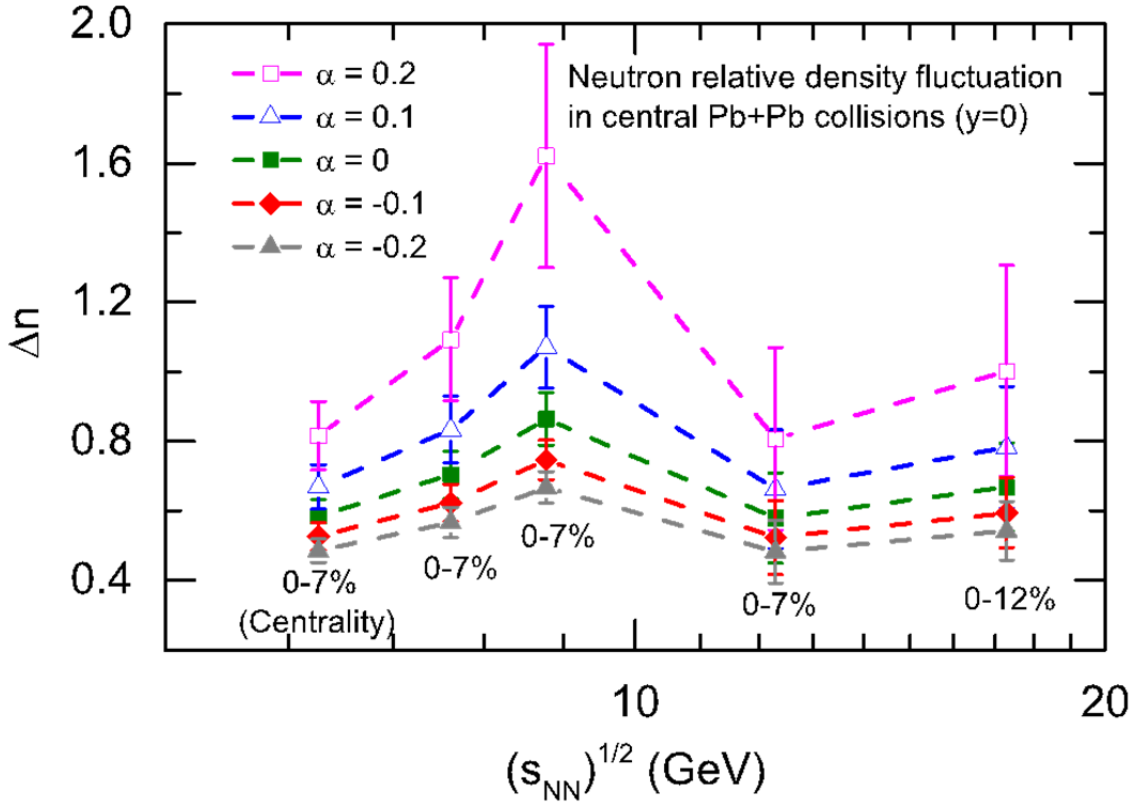
FIG. 1. Collision energy dependence of the neutron relative density fluctuation $\boldsymbol{\Delta n}$ in central Pb+Pb collisions at SPS energies based on data from Ref. [2]. Results for $\boldsymbol{\alpha}$ =-0.2, -0.1, 0, 0.1 and 0.2 are shown by various dotted lines.

$\langle \delta n \delta n_p \rangle = \alpha \frac{\langle n_p \rangle}{\langle n \rangle} \langle (\delta n)^2 \rangle$, indicating that the density fluctuations become the largest in collisions at this energy. With the known chemical freeze-out conditions determined from the statistical model fit to experimental data [3], we obtain a chemical freeze-out temperature of about 144 MeV and baryon chemical potential of about 385 MeV at this collision energy, which are close to the critical endpoint in the QCD phase diagram predicted by various theoretical studies. Our results thus suggest the potential usefulness of the yield ratio of light nuclei in relativistic heavy-ion collisions as a direct probe of the large density fluctuations associated with the QCD critical phenomena.

[1] K J. Sun, L.W. Chen, C.M. Ko, and Z. Xu, Phys. Lett. B **774**, 103 (2017).
[2] T. Anticic *et al.* [NA49 Collaboration], Phys. Rev. C **94**, 044906 (2016).
[3] J. Cleymans, H. Oeschler, K. Redlich, and S. Wheaton, Phys. Rev. C **73**, 034905 (2006).

The JETSCAPE collaboration: v1.0 Release

R.J. Fries and JETSCAPE Collaborators

In the last reporting period the JETSCAPE collaboration reached its first milestone with the release of v1.0 of their software package [1], see Fig. 1. JETSCAPE stands for *Jet Energy-loss Tomography with a Statistically and Computationally Advanced Program Envelope*. It is a collaboration funded with $3.6M through the *Software Infrastructure for Sustained Innovation* (SI2) program of the U.S. National Science Foundation. It involves theoretical and experimental physicists, computer scientists, and statisticians. R. J. Fries has been a PI on the proposal and is representing Texas A&M University in this multi-institutional effort.

The primary goal of the JETSCAPE Collaboration is to design and deploy an overarching software framework that can be used by the entire community of heavy-ion theorists and experimentalists to program, simulate and study complete collision events that can reproduce every aspect of high-energy heavy-ion collisions. The first version of the framework code already covers a lot of ground. It contains code for initial state generation in the soft (TRENTO) and hard sector (PYTHIA). It can run viscous fluid dynamic simulations including freeze-out (MUSIC) for the soft particle sector. It includes four different final state shower Monte Carlo codes for jets: MATTER, MARTINI, LBT and HYBRID [2]. The default hadronization is PYTHIA string fragmentation. The JETSCAPE framework manages the codes and contains a sophisticated scheduler to call and hand over data between modules.

One of the new physics aspects, not possible with single existing generators, is that jet shower Monte Carlo codes can be called in their intended region of applicability and partons can be handed over smoothly between them depending on their energy, virtuality and ambient medium temperature. For example, high virtuality partons are by default handled by MATTER, while low virtuality, high energy partons can be propagated by both LBT and MARTINI. HYBRID is the default choice for low virtuality, low energy partons. This new parton-by-parton interleaving of energy loss mechanisms has first been described by the JETSCAPE collaboration in the previous reporting period [3].

Improvements are on the way for updates to be released soon. This includes hybrid hadronization to replace pure string hadronization with the goal to achieve a realistic description of in-medium hadronization effects, hadronic transport for the final state, event-by-event color glass initial state Monte Carlo, jet feedback on the medium including concurrent running of jet Monte Carlos and fluid dynamics, GPU acceleration, and statistical tools for data analysis.

At the same time efforts are on the way by the collaboration to benchmark the JETSCAPE 1.0 framework. Of particular importance are baseline results for p+p collisions, which have been coordinated at Texas A&M. JETSCAPE 1.0 does very well describing jet cross sections, large momentum hadron spectra, jet shapes and jet fragmentation functions in p+p collisions.

```
[Info] *------------------------------------------------------------------*
[Info] |                                                                  |
[Info] |                      /\                                          |
[Info] |                     /  \                                        |
[Info] |                    / |  \                                       |
[Info] |                   / |   \           /\                          |
[Info] |                  /  |    \        /\/  \                        |
[Info] |                 / \ | /   \     /\/   |  \/\                    |
[Info] |                /   \|/     \   /    %  | %  \                   |
[Info] |              __/     \|/     \__/      %|%      \/\__           |
[Info] |                                                                  |
[Info] |                    JETSCAPE release 1.0 RC1                      |
[Info] |                                                                  |
[Info] |       The Jet Energy-loss Tomography with a Statistically        |
[Info] |         and Computationally Advanced Program Envelope            |
[Info] |                   http://jetscape.wayne.edu                      |
[Info] |                                                                  |
[Info] | Please cite xxx if you use this package for scientific work.     |
[Info] |                                                                  |
[Info] | JETSCAPE is provided without warranty under the terms            |
[Info] | of the GNU GPLv3. It uses xxx code(s).                           |
[Info] | See COPYING file for details.                                    |
[Info] |                                                                  |
[Info] *------------------------------------------------------------------*
```

FIG. 1. The first release of the JETSCAPE code is now available on GITHUB.

[1] https://github.com/JETSCAPE

[2] J. Putschke *et al.* [JETSCAPE Collaboration], *The JETSCAPE User Manual*, to be published.

[3] S. Cao *et al.* [JETSCAPE Collaboration], Phys. Rev. C **96**, 024909 (2017).

The specific shear viscosity of a hot hadron gas

R.J. Fries and Zhidong Yang

More than a decade ago data from experiments at the Relativistic Heavy Ion Collider (RHIC) first seemed to indicate that quark gluon plasma (QGP) at temperatures close to the crossover to a hadron gas behaves like a strongly coupled liquid with a specific shear viscosity η/s close to the conjectured lower quantum bound of $1/4\pi$ [1]. In the years since, rapid developments in viscous relativistic fluid dynamics have helped us quantify η/s in QGP close to the crossover temperature. However, modern estimates rely on hadronic transport models to describe the hadronic phase of nuclear collisions. This leads to a puzzle. Calculations of η/s from various hadronic transport models offer to a wide range of differing predictions. Some popular transport models predict η/s to be almost 10 times the value extracted for QGP around the crossover temperature. No sharp features in η/s as a function of temperature are expected at the crossover.

To improve this situation we attempt an extraction of the hadronic specific shear viscosity directly from data. We use the fact that shear viscosity is not only changing the time evolution of the nuclear collision, but that the presence of shear stress distorts thermal particle distributions away from their equilibrium form, $f \rightarrow f + \delta f$. This can be detected in final freeze-out spectra. The shear stress itself can be expressed through derivatives of the flow field and the specific shear viscosity in the Navier Stokes approximation [2,3].

To this end we have developed a blastwave model including viscous corrections in the Navier Stokes approximation. The blastwave parameterizes the final flow field of the expanding hadron gas. The temperature at freeze out as well as the flow field and η/s appear as fit parameters [2,3]. We have used a Bayesian analysis method to extract the freeze out parameters for various centralities in Au+Au collisions
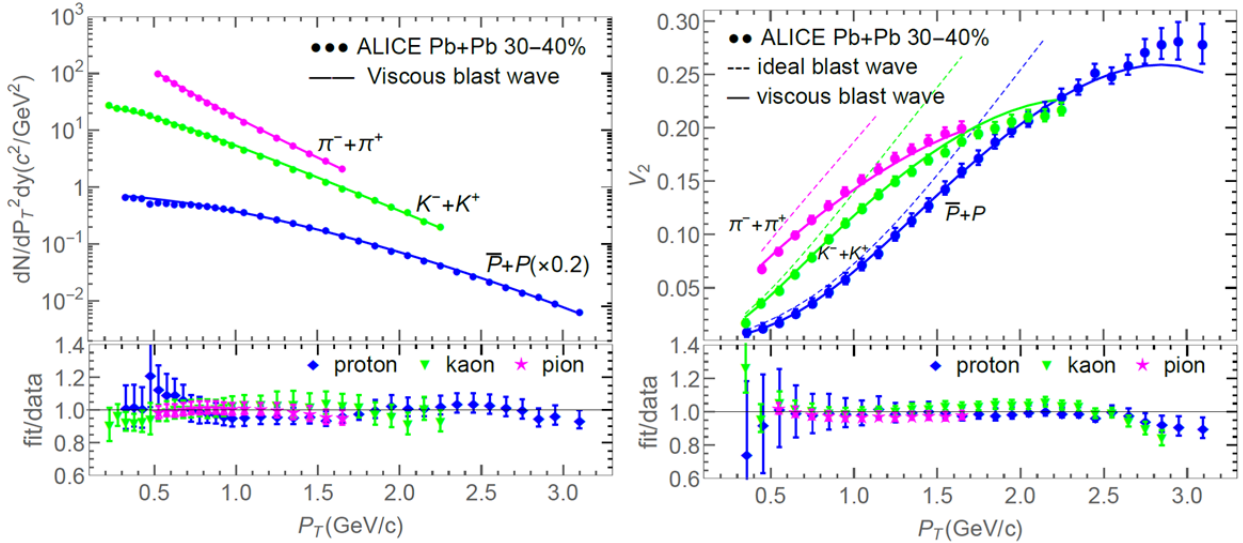
FIG. 1. Results from our blastwave fit for 30-40% centrality data from ALICE [4]. Left: Spectra of pions, kaons and protons. Right: Elliptic flow for the same particles. The ratios of fits over data is shown at the bottom of each plot.

at RHIC and Pb+Pb collisions at the Large Hadron Collider (LHC). We have utilized transverse momentum spectra and elliptic flow data of pions, kaons and protons in our analysis, see Fig. 1 for an example. We also conduct a careful analysis of systematic uncertainties in our extraction of η/s.

We find that the specific shear viscosity drops rather rapidly between 110 and 140 MeV, reaching values close to the quantum bound at the upper temperature reach of our analysis, see Fig. 2. Values extracted from RHIC and LHC are consistent with each other. Note that with changing temperature there is a change in chemical potentials of stable hadrons which needs to be accounted for when interpreting our result.
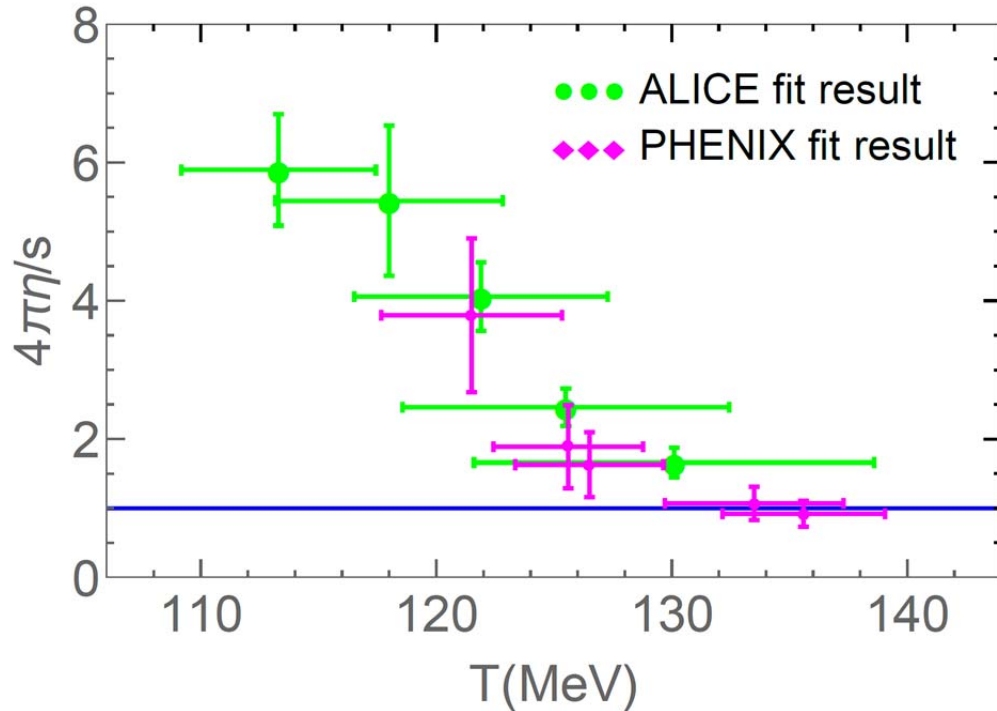
FIG. 2. The specific shear viscosity **η/s** for various temperatures in the hadronic phase extracted from freeze-out data.

[1] E. Shuryak, Prog. Part. Nucl. Phys. **62**, 48 (2009).

[2] Z. Yang and R.J. Fries, (to be published).

[3] Z. Yang and R.J. Fries, J. Phys. Conf. Ser. **832**, 012056 (2017).

[4] B. Abelev *et al.* [ALICE Collaboration], Phys. Rev. C **93**, 034913 (2016).

[5] B. Abelev *et al.* [ALICE Collaboration] JHEP **06**, 190 (2015).

Extraction of heavy-flavor transport coefficients in QCD matter

R. Rapp, P.B. Gossiaux, A. Andronic, R. Averbeck, S. Mascicocchi (editors), and 26 co-authors

The heavy charm and bottom quarks are excellent probes of the transport properties of the quark-gluon plasma (QGP) as produced in ultra-relativistic heavy-ion collisions (URHICs). Due to their large masses heavy quarks undergo a Brownian motion whose associated transport coefficients characterize the coupling strength to the QGP. Furthermore, an incomplete thermalization implies that the modifications of the heavy-quark (HQ) spectra in URHICs (relative to pp collisions) retain a memory of the interaction history which can serve as a direct gauge of the interaction strength. However, a quantitative extraction of the transport coefficients from the finally observed spectra of D- and B-mesons requires good control over several other components that affect these spectra. These include initial-state cold-nuclear-matter modifications of the HQ spectra, the mechanisms leading to the hadronization of the heavy quarks when the QGP converts into hadronic matter, the transport in the hadronic phase, and the modeling of the space-time evolution of the fireball through which the heavy-flavor particles diffuse.

To quantify the impact of these auxiliary components in the heavy-flavor transport models, an EMMI rapid reaction task force was formed where several of the active groups in the field participated [1]. To begin with, a predefined charm-quark transport coefficient (perturbative QCD Born scattering with K-factor 5, or "pQCD*5") has been used by all groups in their QGP evolution and hadronization models for semi-/central Pb-Pb(2.76TeV) collisions. Up to two outliers, a promising agreement between the results of the different groups emerged at the level of the charm-quark nuclear modification factor (R_{AA}) and elliptic flow (v_2). A larger relative uncertainty among the model results is found after applying the different hadronization models, which include various forms of recombination of the charm quark with thermal anti-quarks, as well as independent fragmentation. In attempt to arrive at a theoretical error estimate, an average of the model results for the D-meson R_{AA} and v_2 has been performed (excluding the 2 outliers) and compared to experimental data from the ALICE [2] and CMS [3] collaborations, see Fig. 1. The average suggests that the current theoretical modeling error amounts to about 20%, which is rather encouraging. The comparison also shows that especially the elliptic flow is much underestimated by the underlying pQCD*5 transport coefficient, implying that the corresponding diffusion coefficient of D_s $(2\pi T) \sim 6$ is clearly too large, i.e., a much stronger coupling of the charm quarks to the collectively expanding QGP is required.

Closer inspection of the employed recombination models for the hadronization of charm quarks into D mesons reveals that satisfying basic conservation laws (such as 4-momentum) and the correct thermal equilibrium limit [4] is critical for reliable results.

This project has laid the groundwork for future precision studies and extractions of heavy-flavor transport coefficients in QCD matter from heavy-ion collisions. Follow-up activities are underway and will take full advantage of open heavy-flavor data from the high-luminosity LHC run-3 and -4.
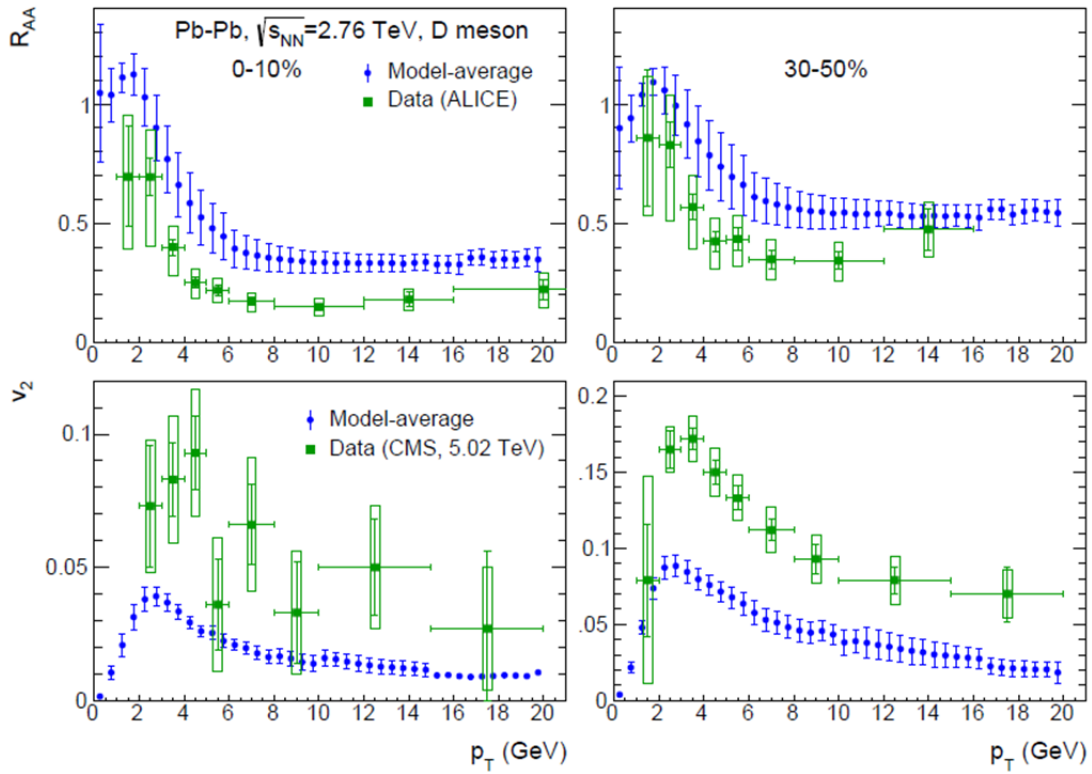
FIG. 1. Average nuclear modification factor (upper panels) and elliptic flow (lower panels) of D mesons in 2.76TeV Pb-Pb collisions for different fireball + hadronization models using a common c-quark transport coefficient in the QGP, compared to ALICE and CMS data.

[1] R. Rapp, P.B. Gossiaux, A. Andronic, R Averbeck, and S. Masciocchi (eds.) *et al.*, arXiv:1803.03824.

[2] J. Adam *et al.* [ALICE Collaboration], J. High Energy Phys. **03**, 081 (2016).

[3] A.M. Sirunyan *et al.* [CMS Collaboration], Phys. Rev. Lett. **120**, 202301 (2018).

[4] L. Ravagli and R. Rapp, Phys. Lett. B **655**, 126 (2007).

Charmonium production in proton-nucleus collisions at RHIC and the LHC

Xiaojian Du and Ralf Rapp

Large efforts in both experimental and theoretical research have been devoted to study hot and dense QCD matter via ultra-relativistic heavy-ion collisions (URHICs) over several decades. Heavy quarkonia can serve as promising probe of the in-medium heavy quark anti-quark force in these reactions [1]. Proton-nucleus (pA) collisions have become a rather hot topic in recent years, to study whether a quark-gluon plasma (QGP) can also form in rather small systems.

In this work, we investigate J/ψ and ψ(2S) production in pA collisions at LHC energies with an earlier constructed transport approach [2,3]. We have extended the fireball evolution model to account for small system sizes and elliptic expansion geometries appropriate for pA collisions using a Monte-Carlo based event generator based on initial-state fluctuations. Final-state interactions of charmonia are implemented in both QGP and hadronic phases. We calculate the nuclear modification factor (R_{pA}) as a function of both collision centrality (Fig. 1) and transverse momentum (Fig. 2). In the proton-going
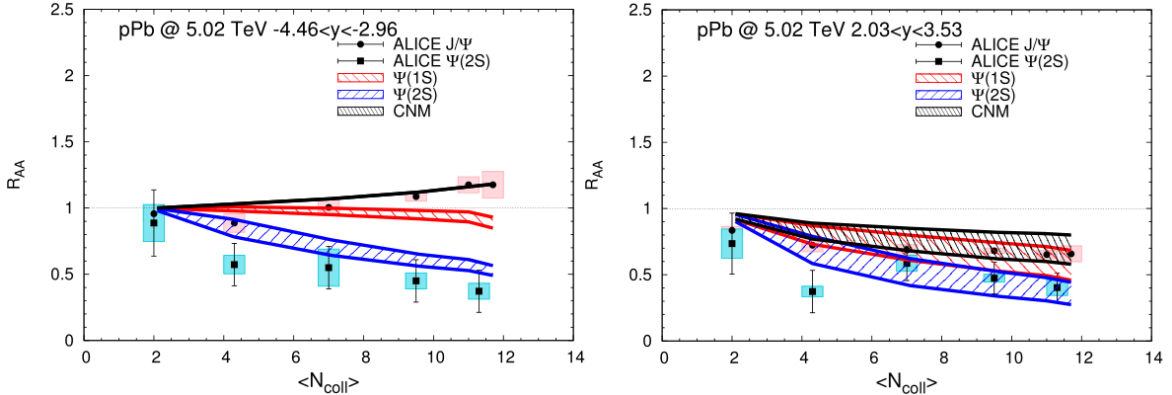
FIG. 1. Centrality dependent R_{pA} calculated for J/ψ (red bands) and ψ(2S) (blue bands) in 5.02 TeV p-Pb collisions at the LHC, compared to ALICE data [5] in the Pb-going direction (left panels) and p-going direction (right panel). Black lines indicate shadowing effects.

direction (positive rapidity), the suppression of J/ψ and ψ(2S) is similar, mostly caused by parton shadowing in the initial incoming nucleus [4]. On the other hand, in the nucleus-going direction (negative rapidity), where the charged-particle multiplicity is much higher, we find significantly stronger suppression for the excited state ψ(2S) than the ground state J/ψ, caused by its smaller binding energy which leads to stronger dissociation due to final-state interactions. The agreement with data [5,6,7] is fair.

We have also studied the elliptic flow (v_2) of the J/ψ due to its transport in the elliptic fireball, characterizing the azimuthal asymmetry in its momentum spectra. In pA collisions, an initial spatial asymmetry is due to fluctuations in the initial nucleon-nucleon collisions. The v_2 of the primordially produced the J/ψ's is mainly due the suppression from different path lengths through the elliptic fireball. The v_2 of J/ψ's regenerated from charm-quark recombination is due to the collective flow picked up from the medium, which is significantly larger. We find that the resulting v_2 of the J/ψ's is rather small since
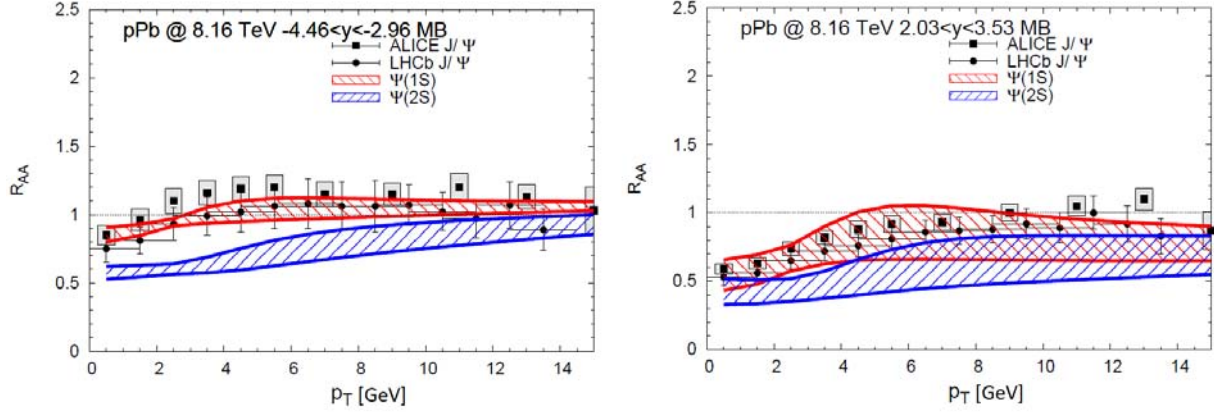
FIG. 2. Transverse-momentum dependent R_{pA} calculated for J/ψ (red bands) and ψ(2S) (blue bands) in 8.16 TeV p-Pb collisions at the LHC, compared to ALICE [6] and LHCb [7] data in the Pb-going direction (right panel) and p-going direction (left panel).

the contribution from primordial production dominates. This is quite different from the experimental data which show appreciable v_2 values, see Fig. 3 [8,9]. Our results therefore imply that the observed large v_2 for J/ψ's in pA collisions is not from final-state interactions, but might rather originate from anisotropies in initial transverse-momentum spectra or cold nuclear matter effects.
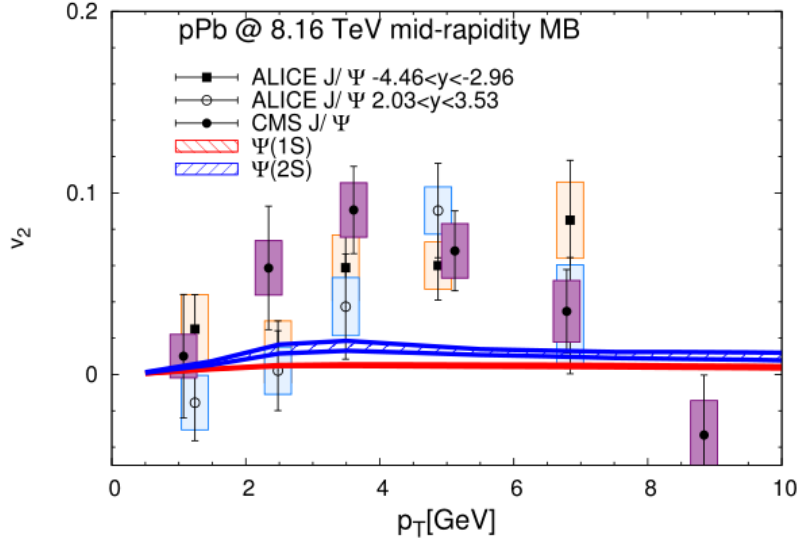
FIG. 3. Transverse-momentum dependent v_2 calculated for J/ψ (blue band) and ψ(2S)(red band) in 8.16 TeV p-Pb collisions at the LHC, compared to ALICE [8] and CMS data [9].

[1] T. Matsui and H. Satz, Phys. Lett. B **178**, 416 (1986).

[2] X. Zhao and R. Rapp, Phys. Rev. C **82**, 064905 (2010).

[3] X. Du and R. Rapp, Nucl. Phys. **A943**, 147 (2015); X. Du and R. Rapp, (in preparation).

[4] R. Vogt, Phys. Rev. C **81**, 044903 (2010).

[5] ALICE Collaboration, J. High Energy Phys. **11**, 127 (2015).

[6] LHCb Collaboration, Phys. Lett. B **774**, 159 (2017).

[7] ALICE Collaboration, arXiv: 1805.04381.

[8] ALICE Collaboration, Phys. Lett. B **780**, 7 (2018).

[9] CMS Collaboration, CMS-PAS-HIN-18-010.

Probing the microscopic properties of quark-gluon plasma by transport phenomena

Shuai Y.F. Liu and Ralf Rapp

Transport processes, such as the flowing of water, transfer of heat, or conduction of electric charge, are common phenomena in physics. On a microscopic level, they provide a window into the underlying many-body physics of the system. In the context of quark-gluon plasma (QGP) research using high-energy heavy-ion collisions, the bulk evolution of the matter can be described by hydrodynamics, while, within this background, the transport of heavy quarks can be described as a Brownian (diffusive) motion. The pertinent transport coefficients — shear viscosity for hydrodynamics and the drag/diffusion coefficients for the heavy-quark (HQ) diffusion — can be constrained by experiments and ultimately allow us to extract the microscopic information such as spectral properties and the underlying color force in the QGP. In particular, the transport properties can help us to distinguish between weakly coupled and strongly coupled scenarios of the QGP. Using a selfconsistent many-body approach, we found that both scenarios are consistent with lattice-QCD data on the equation of state and heavy- quarkonium correlators [1, 2], see Fig. 1. In this contribution, we analyze the shear viscosity and HQ transport coefficients in both scenarios.
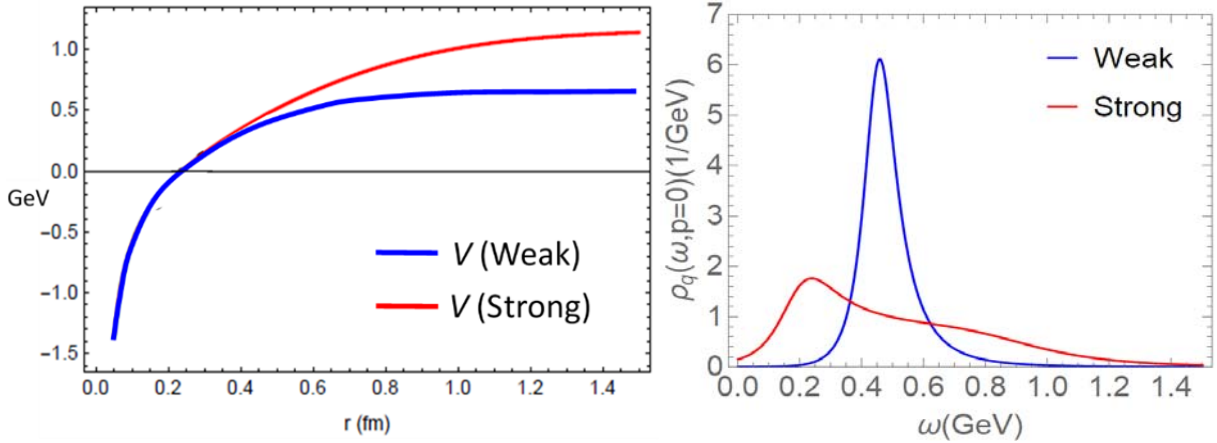
FIG. 1. Color singlet potentials (left panel) and pertinent spectral functions (ight panel) and for WCS and SCS at T=194MeV.

To evaluate the HQ friction coefficient, we extend previous T-matrix calculations [3] to include the off-shell effects as described in Refs. [1, 4], Schematically, one has

$$A(p) = \left\langle \left(1 - \frac{\mathbf{p} \cdot \mathbf{p}'}{p^2}\right) \rho_i \rho_i \rho_c \right\rangle$$

where $\rho_{i(c)}$ are spectral functions for light partons (charm quark) and $\mathbf{p}(\mathbf{p}')$ denotes the incoming (outgoing) charm-quark momentum. The spatial diffusion coefficient is defined as $D_s = T/(A(0)M)$. For the shear viscosity, η, a Kubo formula is employed at the (dressed) one-loop level [1]

$$\eta = \lim_{\omega \to 0} \sum_i \frac{\pi d_i}{\omega} \int \frac{d^3\mathbf{p}}{(2\pi)^3} \frac{p_x^2 p_y^2}{\varepsilon_i^2(p)} \rho_i(\omega + \lambda, p)\rho(\lambda, p)[n_i(\lambda) - n_i(\omega + \lambda)]$$

where d_i and $n_i(\omega)$ are the partons' degeneracies and thermal distribution functions, respectively. The results of the transport coefficients from a weakly-coupled scenario (WCS) and a strongly coupled scenario (SCS) found in Refs. [1, 2] are shown in Fig. 2. The dimensionless quantities $D_s(2\pi T)$ and $4\pi\eta/s$ characterize the interaction strength of the bulk medium (with smaller values indicating stronger
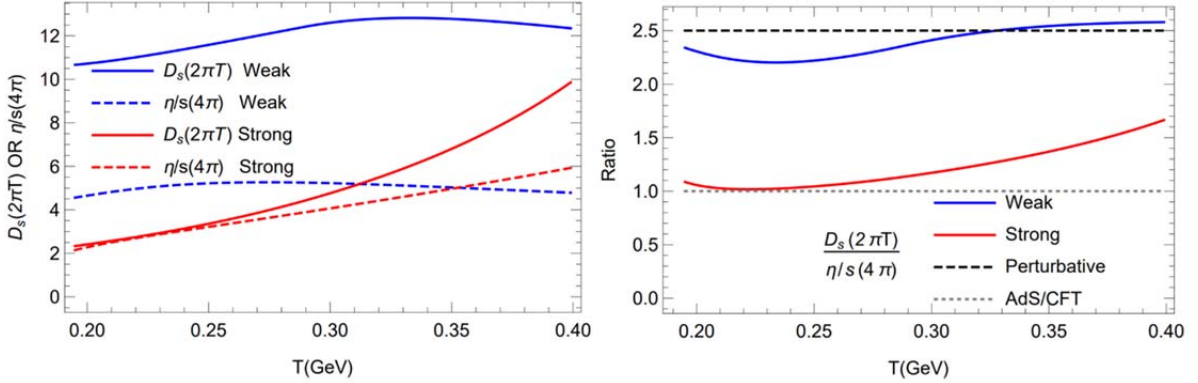
FIG. 2. Spatial diffusion coefficient, $2\pi TD_s$, and the ratio of shear viscosity to entropy density, $4\pi\eta/s$, for WCS (blue lines) and SCS (red lines) (left panel), and their ratio $[2\pi TD_s]/[4\pi\eta/s]$ (right panel).

coupling). For the SCS both transport coefficients are within a factor of two of the conjectured quantum lower bounds of one, and increase with temperature indicating a transition to a more weakly coupled medium. On the contrary, for the WCS both transport coefficients are significantly larger and rather constant with temperature. In an attempt to better quantify the notions of "strongly" and "weakly" coupled media, one can inspect the ratio for the two dimensionless transport coefficients discussed above. In particular, the ratio r $\equiv [2\pi TD_s]/[4\pi\eta/s]$ is expected to be near one in the strong-coupling limit, while perturbative estimates appropriate for a weakly coupled system result in ~5/2. We plot this ratio in the right panel of Fig. 2 for both the SCS and WCS. Interestingly, for the SCS the ratio is around one for low temperatures, slowly increasing with temperature but still significantly below 5/2 at T=400 MeV. On the contrary, for the WCS the ratio is close to 5/2 characteristic for a weakly coupled system even at low temperatures, with insignificant temperature dependence. Implementing the HQ transport coefficients into the Langevin simulation (Brownian motion) [4], we found the experimental results to strongly prefer the SCS.

In summary, within the thermodynamic T-matrix approach, we have calculated transport coefficients of the QGP — shear viscosity and diffusion coefficient — within weakly and strongly coupled scenarios, which turn out to be markedly different. Implementing them into transport simulations

to compare with experimental results, we conclude that the QGP must be strongly coupled and that its microscopic properties are characterized by a long-range color force with spectral functions that exhibit a transition from melting parton spectral functions to emerging hadronic bound states as the phase transition temperature is approached from above [1,2,4].

[1] S.Y.F. Liu and R. Rapp, arXiv:1612.09138
[2] S.Y.F. Liu and R. Rapp, Phys. Rev. C **97**, 034918 (2018).
[3] F. Riek and R. Rapp, Phys. Rev. C **82**, 035201 (2010).
[4] S.Y.F. Liu, M He, and R. Rapp, aXiv:1806.05669

SECTION IV

SUPERCONDUCTING CYCLOTRON, INSTRUMENTATION AND RIB UPGRADE

K500 operations and development

D.P. May, G.J. Kim, B.T. Roeder, H.L. Clark, and F.P. Abegglen

Introduction

During the 2017-2018 reporting period a total of 21 different beams, including 11 newly developed beams, were used for experiments, and there were a total of 24 beam tunings for these experiments. The SEE program and the radioactive-beam effort are treated separately in this progress report.

Ion Sources

During the shutdown ECR1 was opened for examination, and it was found that there had been no further deterioration in the damaged spot that had developed over a plasma flute on the aluminum wall. A new aluminum plasma chamber and NdFeB permanent magnet bars are ready for assembly into a new, more uniformly magnetized hexapole for eventual installation during the next reporting period.

Cyclotron Beams

New beams of ^{12}C at 11 AMeV, ^{28}Si at 36 AMeV, ^{35}Cl at 5.3 AMeV, ^{44}Ca at 5.2 AMeV, ^{58}Fe at 11 AMeV, ^{59}Co at 13 AMeV, ^{58}Ni at 36 AMeV, ^{63}Cu at 10 AMeV, ^{70}Zn at 15 AMeV, ^{84}Kr at 5.1 AMeV and ^{107}Ag at 11 AMeV were developed for experiments. The majority of experiments used the 2A line devoted to the recoil spectrometer MARS.

Operations

For the period April 1, 2017 through March 31, 2018, the operational time is summarized in Table I, while Table II lists how the scheduled time was divided. Unscheduled maintenance remained quite low. Scheduled time for outsider users, exclusively SEE customers increased again, as has been the case for several years.

Table I. 2017-2018 operational time.

Time	Hrs.	%Time
Beam on target	5920.5	67.8
Beam development	1076.0	12.3
Scheduled maintenance	1488.0	17.0
Unscheduled maint	251.5	2.9
Total	**8736.0**	**100.0**

Table II. 2017-2018 Scheduled Beam Time.

Time	Hrs.	%Time
Nuclear physics	1166.0	16.7
Nuclear chemistry	874.0	12.5
Outside collaboration	0.0	0.0
Outside users	3880.5	55.4
Beam development	1076.0	15.4
Total	**6996.5**	**100.0**

Texas A&M cyclotron radiation effects facility
April 1, 2017 – March 31, 2018

H.L. Clark, J. Brinkley, L. Chen, G. Chubarian, V. Horvat, B. Hyman,
B. Roeder, and G. Tabacaru

The activity of the Radiation Effects Facility (REF) increased over the previous reporting year. In this reporting period, the facility was used for 3,681 hours, which is a 9.7% increase over the 3,355 hours used in the 2016-2017 reporting period and is the highest usage year ever. Users of the facility (and hours used) over the past year were: Boeing Satellite Systems (344.5), Radiation Test Solutions (332), Sandia National Lab (305), Air Force (262), International Rectifier (206.5), NASA JPL (180), Intersil (163), Texas Instruments (154.5), NASA GSFC (137), SEAKR (126), Honeywell (96), Naval Surface Warfare Center (87), Airbus (79), Ryoei Technica (64), Lockheed Martin (62), Microsemi (56), Space X (56), VPT Inc (55), Thales Alenia Space (52), Scientic (49), Cobham (48), Raytheon (48), BAE Systems

Table I. Radiation effects facility usage by commercial and government customers for this and previous reporting years.

Reporting Year	Total Hours	Commercial Hours (%)	Government Hours (%)
2017-2018	3,681	2,622 (71%)	1,059 (29%)
2016-2017	3,355	2,501 (75%)	854 (25%)
2015-2016	3,042	2,326 (76%)	716 (24%)
2014-2015	3,024	1,975 (65%)	1,049 (35%)
2013-2014	2,399	1,517 (63%)	882 (37%)
2012-2013	2,626	1,856 (71%)	770 (29%)
2011-2012	2,673	1,630 (61%)	1,043 (39%)
2010-2011	3,042	1,922 (63%)	1,121 (37%)
2009-2010	2,551	1,692 (66%)	859 (34%)
2008-2009	2,600	1,828 (70%)	772 (30%)
2007-2008	2,373	1,482 (62%)	891 (38%)
2006-2007	2,498	1,608 (64%)	890 (36%)
2005-2006	2,314	1,314 (57%)	1,000 (43%)
2004-2005	2,012	1,421 (71%)	591 (29%)
2003-2004	1,474	785 (53%)	689 (47%)
2002-2003	1,851	1,242 (67%)	609 (33%)
2001-2002	1,327	757 (57%)	570 (43%)
2000-2001	1,500	941 (63%)	559 (37%)
1999-2000	548	418 (76%)	131 (24%)
1998-1999	389	171 (44%)	218 (56%)
1997-1998	434	210 (48%)	224 (52%)
1996-1997	560	276 (49%)	284 (51%)
1995-1996	141	58 (41%)	83 (59%)

(45), Northrop Grumman (44.5), ATMEL (40), Ball Aerospace (40), Intel Corporation (40), Johns Hopkins (38), VPT Rad (34.5), Millennium (32), Southwest Research Institute (32), Defense Microelectronics Activity - DMEA (30.5), Harris Corp (28), Aria Labs (28), InnoFlight (24), TESAT (24), TRAD (22.5), Data Device Corp (20.5), Freebird (16), GSI Technologies (16), IMT s.r.l (16), JAXA (16), NASA JSC (16), Cubic Aerospace (15), Controlled Dynamics Inc (13), Vanderbilt University (8), CMOS Sensor (8), CoolCad (8), ispace (8), L-3 Communications (8), MIT Lincoln Labs (8), Nucletudes (8), Suntronics (8), Troxel Engineering (8), Crossfield Technologies (6), Frequency Management (5) and Texas A&M Physics Dept (4). New users included DMEA, Cubic Aerospace, Controlled Dynamics, CMOS Sensor, Croddfield Technologies, ispace, MIT Lincoln Labs, Nucletudes, Troxel Engineering and TESAT.

Table I compares the facility usage by commercial and government customers. While commercial hours still dominate, the ratio from this reporting year (71% to 29%) is similar to usage from the 2016-2017 reporting period (see Fig 1). Both commercial and government hours increased by 5% and 24% compared to hours from 2016-2017. 15 MeV/u ions were the most utilized and especially 15 MeV/u Au. No new beams were added to SEELine users list. Much of the testing conducted at the facility continues to be for defense systems by both government and commercial agencies. Almost 12% (314 hours) of the commercial hours were for foreign agencies from Japan, France and Germany. It is expected that the facility will continue to be as active in future years.
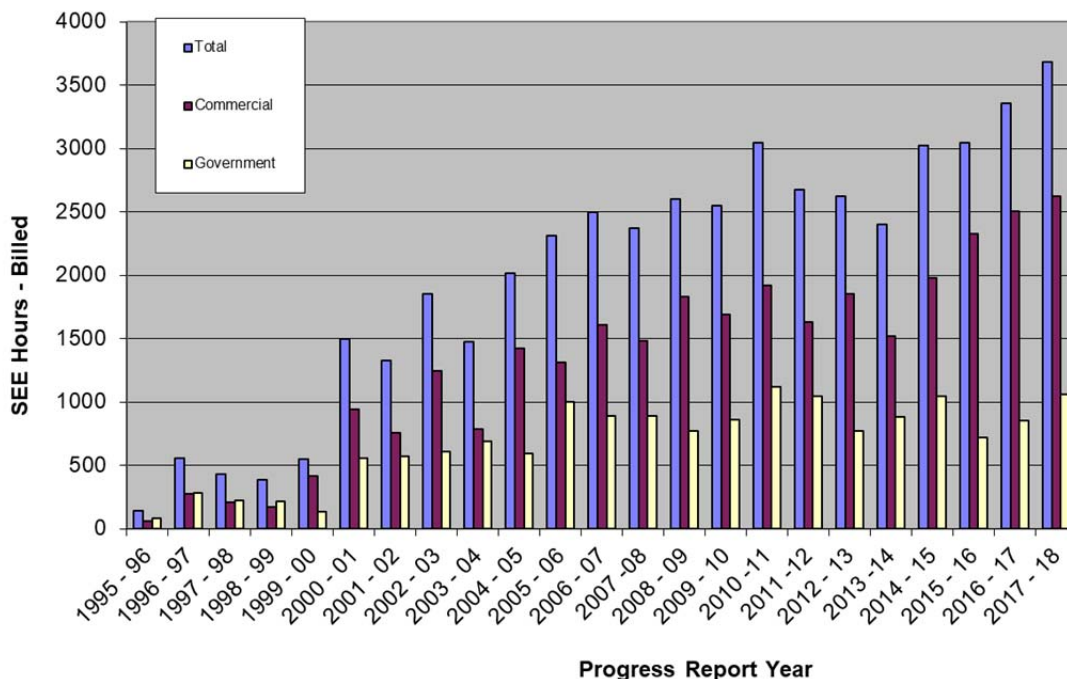
FIG. 1. Radiation Effects Facility usage by commercial and government customers for this and previous reporting years. While commercial hours still dominate, the ratio from this reporting year (71% to 29%) is similar compared to usage from the 2016-2017 reporting period. Almost 12% (314 hours) of the commercial hours were for foreign agencies from Japan, France and Germany.

K150 operations and development

G.J. Kim, B.T. Roeder, F. Abegglen, H.L. Clark, L. Gathings, D.P. May, and H. Peeler

We had another very busy year operating the K150 cyclotron. For the reporting period we logged over 4291 hours of beam-on-target and 2313 hours for beam developments. Included in the beam-on-target time was 3110 hours (2451 for physics and 659 for chemistry) for in-house science experiments, 186 hours for the SEE tests, and 995 hours for LLNL-Burke experiments. The K150 operational time is shown in Table I.

Table 1. 2017-2018 operational time.

Time	Hours	% Time
Beam on target	4291	49.1
Beam development	2313	26.5
Scheduled maintenance	724	8.3
Unscheduled maintenance	1408	16.1
Total	8736	100.0

The big users of the K150 beams were the LIG (light ion guide) project, the Rogachev group, and the LLNL-Burke collaboration.

As was in the past years, 10.3, 14.5 and 15 MeV proton beams were produced for the LIG project throughout the year. In November of 2017, the production of the radioactive ^{114}In (1.2 minute half-life) from a ^{114}Cd target and the subsequent charge-breeding and re-acceleration with K500 were investigated. Using the CB-ECR ion source the charge-bred ^{114}In^{19+} ions, along with ^{12}C^{2+} which was used as a pilot beam, were accelerated to 11 AMeV from the K500 cyclotron and were then sent to the MARS spectrometer for analysis. The beam switch from ^{12}C^{2+} to ^{114}In/Cd^{19+} was accomplished by shifting the K500 RF frequency by +9 kHz. The MARS analysis showed that the beam was ^{114}In/Cd mix and that it was indeed produced from the LIG gas cell, although the proportion of indium to cadmium was not determined. This test is described in detail in a separate section.

Last year we accelerated a 6 MeV proton beam at 330 amps on the main magnet which marked the lowest operating cyclotron field to date. However, this year we developed a 3.4 MeV proton beam at an experimenter's request at 252 amps on the main magnet. This beam has been used twice for an experiment and even once for a SEE testing.

The Rogachev group ran their experiments eight different times using K150 beams to the MDM spectrometer twice and the rest of times to the MARS spectrometer. A low energy, third harmonic, 1.3 AMeV ^{7}Li^{1+} beam was tuned out twice for their MDM runs, once in December 2017 and then in March 2018. The beam transmission to the MDM target was poor due to the poor vacuum (5×10^{-5} torr) through the beam line in the MDM cave in December. For the group's March 2018 run, with improved vacuum

through the MDM cave (~5x10^{-6} torr), the low energy beam transport seemed have improved.   However, due to the experimental setup at the time, no beam current was measured at the target position to verify the beam transmission efficiency.   The Rogachev group's other six experiments ran in the MARS cave, and these gave us many chances to practice beam transport to MARS cave.

The K150 beam transport to MARS has been challenging from the very beginning, especially the beam line section downstream of the Analyzing Magnet. This section contains a 12 degree and a 26 degree bending magnet, and in addition the vertical beam height changes from the K150 cyclotron side to the K500 beam lines in this area. So, trying to decouple the effects of the two dipoles (and at times also the upstream Analyzing Magnet) and the beam height transition and to steer the beam straight can be difficult.   Compounding the problem was that the 26 degree dipole was not correctly installed initially, see Fig. 1.   The 26 degree dipole has a narrow pole face and therefore has a limited region of useable
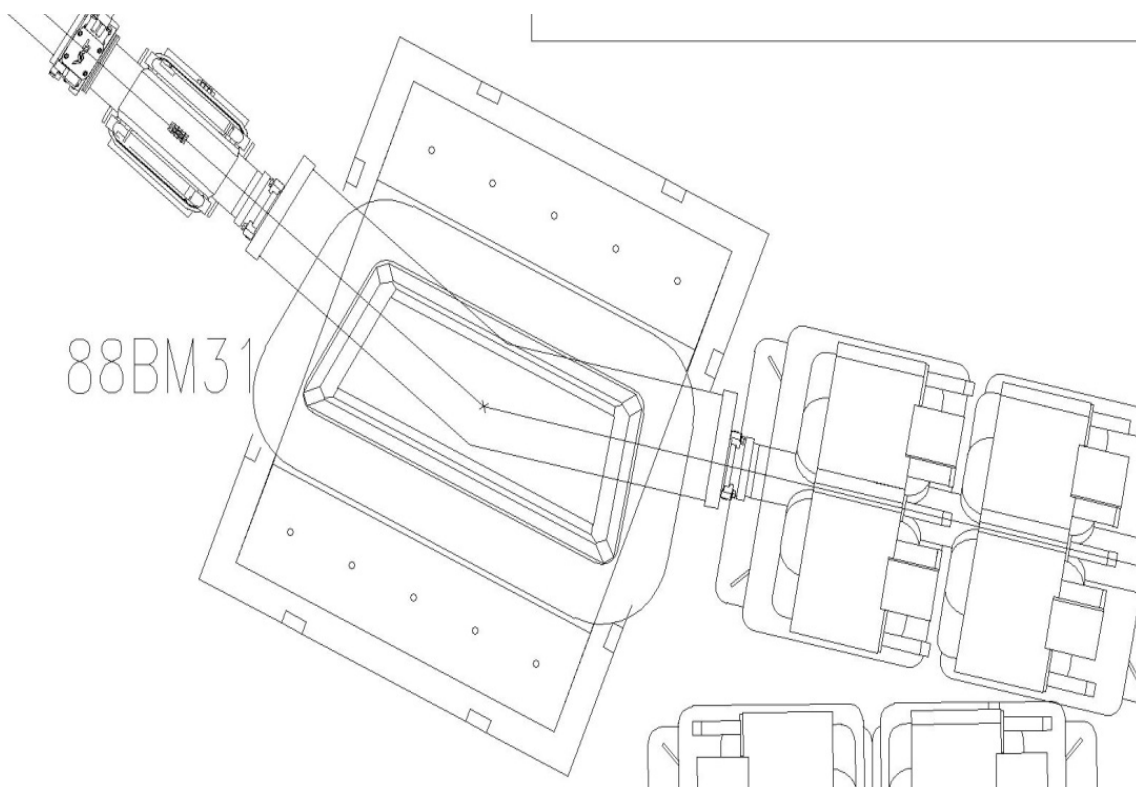
FIG. 1. 26 degree bending magnet BM31, used in the beam line from the K150 cyclotron to the MARS spectrometer. This initial placement of this dipole unfortunately placed parts of the 10 cm wide beam in bad field regions too close to the pole edge of the magnet.

good field of about 12 to 16 cm in width, as can be seen in Fig. 2, whereas the beam envelope would likely occupy 10 cm across. As a consequence the proper alignment of this dipole is very important. After the misalignment of the 26 degree dipole was recognized and corrected (perhaps another 1 cm push might make it even better), the beam transport to MARS has improved.   For the Rogachev group's runs in MARS, 6.3 to 15 AMeV, ^{6}Li, ^{7}Li, ^{10}B, and ^{12}C beams were used, and the beam transport efficiency from FC02 to the MARS production target has achieved about 25%, which corresponds to about 50%

transmission through the 160 degree Analyzing Magnet and then another 50% through to the MARS target.
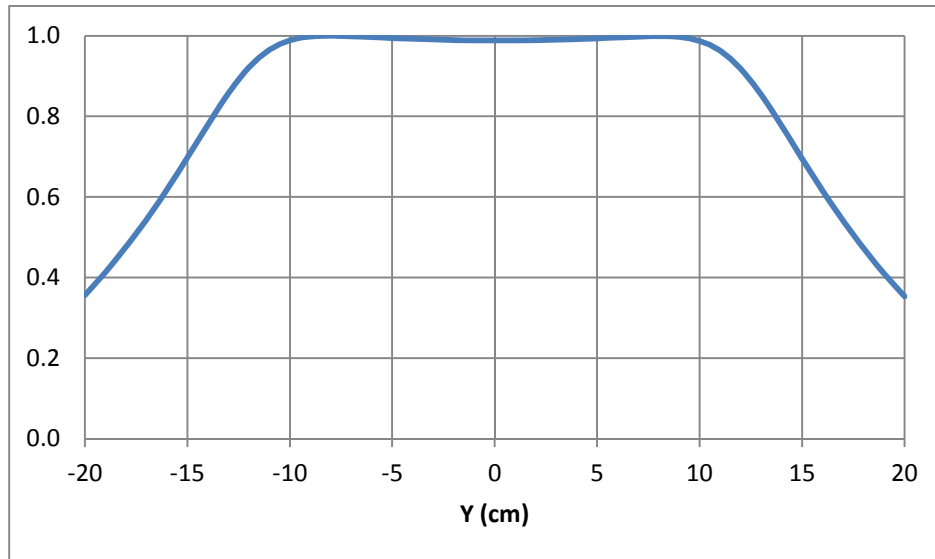
FIG. 2. B field profile across the 26 degree bending maget at the middle of the dipole. The field map was calculated with TOSCA.

Progress on the ECR4 ion source

D.P. May, S. Molitor, F.P. Abegglen, H. Peeler, and R. Ohlsen

All the parts for the new 6.4 GHz ECR4 ion source have been fabricated, and assembly is beginning. Among recent accomplishments, the axial-field coils have been potted and have been mounted into the steel yoke (Fig.1), the steel plug has been machined and is ready for insertion into the injection

FIG. 1. Coils and steel yoke assembly.

end (Fig. 2) and the support stand for the source has been constructed. Finally, the 15º dipole for

FIG. 2. Steel plug for the injection end.

switching between ECR1 and ECR4 injection into the K500 has been installed (Fig. 3).
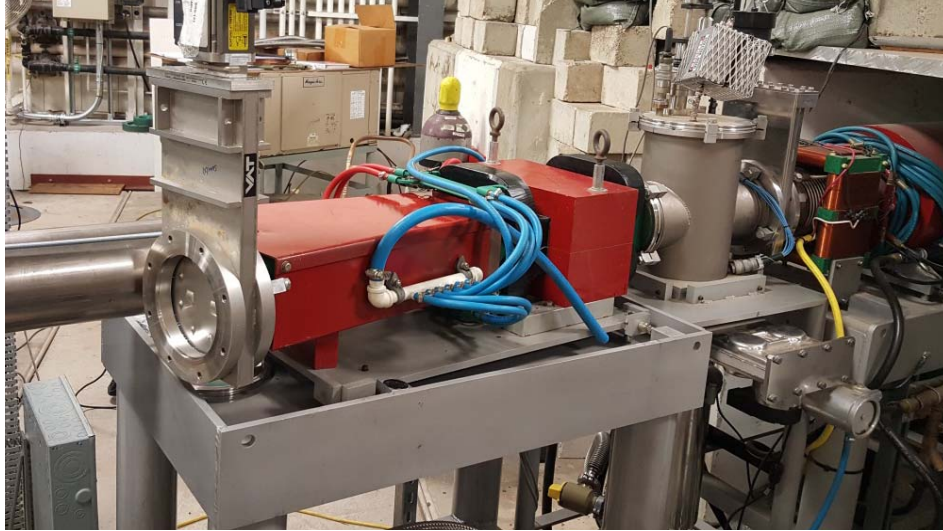
FIG. 1. Dipole on the K500 injection line for switching between ECR1 and ECR4.

In the near future, the cooling-water and electrical connections will be installed on the source, the NdFeB permanent-magnet bars will be inserted into the plasma chamber using the modified mechanism used for the insertion of the bars for ECR2, the potted coil and steel yoke for the Glaser lens will be assembled and the two recently purchased, used 6.4 GHz transmitters will be tested. Next the source, transmitters and power supplies will be installed in place and the analysis/injection line assembled, leading up to all power, microwave and vacuum connections.

Progress on the light ion guide

G. Tabacaru, J. Arje, D.P. May, A. Saastamoinen, F.P. Abegglen, G.J. Kim, S. Molitor, and B.T. Roeder

Introduction

The Light Ion Guide Project [1] continued to advance through the last reporting period. Work focused on the charge-breeding efficiency and on the radioactive ion output of the gas cell coupled with the rf-only sextupole ion guide (SPIG).

Accelerated Injection

The SPIG was extended from the target cell towards the Charge-Breeder ECR ion source (CB-ECRIS), and an improved design of the final acceleration gap assembly was made, making the operation at higher voltages (8 to 10 kV) more stable and free of breakdowns. Extending the SPIG allowed to transition the final acceleration of the radioactive ions from a region of poor vacuum (10^{-3} – 10^{-4} torr) to a region of better vacuum region (10^{-5} – 10^{-6} torr). At the same time, transport of ions through low grade vacuum is more efficient using the SPIG compared with a classical and simplistic vacuum tube. Precise alignment of the gas cell, the SPIG and the two Einzel lenses was made also.

The injection into CB-ECRIS was modified as well, by extending the plasma chamber and coupling the microwave tube in a different place (Fig. 1). Consequently, a better vacuum inside the plasma chamber is present now. The transport of the ions into the plasma chamber was modelled
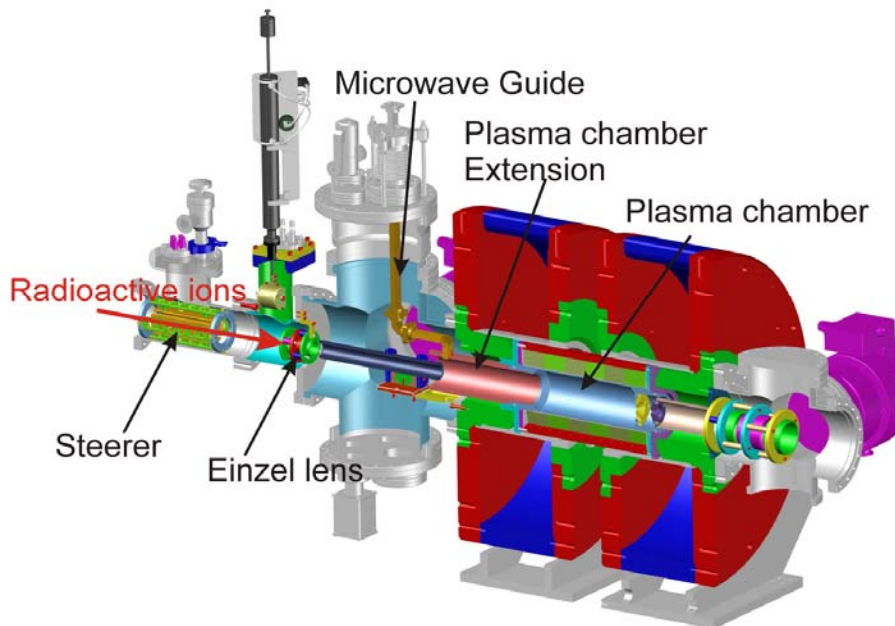
FIG. 1. View of the CB-ECR and the new injection design.

incorporating the injection-end magnetic field of CB-ECRIS using the SIMION [2] code (Fig. 2). The
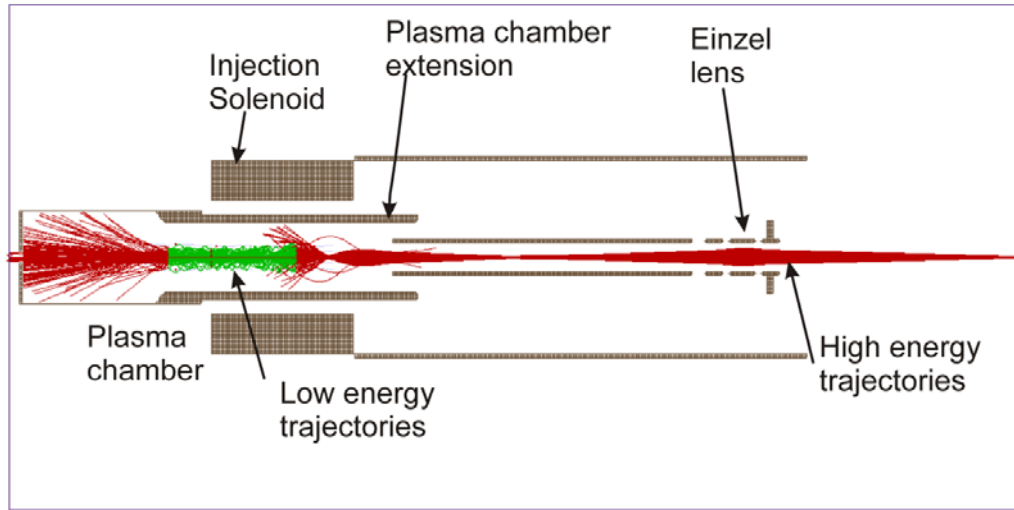
FIG. 2. SIMION ion optics calculations.

simulations showed a 98% transport efficiency of the ions injected into the plasma chamber, but in reality that could be lower due to the fact that the plasma contribution was not taken into consideration in the calculations. Another possibility is that the energy spread of the injected 1+ beam could be excessively wide. Evidence for this is that the acceptance for charge-breeding was much wider in voltage (~11 volts FWHM) than the 5.8 volts FWHM encountered with direct injection, described below.

RIB Studies

The radioactive ions production studies continued with these new improvements. We focused on four major (p,n) reactions listed in Table I, the crossection being calculated with TALYS code:

Table I. Reactions studied at the Light Ion Guide.

Reaction	Crossection [mbarn] @ Proton Energy [MeV]	Half life
$^{64}Zn(p,n)^{64}Ga$	161 @ 14.3	2.6 m
$^{58}Ni(p,n)\,^{58}Cu$	40 @ 14.3	3.2 s
$^{46}Ti(p,n)\,^{46}V$	124 @ 14.3	422 ms
$^{114}Cd(p,n)\,^{114}In$	510 @ 10.3	71.9 s

The Light Ion Guide and the CB-ECRIS were tuned carefully for each of these reactions, the final goal being the maximization of one of the higher charge state. The charge-states studied were 12+, 14+,

16+ and 17+ for ^{64}Ga, 13+ and 14+ for ^{58}Cu, 8+ for ^{46}V and 19+ for ^{114}In. Charge-breeding was observed for ^{64}Ga, ^{58}Cu, and ^{114}In with the highest efficiency obtained (approximately 1%) for ^{114}In^{19+}, ions which were reaccelerated in the K500 cyclotron (see the B. Roeder contribution to this report). The number of radioactive ions injected into CB-ECRIS ranged between approximately $2x10^4$ ions/µCoulomb (^{64}Ga and ^{114}In) to $3x10^3$ ions/µCoulomb. The charge-breeding efficiency was low, under 1%, and this will be the next element to focus on.

Direct Injection

Direct injection of ions via a SPIG was also attempted. A HeatWave alkali source was placed at the entrance of a 0.4 meter long SPIG, and the exit end of the SPIG placed on axis near the maximum axial magnetic field at the injection end of the CB-ECRIS (Fig. 3). This arrangement resulted in a good charge-breeding efficiency (Fig. 4), although this was difficult to quantify due to the difficulty of measuring the output from the SPIG directly. An estimate of the output was made using a measurement of the current hitting the plasma chamber added to the current measured hitting a faraday cup down-stream of the CBE-ECRIS with no high voltage applied to the plasma chamber. This efficiency could be as high as 10 % into one charge-state (8.4 pnA of Cs^{24+} out of 70 pnA of Cs^{1+}) measured hitting the plasma chamber and 15 pnA hitting the down-stream faraday cup. Charge-breeding of potassium was also attempted with similar results.

Conclusions

Improvements made in the SPIG system increased the output of radioactive ions as well as the operating stability. Changes made in the injection side of the CB-ECRIS slightly increased the efficiency of the charge breeding or made the operation in the breeding mode more reliable. Radioactive ions of ^{114}In^{19+} were re-accelerated and few questions were answered about the methodology applied in this process. Next re-accelerated ions will be lighter and conditions might be slightly different. The charge-breeding efficiency needs to be increased substantially in order to achieve a useful re-accelerated ion beams for physics experiments. To this end a 2.5 meter long SPIG is now being constructed in order to transport the 1+ ions directly from the target cell to CB-ECRIS injection.

[1] G. Tabacaru *et al.*, *Progress in Research*, Cyclotron Institute, Texas A&M University (2016-2017) p. IV-13.
[2] SIMION code, http://www.simion.com

Cyclotron computing

R. Burch and K. Hagel

To continue our mission of providing the Cyclotron Institute with the secure computational and networking infrastructure necessary to teach and execute research programs, we increased the Institute's computing capacity and infrastructure over this past year by adding four computational servers and a pair of container servers for service virtualization. We upgraded our authentication service hardware. We are pursuing containerizing legacy administrative services to allow better utilization of server room rack space, power and cooling by reducing our physical machine count. To enhance our security posture, we migrated the Institute's WiFi infrastructure and computational server authentication service to TAMU NetID and we are migrating Institute desktop/laptop computers to the TAMU CONTINUUM which utilizes TAMU NetID.

To increase productivity and reduce turn-around time we added four general lab computational servers, now totaling sixteen. This increases our capacity by 8 2.4GHz late model processors or from 292 to 388 concurrent jobs. Each added server has 32GByte of RAM, allowing users to analyze memory-intensive jobs quickly. These servers are ready to be provisioned and move into production. We migrated our aging authentication server from Raspberry Pi 1's to Pi 2's and update the OS on all four authentication Raspberry Pi's.

In an effort to reduce the number of administrative servers in the data center, and thereby reduce server room power and cooling requirements, we are testing containerizing legacy administrative services. The motivation is to free up physical computers running administrative services, one machine for each service; web, database, list-server, and other services by hosting all these services on one physical server.

These changes and additions allow us to supply the Institute with the resources it needs to execute its mission by increasing our computational and data serving capacity, providing more security by utilizing TAMU authentication services, and by reducing physical machine footprint via migration of administrative services to containers.

High-mass test of the MDM mass-separation capabilities

D.P. Scriven, G. Christian, S. Ota, S. Dede, E.A. Bennett, W.N. Catford,[1]
R. Wilkinson,[1] M. Moukkaddam,[1] and S. Hallam[1]
[1]Department of Physics, University of Surrey, Guildford GU2 5XH, United Kingdom

The Multipole Dipole Multipole (MDM) spectrometer is an integral component our study of astrophysical reactions here at the Texas A&M Cyclotron Institute. Currently it is used in conjunction with the TIARA (Transfer and Inelastic scattering All-angle Reaction Array) experimental setup to study nucleon transfer reactions like (d,p) and (6Li,d) in inverse kinematics. This type of reaction is useful for nuclear spectroscopy, cross section measurements, and reaction spin-transfer dynamics, whose measurements can inform models of nucleosynthesis in stars. So far, all TIARA for Texas (T4T) studies have been done with stable beams in the K150 and K500 cyclotrons, with reactions such as $^{19}F(d,p)^{20}F$, $^{23}Na(d,p)^{24}Na$ and $^{22}Ne(^{6}Li,d)^{26}Mg$. Soon, the Cyclotron Institute will be capable of producing rare isotope beams (RIBs). Transfer reaction experiments with RIBs are especially interesting as many astrophysical reactions occur away from stability. In this report we discuss a recent investigation of the mass separation abilities of the Multipole Dipole Multipole spectrometer in order to extend the mass range of possible experiments done with MDM.

The T4T setup uses a large slew of detectors to so that a nearly perfect reconstruction of each event can be done. TIARA itself consists of a target chamber surrounded by a barrel of resistive strip detectors. TIARA is capped at the end by a modular silicon detector HYBALL which can be placed up- or downstream of the target, depending on the kinematics of the reaction under study. In conjunction these detectors allow for large angular coverage of transfer reaction products and elastically scattered beam. A set of High Purity Germanium (HPGe) clovers used in the HYPERION experiment is also employed for prompt γ-ray detection. These detectors are coupled to the Si and barrel detectors to give coincidence measurements of the de-exciting states populated from transfer reactions. The HPGe's are integral in the PID test in this review. After passing through TIARA the beam moves through MDM for mass-separation before entering the new focal plane detector (FPD) array. The FPD array, utilizes a gas chamber of isobutane with avalanche wires and MicroMegas to measure beam position and energy deposition in the gas. The chamber is capped at the end with a CsI detector to measure energy of the reaction products in coincidence with proton energies in TIARA.

Experiment

In summer 2017 the T4T group ran a ^{63}Cu beam at 10 MeV/u into Cave 3 holding the MDM spectrometer. The beam was impinged on a 500μg/cm2 CD2 target to induce the $^{63}Cu(d,p)^{64}Cu$ reaction. Protons were measured in the HYBALL detector in correlation with the copper recoils, see Fig. 1a and 1d. The MDM was tuned to place the beam centrally in the FPD. The majority of unreacted beam throughput was removed by MDM. Some unreacted ^{63}Cu was observed in the CsI and MicroMegas with the daughter nucleus, see Fig. 1c. The two were further separated in the analysis. The ^{64}Cu nuclei created

in this reaction are pushed into a slew of different excited states. We used the HPGe detectors around the reaction center to observe de-excitation of these states.
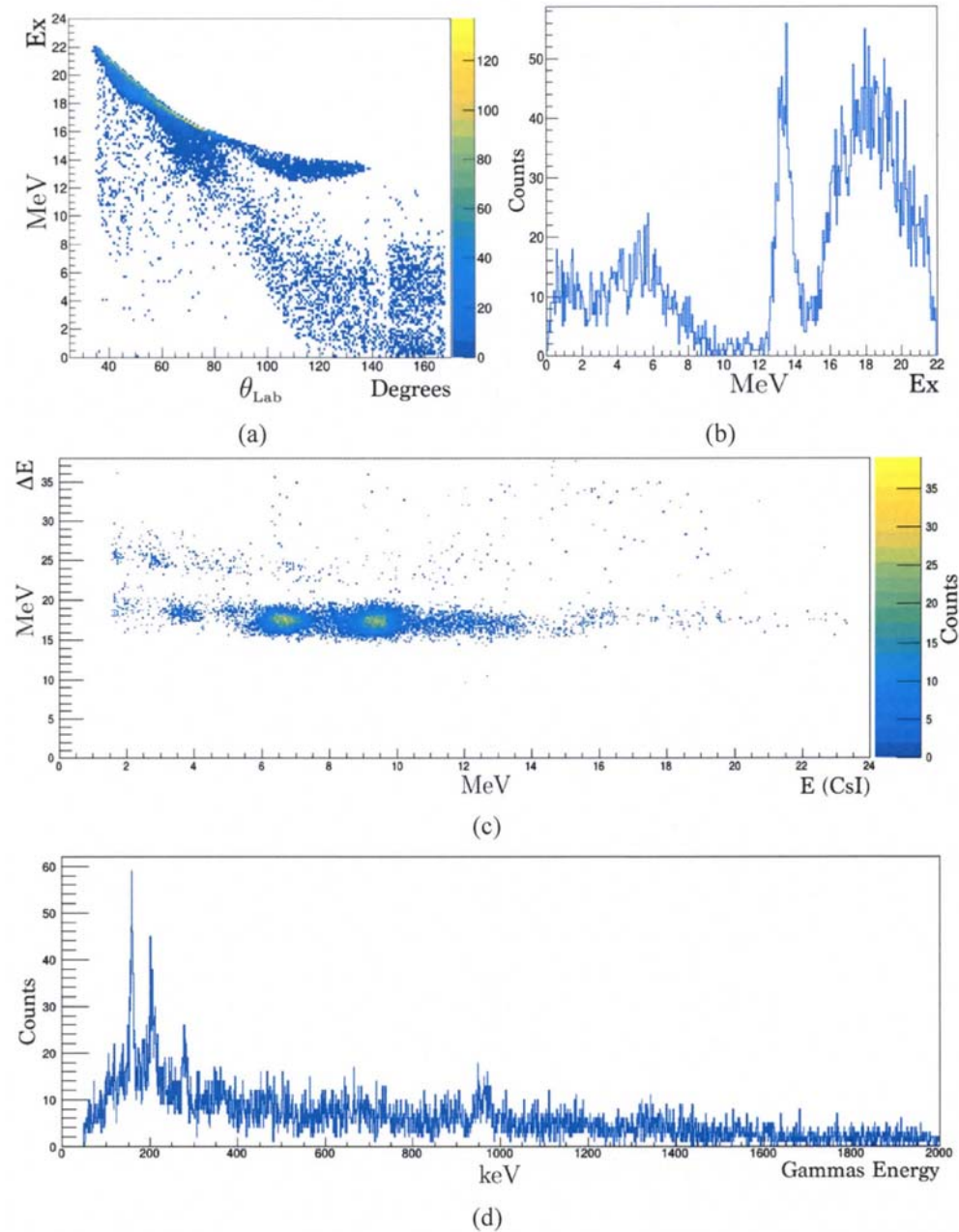
FIG. 1. Above, a) shows the proton impact energy, Ex measured from HYBAL L vs θLab. This gives us the angular distribution of recoiling protons. Plot b) shows ELab vs Ex. c) is the ECsI–ΔE that shows the separation of the two copper nuclei. The blob to the right side is identified to be ^{64}Cu. d) shows the gamma spectrum. We see some features which are shrouded partially by a continuum-like ban.

Analysis

Once our measurements were calibrated the first step in the analysis was to gate on the reaction peak of proton events which triggered the TAC (time-to-amplitude converter). Now gated, we can present the reaction measurements and do rudimentary particle ID. With the ECsI–ΔE plot we can assume that our particles are indeed separated here. However, to convince ourselves of which nuclei are which and that separation was actually achieved we look to the gamma-ray spectrum. Gating on each blob in ECsI–ΔE (Fig. 1c) individually we clearly see distinction in the two spectra. When gated on the suspected ^{64}Cu events a clearer spectrum with strong features is teased out. We compare these features to the NNDC adopted level scheme [1], and notice that each peak match with known levels in ^{64}Cu that have high spectroscopic factors [2, 3]. From this we're confident that the PID is accurate and separation is achieved.

Conclusion
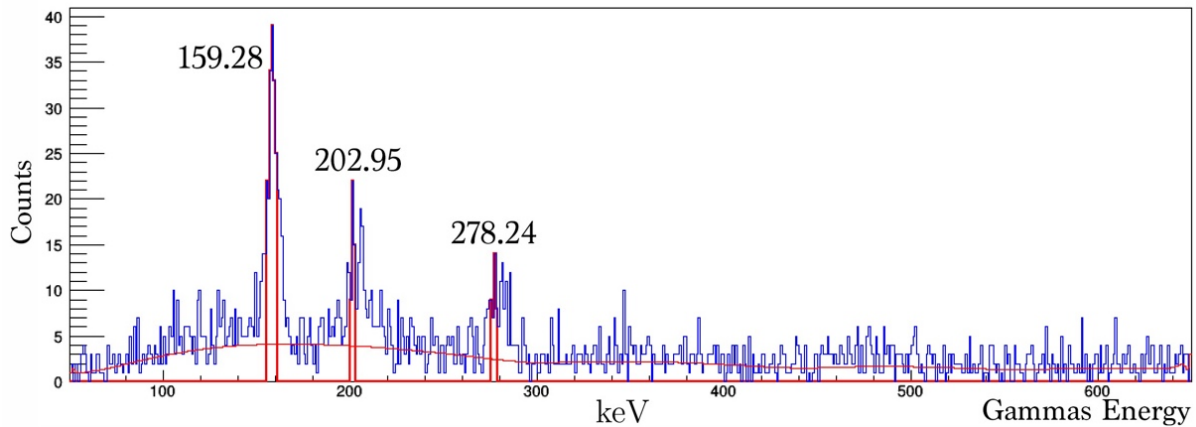
FIG. 2. Here we see the gamma spectrum resulting from gating on the suspected ^{64}Cu

In summary, this experiment has tested the ability of MDM to separate ions at a higher mass range than previously probed. Using the gamma excitation spectrum from HYPERION detectors we can be certain that separation was achieved. In the past the highest mass ranges used in MDM peaked in the A=30 mass range. Through this analysis we've found that MDM is capable of separating ions through the A=60 mass range, and perhaps higher. Coupled with our future RIBs this ability opens and extremely large range of new experiments and nuclei that can be probed at the Cyclotron Institute.

[1] B. Singh, Nucl. Data Sheets, **108**, 197 (2007).
[2] W.W. Daehnick and Y.S. Park, Phys. Rev. **180**, 1062 (1969).
[3] Y. Park and W. Daehnick, Phys. Rev**. 180**, 1082 (1969).

Implementation of PIGE analysis in the Texas A&M Cyclotron Institute

A. Rodriguez Manso, M. McCarthy, A.B. McIntosh, K. Hagel, A. Jedele, A. Zarrella,
A. Wakhle, and S.J. Yennello

Introduction

Ion beam analysis (IBA) is a set of analytical techniques using ion beams for studying structure and composition of samples. PIXE (Particle Induced X-ray Emission) and PIGE (Particle Induced Gamma-ray emission) are examples of traditional ion beam techniques for elemental analysis [1]. The individual IBA techniques are distinguishable by the different exit's channels following after each interaction between the ion beam and the solid target. Particles emitted after the reaction suggest, therefore, the use of a specific type of detection system.

For example, PIXE is used for determination of minor content of elements from Aluminum to Uranium. Each sample is bombarded with protons (or alphas), inducing x-rays that are characteristic for each element. The technique is widely used for quantification of heavy metals in environmental and biological samples as well as studying vintage paints' composition [2].

PIGE, on the other hand, is based on nuclear reactions induced by MeV protons (mainly), where prompt nuclear gamma rays are produced and detected [3]. Considering gamma rays are more energetic than x-rays, the method allows the analysis of light elements in environmental and health related samples [4,5], resulting in PIGE being considered a complementary technique for PIXE in characterizing materials. PIGE is also of interest for energy calibration procedures in accelerators [6], among other applications, and without a doubt, is the most common application of nuclear analysis, both for fundamental physics and analytical applied projects.

PIGE analysis is based on the detection of the prompt gamma rays emitted from the excited nuclei following the nuclear reactions (p, γ), (p, p' γ), (p, α γ), and (p, n γ) induced by protons. The energy of the gamma-ray indicates the identity of the isotope and its intensity gives a measure of the concentration of the isotope present in the sample. PIGE is a multi-elemental method, with high sensitivity and has the advantage of being isotopic in nature with virtually no interference.

In the past year, our laboratory has assembled PIXE and PIGE experiments with the intention of systematically partake with other departments and universities in the study of contaminants' pathways to the environment and characterization of materials and, in addition, contribute didactically to students involved in the project.

Recently, one of our collaborators has been working on an interesting research regarding the study of fluorinated chemical substances [7]. The authors highlight that per and polyfluoroalkyl substances (PFASs) have been detected in a wide range of household products but also food contact materials (FCMs). The latter particularly, may contribute to raise awareness in entities making health policies regarding the fact that this substances can migrate into food, indoor air, dust, etc, contributing to human exposure. Already, epidemiological and toxicological studies in humans and animals, respectively, have found bounds between exposures to some PFASs and different types of cancer, thyroid disease, pregnancy induced hypertension and immune-toxicity in children, among other health effects [8-

10]. Moreover, the exposure to PFASs from fast food packaging must be worse in children according to [7], mainly because in the USA, 1/3 of the children are high consumers (daily) of fast food, and all in all, because in general children are more susceptible than adults to the adverse health effects associated. Nevertheless, PFASs are still globally produced in a wide range of products.

Traditionally, the main screening methods to detect fluorinated chemicals have been HPLC (chromatography) and MS (mass spectroscopy) [11], but PIGE allows to determine total fluorine quickly, no matter the origin of the matrices [12,13].

The implementation of PIGE serves to analyze, non-destructively, a large number of samples and variety of matrices (i.e. environmental or biological), with minimum time frame and requirements for sample's preparation and analysis, and without interferences for determination of total fluorine.

Experimental setup and measurement

The experiment was performed at Texas A&M University Cyclotron Institute, using the K150 cyclotron. Each standard/sample was bombarded with a proton beam that ranged from 3.6 - 6.3 MeV, with an intensity between 5 - 9 nA and a beam spot size of 5 - 10 mm.

The resulting gamma-rays were measured with a XR-100T-CdTe high performance x-ray and gamma-ray detector, located at 45º and 135º with respect to beam direction [14]. The detector consists of a 1mm of CdTe diode thickness located behind a 4mil (100µm) Be window and it is excellent for high detection efficiency applications, at energies up to 100 keV, due to its high stopping power. The specifications about the detector were taken from [15]. Fig. 1 shows the experimental set up.
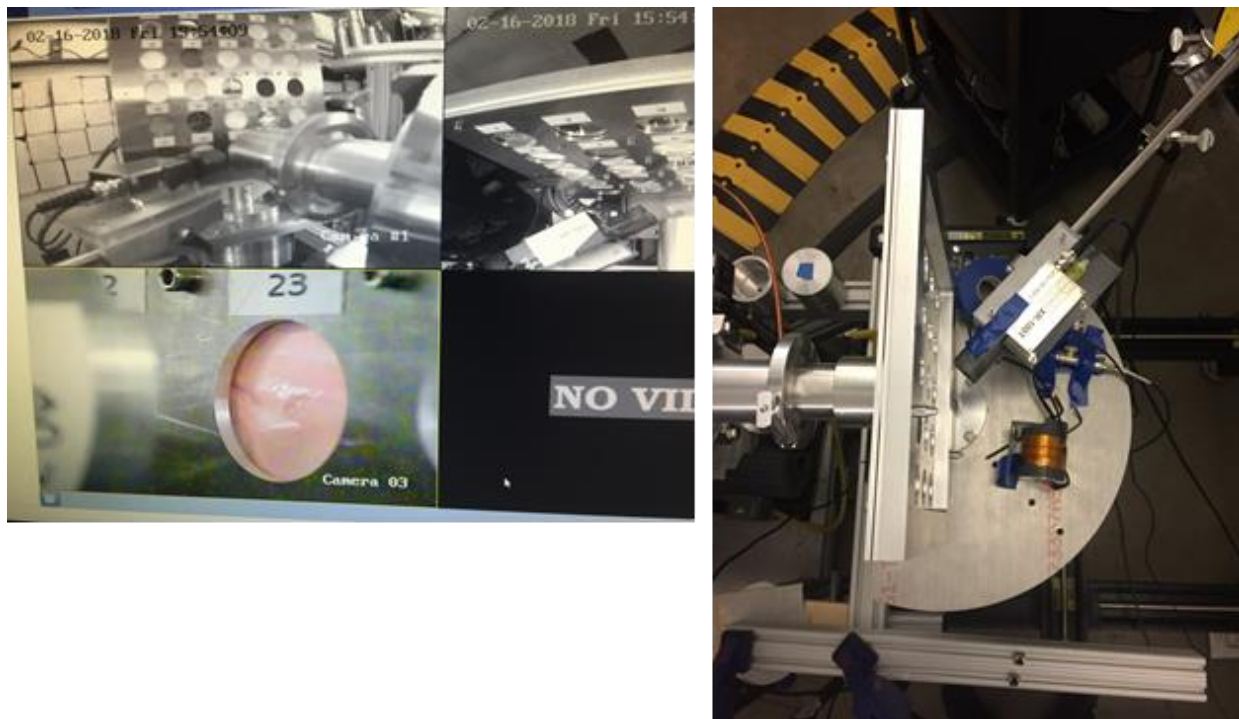
FIG. 1. Left panel shows the target ladder with 25 standards and samples. On display, the toothpaste sample. The right panel shows a top view of our experimental set up. Beam is coming from left to right in the figure, which also displays the target ladder, the CdTe detector and faraday cup.

The analysis of these results are currently in progress. The beam current was measured for 30s at the beginning and at the end of each day of measurements. A linear regression is used to estimate the delivered beam current. Two characteristic gamma rays from the decay of the ^{19}F nucleus will be integrated (110 keV and 197 keV [13]). For total fluorine determination the efficiency of the XR-100T-CdTe detector is about 40% at 100 keV and about 12% at 200 keV. The total number of counts in the two peaks, per beam current in target, per time of beam delivered, is proportional to the total fluorine concentration. The peaks are integrated above a linear background built by selecting manually four points about each peak and subtracting from the integrated peak counts.

Results

The measurements were taken in 30 consumer product samples (paper and textiles), all considered "thin samples" for the purpose of this analysis (i.e. thickness ranges from 0.20 mm to 0.65 mm, as in [7]). The standards used were provided by Dr. Graham Peaslee from University of Notre Dame. We performed measurements in 6 paper standards and 4 inorganic standards. Fig. 2 shows a typical gamma-ray spectrum from a PIGE measurement of a fluorinated compound treated paper (from a
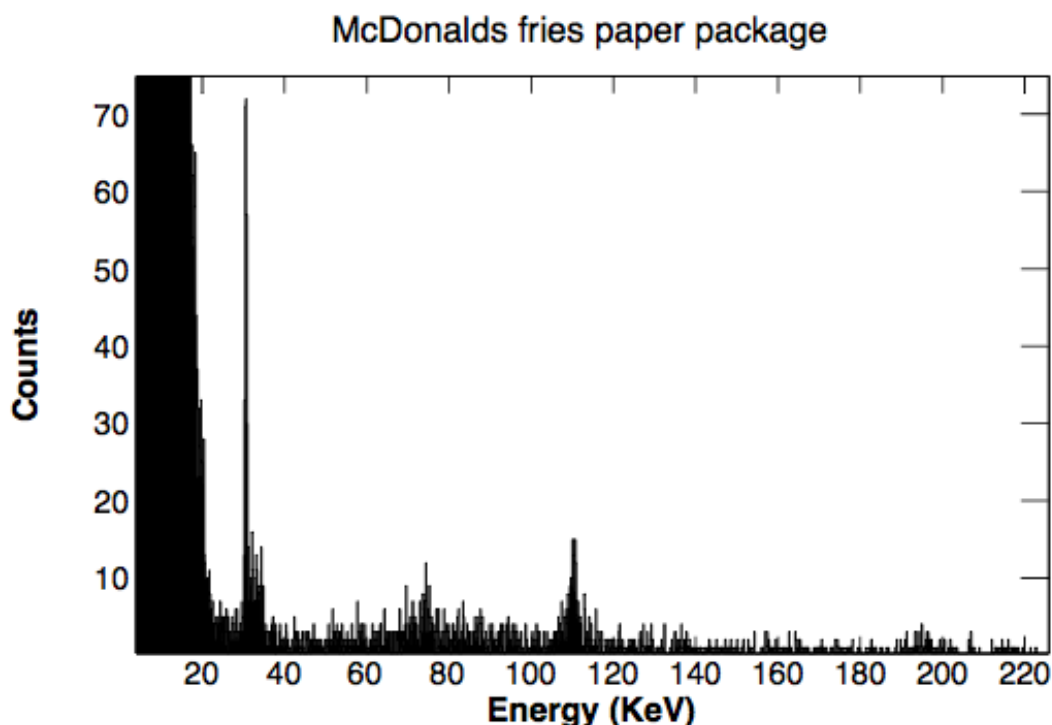
FIG. 2. Typical gamma-ray spectrum from a PIGE measurement of a fluorinated compound treated paper, from a McDonald's fries bag.

McDonald's paper fries bag). The sources of errors for each PIGE measurement come typically from the errors associated with the background subtracted peak and the uncertainty in the integrated beam current measurement. The total uncertainty is estimated to be around 10%. Fig. 3 shows our paper standards measurements, to be used as calibration to estimate our samples' concentration of fluorine. Based on the calibration curve, the concentration of the samples where fluorinated compounds were found were

calculated and are shown in Table I. The table also shows the concentration values reported in [7] for the same type of samples. Both results seem consistent.
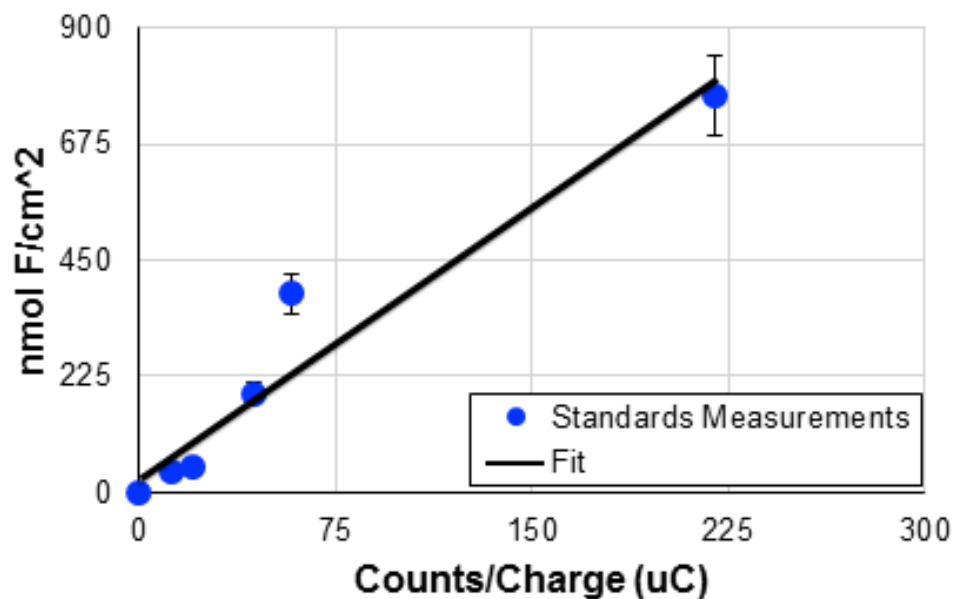
FIG. 3. Paper standards' concentration in nmol F/cm^2 as a function of the counts per charge.

Table I. Concentration of samples compared with literature.

Samples	Concentration (nmol F/cm^2)	Literature [7] (nmol F/cm^2)
McDonald Fries	335 ± 35	161-445
Happy Meal Box	572 ± 57	161-445
Popcorn	733 ± 73	161-445
Pet Proof Carpet	161 ± 16	78-113
Outside Turf	90 ± 9	78-113

The work is still in progress but already the results from the data show the utility of using PIGE techniques for rapid screening for the presence of total fluorinated compounds on consumer products. In addition to that, considering is a non-destructive method, after rapidly determining if a sample is fluorinated, a more elaborated method could be used to specifically identify the fluorinated compound in the product. The applications include environmental studies and human exposure studies.

[1] M.B.H. Breese, D.J. Jamieson, and P.J.C. King, *Materials Analysis using a nuclear microprobe*, (John Wiley & Sons, New York, 1996).

[2] J.L. Campbell, K.G. Malmoqvist, and S.A. Johansson, *Particle–Induced X–Ray Emission Spectrometry (PIXE)*, (John Wiley and Sons, 1995).

[3] C. Boni, E. Cereda, and G.M. Braga Marcazzan, Nucl. Instrum. Method Phys. Res. **B35**, 80 (1988).

[4] A.K.M. Fazlul Hoque, PhD Thesisn, Jahangirnagar University, 2000.

[5] A.K.M. Fazlul Hoque, M. Khaliquzzaman, M.D. Hossain and A.H. Khan, Fluoride, **35**, 1 (2002); **36**, 38, (2002).

[6] S.A. Brindhaban, P.H.Barker *et al*., Nucl. Instrum. Methods Phys. Res. **A340**, 436 (1994).

[7] Schaider *et al.*, Sci. Technol. Lett. **4**, 105 (2017).

[8] V. Barry *et al.*, Environ. Health Perspect **121**, 1313 (2013).

[9] M.J. Lopez-Espinosa *et al.,* Environ. Health Perspect **120**,1036 (2012).

[10] P.A. Fair *et.al.*, J.Immunotoxicol **8**,17 (2011).

[11] K. Jankowski, A. Jackowska, and M. Mrugalska, J. Anal. At. Spectrom **22**, 386 (2007).

[12] A.P. Jesus, B. Braizinha, and J.P. Ribeiro, Nucl. Instrum. Methods Phys. Res. **B161**,186 (2000).

[13] E.E Ritter, M.E. Dickinson, J.P. Harron, D.M. Lunderberg, and G.F. Peaslee, Nucl. Instrum. Methods Phys. Res. **B407**, 47 (2017).

[14] P.R.P. Allegro, M. A.Rizzutto, and N.H. Medina., Microchemical J. **126**, 287 (2016).

[15] Amptek website: http://amptek.com/xr-100t-cdte-cadmium-telluride-detector-efficiency-application-note/

PIXE (Proton Induced X-Ray Emission): determining concentration of samples

A. Rodriguez Manso, M. McCarthy, Y. Pajouhafsar, A.B. McIntosh, K. Hagel,
A. Jedele, A. Zarrella, A. Wakhle, and S.J. Yennello

Introduction

We used Proton Induced X-ray Emission (PIXE) [1] as an analysis technique to determine the composition of samples, in particular, its constituents and concentrations. Each sample is bombarded with protons (or alphas), inducing characteristic x-rays that serve as "fingerprints" for each element. Therefore, the x-rays produced can offer insight to the elemental composition of samples. This process is shown in Fig. 1.
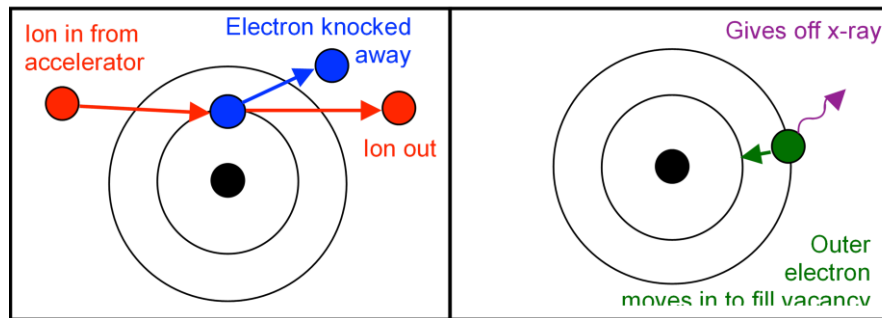
FIG. 1. Induced X-Ray Process. The left panel shows the bombardment of a lower energy level electron, and the right panel shows the displacement of a higher energy level electron and the induced x-ray.

The proton beam is produced and accelerated by the K150 at the Cyclotron Institute at Texas A&M University (TAMU). The setup includes a PX2T-CR Power Supply and Amplifier for the XR-100/CR SiPIN and a Mesytec ADC. The peaks of the spectrum are analyzed using GUPIXwin software tool [2] to determine the concentration of the known elements of each specific sample. The goals of this work are to implement a PIXE experimental set up at the Cyclotron Institute and to determine the concentration of thin films, given by our Chemical Engineering Department.

Experimental setup and measurement

The K150 delivered a 3.6 MeV proton beam over a three-day run. The intensity of the beam ranged from 0.5 - 3 nA. The detector setup consisted of a XR-100T/CR SiPIN detector and preamplifier, connected to its corresponding power-supply and shaping-amplifier. The experimental set up included the detector, a faraday cup, and a target ladder mechanism. These were placed in a vacuum chamber, as shown in Fig. 2, where the bombardment of samples with protons took place. The five-positioned target ladder mechanism, connected to a rod that goes through a slit, enabled to changes the samples within the chamber without breaking vacuum. Each run was approximately 15 minutes long. The target ladder had to be changed out frequently to test different samples and standards. After each target ladder change, an electron suppressed faraday cup was used to measure the beam. When the beam hits the cup, the carbon

backing's electrons are induced and create a signal. This signal gives a measurement of the beam. Throughout the run, there are fluctuations of the beam, and the faraday cup allowed us to precisely measure and record the beam current periodically. Faraday cup measurements lasted around 2 minutes.
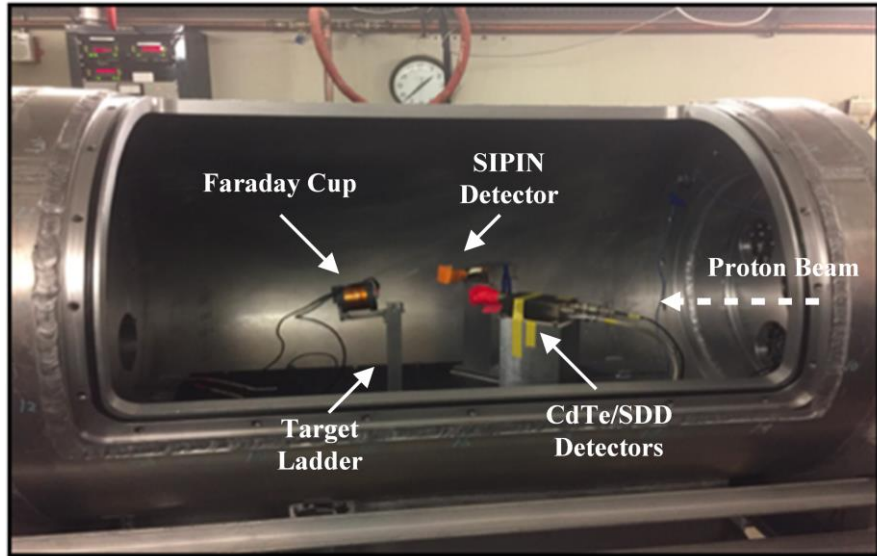
FIG. 2. Vacuum chamber where the experiment was conducted. The CdTe/SDD detectors shown, were used to validate results from the SiPIN detector, as well as the faraday cup. The white dashed line indicates the beam path through the vacuum chamber.

For the calibration of the SiPIN detector, 4 standards were used: CsBr, KCl, NaCl and InS. Fig. 3 corresponds to the spectra of the CsBr standard as an example. The x-ray emission lines are extracted from [3]. With reference to known energy peaks, centroid positions (channels) equivalences were found.
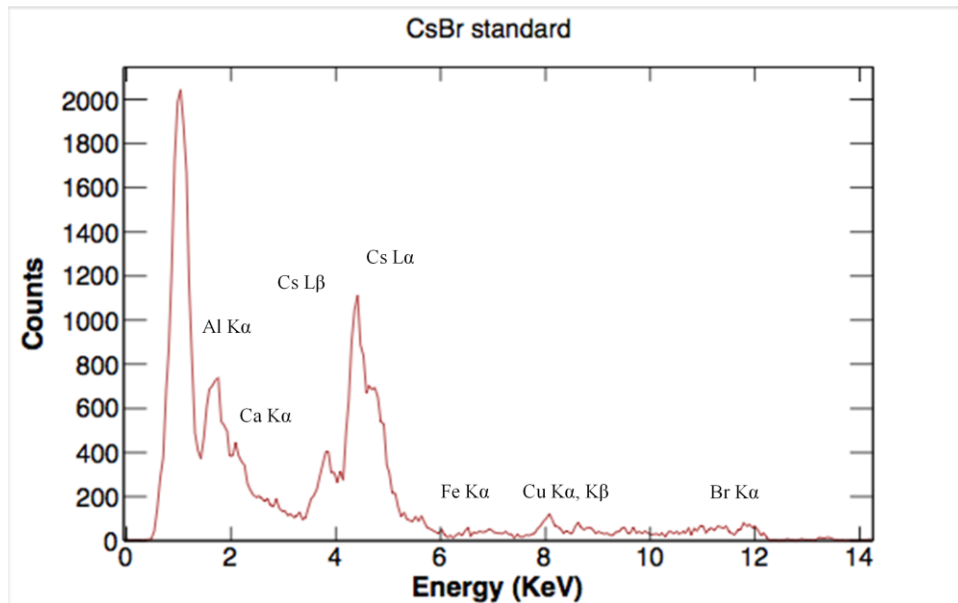
FIG. 3. CsBr standard which noticeable elements include Al, Cs, Ca, Fe, Cu and Br.

The selected standards provided a wide range of energies to form a linear regression by plotting against the energy value, creating a calibration curve, shown in Fig. 4.
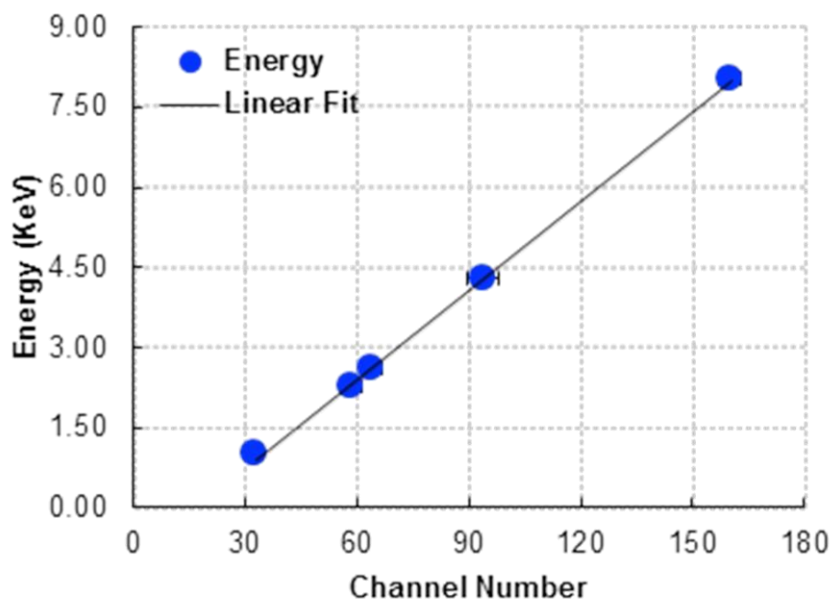
FIG. 4. SIPIN detector calibration curve. Various peaks from the CsBr, KCl, InS and NaCl standards were used.

Results

The samples given by the Chemical Engineering department were poly-dialyldimethyl-ammonium-chloride (a.k.a PDAC) and poly-styrene-sulfonate (a.k.a. PSS) that were treated either with KBr or NaCl. Fig. 5 shows the spectra of one of the KBr and NaCl treated polymers, in the left and right panels, respectively. Additional elements were found in the analysis such as S, Al, Cu, Ca and Fe, the last 4 from the target ladder.

The concentrations of the samples were found using the GUPIXwin software as analysis tool. The software allows the user to enter certain parameters such as beam charge, H-value standardization, starting channel, and the elements contained in the sample, all of which can be tuned to obtain concentration values for the samples, using the standards. The concentrations are calculated using Eq. (1) as follows:

$$Concentration = \frac{I_Z}{I_{Z,0} * Eff * H * Q} \qquad (1)$$

where *Eff* is the efficiency of the detector at a particular energy, Iz is the x-ray intensity, $I_{z,o}$ is the theoretical x-ray intensity, Q is the amount of beam charge hitting the sample and H is a ratio of measured to computed x-rays.
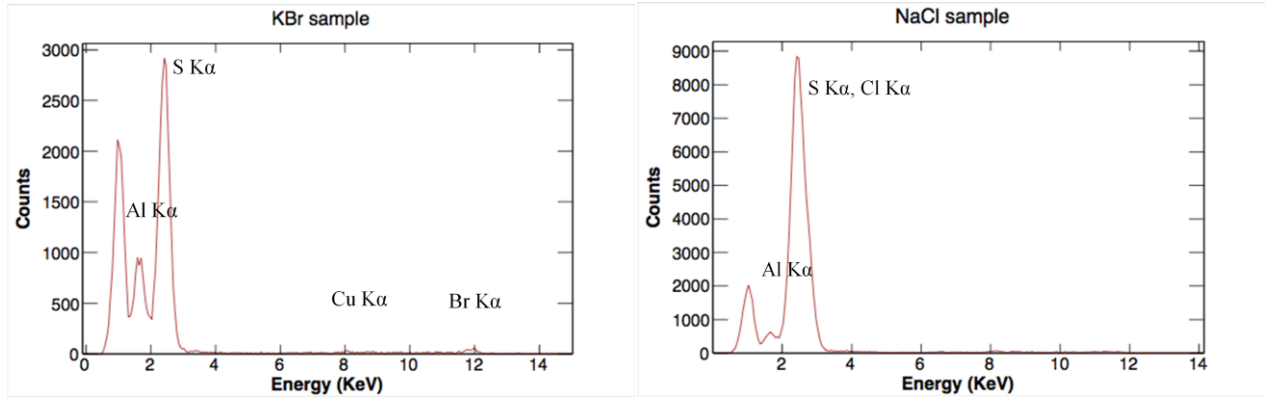
FIG. 5. KBr and NaCl samples in the left and right panels respectively. Both the KBr and the NaCl samples consistently showed a considerable high concentration of S.

With GUPIXwin we analyzed 9 KBr samples and 5 NaCl samples. We found K, Br and Cl concentrations as well as high concentrations of S. The preliminary results are shown in Fig. 6 left and right panels for the KBr and NaCl samples, respectively. The elements found in the samples are consistent with the expectations from the Chemical Engineering Department: the concentration of K is the lowest of all and the appearance of high concentrations of S coming from the sample's production process. The work is still in progress.
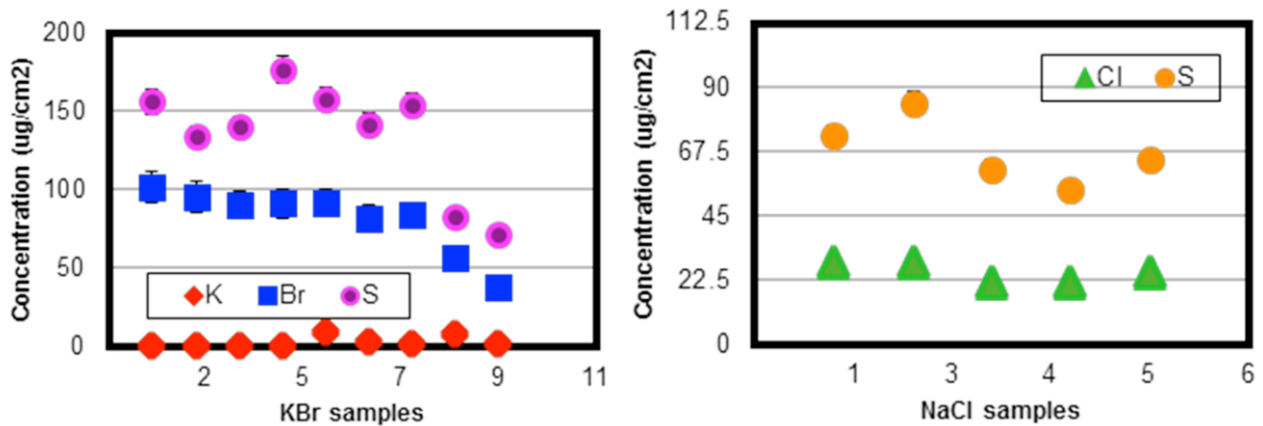
FIG. 6. KBr (left panel) and NaCl (right panel) concentrations. To find the concentration of the samples, the parameters of the standards were calculated and then applied to the samples in GUPIXwin. The 10% error accounts for the uncertainty in the beam current calculation.

In conclusion, the implementation of the PIXE experiment with the K150 cyclotron proton beam was successful. Not only can a spectra's composition be determined through PIXE, but also the concentrations can be calculated.

[1] M.B.H. Breese, D.J. Jamieson, and P.J.C. King, *Materials Analysis using a nuclear microprobe*, (John Wiley & Sons, New York, 1996).

[2] J.A. Maxwell, J.L. Campbell, and W.J. Teesdale, Nucl. Instrum. Methods Phys. Res. **B43**, 218 (1989).

[3] J.A. Bearden, *X-Ray Wavelengths*, XRay Emission Lines, Review of Physics, Jan.1967.

Progress in the calibration of Kr+C with the FAUST-QTS

A.B. McIntosh, A. Keeler, L.A. Heilborn, J. Gauthier, A. Jedele,
A. Rodriguez Manso, A. Zarrella, and S.J. Yennello

To investigate the previously reported asymmetry dependence of the caloric curve [1-3], reactions of ^{78,86}Kr + C @ 15,25,35MeV/u were measured with the FAUST array and the Quadrupole Triplet Spectrometer. Progress in the FAUST calibration and particle identification is discussed in this report.

The particle ID in FAUST [4] is achieved with the ΔE-E technique in Si-CsI. A representative spectrum is shown in the upper panel of Fig. 1 (note the log-log scale). The spectrum shown is for detector 21 for the ^{86}Kr+C @ 25MeV/u. As discussed in [5], the particle ID loci are linearized according to a simple parameterization [You2013]. The linearized distribution is shown in the lower panel of Fig. 1. Here, peaks are seen for ^{1,2,3}H, ^{3,4,6}He, ^{6,7}Li, and ^{7,9,10}Be; gates are set around each of these peaks as indicated by the coloring. In the upper panel, particles inside each cut are redrawn with the corresponding color to illustrate the efficacy of the particle ID. This identification procedure is effective for the majority of detectors, but improvements remain to be made (predominantly for rings A and B).
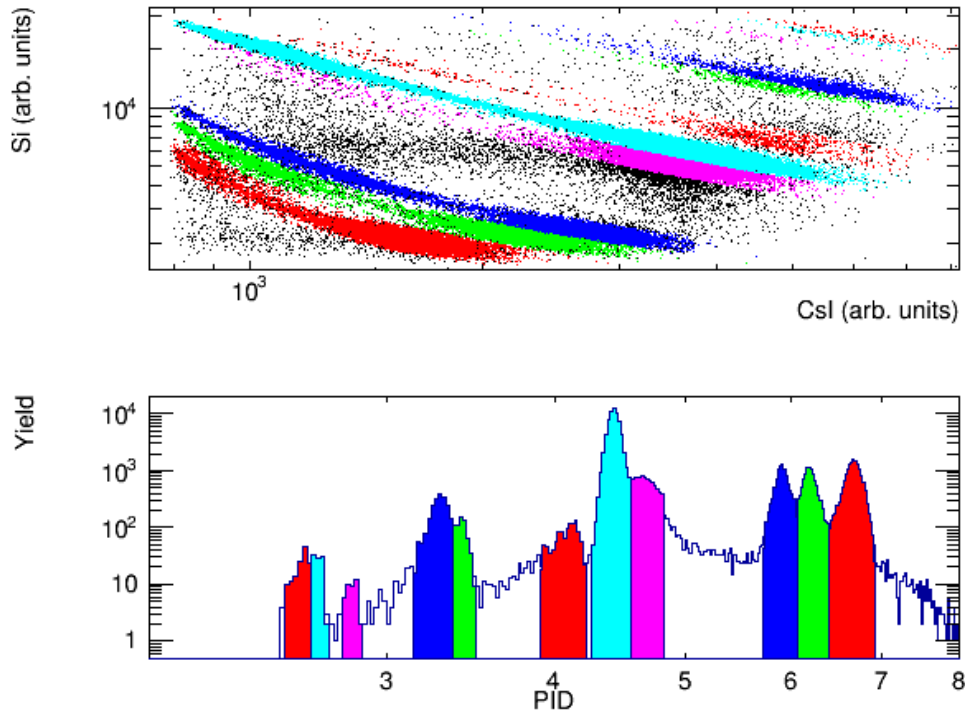
FIG. 1. Particle ID using ΔE-E method. Upper panel: Energy in ΔE(Si) vs energy in E(CsI). Particles are colored according to their extracted ID. Note the log-log scale. Lower panel: linearized PID value. Coloring is the same as in the upper panel. From right to left, isotopes of hydrogen, helium, lithium and beryllium are observed.

The energy calibration of the silicon detectors was previously described [McI17]. To verify the consistency of the calibration, the distribution of energies deposited by a single particle type in silicon detectors is examined. Fig. 2 shows the energy deposited in the silicon by alpha particles in detectors 21, 23, 25, 27, 29, 31, 33, and 35, which are all at the same polar angle in the laboratory. The coloring shifts from yellow (det 21) to red (det 35). The solid lines correspond to the neutron-poor ^{78}Kr @25MeV/u beam; the dashed lines correspond to the neutron-rich ^{86}Kr @25MeV/u beam. The distributions are generally the same shape, scale, and yield, suggesting that the energy calibration is consistent across detectors and across time. This is generally true for detectors in rings C, D, and E; improvements are generally necessary in rings A&B.
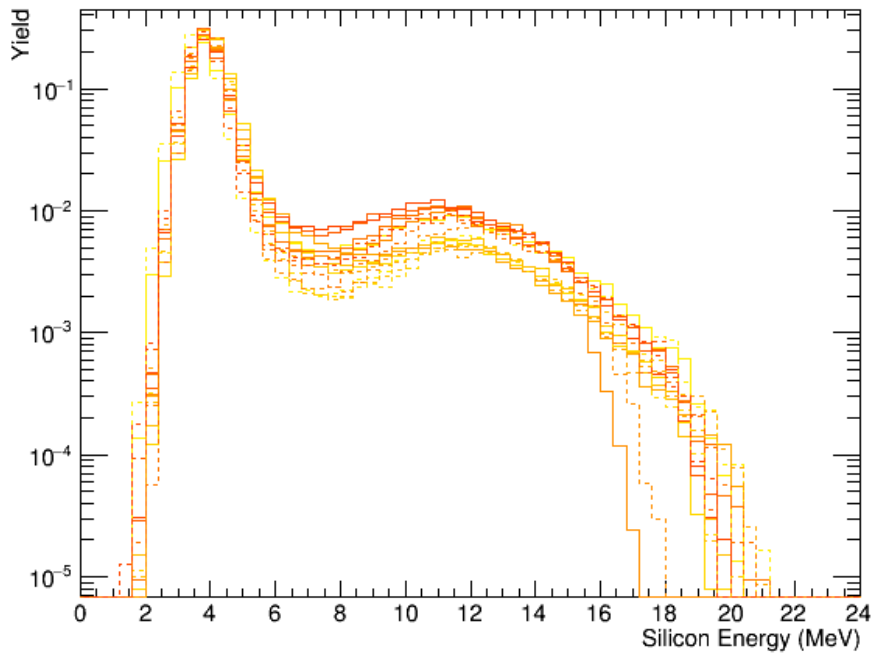
FIG. 2. Calibrated energy deposited in some of the ~300um Si detectors by alpha particles. Detectors shown are all at the same polar angle. Solid lines show spectra for ^{78}Kr beam and dashed for the ^{86}Kr beam; all are at E_{beam}=25MeV/u.

The calibration of the CsI is based on the calibration of the silicon, the particle ID, and energy loss calculations. This is illustrated in Fig. 3 for alpha particles produced in ^{86}Kr+C @ 35MeV/u measured in detector 21. In the upper panel, the measured digitized signal ("light output") in the CsI is plotted on the vertical axis. The measured energy in MeV in the silicon detector is used by CycSrim to calculate the energy the alpha particle deposited in the CsI detector; this latter quantity is plotted on the horizontal axis. The yield is indicated by the color in linear scale; the closed black circles correspond to the mean light output as a function of the energy. This is fit (red curve) according to the parameterization

of Parlog et al. (eqn7) [Par02]. In the lower panel the relative deviation from the fit is shown. This illustrates the procedure, which is in progress.
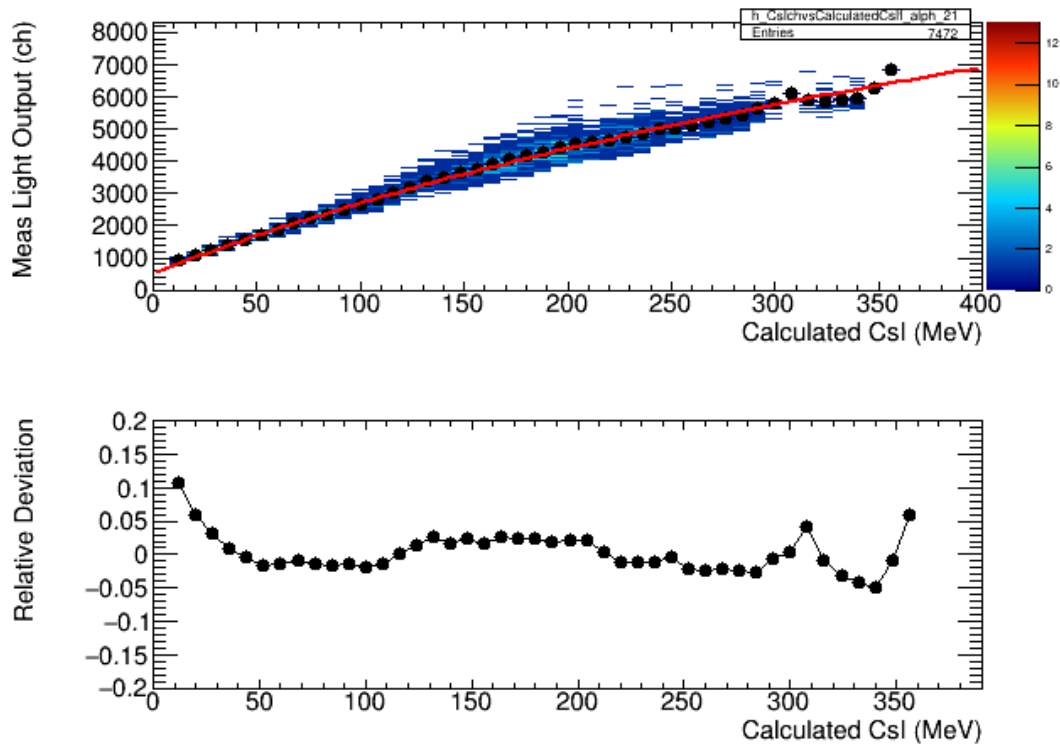
FIG. 3. Method of calibrating the CsI(Tl) detectors based on the calibrated silicon detector and the particle ID. Upper panel: measured (digitized) light output in channels vs energy deposited in the CsI calculated using the silicon energy event by event. The red line shows the result of a fit of the form from Parlog et al. [Par02]. Lower panel: relative deviation describing the accuracy of the fit to the mean light output vs energy.

[1] A.B. McIntosh *et al.*, Phys. Lett. B, **719**, 337 (2012).

[2] A.B. McIntosh *et al.*, Phys. Rev. C **87**, 034617 (2013).

[3] A.B. McIntosh *et al.*, Eur. Phys. J. A **50**, 3 (2014).

[4] F. Gimeno-Nogues *et al.*, Nucl. Instrum. Methods Phys. Res. **A399**, 94 (1997).

[5] A.B. McIntosh *et al.*, Progress in Research, Cyclotron Institute, Texas A&M University (2016-2017) p. IV-44.

[6] M.D. Youngs, Ph.D. Thesis, Michigan State University, 2013.

[7] M. Parlog *et al.,* Nucl. Instrum. Methods Phys. Res. **A482**, 693 (2002).

Test runs the multi-nucleon transfer reaction detector array for synthesis of heavy elements

A. Wakhle, K. Hagel, A.B.Mcintosh, M. Barbui, J. Gauthier, A. Jedele, A. Rodriguez Manso,
J.B. Natowitz, R. Wada, S.Wuenschel, A. Zarrella, and S.J. Yennello

An IC-Si and YAP active catcher array was constructed in 2016 [1] to study multi-nucleon transfer reactions forming heavy elements. The array consists of 40 YAP scintillating detectors coupled to Hamamatsu PMTs via Lucite light guides at forward angles, and 8 IC-Si detectors at backward angles (see Fig. 1). In August 2016, experimental data were taken using this array: a beam of ^{238}U at 7.5 MeV/nucleon was incident on a ^{232}Th target. Digital signal processing was achieved using the Struck SIS3316 250MHz Flash ADC modules, and worked very well in conjunction with the YAP based active catcher array.
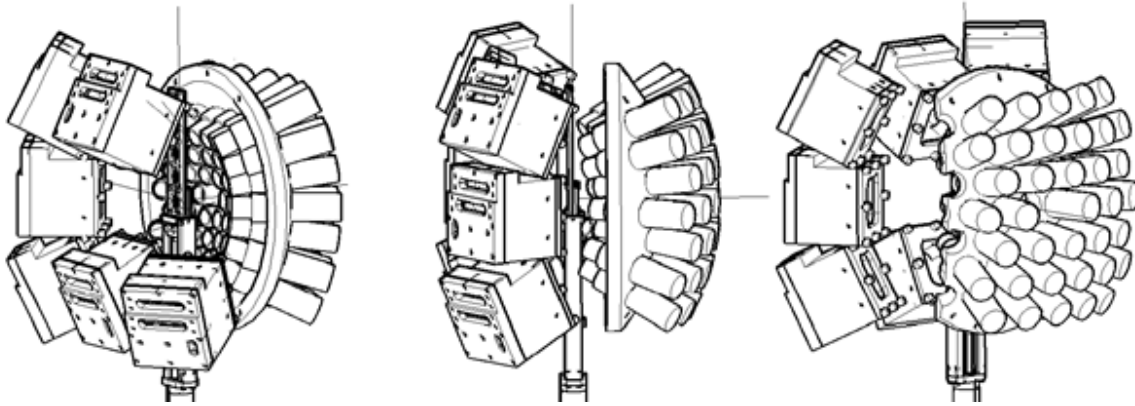
FIG. 1. Schematic of IC-Si and YAP detector array.

The results of this experiment have been recently accepted for publication [2], and this first 'physics' measurement has shown tantalizing glimpses into the synthesis of elements with Z as high as 116. Differential cross sections are also presented in [2]. Clear identification of alpha chains was not possible due to the difficulty of analysis, and the relatively uncharted and violent reaction landscape of ^{238}U+^{232}Th.

We are preparing for a series of test runs with the motivation to benchmark the detector against a previously measured reaction (^{22}Ne+^{232}Th), and a second reaction (^{208}Pb+^{208}Pb) populating residues with known alpha decay energies and half-lives. Details of the two proposed reactions follow:

^{22}Ne + ^{232}Th

A ^{232}Th target will be bombarded with a ^{22}Ne beam at 143 MeV (6.5 MeV/nucleon) to measure the production cross sections of ^{227}Th, ^{226}Ac, ^{225}Ac and ^{224}Ac. These nuclides are long-lived and will be implanted in the forward angle YAP Active Catcher, to determine their activities/cross sections by simple alpha counting in a backward angle Si+IC array. The cross sections will be compared to the measurement

of Kumpf and Donets [3].

^{208}Pb + ^{208}Pb

A ^{208}Pb target will be bombarded with a ^{208}Pb beam at 1456 MeV (7 MeV/nucleon) to measure the production cross sections of nuclei with 82<Z<92 and 208<A<228. These nuclides decay primarily by alpha emission with alpha energies between 7MeV and 10MeV, and half-lives ranging from ~1s down to a few 100ns. The ability (and efficiency) of the detector array to identify alpha chains will be benchmarked against known alpha chains in this region of the nuclear chart, and to establish parent-daughter relationships.

We expect these measurements will streamline the analysis procedure for future campaigns, and help identify alpha chains in decays of nuclides with Z>110. The measurements will be performed under identical trigger logic and detector setup to the previous experiment (see annual report from 2017 [4]). All detector signals will be processed using the Struck SIS3316 250MHz Flash ADC modules.

[1] S. Wuenschel *et al.*, *Progress in Research*, Cyclotron Institute, Texas A&M University (2015-2016), p. II-21.
[2] S. Wuenschel *et al.*, arXiv:1802.03091 (2018).
[3] H. Kumpf and E.D. Donets, Soviet Phys. JETP **17**, 3 (1963).
[4] S. Wuenschel *et al.*, *Progress in Research*, Cyclotron Institute, Texas A&M University (2016-2017), p. II-15.

Timing capabilities of the ParTI phoswich array

A. Zarrella, E. Churchman, J. Gauthier, K. Hagel, A. Jedele, A.B. McIntosh, A. Rodriguez Manso,
A. Wakhle, and S.J. Yennello

The Partial Truncated Icosahedron (ParTI) phoswich array [1] is made up of 15 phoswich detectors arranged on faces of the truncated icosahedrons geometry. The array has approximately 2π solid angle coverage. Its modular design allows for flexibility in its applications as detector units can be easily added or removed from the truncated icosahedron geometry or the detectors can be rearranged to form other geometries such as a wall. The phoswich detectors are designed in 3 different geometries - hexagonal, pentagonal and 3 partial hexagonal constructions. The regular hexagonal and pentagonal geometries correspond to the appropriate faces of the truncated icosahedrons shape. The three partial hexagonal detectors are designed such that there is a hole through the middle and they populate the single hexagonal face that the beam passes through. Each phoswich detector consists of a 3 mm thick piece of EJ-212 fast scintillating plastic, a 1 cm thick CsI(Tl) crystal and a 1 inch thick light guide which mates the face of the CsI to the face of a 1924a Hamamatsu photomultiplier tube (PMT).

The ParTI array has been utilized in two experiments for the purpose of detecting low energy charged pions. The first of those experiments was conducted at the Paul Scherrer Institute (PSI) where beams of charged pions were scattered into ParTI phoswiches to characterize the detector response. The second experiment was a cross section measurement for the pionic fusion reaction ^{4}He + ^{12}C → ^{16}N + π^+ conducted at the Cyclotron Institute. Over the past year, analysis of the data collected during these two experiments has highlighted many of the timing capabilities of the array when used with the Struck SIS3316 digitizers. Specifically, we have shown the capability to measure the mean lifetime of μ+ using the time difference between the pion implantation and the muon decay response, construct event coincidences from two separate detector systems within an experiment, and selectively look for rare decays by searching for events which are uncorrelated with the beam RF frequency.

The pion beam data from PSI has already been used to show that the ParTI phoswiches are capable of identifying charged pions based on their energy lost in the two scintillating components using a fast vs. slow pulse shape discrimination method on the detector's response to the pion's implantation [1]. Once implanted, the pion will quickly decay into a muon with an average lifetime of 26 ns which will be followed by the muon's decay into a positron with an average lifetime of 2.2 μs. Since the entire detector response is being recorded we have access to timing information associated with these particle decays. In general, the pion's decay into the muon happens too fast and deposits too little energy in the detector for its response to be distinguished from the much larger implantation response. The muon's decay, however, is regularly easily separated from the implantation due to its much longer average lifetime and its larger deposited energy. For each event that is identified as a π^+ primary using fast vs. slow particle identification (PID), the time is calculated between the beginning of the particle implantation response and the muon's decay (dt). This distribution of times can then be used to create a decay curve for muons. Fig. 1 shows this experimental curve for one of the phoswiches used in the PSI experiment. An exponential fit of this data (the red curve overlaid on Fig. 1) can then be used to extract

the measured mean lifetime for μ+. For the three phoswiches in the PSI experiment, the measured muon lifetimes are within 2% of the known value. This is an exceptionally strong indication that the ParTI phoswiches are behaving as expected with respect to the detection of π^+.

During the pionic fusion experiment, data was being collected simultaneously using a silicon stack at the focal plane of the Momentum Achromat Recoil Spectrometer (MARS) [2] and inside the
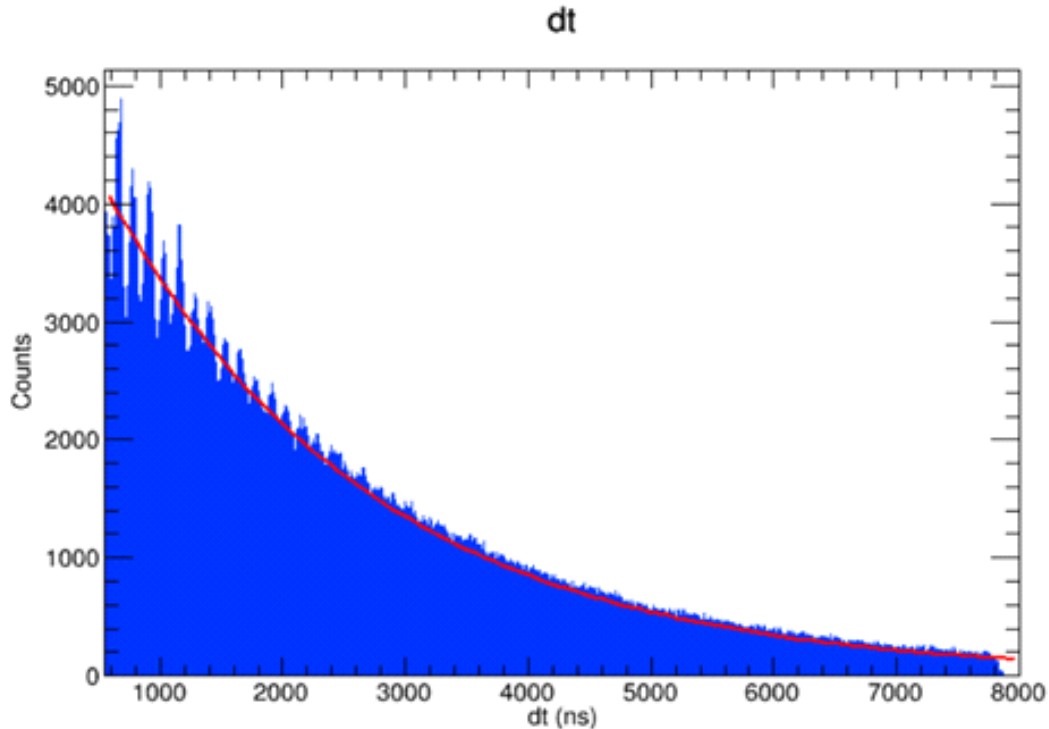
FIG. 1. The decay curve for μ^+ measured by a ParTI phoswich during the PSI charged pion beam experiment. The horizontal axis is the time difference, dt, between the implantation of the charged pion and the pulse due to the decay of the muon in ns. The red curve is an exponential fit of the data from which the average lifetime is extracted.

line's target chamber using the ParTI array, approximately 75' upstream. In the case that a particle was detected in the MARS silicon, the ParTI phoswiches were recorded as slaves. The phoswiches, however, are subject to a much higher rate of incident charged particles in the target chamber so it becomes necessary to determine whether a phoswich response was due to a charged particle originating from the same event as the particle in the MARS silicon. In order to do this, the ParTI signal's time location within its digitization window is found for each event that the phoswich was read as a slave to MARS. When sorted on the identification of the particle in MARS (because the velocity of the transported particle changes with species according to Bρ), the distribution of ParTI signal times shows a sharp peak corresponding to particles detected in the phoswiches from coincident events with the MARS particle.

Fig. 2 (a) shows this distribution of phoswich signal times when the event was triggered by a ^{7}Li particle detected at the MARS focal plane. The horizontal axis is the time bin location of the start of the phoswich signal and a clear peak is present corresponding to event coincidences. This peak location can

be extracted for each MARS-identified particle type (with sufficient statistics) and the time bin location can be compared to the velocity of that particle given the MARS Bρ setting. Fig. 2 (b) shows the calibration of the phoswich signal's relative time bin given the velocity of the particle identified in MARS. On an event-by-event basis, then, a particle detected in a phoswich can be determined to be from the same event as a particle detected at the MARS focal plane if the timing of the phoswich response is consistent with the calibration in Fig. 2 (b).
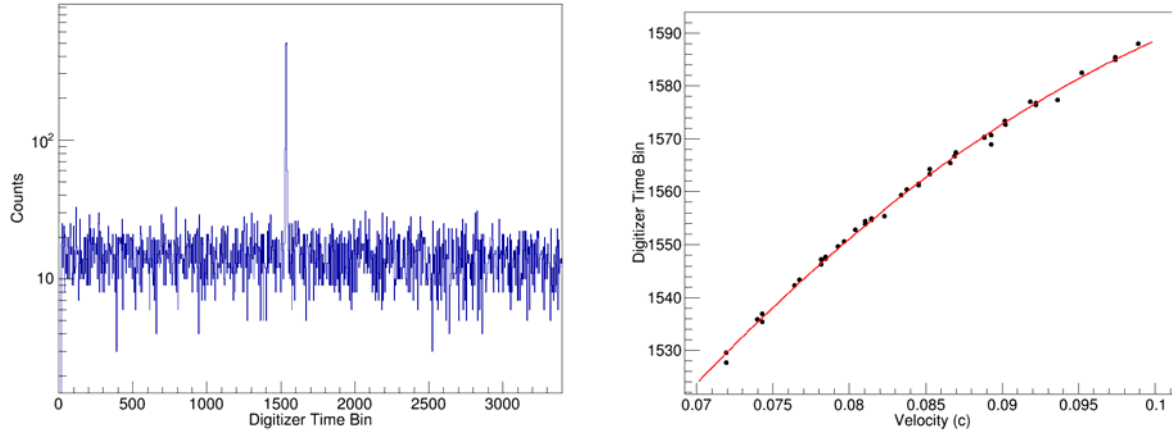
FIG. 2. (a) The distribution of phoswich signal times within the digitization window when the phoswiches are recorded as slaves when a ^{7}Li particle is detected at the MARS focal plane. The horizontal axis is the time bin where the signal begins and the time bins are 4 ns wide. The sharp peak corresponds to phoswich signals which come from the same event as the detected ^{7}Li. (b) After extracting the peak locations for all MARS-identified particles, the time bin location of the phoswich signals can be correlated with the velocity of the particle at the back of MARS. This calibration can then be used to determine on an event-by-event basis whether a phoswich signal is from the same event as the MARS particle.

During the pionic fusion experiment, the phoswiches were also allowed to trigger events according to a muon decay trigger which was developed to selectively identify pion candidate events. The muon decay trigger works by searching for a second instance of a signal passing the CFD threshold within a single digitization window. Fig. 3 (a) shows an example of an experimental signal which passes the muon decay trigger conditions. For a pion primary event, the second pulse corresponds to the decay of the muon daughter of the implanted pion. However, a common background process is true pile up of events within the 8 μs window. Fig. 3 (b) shows the distribution of the times of the first phoswich response within the digitization window. The figure's time axis has been zoomed in so that the structure can be observed. As a feature of the trigger, the second pulse is always located at the same time bin location. The distribution, therefore, is effectively a distribution of the time difference between the first and second phoswich response. The periodic peaks in Fig. 3 (b) correspond to the RF frequency of the cyclotron. Thus, events within these peaks are more likely to be pile up. Pion primary events which are followed by muon decays are not correlated with the cyclotron frequency, though, so one can selectively look for pion candidates by considering only events which populate the valleys between the RF peaks. This reduction of background candidates greatly increases the sensitivity of the search for true pion events.
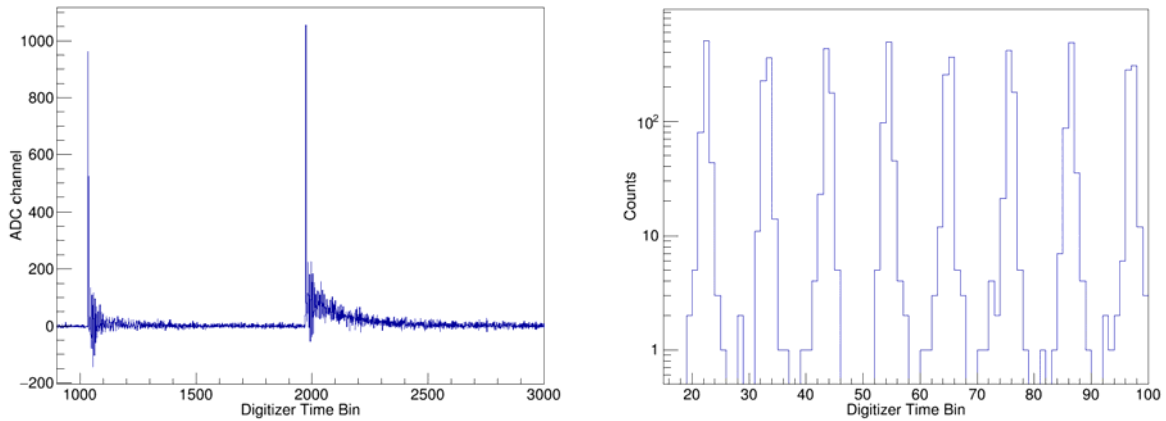
FIG. 3. (a) An example of a phoswich signal recorded during the pionic fusion experiment which satisfied the muon decay trigger conditions. The horizontal axis is in units of the 4 ns digitizer time bins. (b) The distribution of time bin locations of the first phoswich peak in events that satisfy the muon decay trigger zoomed in on an arbitrarily chosen section of the distribution so that the structure can be observed. The peaks in the distribution are due to true pile up events coming from different beam bursts and the frequency in the data corresponds to the cyclotron RF frequency.

Future work regarding the ParTI array will include a detailed publication describing the instrument and its observed pion and light charged particle detection capabilities. Analysis of the data collected in the PSI and pionic fusion experiments is also still ongoing.

[1] A. Zarrella, *et al*. Physics Procedia. **90**, 463 (2017).

Progress with testing automated particle identification

J. Gauthier, A.B. McIntosh, K. Hagel, S.J. Yennello, S. He[1] and J. Huang[1]

[1]*Department of Statistics, Texas A&M University, College Station, Texas*

In references [1] and [2], a new method to automatically identify particles in dE-E raw spectra has been described. In summary, the dataset for each spectrum is put to a square-root scale to equalize the distance between each atomic element group (Z) and a Fourier transform is applied to filter the frequency components. Then the program runs in three steps: it first searches for local maxima, then builds groups around those maxima (corresponding to the atomic elements) and finally fits the lines with a spline interpolation in order to linearize the data and separate the different isotopes.

In September 2017, the program was installed on a local Cyclotron computer and during the last few months several tests have been performed to evaluate the performance of the technique when confronted with different spectra from different detectors and experimental datasets. To test the program with a perfect-like spectrum, we simulated dE-E correlation data files using the CycSrim application as shown in Fig. 1. Fig. 2 shows the fit result at the end of the procedure. So, for generated data the program seems to work fine.
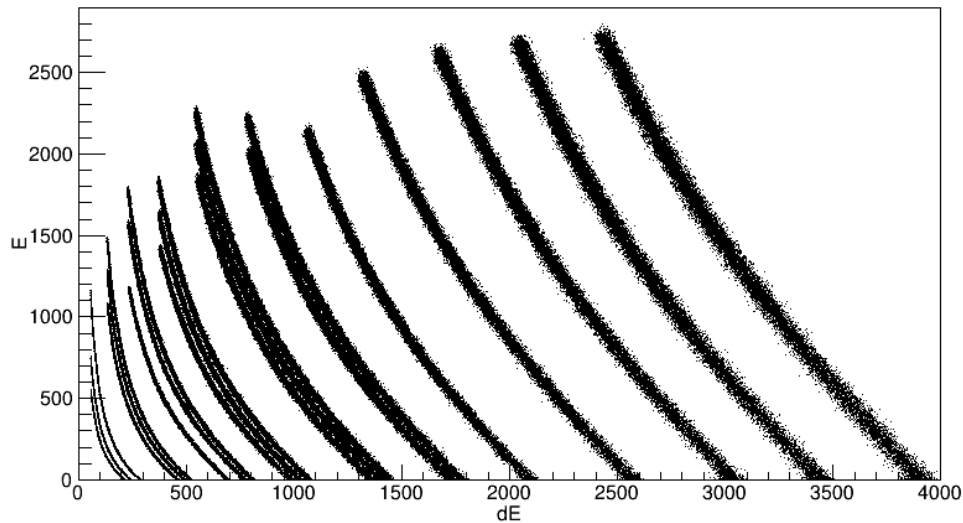
FIG. 1. CycSrim generated E vs dE spectra. Energy resolution is set to 2%.

For the initial program development and parameter tuning a real experimental dataset from a NIMROD Si-CsI(Tl) detector [3] was used. This spectrum has high statistic and very good charge and isotopic resolution. We can see in Fig. 3 that the procedure works well for this particular dataset. So we tested the program with several other detectors from different experiments and unfortunately, it seems that the program is not able to fit any other dataset than the one used for its development. In Fig. 4, we present an example of one of those failed attempts. As we can see, some fit lines are incomplete and some groups
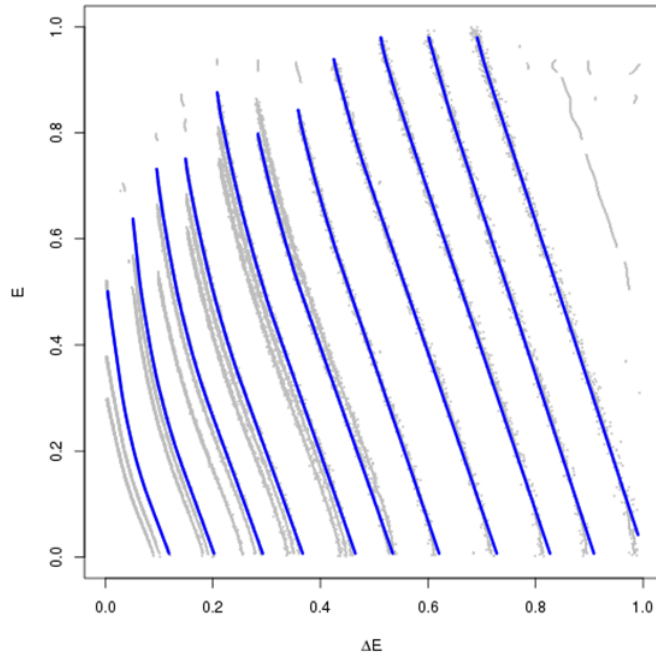
FIG. 2. Fit results from Figure 1 spectrum. Grey points are the square-root transformed data and the blue lines are the final fits for each Z.

are ignored. There are several possible explanations for these malfunctions. First, the program parameters have been tuned using the original dataset and might not be optimal for any others. Secondly, not enough statistics prevents the program to find enough maxima and thus leads to incapacity to create groups. Also, when the top of two Z lines in E vs dE spectra are too close to each other the program thinks it's a single group and merges them together.
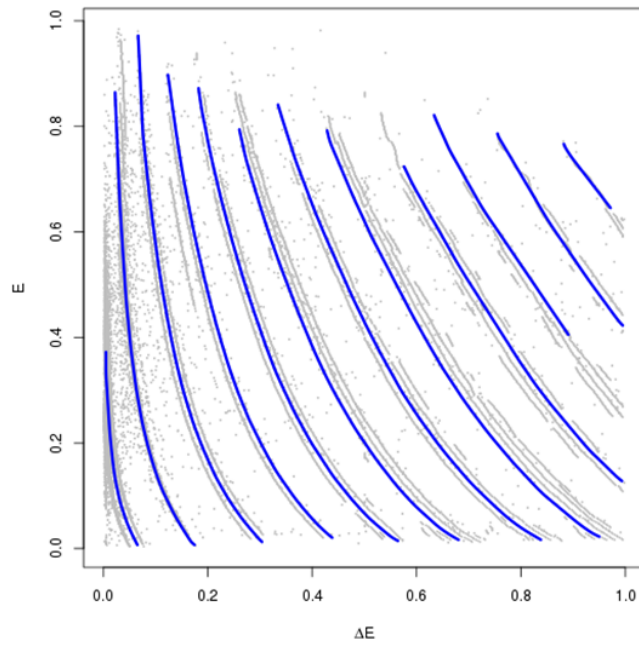
FIG. 3. Fit result for the program development experimental dataset.
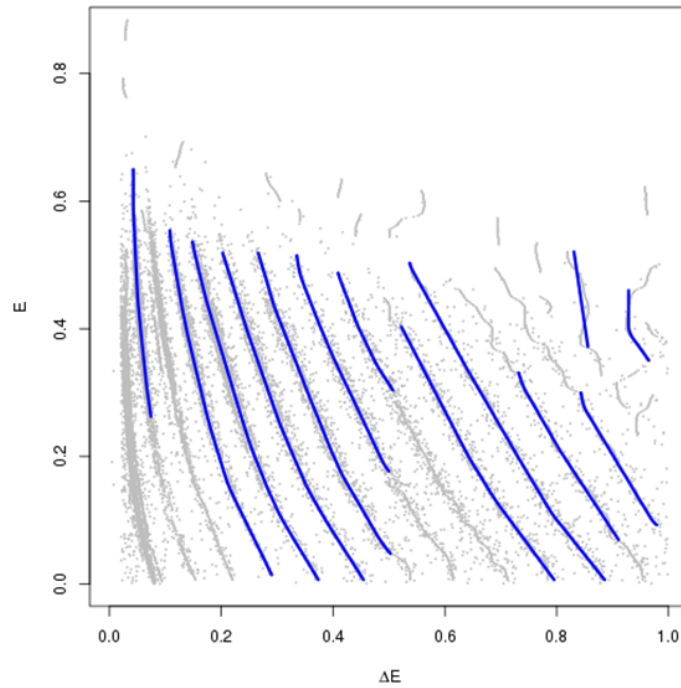
FIG. 4. Fit result for a random experimental dataset.

The technique has thus to be rethought and overhauled to work with imperfect and low statistic dataset, which are most of the real world experimental spectra. A solution could be to tell the program where the groups are by manually putting a single point on the top of each Z line. We are currently still working with the Department of Statistics to find a solution to make this program a suitable tool for our analysis.

[1] A.B. McIntosh *et al., Progress* in Research, Cyclotron Institute, Texas A&M University (2015-2016), p. IV-65.
[2] A.B. McIntosh *et al.*, *Progress in Research*, Cyclotron Institute, Texas A&M University (2016-2017), p. IV-47.
[3] S. Wuenschel *et al.,* Nucl. Instrum. Methods Phys. Res. **A604**, 578 (2009).

TAMUTRAP commissioned: 1st mass measurement using a uniquely-designed cylindrical Penning trap

V.S. Kolhinen, Nasser Morgan, Asim Ozmetin, D.Melconian, P.D.Shidling, and B. Schroeder

The Texas A&M Unviersity Penning Trap faiclity (TAMUTRAP) facility was commissioned with a prototype cylindrical Penning Trap by performing high precision mass measurement of stable isotope of sodium (^{23}Na). The electrode structure is based on our novel design [1] with a much larger radius-to-length ratio compared to any other existing trap [1]. The details of the prototype Penning trap system have been discussed in our previous year annual report [2, 3].

Mass measurements in a Penning trap are based on a comparison of the cyclotron frequencies of the ion of interest and that of a mass reference ion. It is here assumed that the change in the magnetic field can be neglected during the time the cyclotron frequencies of the two ion species are measured. If the reference ion is denoted by subscript 1 and the ion whose mass is to be measured by subscript 2 the following relation is obtained:

$$\omega_{c1}(2\pi f_1) = \frac{q_1 B}{m_1}; \ \omega_{c2}(2\pi f_2) = \frac{q_2 B}{m_2} \ ; \ \frac{f_1}{f_2} = \left(\frac{q_1}{q_2}\right)\left(\frac{m_2}{m_1}\right)$$

In our case, we used ^{39}K as our reference mass (f_1) and performed mass measurement of ^{23}Na (f_2). As mentioned in previous annual reports [2], the mass of an ion is determined via its cyclotron frequency. At the TAMUTRAP facility, we measured the cyclotron frequency by the time-of-flight ion cyclotron resonance method (TOF-ICR). The TOF-ICR is a destructive technique in the sense that the trapped ion is lost in the detection process and the trap has to be reloaded in each cycle. The technique involves manipulating the ions eigenmotions and probing the cyclotron frequency using an external radiofrequency field and measuring the flight time of the ions ejected from the trap to a detector. Within the TOF-ICR technique, a resonant quadrupolar radiofrequency excitation signal with properly chosen amplitude and duration is applied on the four fold segmented ring electrode. The radial motions couple and the magnetron motion is completely converted into the modified cyclotron motion leading to a large increase in radial energy. The excited ions are ejected from the trap towards a counting detector. While travelling through the fringe field of the magnet, the ions get accelerated due to the gradient force. Thus the radial energy of the ions is the largest at resonance. This energy gain is directly transformed into a change in time of flight, and for optimum energy conversion into the cyclotron motion a minimum in flight time is observed at the frequency of the unperturbed cyclotron frequency.

A MCP detector with an active area of 32 mm was placed 1.5 m downstream from the center of the trap to detect the ions ejected from the trap. As a first step towards the mass measurement, we optimized the cooling time before the excitation by recording timing spectrum for different trapping time. A Gaussian shape timing spectrum was observed for trapping time more than 250 ms, which indicated that the ion motion were cooled by collision with background buffer gas (He) atoms present in the beam line. After estimating the cooling time, ion motion were manipulated by applying a quadrupole excitation

for 20 ms. The quadrupole excitation was applied to four-fold segmented ring electrode, where the RF voltage was applied to one pair of opposite segments is phase-shifted by 180 degree with respect to the RF voltage applied to the other pair of opposite segments. The TOF was recorded for 30 different frequencies close to the resonance value in steps of 10 Hz. We started the measurement with ^{39}K and switched to ^{23}Na. The first frequency scan for both the masses was carried out in less than 8 hours. Fig. 1 shows our first resonance curve observed for ^{23}Na and ^{39}K.
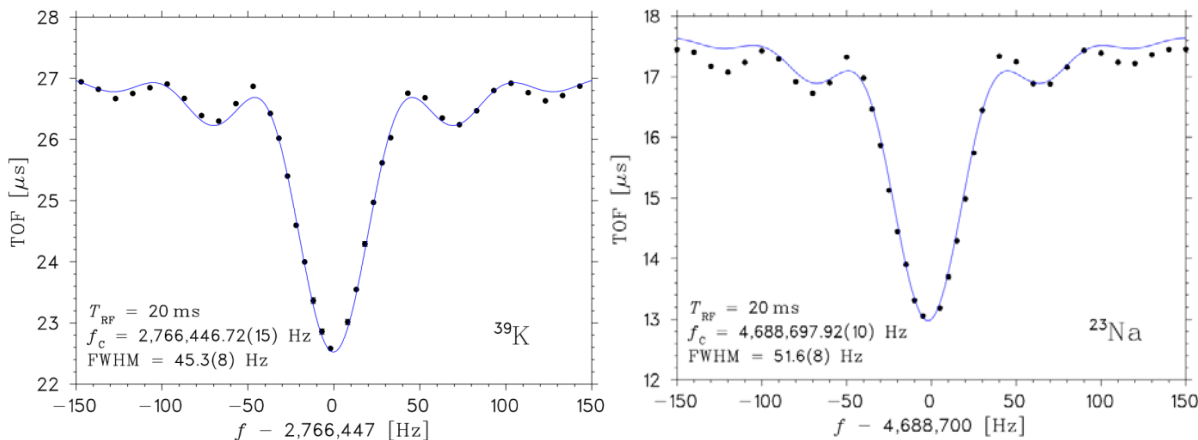
FIG. 1. Ion time-of-flight as a function applied cyclotron frequency for ^{23}Na^{1+} (left) and ^{39}K^{1+} (right) with an excitation time of 20 ms. The TOF is minimum at cycltron frequency, f_c. The mass resolving power of this resonance corresponds to 10 ppm.

We further performed the mass measurement with exciation time of 100 ms. For longer exciation time, we had slightly different configuration of quadrupole excitation. We first applied a dipole excitation at the magetron frequency ($f_{magnetron}$ = 830 Hz, excitation time t_{exc} = 10 ms, and amplitude V$_{pp}$ = 6.25 V) by applying RF voltage to one of the segment of ring electrode, and then the quadrupole excitaiton was applied for 100 ms by applying the RF voltage with same phase to one pair of opposite segments. There was no RF voltage applied to the fourth segment of the ring electrode. So far, we have performed around 10 mass scan with excitation time of 100 ms. During these scans the parameters of the Penning trap were set to 350 ms for cooling time , 10 ms t_{exc}, and 6.25 V$_{pp}$ for the magnetron excitation, while 100 ms t_{exc} and 3 V$_{pp}$ were used for the cyclotron excitation. The trap depth for all these scans was set to 200 V and the trapped ion energy was around 150 eV. After the quadrupole excitation, ions were ejected immediately without any additional cooling and that allowed for a better transport of ions to the detector. The mean value of the measured atomic mass value of ^{23}Na is:

$$m(^{23}Na) = 22.9897695 \ (10) \ u$$

The measured mass of ^{23}Na agrees with the literature value within a precision of 1.2×10^{-8} with measurement precision of $\delta m/m = 4 \times 10^{-8}$.

With the prototype trap commissioned and abiltiy to perform mass measurements demonstrated, we will be installing the TAMU Penning trap which is twice the dimension of the prototype Penning trap by end of June 2018.

[1] M.Mehlman *et al.*, Nucl. Instrum. Methods Phys. Res. **A712**, 11 (2010).

[2] E. Bennett *et al.*, Progress in Research, Cyclotron Institute, Texas A&M University (2015-2016), p.I-62.

[3] B.Fenker *et al.*, Progress in Research, Cyclotron Institute, Texas A&M University (2015-2016), p.I-50.

Making the world's largest Penning trap 2x bigger for beta-delayed proton decay studies

V.S. Kolhinen, D. Melconian, M. Nasser, A. Ozmetin, B. Schroeder, and P.D. Shidling

The goal of the TAMUTRAP project is to carry out β decay studies of superallowed $T = 2$ β-delayed proton transitions in order to gain information on the β-ν correlation parameter by observing the angular distribution of β and proton. The aim is to start with ^{32}Ar.

Our prototype cylindrical Penning trap, which has an inner diameter of 90 mm and thus is presently the world largest Penning trap, has been build and commissioned. We have performed mass measurements with stable ^{23}Na and ^{39}K singly-charged ions for the test purposes. See our other report [1] for details. However, in order to be able to carry out the planned measurement program, we need a cylindrical Penning trap that is double the size to contain the β-delayed protons which have a Larmour radius of $R_L \leq 45\,\text{mm}$.

The upgraded trap, which has a 180 mm inner diameter, has been designed with Autodesk Inventor program, the design of which is illustrated in Figure 1. The lengths of the electrodes are based on a novel design [2] that has a much larger radius-to-length ratio compared to open-ended cylindrical Penning traps. This made it possible to keep the trap length reasonable even given the large radius. See Table I for the electrode dimensions.

Table 1. Dimensions of electrodes of the new 180 mm Penning trap. The electrodes are 4 mm thick and distances between them are 0.5 mm. Injection and extraction holes in end plates have diameter of 5 mm..

Description	Length in mm
Ring electrode	29.17
Correction electrode	71.36
End electrode	80

The axial magnetic field for the trap will be created by using the present 7-T superconducting solenoid from Agilent Technologies with a warm bore 210 mm diameter. The new 180 mm Penning trap will be inserted in a 316LN-grade steel vacuum tube that will be inside the bore of the magnet. The vacuum tube has inner diameter of 197 mm which made the trap design challenging, since the outer diameter of the trap is 188 mm and the diameter of aluminium holders are 195 mm.

The design has been completed and the electrodes will be made of oxygen-free (OFE) copper and will be gold-plated. Electrodes are isolated from each other by ceramic (Aluminium Oxide) insulators and the trap structure will be held together by aluminium holders that have cylindrical shape.

Injection drift tube and extraction electrodes are also redesigned. They both have now 37 mm diameter and the extraction side electrode has been divided in three in order to be able control time-of-flight effect from trap to Microchannel-plate (MCP) detector in case the trap will be used in mass measurements.

We expect to get the all the parts from the workshop in mid May. After that the trap shall be assembled during the summer 2018 and tested with stable ions. Later the end plates will be replaced with silicon strip detectors that will used for detecting the out coming decay particles, see B. Schroeder's report [3].
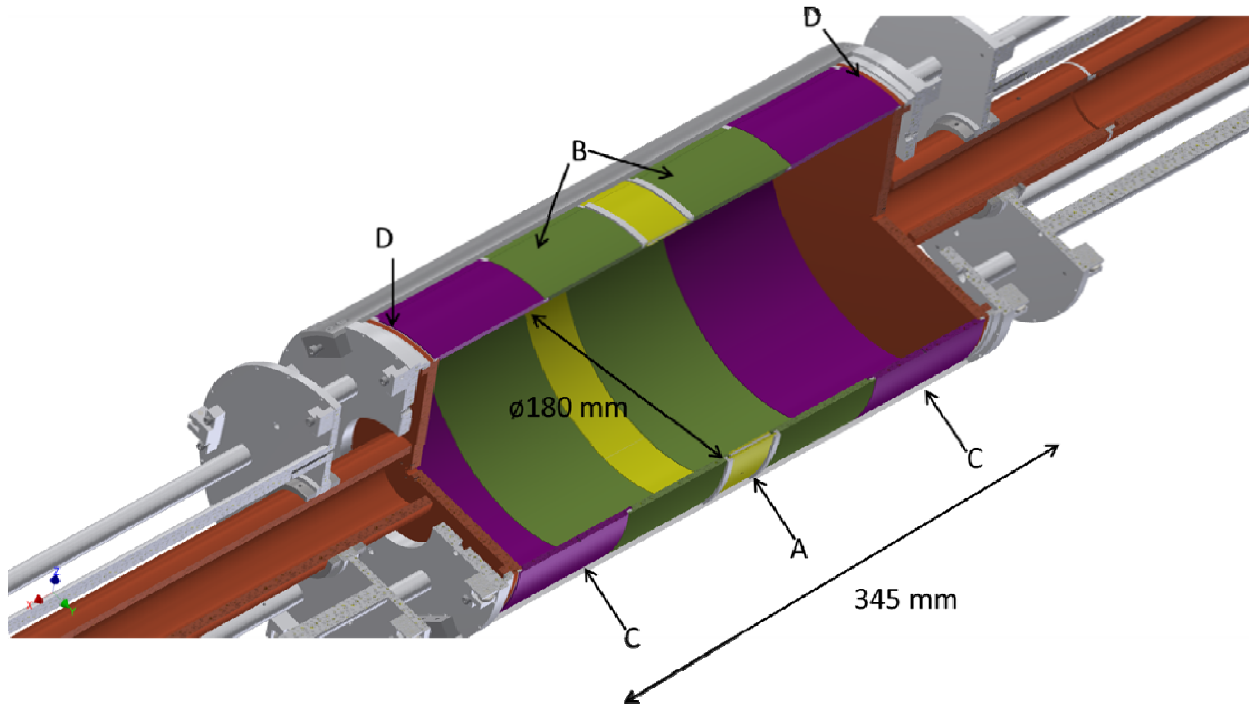
FIG. 1. The electrode structure of 180 mm diameter TAMUTRAP. The 4-fold split ring electrode has been marked as A, correction electrodes as B and end electrodes as C and end plates which are crucial part of this trap design as D.

[1] P.D. Shidling *et al.*, *Progress in Research*, Cyclotron Institute, Texas A&M University (2017-2018) p. IV-39.

[2] M. Mehlman *et al.*, Nucl. Instrum. Methods Phys. Res. **A712**, 11 (2010).

[3] B. Schroeder *et al.*, *Progress in Re*search, Cyclotron Institute, Texas A&M University (2017-2018) p. IV-44.

GEANT4 simulations of the TAMUTRAP facility

V.S. Kolhinen, D. Melconian, M. Nasser, A. Ozmetin, B. Schroeder, and P.D. Shidling

The TAMUTRAP facility has been built for β decay studies of superallowed $T = 2$ β-delayed proton transitions. The goal is to deduce the β-ν correlation parameter, $a_{\beta\nu}$, which is sensitive to possible scalar currents contributing to the dominant vector interaction of the standard model. By doubling [1] the world's largest Penning trap [2] to an inner diameter of 180 mm, the 7 T uniform field will fully contain delayed protons emitted with $E_p \leq 4.8$ MeV, and direct them to detectors regardless of the direction they are emitted. The program will start with 32Ar, and continue with a number of other similar T=2 β-delayed proton emitters: ^{20}Mg, ^{24}Si, ^{28}S and ^{36}Ca.

The protons are emitted isotropically in the intermediate nucleus's frame, but the intermediate nucleus recoils from the initial β decay and causes a Doppler broadening of the proton's energy spectrum. If the interaction is purely vector the β and ν tend to be emitted the same direction, whereas if it is scalar they tend to be emitted in opposite directions. The effect on the proton energy is shown in the left panel of Fig. 1 for the two interactions. Essentially, a measurement of the shape of the proton's energy spectrum can be used to test for scalar contributions, as has been demonstrated in Ref. [3] where they reached 0.5% precision. To reach our goal of 0.1% precision, we will measure the β as well, and whether it went in the same hemisphere as the proton or the opposite, thus breaking up the spectrum into the two shown in the right panel of Fig. 1. In this way, we will obtain a cleaner spectrum (due to the coincidence condition with the β) as well as increase our sensitivity by measuring the means (1st moments) of the two distributions instead of the shape (2nd moment) to deduce $a_{\beta\nu}$.
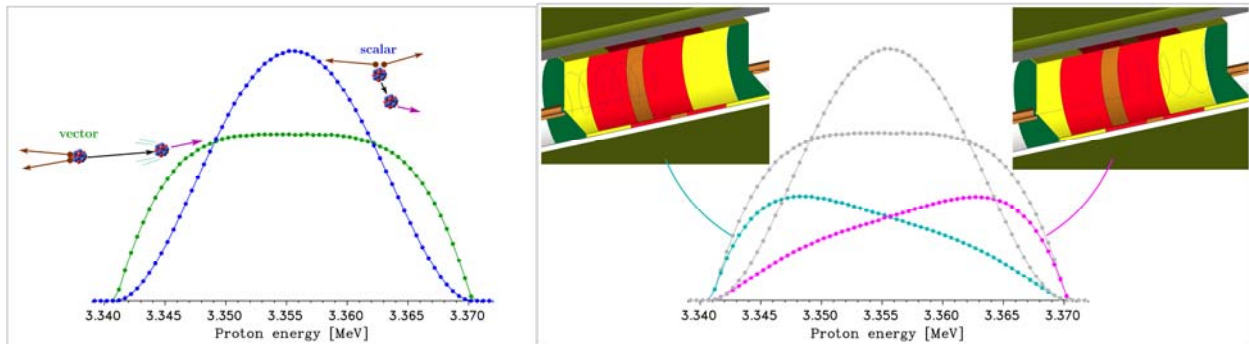
FIG. 1. Simulated energy spectrum from the decay of ^{32}Ar assuming a vector interaction compared to a scalar (left plot). Using a Penning trap to confine the ions and observing both the proton and β, we can break up the spectrum into two: one where the β went in the same hemisphere as the proton, and another where it was emitted in opposite hemisphere (right panel).

The design of the full-sized trap is completed and we have included the new geometry in our GEANT4 simulations. We are using these simulations to guide us towards an optimal detection system as we consider the specific geometry of the position-sensitive Si detectors we will use at either end of the Penning trap. SRIM simulations have determined the minimum thickness of the silicon detectors to capture the full energy of even the highest energy protons from the T = 2 β -delayed proton transitions.

While already useful for checking geometric efficiencies, the slight non-uniformities of our *B* field (far from the center of the bore), and effects arising from β backscattering, trap size, etc., there are many improvements yet to be implemented. These include: incorporating recoil-order corrections in the decay generator, adding branches to excited states other than the superallowed transition, and including a more realistic geometry once the design of the detectors is finalized. We will also use these simulations to optimize the analysis so we maximize our sensitivity to non-standard model physics.

[1] V.S. Kolhinen, *et al*., Progress in Research, Cyclotron Institute, Texas A&M University (2017-2018) p. IV-42.

[2] M.Mehlman, *et al*., Nucl. Instrum. Methods Phys. Res. **A712**, 11 (2010).

[3] E.G. Adelberger, *et al.*, Phys. Rev. Lett. **83**, 1299 (1999).

Control system for the TAMUTRAP beamline and Penning trap

R. Burch, V.S. Kolhinen, D. Melconian, M. Nasser, A. Ozmetin, B. Schroeder, and P.D. Shidling

TAMUTRAP is currently preparing itself for the installation of its newly designed Penning trap [1]. As we wait for the RIBs to become available, we are commissioning TAMUTRAP by measuring the masses of stable ^{23}Na [2]. For this, we need to scan the excitation of the ions with respect to the frequency of the RF applied to the trap. The present report discusses the progress on automating these scans.

The present setup in terms of instrumentation control and data acquisition is one that gets the job done, but not as efficiently as it could be. Much of our equipment is initialized for experiments via a mixture of hands-on adjustments, LabVIEW, and 3rd party software. The computer-controlled components are done primarily on a Windows computer. This is only worth mentioning given that we acquire data through a separate Linux computer utilizing our ROOT driven data-acquisition software.

The control system for TAMUTRAP is a two-phase project. In the first phase, we will automate the scanning process so that it does not have to be continuously tended to (every 2-3 minutes.) This is done over a length of typically 30 to 40 minutes. We have begun this by programming a Python script that will handle all processes through TCP connections. This design choice is powerful in that it allows us to communicate not only with instrumentation controls such as LabVIEW, but also other computers involved in the scanning process. This removes complications from running the system across two operating systems. In addition to improving the efficiency of time, such a system will allow us to preform many short scans instead of one long one for each frequency, thereby reducing the effect of drifts in the beam current and RF power. Another bonus is that the TCP communication method means we can run the 'handler' on either the Windows, Linux, or any other computer on the network in our offices.

Phase two is to merge and rebuild our many means of instrumentation control into fewer entities. The 3rd party software's in use are convenient, but can with some fortitude be replaced by LabVIEW scripts. From here we will combine our numerous arrangements into one grand LabVIEW controller (with only a few other less complaint to upgrade mechanisms). At this point we will have two main components for experimentation: the LabVIEW master controller, and the Python scan handler.

As it stands, we have our 'handler' operational, but is still accepting improvements. Its current operation is updating scan frequencies and running a placeholder Python scan script which will be replaced by the data acquisition system as soon as it's done upgrading to become compatible with the 'handler.'

[1] V.S. Kolhinen *et al*., *Progress in Research*, Cyclotron Institute, Texas A&M University (2017-2018) p. IV-42.

[2] V.S. Kolhinen *et al*., *Progress in Research*, Cyclotron Institute, Texas A&M University (2017- 2018) p. IV-39.

Update on the TAMUTRAP facility

V.S. Kolhinen, D. Melconian, N. Morgan, A. Ozmetin, B. Schroeder, and P.D. Shidling

The primary goal of the TAMUTRAP facility is to test the Standard Model for a possible admixture of a scalar (S) or tensor (T) type of interaction in $T=2$ super-allowed beta-delayed proton decays. This information will be inferred from the shape of the proton energy spectrum. The main components of the facility are a Radio Frequency Quadrupole (RFQ) Paul trap used to cool and bunch the ions, and a measurement system based on a large-diameter cylindrical Penning trap. Additional scientific goals for this system are mass measurements, and providing a low-energy radioactive ion beam (RIB) for various other applications.
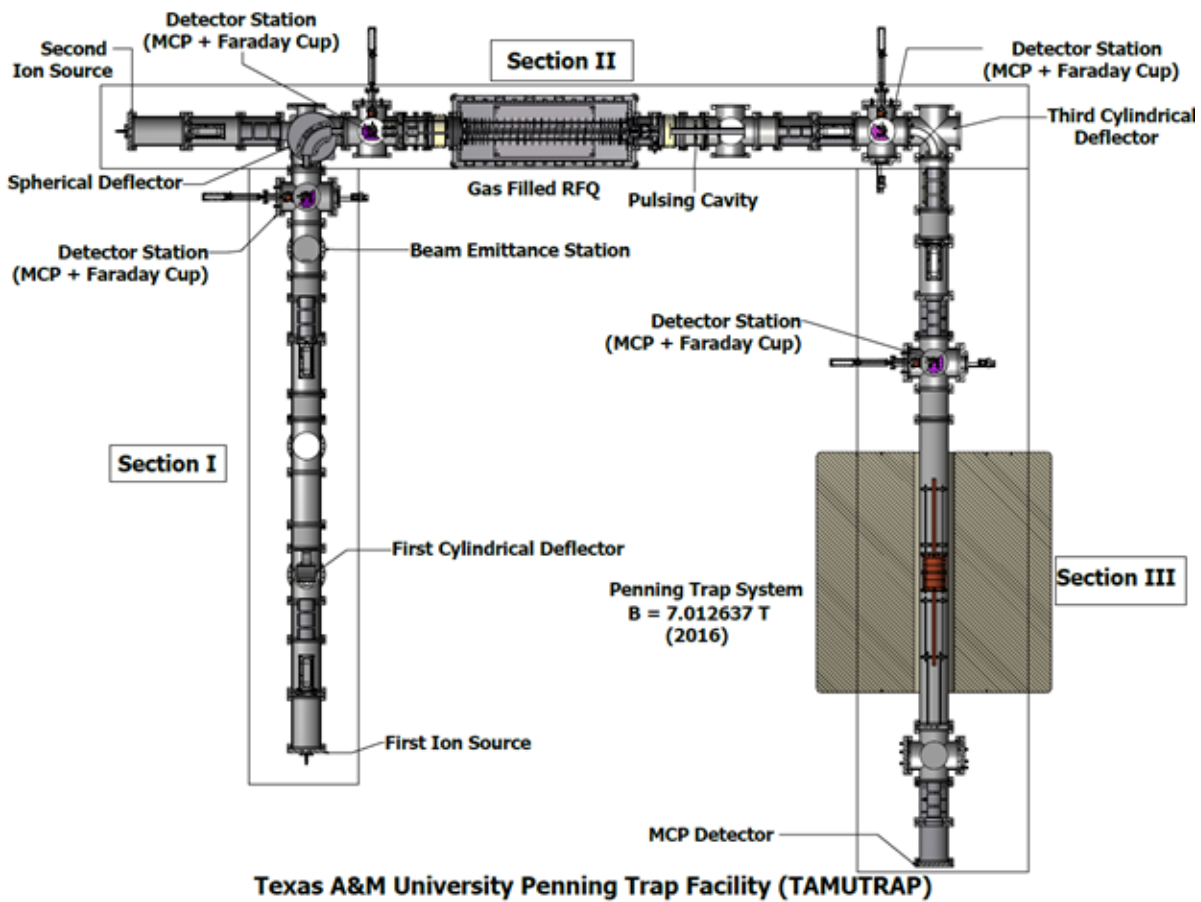
FIG. 1. Texas A&M University Penning Trap Facility (TAMUTRAP).

After demonstrating the ability of trapping and manipulate the ion motions, we began the year by demonstrating the ability to perform high precision mass measurement. The relevant observable in mass measurements using a Penning trap is the ratio of the cyclotron frequencies of the ion of interest and ion used as a mass reference. High precision requires that the two frequencies are measured after one another in the shortest possible time. An in-house-designed ion gun employing a stable sodium (^{23}Na) ion source

("First Ion Source" in Fig.1) was installed at the location of first cylindrical deflector. At TAMUTRAP facility, we measured the cyclotron frequency by the time-of-flight ion cyclotron resonance method (TOF-ICR). The frequency of the minimum TOF would correspond to the mass of the trapped ions. In our case, we used ^{39}K as our reference mass and performed mass measurement of ^{23}Na. At first we used a simplfied excitation scheme, where the quadrupole excitation was applied to four-fold segmented ring electrode for 20 ms to couple two eigen motions. The frequency scan was performed for ^{39}K and the TOF was recorded for 30 different frequencies in steps of 10 Hz close to the expected resonance value. The procedure was repeated by changing the source to ^{23}Na. Both these measurements were carried out on the same day. The reduction in TOF at resonance was around 20%. Normally, the reduction in TOF at resonance is considerable, typically 30%. In order to increase the TOF depth, the beam line at the exit of the magnet (Section III in Fig. 1) was extended by close to 2 feet and einzel lens was installed before the MCP detector. The extended beamline and positive voltage on the extraction drift tube helped us in observing close to 30% reduction in TOF at resonance for excitation time ranging from 20-100 ms. More details on the mass measurement will be discussed in our other report[2].

Apart from mass measurements, the settings of different electrostatic components were optimized to improve the transport efficiency of TAMUTRAP beamline. In particullary, we made close to two order of magnitude improvement in the transport efficiency of section 1 (see Fig.1). There was signifcant loss in bending the beam by 90° using spherical deflector and it was due to the fringe field effects. The huge improvement in the efficiency was possible by adding ground cylinders at the entrance and exit of the spherical deflector with certain aperture which helped to reduce the fringe field effects. In addition to this, we have built a third spherical deflector which will replace the third cylindrical deflector (see Fig. 1) and this replacement will certainly bend the bunched beam by 90° with better efficiency.

The performance of RFQ in bunched mode was improved by rewiring the RFQ electronics and changing the resistors value of last segment which is used to bunch the beam. The change in resistor value of the last segment improved the switching of the last segment during ejection and gave a satisfactory results.

The current prototype Penning trap has an inner diameter of 90 mm and is presently the world's largest Penning trap. However, in order to perform the planned measurement the diameter of the Penning trap needs to be twice the dimension of prototype Penning trap. The mechanical design of the TAMU-Penning trap (180 mm diameter) has been completed. The drawings of the entire TAMU-Penning trap system have been finalized and submitted to different sources for fabrication, including our in-house machine shop. More details of the 180 mm diameter Penning trap has been described in our other report [3]. Geant4 Monte Carlo simulations for the TAMUTRAP Penning trap setup has been initiated and more detail can be found in our other report [4]. We also made significant progress in automating the frequency scan for performing mass measurements and details on this automation has been described in our other report [5].

The immediate outlook for the TAMUTRAP facility involves beam alignment of section 1 (see Figure 1) of the TAMUTRAP facility collinear to Heavy Ion Guide and install gate valves at three different places along the TAMUTRAP beam line. After that, the third cylindrical deflector will be replaced by spherical deflector. We expect all the parts of TAMU-Penning trap system to be ready by mid

of June, 2018. We will start assembling the TAMU-Penning trap system and install it in the beamline by mid of July 2018. We will also test the frequency automated scan program sometime in May 2018. We expect to complete the simulation and finalize the dimensions of the detectors by fall 2018.

[1] E. Bennett *et al.*, *Progress in Research*, Cyclotron Institute, Texas A&M University (2015- 2016) p. I-62.

[2] V.S. Kolhinen *et al.*, *Progress in Research*, Cyclotron Institute, Texas A&M University (2017- 2018) p. IV-39.

[3] V.S. Kolhinen *et al.*, *Progress in Research*, Cyclotron Institute, Texas A&M University (2017-2018) p. IV-42.

[4] V.S. Kolhinen *et al.*, *Progress in Research*, Cyclotron Institute, Texas A&M University (2017-2018) p. IV-44.

[5] R. Burch *et al.*, *Progress in Research*, Cyclotron Institute, Texas A&M University (2017-2018) p. IV-46.

Measurements of conversion coefficients using a Si(Li) detector

V. Horvat, J.C. Hardy, N. Nica, and V.E. Iacob

As part of our program to make precise measurements of internal conversion coefficients (ICCs) [1], we neutron-activated a natural ruthenium sample to produce ^{103}Ru [2]. The β decay of ^{103}Ru populates a 40-keV isomeric state in ^{103}Rh, which decays by an $E3$ transition, whose ICC we seek to measure. The low-energy region of the photon spectrum from ^{103}Ru decay is dominated by the K x rays from rhodium, the intensity of which we must determine, but there is also a weak but significant contribution from ruthenium K x rays excited by fluorescence of the activated-source material. Unfortunately the K x rays of ruthenium and rhodium could not be resolved in our well-calibrated HPGe detector, so we also recorded the spectrum in a Si(Li) detector.

A portion of the Si(Li) spectrum containing peaks due to both ruthenium and rhodium K x rays is shown in Figure 1 by the blue line. The red (green) lines indicate the expected peak centroids and relative intensities of rhodium (ruthenium) peaks. It was found that the observed number of ruthenium K x rays amounts to 3.1% of the observed number of rhodium K x rays.
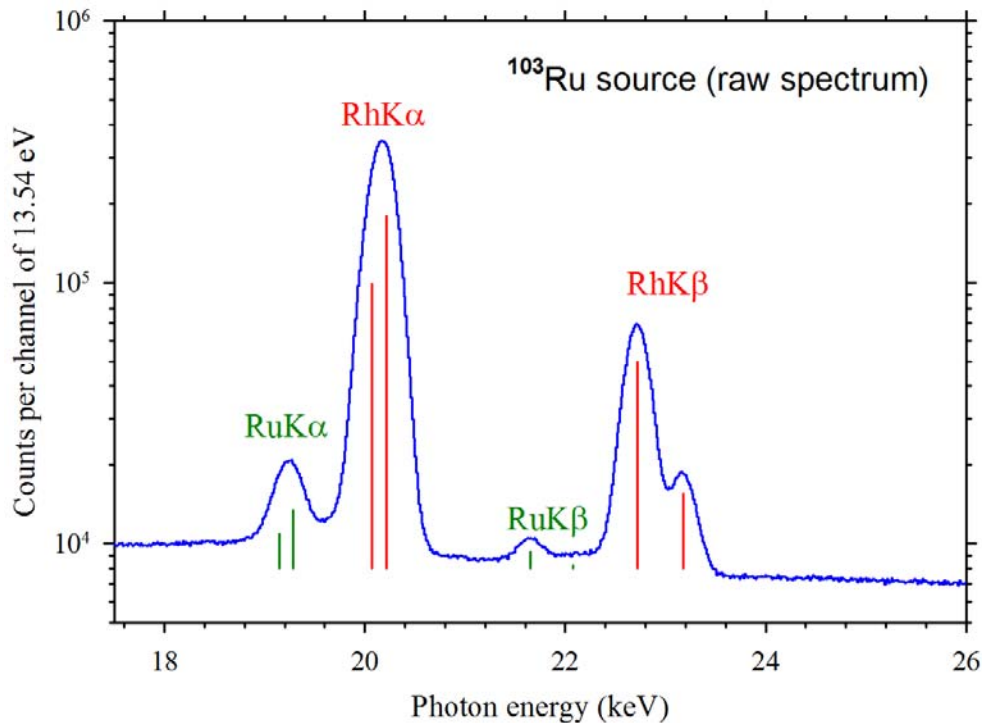
FIG. 1. Spectrum of x rays from the ^{103}Ru source measured using our Si(Li) detector.

Since there is no overlap between the peaks in the K_α group and those in the K_β group, the two groups were analyzed separately in order to simplify modeling of the peaks and the background and to

make the model more realistic. Specifically, the background in each group was modeled with an exponential decay curve using only two parameters, whose best values were adjusted based on visual inspection and then fixed. This was done in order to estimate the background with good accuracy and to make sure that the result is not affected by the peak-fitting procedure. The peaks were initially modeled with single Gaussian functions, but this model was subsequently refined.

In the peak-fitting procedure, the intensity of the peak due to Rh $K_{\alpha2}$ x rays was fixed relative to the intensity of the peak due to Rh $K_{\alpha1}$ x rays based on the calculated intensity ratio [3]. The same was done for the two peaks in the Ru K_{α} doublet. This way the centroids and intensities of the four peaks in each group were described by only three variable parameters. In the K_{α} group those were the Rh $K_{\alpha1}$ and Ru $K_{\alpha1}$ peak intensities and the Rh $K_{\alpha1}$ peak centroid; while the variable parameters in the K_{β} group were the Rh $K_{\beta1}$ and Ru $K_{\beta1}$ peak intensities and the Rh $K_{\beta1}$ peak centroid. The widths of the peaks were defined well enough to be fitted individually.

This simple model had to be adjusted in order to account for relatively small tails that were observed on the low-energy sides of the peaks. Contributions from these tails were evident in the plots of the fit residuals. It was found that these contributions could be described well with Gaussian functions having a lower centroid and an increased width compared to those describing the principal contributions to the peaks. In order to have a consistent peak profile for all peaks, we fixed the ratio of secondary-to-primary Gaussian areas for all peaks. The best-fit value of this fraction was found to be 4.2%. Also, the centroid energy difference between the secondary and primary peaks was taken to be proportional to the corresponding photon energy. For Rh $K_{\alpha1}$, at 20.2163(1) keV [3], the best-fit value of the difference was found to be 190 eV.

Finally, for the Rh $K_{\alpha1}$ peak, the best-fit widths (standard deviations) of the primary and the secondary Gaussian were found to be 115 eV and 331 eV, respectively. We then imposed the same ratio
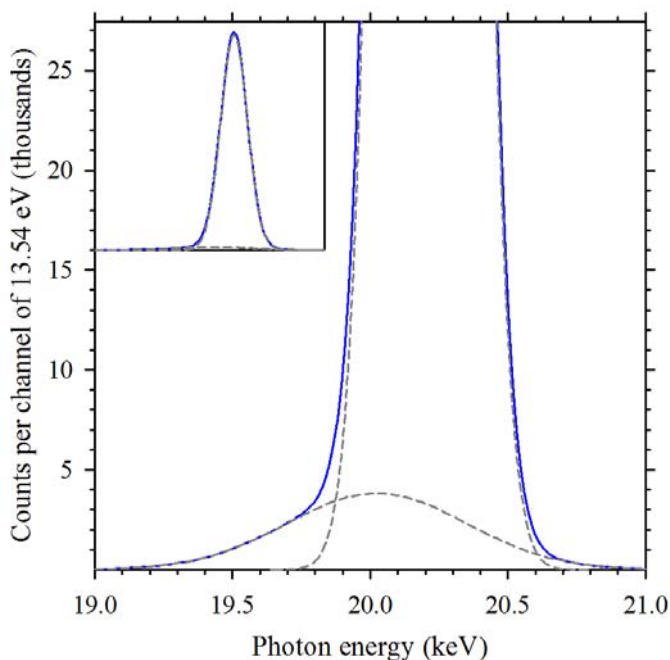
FIG. 2. Model of the fitted peak profile applied to the RhKα1 peak.

of widths when fitting the remaining peaks, so that only one variable parameter was used to describe the widths of all secondary Gaussians. This was implemented in a procedure that involved several iterations, and yielded the values given above.

Figure 2 shows the modeled shape of the Rh $K_{\alpha1}$ peak. Note that the vertical scale covers only 10% of the full range in order to enhance the details. The full coverage is shown in the insert.

Figure 3 shows the energy region containing the K_{α} group of peaks. The blue dots with error bars are the measured data with the fitted *primary* Gaussians and background subtracted. The dashed grey lines represent the individual *secondary* Gaussians, with their sum being the solid red line. In addition, the solid green line shows the full spectrum as predicted by CYLTRAN calculations folded with the appropriate instrumental resolution function (assumed to be Gaussian). Evidently, the red line describes the data extremely well down to the energy at which CYLTRAN predicts a substantial contribution from Compton scattering, which was not included in our model. It is obvious from Figure 3 that inclusion of Compton scattering in the model would lead to a satisfactory description of the data over the entire region of interest. However, we did not try this, not only because it would add to the complexity of the analysis, but also because it was unnecessary: The peak areas are not influenced by the Compton scattering.
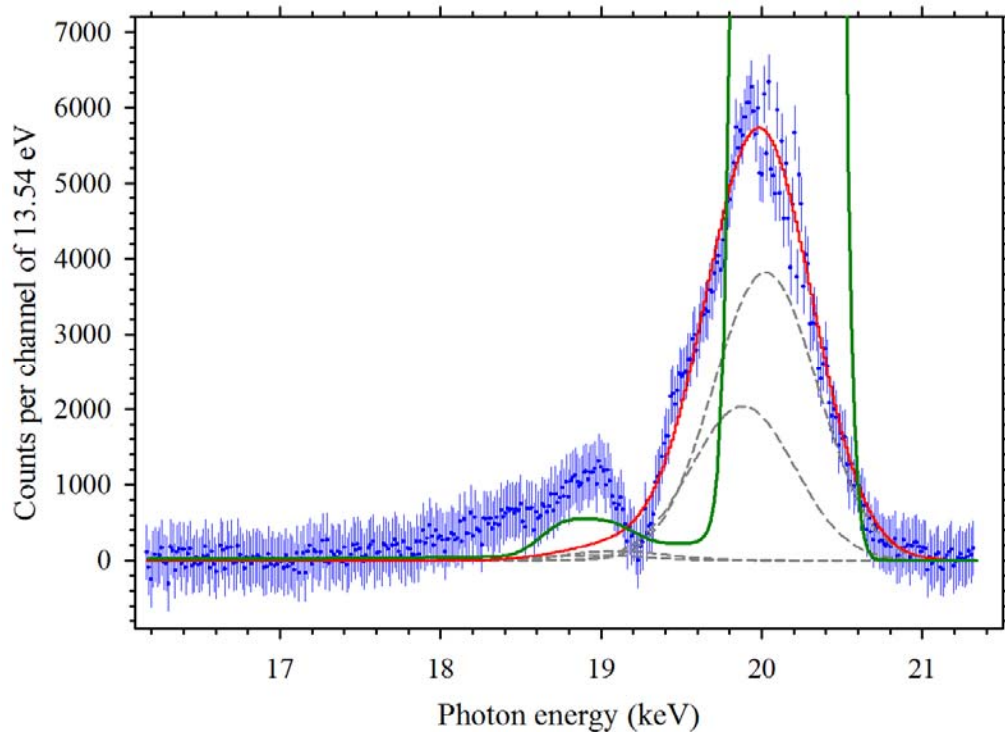
FIG. 3. Portion of the measured spectrum containing the K_{α} group of peaks, showing data from which we subtracted the fitted primary Gaussians and the background. Also shown are the fitted secondary Gaussians (dashed grey lines) and their sum (solid red line). In addition, the solid green line shows the spectrum predicted by CYLTRAN calculations folded with the appropriate instrumental resolution function (assumed to be Gaussian).

The peak due to the [103]Ru gamma ray at 39.757 keV [4] did not have a low-energy tail; therefore it was fitted with a single Gaussian function. The result is illustrated in Figure 4.
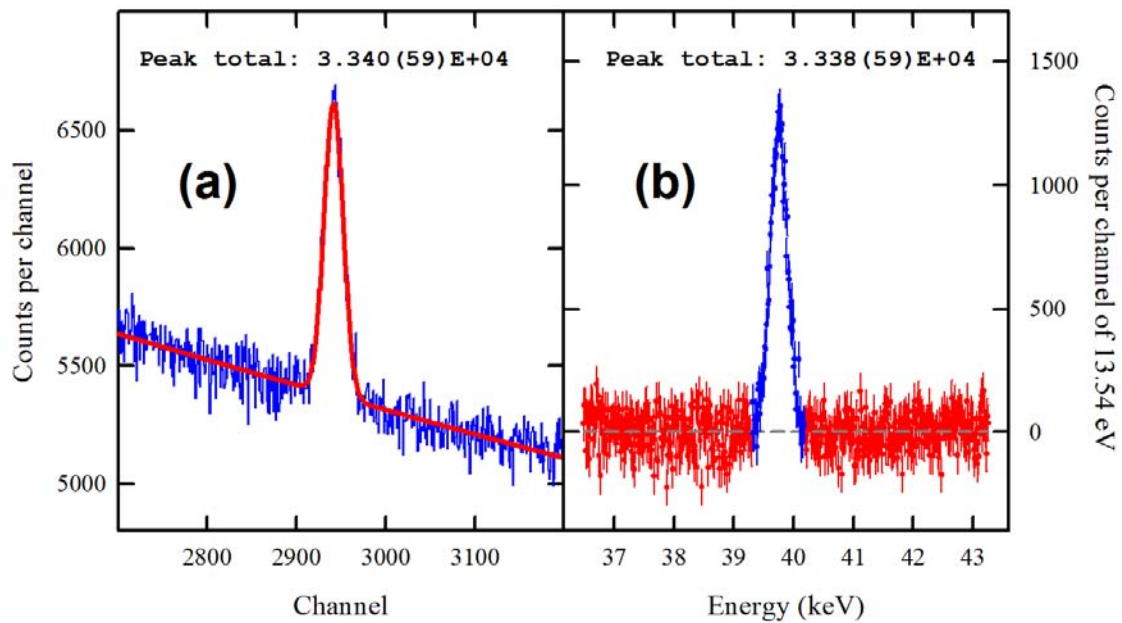
FIG. 4. Region of the measured spectrum containing the peak due to the [103]Ru gamma ray at 39.757 keV and the results of the analysis. The spectrum shown on the right is background-subtracted.

Analysis of the measured spectrum produced the results shown in Table I, for which we used Si(Li)-detector efficiencies as calculated with the CYLTRAN code [5], based on the nominal detector geometry, the actual [103]Ru source size, and the actual source position. Note that the number of Ru K x rays includes those resulting from internal conversion of all the other [103]Ru gamma rays, as well as those created in the decay of all other Ru isotopes present in the source.

Table I. Results of the analysis of the measured spectrum of x rays and gamma rays from the [103]Ru source.

Component	Efficiency-corrected number of events
RhKα	4.1290(19) E8
RhKβ1'	7.0792(96) E7
RhKβ2'	1.2766(59) E7
Total RhKx	4.964(24) E8
Rhγ(39.757 keV)	4.216(74) E6

[1] J.C. Hardy *et al.*, *Progress in Research*, Cyclotron Institute, Texas A&M University (2017-2018), p. I-25.

[2] N. Nica *et al.*, *Progress in Research*, Cyclotron Institute, Texas A&M University (2017-2018), p. I-28.

[3] E. Schönfeld and G. Rodloff, PTB Report: PTB-6.11-1999-1 (1999).

[4] http://nucleardata.nuclear.lu.se/toi/, accessed on 05/08/2018.

[5] J.A. Halbleib, R.P. Kensek, T.A. Mehlhorn, G.D. Valdez, S.M. Seltzer, and M.J. Berger, CYLTRAN 3.0, Sandia National Labs (Albuquerque, NM), Report SAND91-1634 (1992).

HPGe detector pumping/temperature history

V.E. Iacob and J.C. Hardy

We report here a short history of "vacuum interventions" required to sustain our high-precision efficiency-calibrated HPGe detector, whose absolute efficiency was determined more than 15 years ago to a precision of ~0.15%, as initially reported in [1]. Over its lifetime, this detector has lost vacuum a number of times. In all cases, no major damage was done since the built-in protection circuitry ensured that the detector was shut-down whenever the crystal temperature rose above about -160°C. However, in order for us to effect repairs the detector had to be warmed to room temperature for a few days on each occasion. This could have affected the detector's efficiency calibration so we routinely verified its stability by measuring the activity of our "standard" precisely calibrated ^{60}Co source, which was used in the original calibration.

The first major vacuum failure occurred in 2002. Using a high-vacuum leak-checker, we were able to locate the leak at the bond between the Be window and the Al cap. While there was no mechanical problem with the bond, the epoxy wasn't able to maintain the vacuum. After contacting the manufacturer (ORTEC) we learned that a permanent fix would imply a brand-new cap for the crystal. Such a major overhaul would have tampered with the geometry of the HPGe and turned our detector into a good-but-uncalibrated one. To avoid this major inconvenience, we tried a less-radical fix: we patched externally the cap at the Al-Be contact. For this purpose, we used a manufacturer-recommended low-vapor-pressure epoxy. After leak-testing the patch, the HPGe was cooled to liquid-nitrogen (LN) temperature. The last important step of the repair consisted in the verification of the absolute efficiency with our ^{60}Co source. The relatively tedious work payed off: The repaired HPGe showed no change from the previously determined efficiency curve.

During the next 14 years, there were five more vacuum-loss incidents, each handled the same way and each leaving the detector's efficiency unaltered. However, starting in 2016, the seal of the Be window appeared to be in a less stable situation: during that year alone we performed four interventions. While each patch appeared to work, it nevertheless ended up in a vacuum loss after a few months.

In the spring of 2017, we completely removed all the old epoxy and added a thin fresh layer of low-vapor-pressure epoxy (see Fig. 1). Again, we leak checked, re-cooled the detector and returned it to use. At that point though, we started monitoring the temperature of the crystal, using the ORTEC calibrated thermal element. This allowed us to effectively monitor the pressure and prevent unexpected shut-downs. Subsequently when the temperature (consequently, pressure) rose to near the shut-down threshold (~-160°C), we intervened to pump the detector out. On no occasion was there any indication of a leak in the Be window seal. Fig. 2 shows the evolution of the crystal temperature after each pumping.

FIG. 1. Externally patched epoxy seal of the Be window in early 2017.
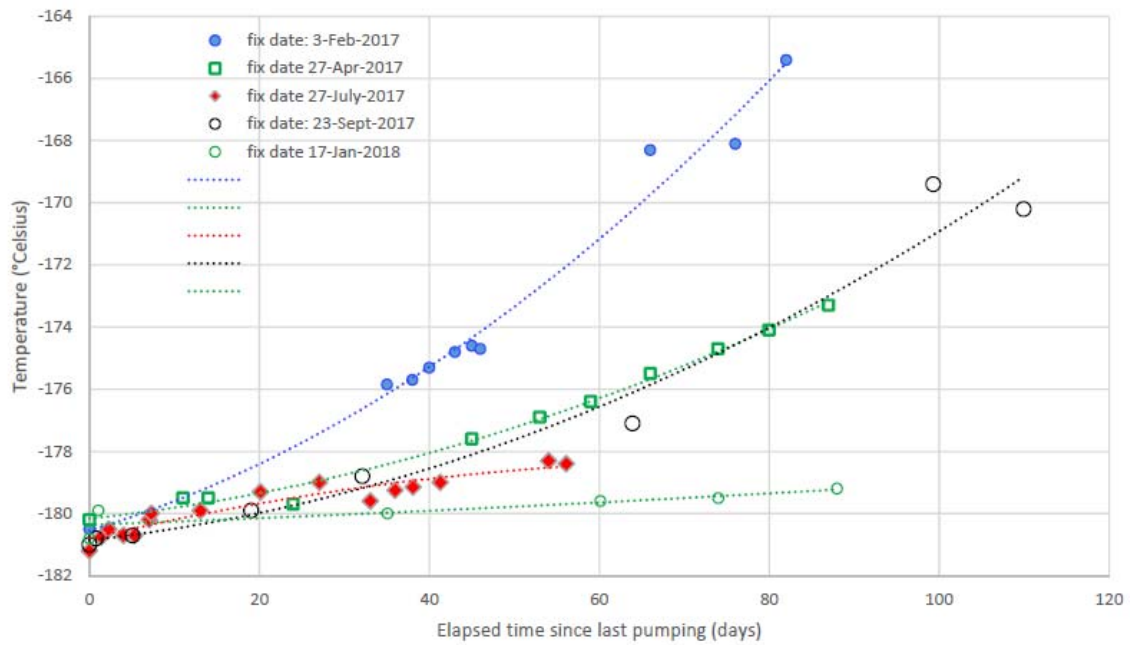
FIG. 2. Evolution of the HPGe temperature post vacuum-intervention in 2017 and 2018.

We performed three more (preventive) vacuum restorations during 2017. Since no significant leak was detected, we concluded that the increased heating rate was related to a reduced capacity of the molecular sieve to maintain the required high vacuum. As these interventions were preventive, we did not expect any negative impact on the detector's performance. However, each intervention increased the time required to bias the detector after cool-down: from a few minutes, to hours, then days. Thus, the last 2017 intervention required 4 steps to bias the HPGe to the nominal voltage of -4300 V: The step limits were -3200, -3700, -4100, and -4300 V. In each step we biased the detector to the maximum voltage it could sustain with normal energy-resolution, leaving it for several hours at that voltage before moving to the next step.

Clearly something had to be done to restore the effectiveness of the molecular sieve. Heating it to high temperature was out of the question since that would have seriously compromised our detector's performance, so in January 2018 we tried a "minimal" cure. With the detector operating normally, we stopped the LN cooling and brought the detector to room temperature while continuously pumping. We then continued pumping for five days, considerably longer than ever before. This time, after the detector had been cooled again it behaved normally: only a few minutes was required to bring the bias to the nominal -4300 V. Moreover, the evolution of the crystal temperature (see Fig. 2) indicates a partial restauration of the pumping capacity of the molecular sieve: The temperature increases at a rate of 0.1°C/week, much less than after previous fixes.

Because of the abnormal behavior in detector biasing observed in 2017 we became concerned that our efficiency calibration might have been affected. We are currently preparing for a high-precision evaluation of our HPGe absolute efficiency as it stands after the January 2018 fix.

[1] R.G. Helmer, J.C. Hardy, V.E. Iacob, M. Sanchez-Vega, R.G. Neilson, and J. Nelson, Nucl. Instrum. Methods Phys. Res. **A511**, 360 (2003).

Recent developments in the fast tape-transport system

H.I. Park, L. Gathings, F.P. Abegglen, and J.C. Hardy

The fast tape-transport system has been used for 20 years as part of the precision on-line β-decay facility mounted at the end of the Momentum Achromat Recoil Spectrometer (MARS). It is used to rapidly move high-purity sources collected from MARS to a well-shielded counting location. It consists of two reels, a reservoir reel and a take-up reel, which are mounted independently on two separate decks. Each tape deck has its own vacuum buffer and controls, and the height of the deck is adjustable by motor drive. The distinctive features of our tape-transport system are that it operates entirely in air and it moves collected sources very rapidly, covering the 90 cm to the counting location in less than 200 ms.

In recent years we have maintained and optimized the tape-transport system to study short-lived nuclides. Most recently, we have pushed its limits by using it to measure ^{42}Ti, which has a half-life as short as ~200 ms. The measurements of such decay studies require more than 150,000 repeat cycles defined as *collect-move-count* to obtain high statistics, and each cycle period of the tape transport can be as short as ~6.5 s. There is no doubt that under these conditions, the tape system is operating at the limit of its mechanical capabilities.

Our first task in preparing the unit for such a demanding measurement was to check the quality of new aluminized Mylar tapes, produced by our new suppliers, by cycling them through the tape-transport system. High-quality metallization and the precise width of the tapes permitted the tape reels to be completely filled. We then repaired a failure of the tape-transport system to place the collected source consistently into the center of the detector, a new problem we recently encountered [1]. Critical to this repair was a very fine alignment of the pinch roller with the capstan, both being located on the take-up reel deck. The effect of every alignment change we made was evaluated by repeatedly measuring the distance that the tape moves during the pre-set time between the engagement of the pinch roller and the closing of the brakes. That distance is now reproducible from cycle to cycle within ±5 mm, but there is still room for improvement. We also cleaned two brakes located on both sides of the counting location to stop the tape promptly and to stretch it tightly in front of the detectors.

The tape-transport system also showed its age by developing very low-level noise signals from the installed motors. We first noticed this issue at the beginning of our latest online half-life experiment on ^{42}Ti [2]. The symptom was that unphysical structure appeared in the middle of the cumulative time-decay spectrum recorded from the 4π proportional gas counter at the lowest discriminator level. We observed this effect as the tape reel on the take-up deck became heavier as more tape wound onto it. This relationship made us suspect that the observed structure was due to noise pickup arising from the servo-motors that control the tape reels.

For the experiment, we resolved the problem by restricting ourselves to using approximately two-thirds of the tape roll before imposing a tape rewind. Diagnostic tests following the online experiment confirmed that the gas counter picked up the noise generated by the servo-motor at the take-up deck. We also identified another source of noise: the motor that regulates the capstan which drives the tape at a precise and constant speed. The elimination of these unwanted noise signals, which interfered with valid

detector signals, was successfully accomplished by our screening the area where the servomotors and capstan motors are installed with 0.25-inch thick Al plates, and by improving the grounding of the gas detector.

We are currently putting our efforts into getting spare parts for the tape-transport system to maintain its prime operating condition in future.

[1] H.I. Park *et al.*, *Progress in Research*, Cyclotron Institute, Texas A&M University (2016-2017), p. I-15.
[1] H.I. Park *et al.*, *Progress in Research*, Cyclotron Institute, Texas A&M University (2017-2018), p. I-24.

Production of radionuclides for online chemistry experiments

C.M. Folden III,[1] M. Block,[2] Ch.E. Düllmann,[2,3,4] K.J. Glennon,[1] S. Götz,[2,3,4] C.M. Hivnor,[1]
S. Raeder,[2] E.E. Tereshatov,[1] M.F. Volia,[1] and A.B. Yakushev[2]

[1]*Texas A&M University, College Station, TX 77843-3366 USA*
[2]*GSI Helmholtzzentrum für Schwerionenforschung, Darmstadt D-64291, Germany*
[3]*Johannes Gutenberg University Mainz, 55099 Mainz, Germany*
[4]*Helmholtz Institute Mainz, 55099 Mainz, Germany*

The heavy elements group conducted two experiments during the past year related to producing short-lived radionuclides for online chemistry experiments. The first experiment produced activity that was delivered to the Cryo-Online Multidetector for Physics And Chemistry of Transactinides (COMPACT) device developed at the GSI Helmholtzzentrum für Schwerionenforschung (Darmstadt, Germany) [1]. COMPACT was used in a configuration where a gas cell (also developed at GSI) was used to thermalize ions and extract them into COMPACT using an RF funnel. Such a setup would minimize the extraction time of the ions, which will be important in future studies of very short-lived species. This is a natural extension of our previous work, which showed that pre-separation of activity for delivery to a "recoil transfer chamber" (gas cell) is feasible [2]. The COMPACT Si detectors were covered in a thin layer of Au, and three different elements ($^{182\text{-}183}$Hg, ^{187}Pb, and ^{199}At) were used to test the feasibility of such a setup. The second experiment was a proof-of principle for production of ^{184}Tl (10 s, ~2% α branch), which is expected to be a homolog of nihonium (element 113). In both experiments, beams were accelerated by the K500 cyclotron and delivered to the MARS beamline. MARS acted as a pre-separator [3], and purified beams were delivered to either COMPACT in the first experiment or a position-sensitive strip detector in the second experiment. Table I summarizes the irradiations and Fig. 1 shows the gas cell and COMPACT installed on MARS. Preliminary results are reported here.

Table 1. Summary of irradiations related to production of short-lived radionuclides for chemistry experiments.

Date	Primary Reactions	Detection System
May 2017	^{144,147}Sm(^{40}Ar, xn)$^{182\text{-}183}$Hg ^{152}Gd(^{40}Ar, 5n)^{187}Pb ^{165}Ho(^{40}Ar, 6n)^{199}At	COMPACT
March 2018	^{152}Gd(^{35}Cl, 3n)^{184}Tl ^{103}Rh(^{84}Kr, 3n)^{184}Tl	Si Strip Detector
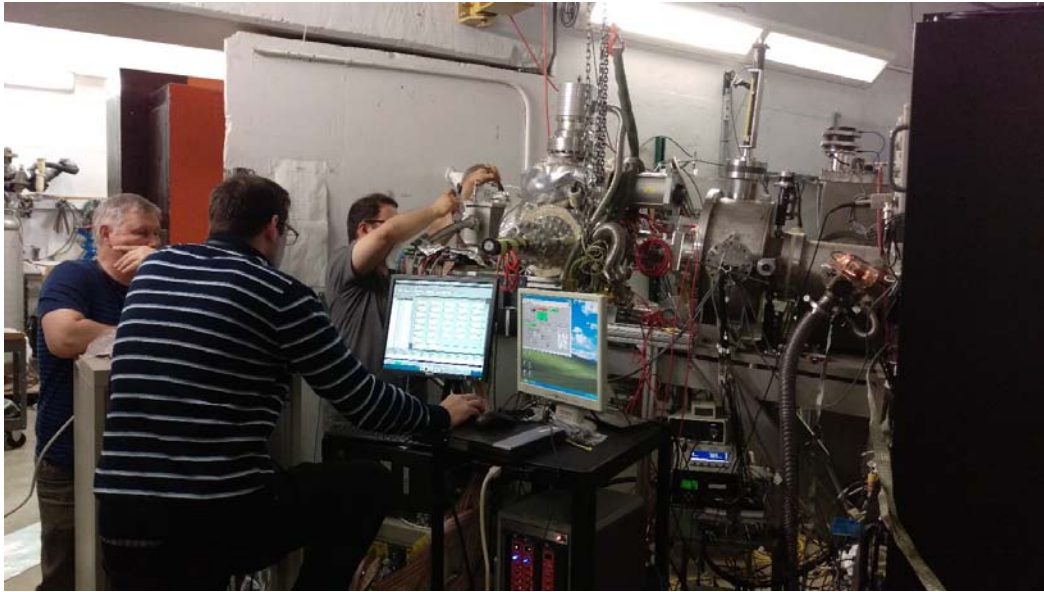
FIG. 1. The gas cell and COMPACT mounted on the detection chamber of MARS.

The COMPACT experiment was successful, as $^{180,182-183}$Hg were detected due to adsorption on the Au-coated Si detectors. A significant yield of ^{199}At was also observed, as was a very small yield of ^{187}Pb. The primary goal of demonstrating that a gas cell with an RF funnel can be used to provide fast extraction of activity to COMPACT was achieved.

The second experiment tested the feasibility of producing ^{184}Tl using the ^{152}Gd(^{35}Cl, 3n) and ^{103}Rh(^{84}Kr, 3n) reactions. The ^{35}Cl-based reaction may have produced ^{184}Tl, but the magnetic rigidity of the primary beam was similar to that expected for the products, and a high rate of background was
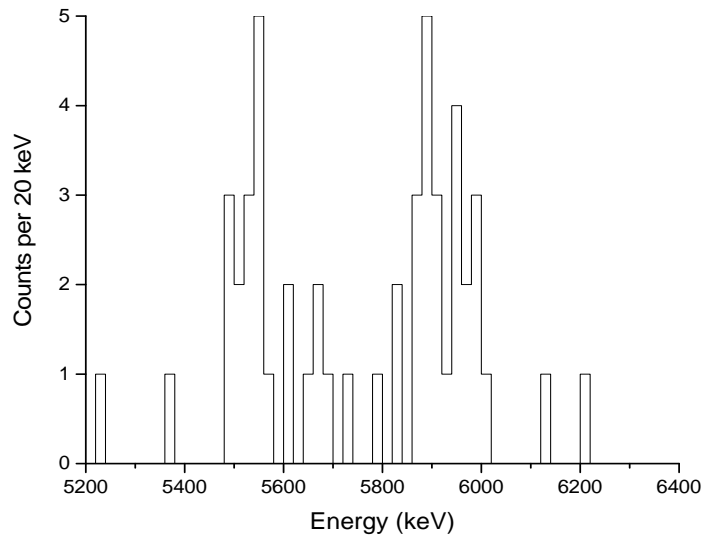
FIG. 2. Alpha spectrum observed at the focal plane detector in the reaction ^{84}Kr + ^{103}Rh. The peak near 5.50×10^3 keV is assigned to ^{184}Hg and the peak just below 6.00×10^3 keV is assigned to ^{184}Tl based on a preliminary calibration. These data represent approximately 1 h of irradiation.

observed. However, the ^{84}Kr-based reaction was successful, and a sample alpha spectrum is shown in Fig. 2. Due to the small alpha branch of ^{184}Tl, only small numbers of counts were observed. In order to make a future chemical experiment feasible, an alpha count rate of ≈ 1 min^{-1} is needed. The actual observed rate was ≈ 0.3 min^{-1}, suggesting that relatively modest improvements could make such an experiment feasible. The analysis of these data is ongoing.

In total, these experiments show the feasibility of conducting online chemistry experiments at the Cyclotron Institute.

[1] J. Dvorak *et al.*, Phys. Rev. Lett. **97**, 242501 (2006).
[2] M.C. Alfonso *et al.*, Nucl. Instrum. Methods Phys. Res. A**798**, 52 (2015).
[3] C.M. Folden III *et al.*, Nucl. Instrum. Methods Phys. Res. A**678**, 1 (2012).

Acceleration and identification of charge-bred ions from the light-ion guide with MARS: Identification of ^{114}Cd

B.T. Roeder, F. Abegglen, J. Arje, G.J. Kim, A. Saastamoinen, and G. Tabacaru

During the last two years, experiments have been carried out to accelerate and identify charge-bred ions from the light-ion guide at the Cyclotron Institute as part of the facility upgrade project. In 2016, ^{85}Rb from the charge-breeding electron-cyclotron resonance ion source (CB-ECR) was accelerated with the K500 and identified with the Momentum Acromat Recoil Separator (MARS) [1] and associated silicon detectors [2]. Last year, a follow-up experiment was designed to search for ^{64}Zn and ^{64}Ga ions that had been produced and transported with the Light-Ion Guide (LIG) to the CB-ECR and then re-accelerated with the K500 [3]. While some ^{64}Zn was identified with MARS, it was difficult to determine if the ^{64}Zn come from the LIG because ^{64}Zn was present as part of the background beam from the CB-ECR. ^{64}Ga was not observed unambiguously at MARS either.

This year, following a series of design changes to the injection side of the CB-ECR, a new reaction was attempted to produce the first charge-bred and accelerated beam from the Light Ion Guide project. Using 10 MeV protons from the K150 cyclotron on a thin, enriched target of ^{114}Cd, ^{114}In was produced via the ^{114}C(p,n)^{114}In reaction. This reaction was chosen because of its high cross section, the reasonably short half-life of ^{114}In (71.9 s), and the heavier mass of the ^{114}In relative to the ^{64}Ga which was thought to make it easier to charge-breed. Leading up to the attempt to re-accelerate the ions through the K500, ^{114}In^{19+} was observed after the CB-ECR at a rate of 238 decays/sec per µA of proton beam on the LIG target.

The experiment was carried out in a similar way as the previous experiments to measure ^{85}Rb and ^{64}Zn from the CB-ECR. To calibrate the detectors at the focal plane of MARS, a beam of ^{107}Ag at 11 MeV/u was accelerated with the K500 cyclotron and was transported to the target chamber of MARS. The ^{107}Ag beam impinged on a thin ^{12}C stripper foil that was 47.7 µg/cm^2 thick. The stripper foil removed electrons from the beam such that the resulting charge states of the beam could be tuned through MARS at rigidities calculated with the LISE++ model of MARS [4]. Once each charge state was tuned through MARS, it was measured at the focal plane with detectors consisting of a ΔE-E silicon telescope. The ΔE detector was a 63 µm thick, position sensitive silicon strip detector and the E detector was a single pad detector that was 500 µm thick. The type and thicknesses of the detectors were chosen such that the ^{107}Ag, and also the desired ^{114}Cd and ^{114}In, could be detected and identified using their energy loss in the silicon detectors and their position at the MARS focal plane. During the calibration, charge states 36+ through 39+ for ^{107}Ag were measured. An average energy of 1170 ± 2 MeV was observed by calculating the beam energy based on a prior calibration of the MARS D1 dipole field and comparing the energy deposits in the silicon telescope for each charge state. Due to the relatively high mass and low energy of the desired ^{114}Cd and ^{114}In, it was noted that this detector setup would not be sufficient to separate ^{114}Cd from ^{114}In. However, as any product with mass 114 could be identified versus other atomic masses by measuring their total energy, this setup was sufficient to determine if ions from the LIG were being re-accelerated by the K500.

To search for ^{114}Cd and ^{114}In ions that had been accelerated by the K500, first a pilot beam of ^{12}C^{2+} at 11 MeV/u was tuned through the K500 cyclotron. The charge-to-mass ratios (Q/M) for ^{12}C^{2+}, ^{114}Cd^{19+}, ^{114}In^{19+} are 0.16667, 0.16683 and 016683 respectively. Taking into account that the percent change in the charge to mass ratio here is +0.096%, to shift the frequency for ^{12}C^{2+} to ^{114}Cd^{19+} and ^{114}In^{19+} corresponding to ΔQ/ΔM ≈ 0.00016, a frequency shift of about +9 kHz was expected. However, it was also noted in the ^{85}Rb experiment that the ^{16}O^{3+} pilot beam could still be observed as much as 12 kHz away from the optimum frequency. As a result, it was expected that all three beams in this case, ^{12}C^{2+}, ^{114}Cd^{19+} and ^{114}In^{19+} would be transported to the MARS target chamber simultaneously despite the slight change in the frequency of the K500 cyclotron. But, after being stripped with the thin carbon stripper foil, the ^{114}Cd and ^{114}In for the charge states where the Q/M were different would be cleanly separated in rigidity from the ^{12}C pilot beam.

The ^{114}Cd and ^{114}In ions were produced by bombarding a thin, enriched ^{114}Cd target with between 1 and 4 μA of 10 MeV protons from the K150 cyclotron for the test run. The ^{114}Cd ions, produced from sputtering and proton elastic scattering, and the ^{114}In ions, produced from the ^{114}Cd(p,n)^{114}In reaction, were stopped in pure He gas and transported by the Light Ion Guide (LIG) [5] to the CB-ECR. Inside the CB-ECR, the ions were charge-bred in the plasma to ^{114}Cd^{19+} and ^{114}In^{19+} ions. Since ^{12}C^{2+} is also extracted from the CB-ECR with the same extraction voltage and magnet settings as the ^{114}Cd^{19+} and
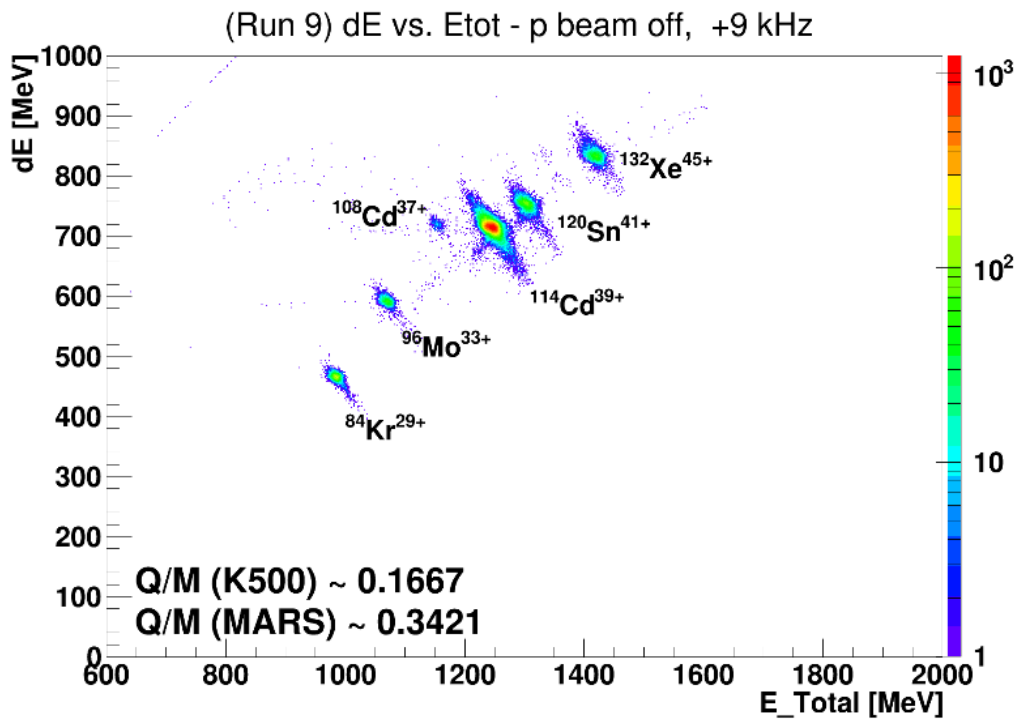
FIG. 1. Energy Loss (ΔE) vs. Total Energy spectrum obtained for the ^{114}Cd^{39+} MARS tune.

^{114}In^{19+} ions, the ^{12}C^{2+} was used as a pilot beam to develop the tune from the CB-ECR through the K500 cyclotron and eventually to MARS. Then, once the ^{12}C^{2+} beam was tuned to the entrance of MARS, the

frequency of the K500 cyclotron was shifted +9 kHz (to optimize for the ^{114}Cd^{19+} and ^{114}In^{19+}) to begin the search for the re-accelerated ions.

MARS was tuned with magnetic rigidity settings optimized to observe the ^{114}Cd and ^{114}In in charge states 37+ though 39+ as predicted by the LISE++ charge-stripping models and the observations of the stripping of the ^{107}Ag beam. The magnetic rigidity of MARS was set with the currents on the magnets as determined by the LISE++ model of MARS [4,6]. The ΔE vs. E spectrum obtained with MARS set to measure the ^{114}Cd^{39+} and ^{114}In^{39+} after the stripper foil is shown in Fig. 1. Mass 114, mostly ^{114}Cd, was clearly visible and the most intense ion measured. A few other ions with Q/M ≈ 1/6, similar to the ^{12}C^{2+} pilot beam, were also observed. The origin of these other ions is unknown, but they should be related with some contamination in the CB-ECR as they were present independent of the proton beam on the LIG target.

Measurements were conducted with the proton beam "on" and "off" the LIG target for 1 minute each. The intensity of the proton beam on the LIG target was also varied from 1 μA to 4 μA. The results of these measurements are shown in Fig. 2 for the ^{114}Cd^{38+} and ^{114}Cd^{39+} settings. While there was some ^{114}Cd background present when the proton beam was "off", the ^{114}Cd rate increased when the proton
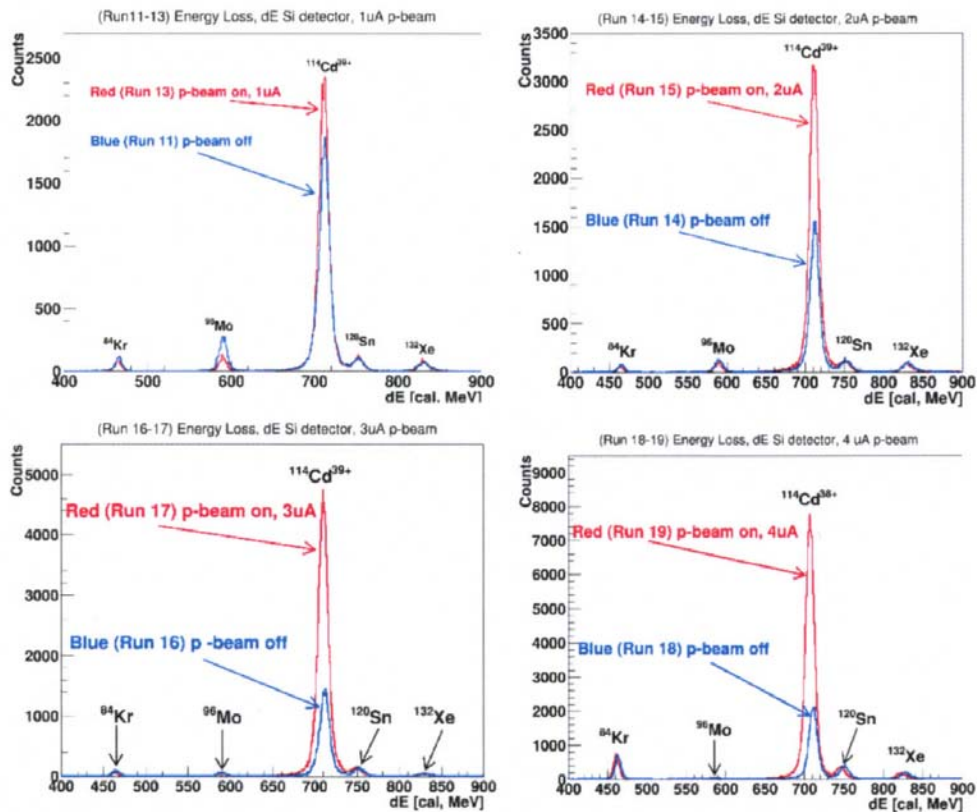
FIG. 2. Spectra showing the ^{114}Cd peak for 39+ and 38+ charge state settings. The measurements for each spectrum were taken for 1 minute. Identification of the ^{114}Cd from the LIG is shown by the red spectrum where the intensity of the ^{114}Cd is clearly increased with the K150 proton beam "On" versus the blue spectrum with the beam "Off".

beam was "on". Accounting for the background, the ^{114}Cd rate at MARS also appeared to increase linearly with the amount of proton beam on target. A maximum rate of 1.4×10^3 counts/sec above the

background was observed on the MARS silicon detector telescope with MARS tuned for ^{114}Cd^{38+} and 4 µA of proton beam on the LIG target. It should be noted here that the background rate for ^{114}Cd was around 400 counts/sec with the proton beam "off". ^{114}In was likely also present for the same MARS settings, but could not be observed directly from its energy loss due to its similar mass with the ^{114}Cd and the large intensity of the ^{114}Cd transmitted.

In conclusion, re-acceleration of ^{114}Cd^{19+} and ^{114}In^{19+} ions from the LIG and CB-ECR has been attempted. Peaks from ^{114}Cd^{38+} and ^{114}Cd^{39+} ions, obtained after passing the beam through a stripper-foil, were clearly observed confirming that the tune of the K500 cyclotron, the beam-line optics, and MARS was correct. The peak arising from the ^{114}Cd^{39+} ions varied in intensity depending on if the K150 proton beam was "on" or "off", if the LIG was "on" or "off", and also the intensity increased linearly if the amount of proton beam on the LIG was increased. The observation of the ^{114}Cd ions represents the first confirmed re-accelerated ions from the LIG and the CB-ECR. Further experiments with higher resolution detector systems and/or the ability to measure β-decay are envisioned to observe the ^{114}In decay that should have been simultaneously present.

[1] R.E. Tribble, R.H. Burch, and C.A. Gagliardi, Nucl. Instrum. Methods Phys. Res. **A285**, 441 (1989).
[2] B.T. Roeder *et al.*, *Progress in Research*, Cyclotron Institute, Texas A&M University (2015-2016) p. IV-16; http://cyclotron.tamu.edu/progress-reports/2015-2016/SECTION IV.html.
[3] B.T. Roeder *et al.*, *Progress in Research*, Cyclotron Institute, Texas A&M University (2016-2017) p. IV-17;, http://cyclotron.tamu.edu/progress-reports/2016-2017/SECTION IV.html.
[4] B.T. Roeder *et al.*, *Progress in Research*, Cyclotron Institute, Texas A&M University (2013-2014) p. IV-40; http://cyclotron.tamu.edu/progress-reports/2013-2014/SECTION IV.html.
[5] H.L. Clark *et al.*, *Progress in Research*, Cyclotron Institute, Texas A&M University (2014-2015) p. IV-15; http://cyclotron.tamu.edu/progress-reports/2014-2015/SECTION IV.html.
[6] O.B. Tarasov and D. Bazin, Nucl. Instrum. Methods Phys. Res. **B266**, 4657 (2008).

β decay of ^{22,23}Si studied at MARS with the optical time projection chamber

A.A. Ciemny,[1] C. Mazzocchi,[1] W. Dominik,[1] A. Fijałkowska,[2] J. Hooker,[3] K. Hunt,[3]
H. Jayatissa,[3] Z. Janas,[1] Ł. Janiak,[1] G. Kamiński,[4] Y. Koshchiy,[3] M. Pfützner,[1] M. Pomorski,[1]
B. Roeder,[3] G. Rogachev,[3] A. Saastamoinen,[3] S. Sharma,[1] and N. Sokołowska[1]

[1]*Faculty of Physics, University of Warsaw, Warsaw, Poland*
[2] *Rutgers University, New Brunswick, New Jersey*
[3]*Cyclotron Institute, Texas A&M University, College Station, Texas*
[4] *JINR Dubna, Russia*

Nuclei at or very close to the proton drip-line are characterized by large Q-value windows for delayed charged particle emission, with one, two and even three protons emitted promptly after β decay (βp, β2p, β3p). The investigation of such nuclei using charged-particle spectroscopy illuminates the structure of highly-unbound states in these exotic nuclei.

An experiment was conducted in Spring 2017 at the focal plane of the MARS spectrometer at the Cyclotron Institute of Texas A&M University, in order to search for unobserved decay channels of ^{22,23}Si. βp and β2p emission has been reported for these two isotopes, mostly proceeding via the isobaric analogue state (IAS) in the daughter nucleus [1, 2]. The β3p decay channel, as well as the delayed alpha-proton and the new ^{3}He channels, are open and so-far unobserved, as well as decay through other states than IAS. These nuclei were investigated using silicon-detector based arrays, which are sensitive only to the higher-energy portion of the proton spectrum. Therefore, the previously measured branching ratios for (multi-) proton emission in this region very often need to be (re)measured and corrected.

A ^{28}Si beam at 45 AMeV with a 150 μm-thick Ni target, was used to produce the ^{22,23}Si ions. The nuclei of interest were separated from the unwanted reaction products by using the MARS separator, optimized for transmission of ^{23}Si first and later of ^{22}Si, and implanted into the Optical Time Projection Chamber (OTPC) [3], which was installed at the MARS focal plane. The experimental set-up is described in detail in the 2016/17 Progress Report [4]. In brief, the OTPC is a time-projection chamber in which photons are emitted during the charge amplification. These are recorded by a sensitive CCD camera and two photomultiplier tubes (PMT). The former provides the projection of the tracks generated by charged particles on the plane of the anode (horizontal), while the latter provides the projection of the signal along the electric field lines (vertical). The PMTs were read out by fast oscilloscopes, providing the time distribution of the light emitted in the chamber.

A total of 6000 ions of ^{23}Si ($T_{1/2}$ = 42 ms) and less than 100 of ^{22}Si ($T_{1/2}$ = 29 ms) were implanted into the active volume of the OTPC detector. In both cases the observation window for detecting the decay was set to ~160 ms. After implantation of the ion the beam was stopped while waiting for the decay to happen and the data acquisition to record the event. For the analysis, only identified ^{22}Si and ^{23}Si ions implanted into the active volume were considered.

βp and β2p emission was observed as well as candidate events for β3p emission. The branching ratio for βp emission was measured to be 82.2(12) %, while the one for β2p emission about two times larger than reported in the literature. This discrepancy can be explained by the fact that the literature

values (71% and 3.6% [5], respectively) stem from measurements based on a silicon-detector set-up, which has a higher threshold for observing the protons unambiguously because of the β background. The
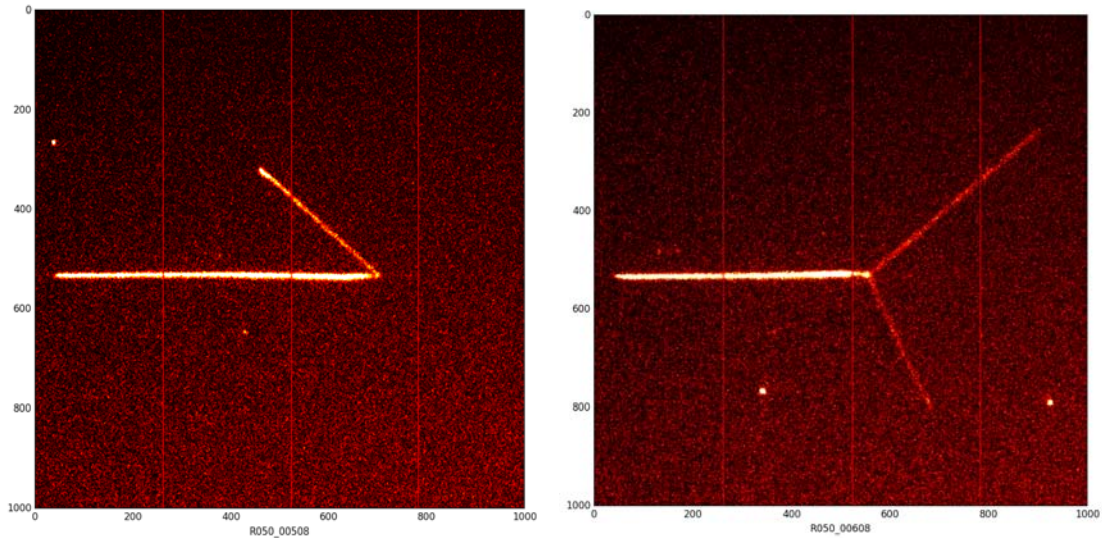
FIG. 1. On the left: CCD image of βp emission event from ^{23}Si. The track of the implanted ion is seen from left to right at the end of which the delayed proton is seen. The proton was stopped into the active volume of the detector (the Bragg peak is visible at the end of the proton trajectory). On the right: CCD image of β2p emission event from ^{23}Si. The two delayed protons are seen starting from the end of the ion trajectory. Both escape the active volume of the detector.

analysis is ongoing in order to reconstruct the energy spectrum for those protons that did not escape the active volume of the detector. In Fig. 1 two sample events of βp and β2p emission respectively are shown. The candidate events for β3p events are being analyzed.
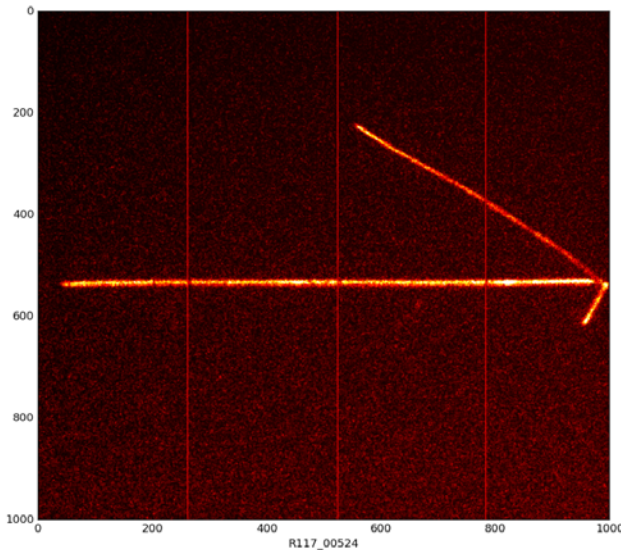
FIG. 2. Example of β2p emission decay event from ^{22}Si. In the CCD image the track of the ion (from left to right) and of the two protons can be seen.

The analysis of the decay of ^{22}Si is ongoing. Preliminarily, both the βp and β2p decay branches were seen. In Fig. 2 an example of β2p event is shown.

[1] B. Blank *et al.*, Z. Phys. A **357**, 247 (1997).
[2] X.X. Xu *et al.*, Physics Letters B **766**, 312 (2017).
[3] M. Pomorski *et al.*, Phys. Rev. C **90**, 014311 (2014).
[4] C. Mazzocchi *et al.*, *Progress in Research*, Cyclotron Institute, Texas A&M University (2016-2017), p. IV-28.
[5] http://www.nndc.bnl.gov/chart/chartNuc.jsp

The 2017 REU experiment: Rare isotope beam production from the ^{58}Ni+^{58}Ni reaction with MARS

B.T. Roeder, R. Roundey,[1] M. Youngs, and Summer 2017 REU students

[1]*Hillsdale College, Hillsdale, Michigan*

During our Research Experience for Undergraduates (REU) program for summer 2017, a dedicated experiment for the undergraduate students was conducted using the Cyclotron Institute facilities. The experiment was designed to give the students some "hands-on" experience with the setting up and execution of a real nuclear physics experiment. The REU students received one day of introductory lectures prior to their participation in the experiment, followed by two days of experiment. During the experiment, the students aided in debugging the detector electronics, tuning rare isotope beam through the Momentum Acromat Recoil Separator (MARS) spectrometer [1], and analyzing the online data as it was collected. In addition, the REU student directly associated with the project, R. Roundey, participated in the planning of the experiment by performing simulations prior to the experiment. The student also analyzed the data in detail following the experiment and reported the results in a poster at the Fall 2017 meeting of the Department of Nuclear Physics of the American Physical Society.

Leading up to the experiment, R. Roundey conducted simulations for the experiment with the model of MARS in the program LISE++ [2]. She was instructed to study the reaction ^{58}Ni+Ni for the purpose of investigating what isotopes could be produced and separated near the proton dripline in the region near mass A=50. To maximize production of these isotopes, she performed simulations to optimize the predicted beam energy, intensity, target thickness, and whether or not a stripper foil following the target could improve the production. Following extensive calculations, it was determined that ^{58}Ni at 36 MeV/u on a nickel target 100 μm would give the best results based on the beam intensities available at the Cyclotron Institute. It was also predicted that a carbon stripper foil would increase the rate measured for the isotopes produced in the "fully-stripped" charge state. Reactions for ^{58}Ni on a ^{9}Be target were also simulated for comparison.

The ^{58}Ni+Ni and ^{58}Ni+Be experiment was conducted over two days with one day for each target. For the ^{58}Ni+Ni, a 36 MeV/u ^{58}Ni^{19+} beam from the K500 impinged on a 100 μm natural Nickel foil at the entrance of MARS [1]. A thin carbon stripper foil, 47.7 μg/cm^2, was also mounted after the target in an attempt to increase the reaction products in the "fully stripped" charge state. This foil was found in subsequent analysis to have a negligible effect. About 35 enA of beam was available for the measurement. To investigate the nuclei produced near the proton dripline, MARS was tuned for magnetic rigidities consistent with the production of ^{53}Ni. While this setting was not close to the proton dripline for Ni isotopes, it did allow a search for isotopes near the dripline for odd "Z" elements, such as Co and Mn. The results for a data run taken for about 12 hours are shown in Fig. 1. To remove background due to scattered primary beam, the particle identification plot ΔE vs. Y-position shown was gated with a large gate in the ΔE versus E spectrum. This ensures that only particles with the proper predicted energy losses are taken into account for the identification. As shown, isotopes in the N=Z-3 line, such as ^{53}Ni and ^{47}Mn were clearly populated. A few counts consistent with the production of N=Z-4 isotopes are also observed

at the very low rate of a few counts/hour. More primary beam or more time to take data would have made the results more conclusive.
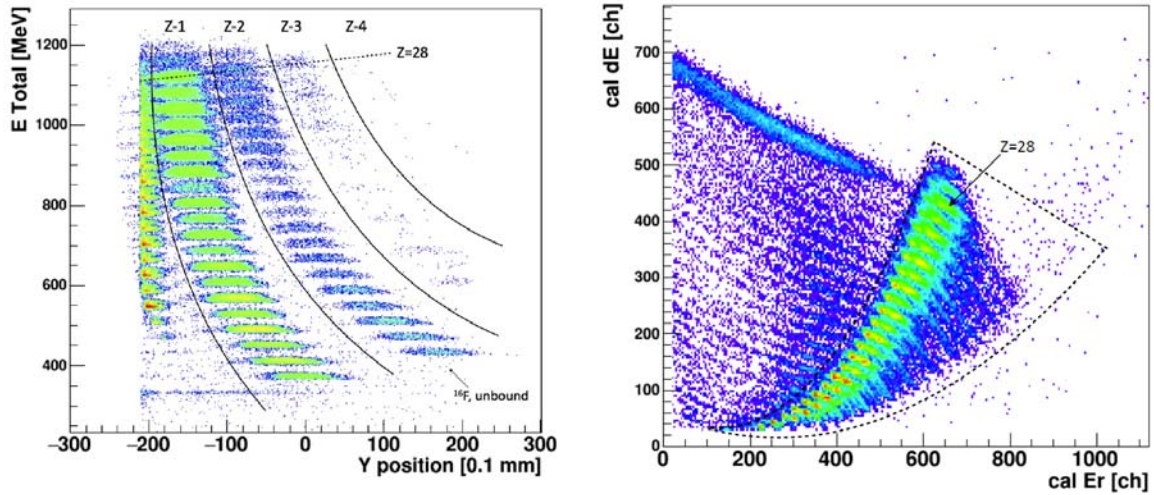
FIG. 1. Particle identification plots for the ^{58}Ni+Ni data. N=Z-3 and a few N=Z-4 isotopes were populated. See text for explanation.

For the ^{58}Ni+Be target data, the same ^{58}Ni beam at 36 MeV/u from the K500 cyclotron impinged on a Be foil 304 μm thick. The reaction was measured for about 7 hours. The result of that series of runs
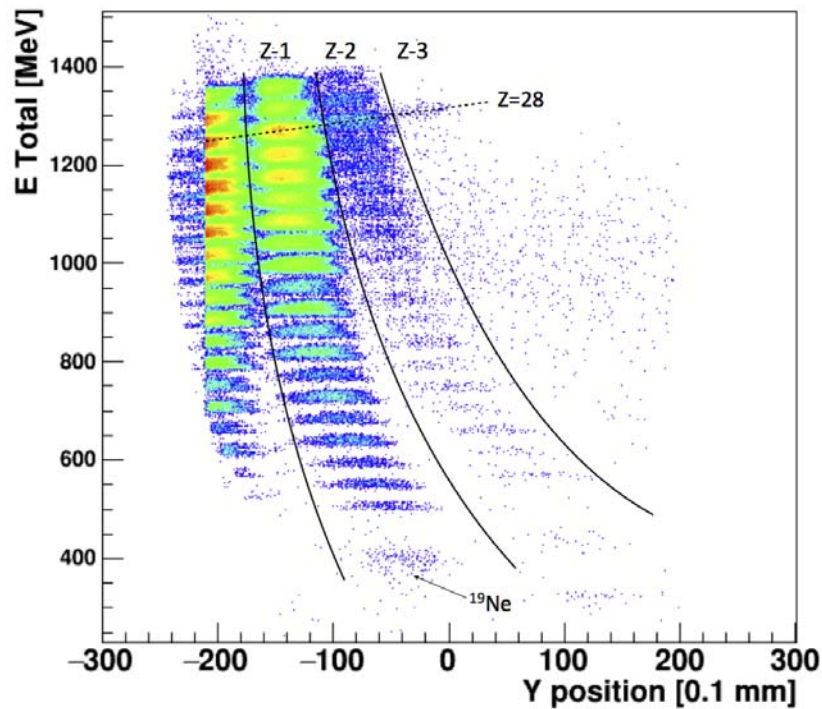
FIG. 2. Particle identification plot for the ^{58}Ni+Be data. N=Z-3 isotopes were populated, but with lower intensity than with the Ni target. See text for explanation.

is shown in Fig. 2. In this case, the only clearly observed N=Z-3 isotope was ^{53}Ni, although a few counts consistent with other N=Z-3 isotopes were noted. No counts consistent with N=Z-4 isotopes were observed.

In conclusion, N=Z-3 and N=Z-4 nuclei in the mass region of A=50 have been produced and observed using a beam, in this case ^{58}Ni at 36 MeV/u, available at the Cyclotron Institute. However, contrary to the predictions of LISE++ [2,3], more exotic isotopes closer to the proton dripline were produced with the Ni target as opposed to the Be target, as was predicted by the model. This reaction was studied as part of an on-going study that has shown that using nickel as a production target produces nuclei further from stability and removes more particles from the primary beam than a beryllium target.

[1] R.E. Tribble, R.H. Burch, and C.A. Gagliardi, Nucl. Instrum. Methods Phys. Res. **A285**, 441 (1989).
[2] B.T. Roeder *et al.*, *Progress in Research*, Cyclotron Institute, Texas A&M University (2013-2014) p. IV-40; http://cyclotron.tamu.edu/progress-reports/2013-2014/SECTION IV.html.
[3] O.B. Tarasov and D. Bazin, Nucl. Instrum. Methods Phys. Res. **B266**, 4657 (2008).

MARS status report for 2017-2018:
Tuning of rare isotope beams of ^{59}Fe, ^{42}Ti, ^{10}C, ^{8}B, ^{8}Li, ^{35}K, and ^{32}Cl

B.T. Roeder and A. Saastamoinen

This year, we continued the program of providing rare isotope beams for the physics program at the Cyclotron Institute at Texas A&M University with the Momentum Achromat Recoil Separator (MARS) [1]. ^{10}C and ^{42}Ti beams provided to Dr. Hardy's research group were prepared for their continuing studies of super-allowed β-decay. ^{8}B and ^{10}C beams at lower energy around 8 MeV/u were prepared for experiments with Dr. Rogachev's research group in collaboration with the University of São Paulo in Brazil. An ^{59}Fe beam was developed for Dr. Yennello's group. Beams of ^{8}B and ^{8}Li were tuned for Dr. Rogachev's group as part of the commissioning run for the new TexAT detector. Finally, beams of ^{35}K and ^{32}Cl beam were made for Dr. Tribble's group for their continuing studies of β-delayed proton decay with the Astrobox2 detector.

With the exception of ^{59}Fe, most of the beams made this year were made before and reported in annual reports from previous years [2,3]. A summary of the ^{59}Fe beam preparation results is given in this report.

An ^{59}Fe beam has been requested by Dr. Yennello's group for an experiment in collaboration with Los Alamos National Laboratory. Despite the long half-life of ^{59}Fe, which would make it a candidate for production via neutron capture in a reactor, the in-flight production method with MARS may be preferred for the experiment due to safety concerns. In the beam production test, two reactions were investigated using beams from the K500 cyclotron: d(^{59}Co,^{59}Fe)2p at 13 MeV/u and d(^{58}Fe,^{59}Fe)p at 11 MeV/u. A third possible reaction, ^{9}Be(^{61}Ni,^{59}Fe)X (2p-removal) was also proposed but not investigated due to the cost of the ^{61}Ni isotope.

For the d(^{59}Co,^{59}Fe)2p case, ^{59}Co at 13 MeV/u bombarded the MARS gas target filled with 0.5 atm of D_2 gas at 77K. A 1 mil thick Al degrader was placed after the target, but before MARS, to attempt to separate the ^{59}Fe from the ^{59}Co primary beam via energy loss and magnetic rigidity. This method would have produced ^{59}Fe secondary beam via a direct transfer reaction with an energy of about 8.0 MeV/u, as desired by the experimenters. However, due to the low beam energy, the reaction products were not fully stripped of their electrons and were difficult to identify separated from the charge states of the primary beam. A reaction product was identified in between the 4 charge states of the beam using a passive, 1 mil Al degrader in front of the silicon detector at the focal plane. The energy loss through this degrader suggested this product was more consistent with an excited state of the ^{59}Co, not with ^{59}Fe. Due to the inconclusive results, and the difficulty in separating the ^{59}Fe from the charge states of the ^{59}Co primary beam, this production method was abandoned.

For the d(^{58}Fe,^{59}Fe)p case, ^{58}Fe at 11 MeV/u bombarded the MARS gas target filled with 0.5 atm of D$_2$ gas at 77K. This setup produced a ^{59}Fe secondary beam via a direct transfer reaction with an energy of 7.5 MeV/u. As with the previous reaction, the reaction products were not fully stripped of their electrons and charge states 23+ through 26+ were populated. It was noted in this case, however, that mass-59 reaction products were separated from the ^{58}Fe primary beam charge states by about 1 cm at the focal plane. Thus, the ^{58}Fe charge states could be mostly blocked with the focal plane slits of MARS. To identify the ^{59}Fe, the mass-59 reaction products were centered on the 1 mm thick position sensitive silicon detector, and then a 1 mil thick passive aluminum degrader was placed in front of the detector. This allowed a separation via energy loss between ^{59}Co, produced from d(^{58}Fe,^{59}Co)n and ^{59}Fe from the (d,p) reaction. Once this separation was achieved in the spectrum, then the rigidity of MARS was tuned until the production of ^{59}Fe was optimized at the focal plane. The resulting beam tune, with the focal plane slits inserted and the 1 mil aluminum degrader inserted in front of the detector, is shown in Fig. 1.

The best tune for ^{59}Fe gave about 650 eV/nC for ^{59}Fe^{23+}. The total secondary beam was composed
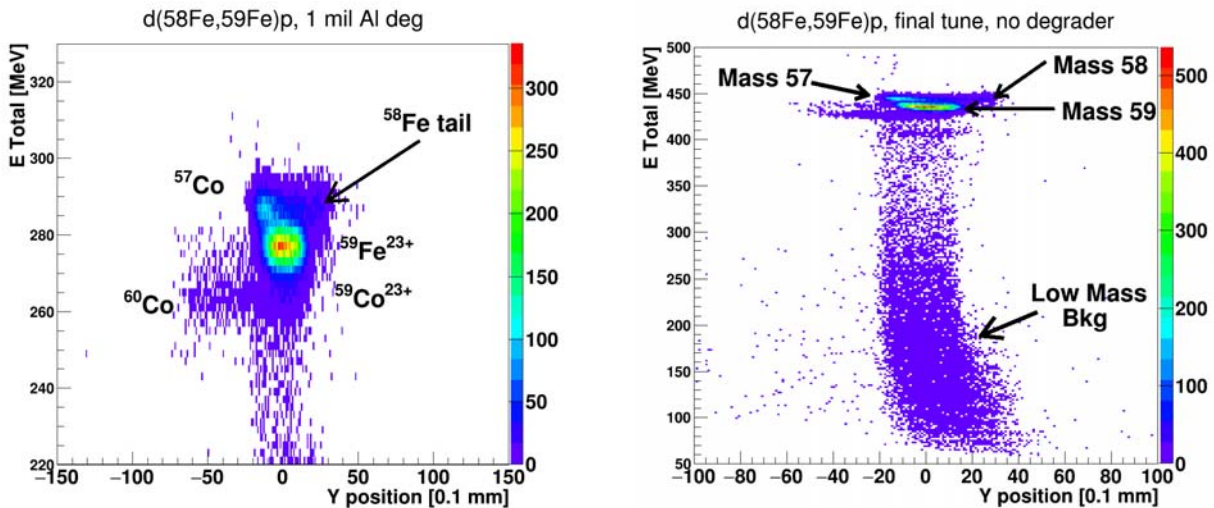
FIG. 1. Resulting secondary beam for d(^{58}Fe,^{59}Fe^{23+})p. The MARS rigidity tune has been optimized for the ^{59}Fe production. To obtain the left spectrum, a 1 mil Al degrader was placed in front of the silicon detector so that the products could be identified via energy loss in the spectrum. See text for further explanation.

of 80% ^{59}Fe, 7% ^{59}Co and 13% ^{57}Co, where the latter two isotopes could not be separated. Some low-mass background was also present in the beam. With 40 enA of ^{58}Fe beam on the faraday cup at the exit of the cyclotron, a rate of 42 kHz was observed for this secondary beam on a scintillator at the MARS focal plane, implying about 30 kHz of ^{59}Fe was possible. With these parameters, a rate of about 10^5 particles/sec ^{59}Fe would be possible with about 3 times more primary beam on target. 100-200 nA of ^{58}Fe primary beam should be achievable if the ^{58}Fe is produced with an oven in the ECR source instead of via sputtering, as was done for this test run.

[1] R.E. Tribble, R.H. Burch, and C.A. Gagliardi, Nucl. Instrum. Methods Phys. Res. A**285**, 441 (1989).
[2] B.T. Roeder *et al.*, *Progress in Research*, Cyclotron Institute, Texas A&M University (2014-2015), p. IV-25;

[3] B.T. Roeder *et al.*, *Progress in Research*, Cyclotron Institute, Texas A&M University (2016-2017), p. IV-23.

Neutron monitors for MINER experiment

J. Hooker, G.V. Rogachev, E. Koshchiy and A. Moya for MINER collaboration

The Mitchell Institute Neutrino Experiment at Reactor (MINER) is an international collaboration across 10 institutions over 4 countries that aims at measuring coherent neutrino-nucleus scattering (CNS) and sterile neutrinos. Measuring CNS is a sensitive probe for physics beyond the Standard Model and has cross section that is two-three orders of magnitude higher than a neutrino-nucleon cross section, making it possible to observe CNS using relatively small quantities of detector material (~10 kg of high purity Germanium or Silicon detectors). The CNS events are identified by the low energy nuclear recoils (Si or Ge) they produce as a result of neutrino elastic scattering. There are many challenges associated with this project. Since energy of the nuclear recoils is in the range from 0 to 2 keV a state-of-the-art detector technology has to be implemented to make these measurements feasible. Another challenge, and the one that we focus on in this report, is accurate characterization and in-situ measurement of neutron background. Neutron scattering may produce events that have signatures identical to CNS. The MINER experiment uses the TAMU megawatt reactor at the Nuclear Science Center (NSC) as the neutrino source, therefore neutron flux is a major issue, even after careful shielding is implemented. Development of neutron detectors for neutron background measurements is the main contribution of the Cyclotron Institute to MINER collaboration. A detailed description of the two neutron detectors, ^{6}Li glass for thermal neutrons and p-terphenyl for fast neutrons, can be found in [1].
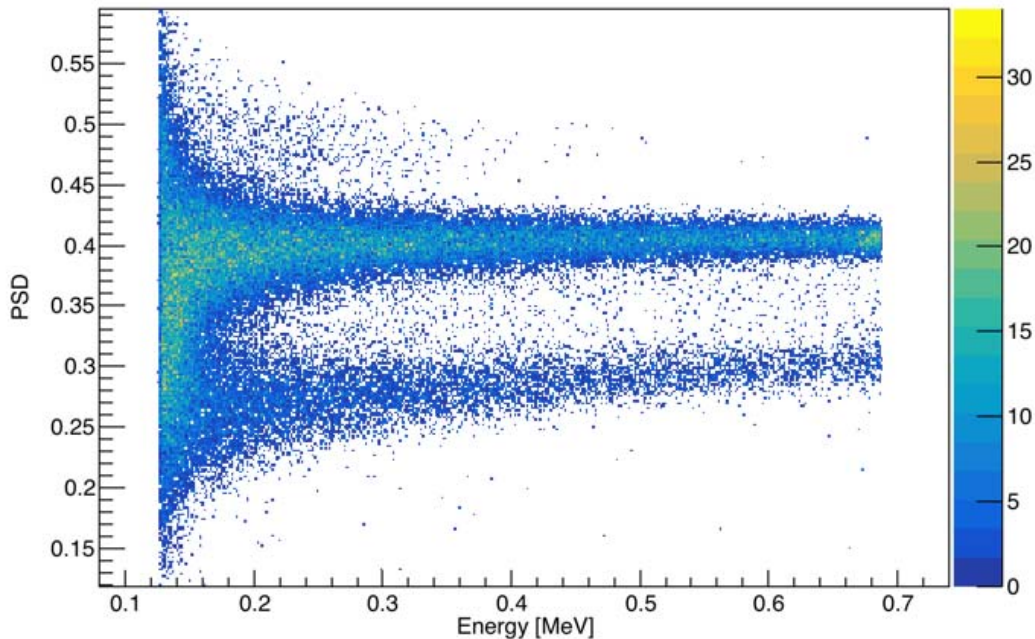
FIG. 1. The PSD vs recoil energies. The top band corresponds to gammas while the bottom band are the neutrons. Pulse shape discrimination is possible down to 160 keV.

An improvement that has been made to the p-terphenyl detector is the addition of a second photomultiplier tube (PMT). This allows for more light collection and subsequently can achieve better pulse shape discrimination (PSD) of fast neutrons and gammas at lower energies. As we record the waveforms of the signals, both PMT signals can be added together and continuous wavelet transforms (CWT) are used for PSD similar to the method used in [2]. The PSD is plotted vs neutron recoil energy in Fig. 1. There is clear separation down to neutron recoil energies of 160 keV.

To measure how well the PSD is between the neutrons and gammas, we can calculate the figure of merit (FOM) at different energies by fitting the neutron and gamma peak with a Gaussian function and calculating

$$FOM = \frac{\mu_n - \mu_\gamma}{2.36(\sigma_n + \sigma_\gamma)}$$

Where μ_n and μ_γ are the means of the peaks for the neutrons and gammas respectively while σ_n and σ_γ are the standard deviations of the peaks. A higher FOM means that the separation and PSD is much better. The FOM vs. energy is shown in Fig. 2. It is clear that the summation of the two PMT signals (purple) provides much better PSD compared to just a single PMT (red and blue). For neutron recoil energies above 500 keV, there is 5σ separation between the neutrons and gammas when summing the two PMTs. 3σ separation is achieved down to 230 keV.
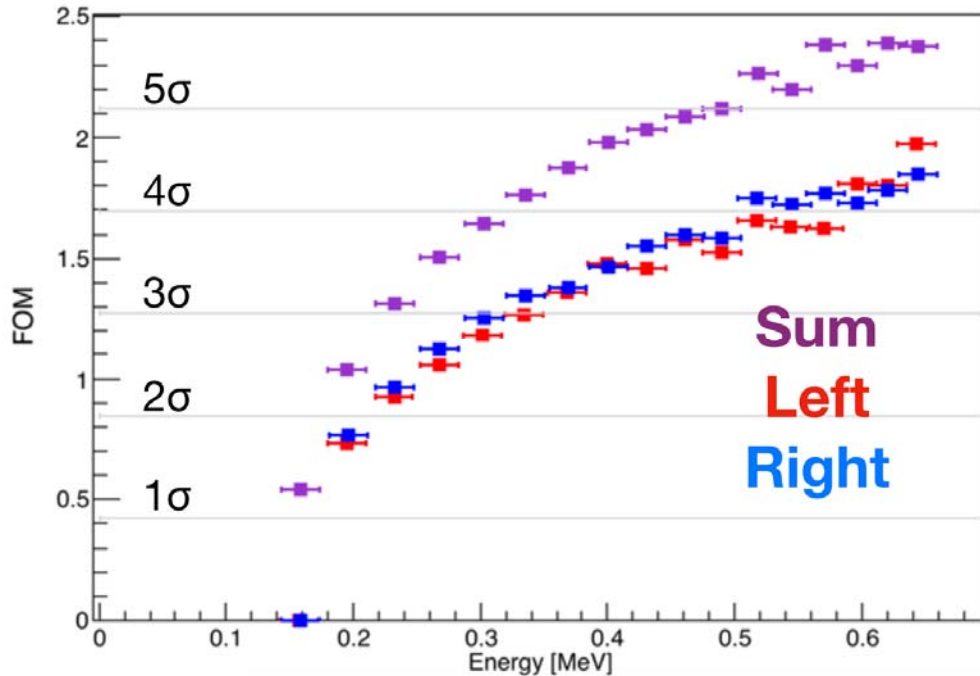
FIG. 2. The Figure-Of-Merit calculated for different neutron recoil energies. The red and blue points correspond to the individual PMT signals, the purple are the combined sum of both PMTs.

With the addition of the second PMT and the improved PSD we now achieve, we can provide even better neutron background measurements for the MINER collaboration. By measuring the flux of neutrons in both detectors, we can then test configurations of materials that reduce neutron background. A measurement of the integrated flux of fast neutrons inside the thermal column at the NSC was performed between 11/13/2017 and 11/17/2017 and is shown in Fig. 3. The neutron flux increases only by about a factor of two relative to the background when the reactor is "on" indicating that the shielding is working very well. The ^{6}Li glass scintillator measuring the thermal neutrons produced similar results when compared to the reactor "off" background. Another measurement was done between 04/20/2018 – 04/25/2018 outside the thermal column where the first MINER measurements are expected to take place. We saw no increase in the flux when the core was on.
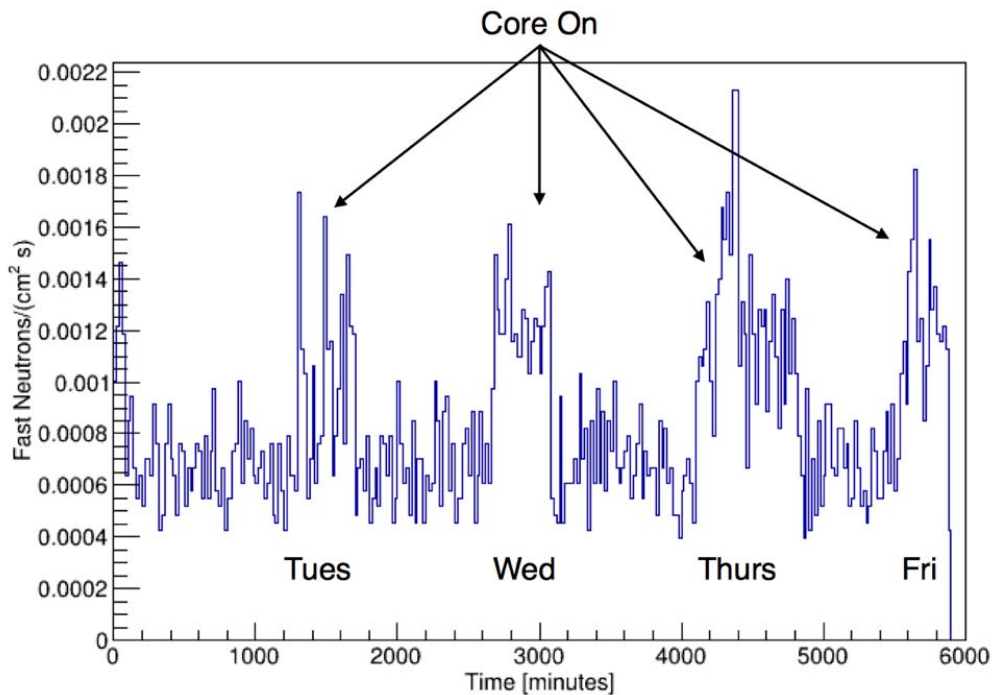
FIG. 3. The integrated fast neutron rate from measured in the p-terphenyl at the NSC.

Advanced computational techniques such as machine learning are currently being investigated to provide further improved discrimination of neutrons and gammas in both the p-terphenyl and ^{6}Li glass detectors.

[1] J. Hooker, G.V. Rogachev *et al.*, *Progress in Research*, Cyclotron Institute, Texas A&M University (2016-2017) p. IV–53.
[2] S. Yousefi, L. Lucchese, and M.D. Aspinall, Nucl. Instrum. Methods Phys. Res. **A558**, 551 (2009).

Toward development of fast neutron portal monitors

E. Aboud, G.V. Rogachev, E. Koshchiy, J. Hooker, S. Ahn, P. Kuchment, W. Baines, and F. Terzioglu

Smuggling of fissile material into the United States is a major national security issue. Current portal neutron monitors primarily rely on thermal neutron detectors and require expensive materials such as ^{3}He gas. Besides significant cost of ^{3}He gas, another disadvantage is the loss of information about the direction for the measured neutrons. If fast neutrons are detected before thermalisation then momentum vector can be recovered and may be used for point-like source identification. Techniques have been developed to challenge these limitations in the past [1], but still require complex detection systems. Currently, we are developing a novel technique of fast neutron detection. It is a collaborative effort with the mathematics department. By developing an array of hydrocarbon scintillators (p-terphenyl, the brightest organic scintillator with excellent PSD properties) in an arrangement that optimizes the probability of a neutron scattering in two scintillators (double scattering events), we hope to achieve better sensitivity to elevated neutron flux from a point-like source. Primarily, this technique preserves information of the incoming neutron direction which allows for source location reconstruction using the techniques proposed by our colleagues [2,3].

As a prelude to the development of this detector apparatus, simulations of the setup were done with the Monte Carlo software MCNP [4]. Simulations were conducted with sampled neutron background libraries and real fission spectra for isotopes of interest. Results from the simulations were used as preliminary data sets for the development of the location reconstruction techniques provided by the mathematics group. Initial testing has provided positive results for the algorithm with successful location recovery for all data sets.

A key factor in the design of the detector apparatus involves the choice of light detector. An attractive option is silicon photomultiplier (SiPM), because of its small footprint, low bias requirement and flexible configuration. We have tested two brands of SiPMs: a Hamamatsu S-13360 and the other a C-Series SensL.

Initially, testing was done for a single Hamamatsu SiPM in order to observe neutron and gamma waveforms from p-terphenyl using a ^{252}Cf source. While waveforms were observed, they were significantly smaller than expected (10mV amplitude scale). For accurate waveform analysis, we would need amplitudes on the 100mV scale. Various attempts were made in order to determine the cause of the small signals and to amplify the signals. The amplification lead to distortion of the signal preventing reliable pulse-shape discrimination.

The C-Series SensL SiPM were tested next. Similar results were found initially, but after reviewing alternative methods in [5], it was found that biasing the SiPM on the cathode (instead of the anode) produced a signal in the 100mV-1V scale. Similar tests were done using the Hamamatsu SiPMs, but to no avail. Further testing of the SensL SiPMs were done to compare directly with [5] with the only major difference being the scintillator used.

Parallel to the testing of the light detectors, an analysis code was developed. An integral part of the analysis includes pulse shape discrimination (PSD). Utilizing the properties of the waveforms, we are able to distinguish between the neutron and γ-events. Two main techniques were used: a simple method of calculating the charge (integral) and the amplitudes of the waveforms and a method involving a tail charge and total waveform charge [5]. While both techniques are still under development, preliminary PSD was done for both Hamamastu and SensL SiPMs, an example is shown in Fig. 1. So far, PSD with SiPM cannot compete with PSD that we are achieving with photomultiplier tubes. Further tests and developments are under way.
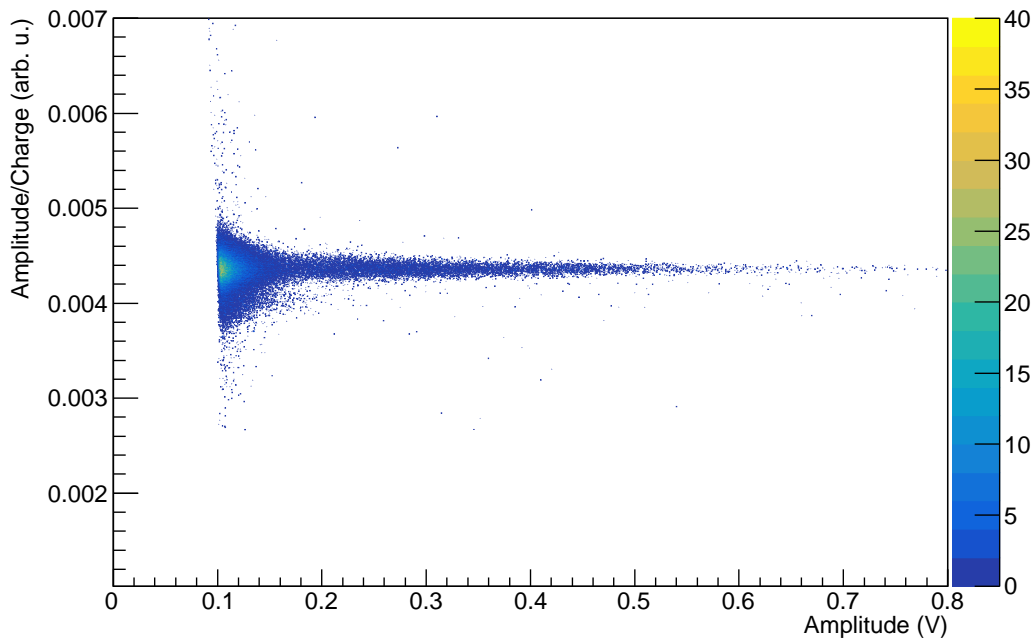
FIG. 1. Preliminary pulse shape discrimination using the amplitude over charge method and the C-Series SensL SiPM. A clear gamma-ray band is visible around 0.0045 (y-axis) and extends from 0.1 to past 0.8 V. Another band is visible around 0.004 (y-axis) that corresponds to neutron waveforms. Discrimination for this case is not ideal and new techniques (both physical and computational) are being looked at in order to enhance our PSD abilities.

[1] P.B. Rose *et al.*, Scientific Reports **6**, 24388 (2016).

[2] M. Allmaras *et al.*, Inverse Problems and Imaging, **7**, 47 (2013).

[3] A. Olson *et al.*, Nuclear Science and Engineering, **184**, 125 (2016).

[4] MCNP, X. LA-UR-03, Los Alamos National Laboratory (1987).

[5] M. Ruch *et al.*, Nucl. Instrum. Methods Phys. Res. **A793**, 1 (2015).

Status of Texas active target data manager development

S. Ahn, G.V. Rogachev, E. Koshchiy, J. Hooker, and S. Upadhiajula

In order to address questions in nuclear structure, nuclear reactions and nuclear astrophysics, Texas Active Target (TexAT) detector system is developed and commissioned at the Cyclotron Institute [1]. The system includes a Micro-MEsh Gaseous detector system ("micromegas"), a Silicon detector array and a CsI(Tl) detector array as shown in Fig. 1. It enables a time projection chamber (TPC) which provides 3D particle track information and measures its total energy deposition in Si and CsI(Tl), if particle escapes the active TPC volume.
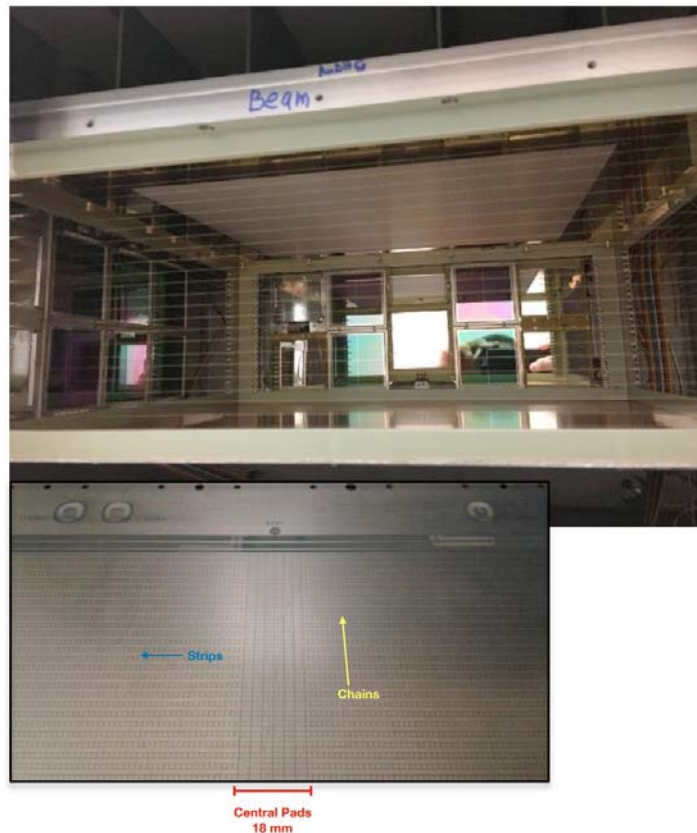
FIG. 1. A picture of TexAT detectors (top) and details of the Micromegas plate (bottom). The Micromegas plate is installed on top of the field cage. The Silicon detector array is surrounding the field cage to detect light particles from reactions and the CsI(Tl) detectors are placed at the back of the Silicon detector array to detect silicon-punch-through particles.

The readout of signals from the TPC is processed by the General Electronics for TPC (GET) [2] handling about 1300 total number of channels. The TexAT setup for an experiment is shown in Fig. 2. The GET electronics for the TexAT detector consists of 1 microTCA crate, 1 Mutant trigger module, 2

FIG. 2. A photo of TexAT full setup for an experiment with RIB beam. AsAd motherboards are placed on top of the TexAT chamber.

CoBo com- munication modules and 6 AsAd motherboards. Each AsAd motherboard includes four Application Specific Integrated Circuit (ASIC) chips (named as "ASIC for GET" or AGET chips) performing signal processes such as charge sensitive amplifier, shaping amplifier, analog digital converter, leading edge discriminator. Photos of the electronics are shown in Fig. 3. Digitized waveforms of signals are transferred from the AsAd boards to a computer storage by Ganil Data Acquisition System
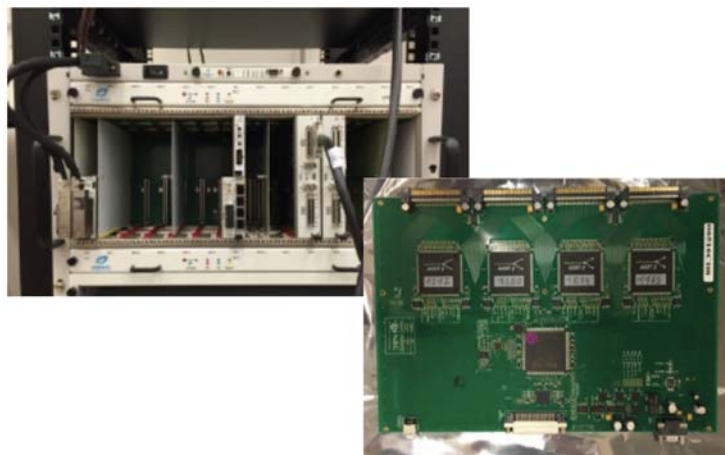
FIG. 3. Pictures of Cobo module in the TCA crate (left) and AsAd motherboard containing 4 AGET chips(right).

(Ganil DAQ) [3]. The Ganil DAQ has basically four main functionalities:

1. an electronics slow control for Mutant, CoBo, AsAd and AGET,
2. a run control manager for DAQ users to control and monitor data streams,
3. data transfer between electronics and the data storage,
4. data analysis tool (online and offline).

The implementation of the Ganil DAQ has been completed to the GET electronics for the TexAT system and users can conveniently manage and access stored data during experiments. An example snapshot of the DAQ system is shown in Fig. 4.
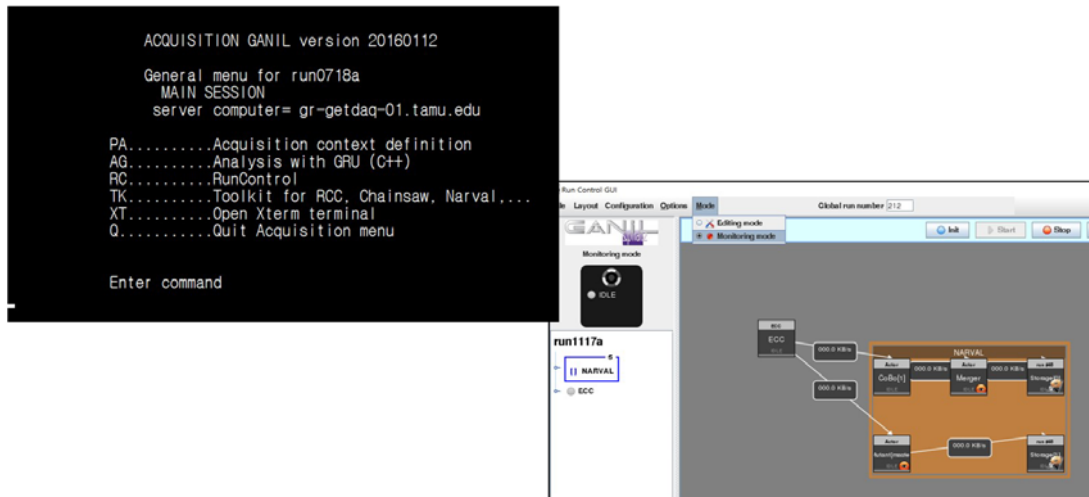
FIG. 4. Main menu of the Ganil DAQ (left) and run control GUI (right). In the menu, one can launch/restart a run control server, a run logger and so on. User can define number of electronics to use, initialize/reset the GET electronics, start/stop taking data and monitor data rate during runs with the GUI.

As mentioned above, data from the detector can be analyzed by a newly developed online/offline analysis tool, named as MFMHistServer, using libraries of Ganil DAQ software. The data analysis process has been performed with two tasks, one for data format conversion (from MFM to ROOT format) and another for visualization of data. Fig. 5 shows an example of waveforms read by a data diagnostics tool, cobo- frame-viewer, on the left. The MFMHistServer creates histograms and runs a histogram server to provide spectrum to a client program, vigru, which visualizes them for users. As data is analyzed and histograms filled by the MFMHistServer, the software, vigru, can update spectrum (similar to web server and web browser communication). Fig. 5 shows a snapshot of the vigru software. The MFMHistServer can read data from either online buffer stream or recorded data files, and online analysis function is very useful for troubleshooting of detector setup.
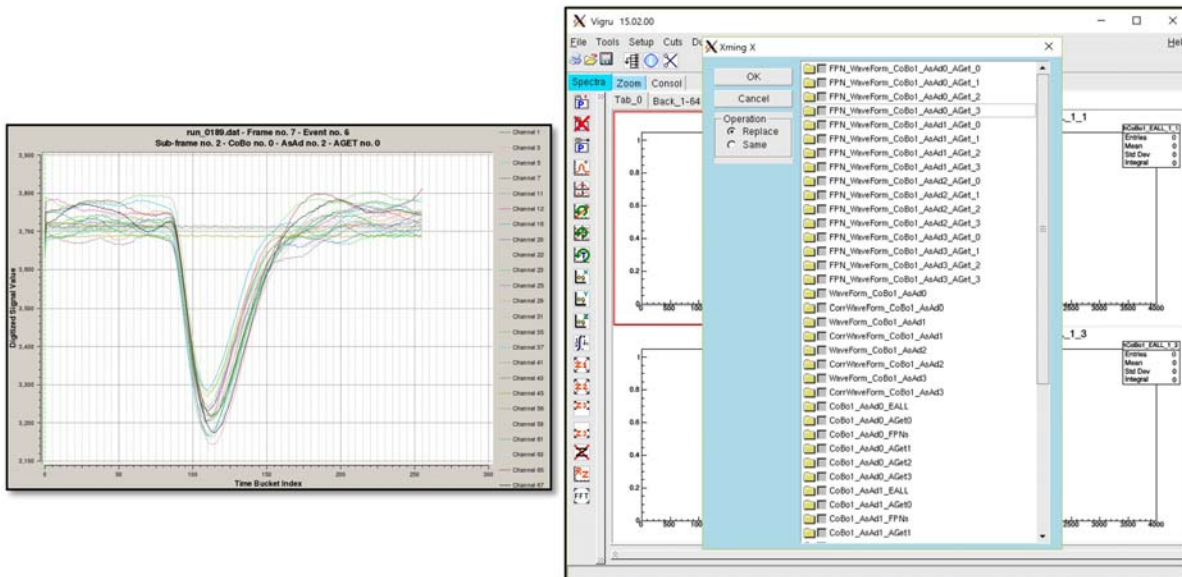
FIG. 5. An example of signal waveform data (left) and a screenshot of histogram visualization software (vigru) on the right. Total time length of the waveform is about 20 *μs*.

The MFMHistServer can also reconstruct particle tracks from hit pattern of Micromega plate. By per- forming the Hough Transformation method [4], one can find a slope and offset value of linear track as shown in Fig. 6. Alpha particle tracks from a source reproduced very well, as is evident in Fig. 7. Track
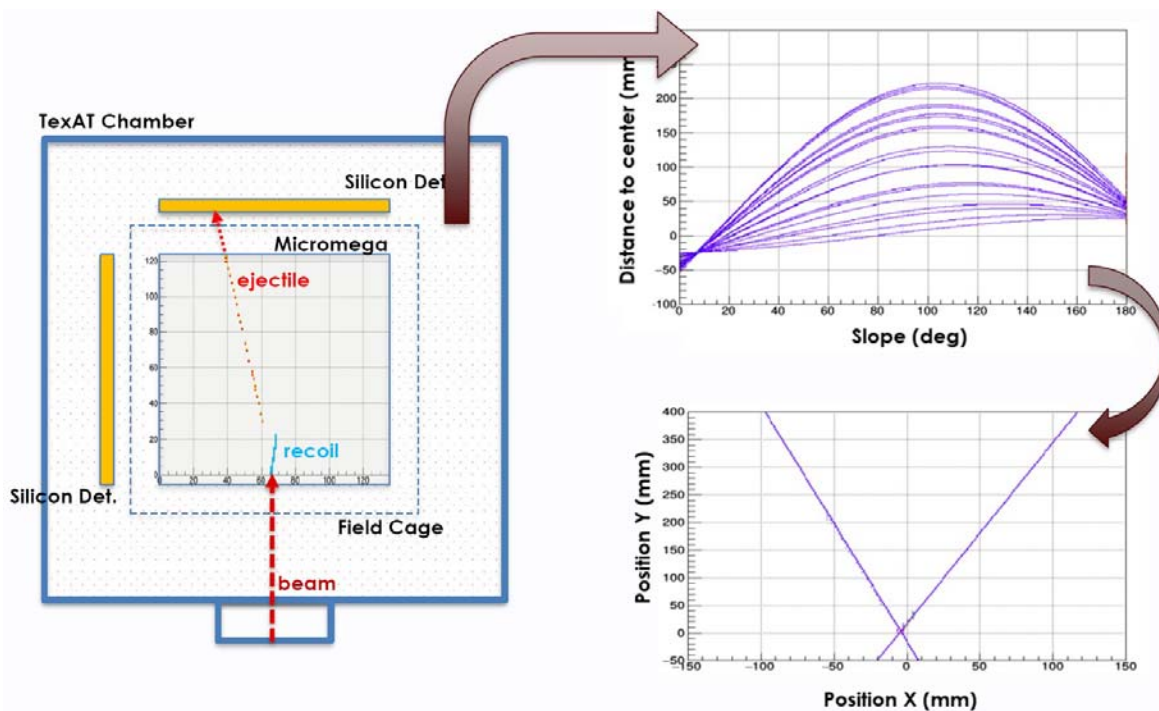
FIG. 6. An example of track reconstruction from the hit pattern of Micromega plate. From the track hit pattern (left), a 2D plot in the Hough parameter space can be drawn (top right) and the most focused point in the graph is picked for the slope and offset of the track. The bottom right graph shows two tracks found by the transformation method in two independent regions, respectively.

reconstruction for two body reactions is somewhat less reliable at the moment and improvements to track reconstruction are still being made.

In summary, the data manager for the TexAT active target detector system has been developed and already used for several experiments with beam rare isotope beams from Momentum Achromat Recoil Separator (MARS). The Ganil DAQ system is implemented in the TexAT GET electronics, to manage run controls and record data of digitized waveforms. In order to analyze online/offline data, the MFMHistServer has been developed and this provides a benefit of online data validation as well as a reconstruction of particle tracks.
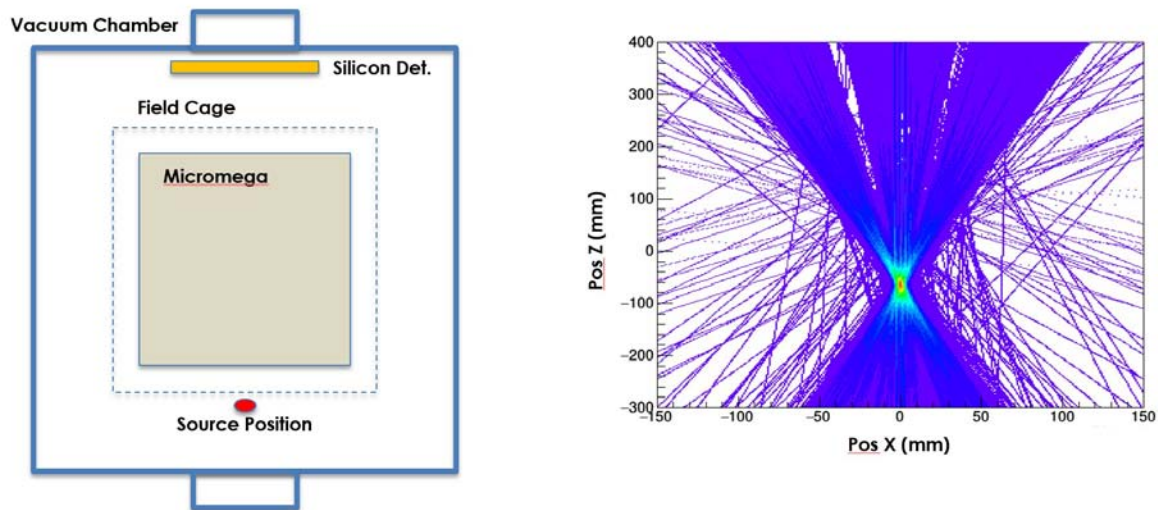
FIG. 7. Accumulated reconstructed tracks for alpha particles from the 241Am source. It shows the Hough transformation method works very well for one track per event.

[1] G.V. Rogachev, E. Koshchiy, E. Uberseder, and E. Pollacco, *Progress in Research*, Cyclotron Institute, Texas A&M University (2014-2015) p. IV-42.

[2] E.C. Pollacco *et al.*, Nucl. Instrum. Methods Phys. Res. **A887**, 81 (2018).

[3] A. Boujrad and F. Saillant, *2000 IEEE Nuclear Science Symposium*, Conference Record (Cat. No.00CH37149), Lyon, 2000, pp. 12/192-12/193 vol.2.

[4] P.V.C. Hough, *2ⁿᵈ International Conference on High-Energy Accelerators (HEACC 59)*, Conf. Proc. C **590914**, 554 (1959).

SECTION V

PUBLICATIONS

Statistical analysis of experimental multifragmentation events in ^{64}Zn+^{112}Sn at 40 MeV/nucleon, W. Lin, H. Zheng, P. Ren, X. Liu, M. Huang, R. Wada, Z. Chen, J. Wang, G.Q. Xiao, and G. Qu, Phys. Rev. C **97**, 044603 (2018).

^{7}Li(^{15}N,^{14}C)^{8}Be reaction at 81 MeV and ^{14}C+^{8}Be interaction versus that of ^{13}C+^{8}Be, A.T. Rudchik, A.A. Rudchik, L.M. Muravynets, K.W. Kemper, K. Rusek, E.I. Koshchy, E. Piasecki, A. Trzcińska, Val. M. Pirnak, O.A. Ponkratenko, I. Strojek, A. Stolarz, V.A. Plujko, S.B. Sakuta, R. Siudak, A.P. Ilyin, Yu. M. Stepanenko, Yu.O. Shyrma, and V.V. Uleshchenko, Nucl. Phys. **A971**, 138 (2018).

Analysis of pairing correlations in neutron transfer reactions and comparison to the constrained molecular dynamics model, C. Agodi, G. Giuliani, F. Cappuzzello, A. Bonasera, D. Carbone, M. Cavallaro, A. Foti, R. Linares, and G. Santagati, Phys. Rev. C **97**, 034616 (2018).

Azimuthal transverse single-spin asymmetries of inclusive jets and charged pions within jets from polarized-proton collisions at $\sqrt{s_{NN}}$ = 500 GeV, L. Adamczyk *et al.*, Phys. Rev. **D** 97, 032004 (2018).

Beam-energy dependence of directed flow of Λ, $\overline{\Lambda}$, $K^{\pm}$, K^0_s ,and ϕ in Au+Au Collisions, L. Adamczyk *et al.* (STAR Collaboration), Phys. Rev. Lett. **120**, 062301 (2018).

Cluster correlation and fragment emission in ^{12}C+^{1}2C at 95 MeV/nucleon, G. Tian, Z. Chen, R. Han, F. Shi, F. Luo, Q. Sun, L. Song, X. Zhang, G.Q. Xiao, R. Wada, and A. Ono, Phys. Rev. C **97**, 034610 (2018).

Density dependence of the nuclear energy-density functional, Panagiota Papakonstantinou, Tae-Sun Park, Yeunhwan Lim and Chang Ho Hyun, Phys. Rev. C **97**, 014312 (2018).

Direct measurement of astrophysically important resonances in ^{38}K(p,γ)^{39}Ca, G. Christian, G. Lotay, C. Ruiz, C. Akers, D.S. Burke, W.N. Catford, A.A. Chen, D. Connolly, B. Davids, J. Fallis, U. Hager, D. Hutcheon, A. Mahl, A. Rojas, and X. Sun, Phys. Rev. C **97**, 025802 (2018).

Effect of short-range correlations on the single proton 3s$_{1/2}$ wave function in ^{206}Pb, S. Shlomo, I. Talmi, M.R. Anders, and G. Bonasera, The 12th International Spring Seminar on Nuclear, Sant' Angelo d'Ischia, Ischia (Napoli), Italy, J. Phys. Conference Series **966**, 012013 (2018).

Extrapolation of scattering data to the negative-energy region. II. Applicability of effective range functions within an exactly solvable model, L.D. Blokhintsev, A.S. Kadyrov, A.M. Mukhamedzhanov, and D.A. Savin, Phys. Rev. C **97**, 024602 (2018).

Neutron enhancement from laser interaction with a critical fluid, H.J. Quevedo, G. Zhang, A. Bonasera, M. Donovan, G. Dyer, E. Gaul, G.L. Guardo, M. Gulino, M.La Cognata, D. Lattuada, S. Palmerini, R.G. Pizzone, S. Romano, H. Smith, O. Trippella, A. Anzalone, C. Spitaleri, and T. Ditmire, Phys. Lett. A **382**, 94 (2018).

New result for the neutron β-asymmetry parameter A$_0$ from UCNA, M.A.-P. Brown, E.B. Dees, E. Adamek, B. Allgeier, M. Blatnik, T.J. Bowles, L.J. Broussard, R. Carr, S. Clayton, C. Cude-Woods, S. Currie, X. Ding, B.W. Filippone, A. García, P. Geltenbort, S. Hasan, K.P. Hickerson, J. Hoagland, R. Hong, G.E. Hogan, A.T. Holley, T.M. Ito, A. Knecht, C.-Y. Liu, J. Liu, M. Makela, J.W. Martin, D. Melconian, M.P. Mendenhall, S.D. Moore, C.L. Morris, S. Nepal, N. Nouri, R.W. Pattie, A. Pérez Galván, D.G. Phillips, R. Picker, M.L. Pitt, B. Plaster, J.C. Ramsey, R. Rios, D.J. Salvat, A. Saunders, W. Sondheim, S.J. Seestrom, S. Sjue, S. Slutsky, X. Sun, C. Swank, G. Swift, E. Tatar, R.B. Vogelaar, B. VornDick, Z. Wang, J. Wexler, T. Womack, C. Wrede, A.R. Young, and B.A. Zeck, Phys. Rev. C **97**, 035505 (2018).

Non-perturbative approach to equation of state and collective modes of the QGP, Shuai Y. F. Liu and Ralf Rapp, ISMD 2017 Tlaxcala, Mexico, Eur. Phys. J. Web of Conferences **172**, 05001 (2018).

Nuclear dipole polarizability from mean-field modeling constrained by chiral effective field theory, Zhen Zhang, Yeunhwan Lim, Jeremy W. Holt and Che Ming Ko, Physics Letters B **777**, 73 (2018).

On unitarity of the particle--hole dispersive optical model, M.L. Gorelik, S. Shlomo, B.A. Tulupov, and M.H. Urin, Nucl. Phys. **A970**, 353 (2018).

Precise half-life measurement of the superallowed emitter ^{30}S, V.E. Iacob, J.C. Hardy, L. Chen, V. Horvat, M. Bencomo, N. Nica, H.I. Park, B.T. Roeder, and A. Saastamoinen, Phys. Rev. C **97**, 035501 (2018).

Precision masurement of the β asymmetry in spin-polarized ^{37}K decay, B. Fenker, A. Gorelov, D. Melconian, J.A. Behr, M. Anholm, D. Ashery, R.S. Behling, I. Cohen, I. Craiciu, G. Gwinner, J. McNeil, M. Mehlman, K. Olchanski, P.D. Shidling, S. Smale, and C.L. Warner, Phys. Rev. Lett. **120**, 062502 (2018).

Reexamination of a novel determination of density, temperature, and symmetry energy based on a modified Fisher model, X. Liu, H. Zheng, W. Lin, M. Huang, Y.Y. Yang, J.S. Wang, R. Wada, A. Bonasera, and J.B. Natowitz, Phys. Rev. C **97**, 014613 (2018).

Study of excited states of ^{35}Ar through β-decay of ^{35}K for nucleosynthesis in novae and X-ray bursts, A. Saastamoinen, G.J. Lotay, A. Kankainen, B.T. Roeder, R. Chyzh, M. Dag, E. McCleskey, A. Spiridon and R.E. Tribble, Nuclear Physics in Astrophysics Conference (NPA VII) York, United Kingdom, J. Phys. Conference Series **940**, 012004 (2018).

Sub-Coulomb ^{3}He transfer and its use to extract three-particle asymptotic normalization coefficients, M.L. Avila, L.T. Baby, J. Belarge, N. Keeley, K.W. Kemper, E. Koshchiy, A.N. Kuchera, G.V. Rogachev, K. Rusek, and D. Santiago-Gonzalez, Phys. Rev. C **97**, 014313 (2018).

Supplemental material for precision measurement of the β asymmetry in spin-polarized ^{37}K decay, B. Fenker, A. Gorelov, D. Melconian, J.A. Behr, M. Anholm, D. Ashery, R.S. Behling, I. Cohen, I. Craiciu, G. Gwinner, J. McNeil, M. Mehlman, K. Olchanski, P.D. Shidling, S. Smale, and C.L. Warner, Supplemental Material to Fenker *et al*., Phys. Rev. Lett. **120**, 062502 (2018).

Equilibration chronometry: characterizing neutron-proton equilibration within a strongly deformed nuclear system with sub-zeptosecond resolution, A. Jedele, A. McIntosh, K. Hagel, L. Heilborn, Z. Kohley, E. McCleskey, A. Rodriguez Manso, M. Youngs, A. Zarrella, and S. Yennello, Proceedings of Science **281**, 0229 (2017).

α-conjugate neck structures in the collisions of 35 MeV/nucleon ^{40}Ca with ^{40}Ca, K. Schmidt, X. Cao, E.-J. Kim, K. Hagel, M. Barbui, J. Gauthier, S. Wuenschel, G. Giuliani, M.R.D. Rodrigues, H. Zheng, M. Huang, N. Blando, A. Bonasera, R. Wada, C. Bottosso, G. Liu, G. Viesti, S. Moretto, G. Prete, S. Pesente, D. Fabris, Y. El Masri, T. Keutgen, S. Kowalski, A. Kumar, G. Zhang, and J.B. Natowitz, Phys. Rev. C **95**, 054618 (2017).

A novel method for determining the mean-field directly from the single particle matter density, S. Shlomo and M.R. Anders, Exotic Nuclei and Nuclear/Particle Astrophysics (VI). Physics with small accelerators: Proceedings of Carpathian Summer School of Physics 2016 (CSSP16), Sinaia, Romania, AIP Conference Proceedings **1852**, 020003 (2017).

A novel method for determining the single particle potential directly from the measured single particle density: Application to the charge density difference between the isotones ^{206}Pb$-^{205}$Tl, S. Shlomo and M.R. Anders, Bulletin of the Russian Academy of Sciences: Physics **81**, 1230 (2017).

An active base designed in high-counting-rate applications for Hamamatsu R1924A photomultiplier tube, Pei-Pei Ren, Wei-Ping Lin, Roy Wada, Xing-Quan Liu, Mei-Rong Huang, Guo-Yu Tian, Fei Luo, Qi Sun, Zhi-Qiang Chen, Guo-Qing Xiao, Rui Han, Fu-Dong Shi, and Bo-Xing Gou, Nuclear Science and Techniques **28**, 145 (2017).

ANASEN: The array for nuclear astrophysics and structure with exotic nuclei, E. Koshchiy, J.C. Blackmon, G.V. Rogachev, I. Wiedenhöver, L. Baby, P. Barber, D.W. Bardayan, J. Belarge, D. Caussyn, E.D. Johnson, K. Kemper, A.N. Kuchera, L.E. Linhardt, K.T. Macon, M. Matos, B.S. Rasco, and D. Santiago-Gonzalez, Nucl. Instrum. Methods Phys. Res. **A870**, 1 (2017).

Bulk and isospin instabilities in hot nuclear matter, V.M. Kolomietz and S. Shlomo, Phys. Rev. C **95**, 054613 (2017).

Bulk properties of the medium produced in relativistic heavy-ion collisions from the beam energy scan program, L. Adamczyk *et al.*(STAR Collaboration), Phys. Rev. C **96**, 044904 (2017).

Chemical potential and symmetry energy for intermediate-mass fragment production in heavy ion reactions near the Fermi energy, X. Liu, W. Lin, M. Huang, R. Wada, J. Wang, A. Bonasera, H. Zheng, Z. Chen, S. Kowalski, T. Keutgen, K. Hagel, L. Qin, J.B. Natowitz, T. Materna, P.K. Sahu, M. Barbui, C. Bottosso, and M.R.D. Rodrigues, Phys. Rev. C **95**, 044601 (2017).

Coherent diffractive photoproduction of ρ^0 mesons on gold nuclei at 200 GeV/nucleon-pair at the relativistic heavy ion collider, L. Adamczyk *et al.* (STAR Collaboration), Phys. Rev. C **96**, 054904 (2017).

Color screening and regeneration of bottomonia in high-energy heavy-ion collisions, X. Du, M. He, and R. Rapp, Phys. Rev. C **96**, 054901 (2017).

Description of charged particle pseudorapidity distributions in Pb+Pb collisions with Tsallis thermodynamics, Y. Gao, H. Zheng, L.L. Zhu, and A. Bonasera, Eur. Phys. J. A **53**, 197 (2017).

Detailed characterization of neutron-proton equilibration in dynamically deformed nuclear systems, A. Rodriguez Manso, A.B. McIntosh, A. Jedele, K. Hagel, L. Heilborn, Z. Kohley, L.W. May, A. Zarrella, and S.J. Yennello, Phys. Rev. C **95**, 044604 (2017).

Dijet imbalance measurements in Au+Au and pp collisions at $\sqrt{s_{NN}}$ = 200 GeV at STAR, L. Adamczyk *et al.* (STAR Collaboration), Phys. Rev. Lett. **119**, 062301 (2017).

Direct measurement of the key E$c.m.$ = 456 keV resonance in the astrophysical ^{19}Ne(p,γ)^{20}Na reaction and its relevance for explosive binary systems, R. Wilkinson, G. Lotay, A. Lennarz, C. Ruiz, G. Christian, C. Akers, W.N. Catford, A.A. Chen, D. Connolly, B. Davids, D.A. Hutcheon, D. Jedrejcic, A.M. Laird, L. Martin, E. McNeice, J. Riley, and M. Williams, Phys. Rev. Lett. **119**, 242701 (2017).

Direct virtual photon production in Au+Au collisions at $\sqrt{s_{NN}}$ = 200 GeV, L. Adamczyk *et al.* (STAR Collaboration), Phys. Lett. B **770**, 451 (2017).

Energy dependence of J/Ψ production in Au+Au collisions at $\sqrt{s_{NN}}$ = 39, 62.4 and 200 GeV, L. Adamczyk *et al.* (STAR Collaboration), Phys. Lett. B **771**, 13 (2017).

Equation of state and radii of finite nuclei in the presence of a diffuse surface layer, V.M. Kolomietz, S.V. Lukyanov, A.I. Sanzhur, and S. Shlomo, Phys. Rev. C **95**, 054305 (2017).

Extrapolation of scattering data to the negative-energy region, L.D. Blokhintsev, A.S. Kadyrov, A.M. Mukhamedzhanov, and D.A. Savin, Phys. Rev. C **95**, 044618 (2017).

First direct constraints on Fierz interference in free-neutron β decay, K.P. Hickerson, X. Sun, Y. Bagdasarova, D. Bravo-Berguño, L.J. Broussard, M.A.-P. Brown, R. Carr, S. Currie, X. Ding, B. W. Filippone, A. García, P. Geltenbort, J. Hoagland, A.T. Holley, R. Hong, T.M. Ito, A. Knecht, C.-Y. Liu, J. L. Liu, M. Makela, R.R. Mammei, J.W. Martin, D. Melconian, M.P. Mendenhall, S.D. Moore, C.L. Morris, R.W. Pattie, A. Pérez Galván, R.Picker, M.L. Pitt, B. Plaster, J.C. Ramsey, R. Rios, A. Saunders, S.J. Seestrom, E.I. Sharapov, W.E. Sondheim, E. Tatar, R.B. Vogelaar, B. VornDick, C. Wrede, A.R. Young, and B.A. Zeck, Phys. Rev. C **96**, 042501(R) (2017).

Global Λ hyperon polarization in nuclear collisions, L. Adamczyk *et al.* (STAR Collaboration), Nature **548**, 62 (2017).

Halo-induced large enhancement of soft dipole excitation of ^{11}Li observed via proton inelastic scattering, J. Tanaka, R. Kanungo, M. Alcorta, N. Aoi, H. Bidaman, C. Burbadge, G. Christian, S. Cruz, B. Davids, A. Diaz Varela, J. Even, G. Hackman, M.N. Harakeh, J. Henderson, S. Ishimoto, S. Kaur, M. Keefe, R. Krücken, K.G. Leach, J. Lighthall, E. Padilla Rodal, J.S. Randhawa, P. Ruotsalainen, A. Sanetullaev, J.K. Smith, O. Workman, and I. Tanihata, Phys. Lett. B **774**, 268 (2017).

Heavy-ion beam induced effects in enriched gadolinium target films prepared by molecular plating, D.A. Mayorov, E.E. Tereshatov, T.A. Werke, M.M. Frey, and C.M. Folden, III, Nucl. Instrum. Methods Phys. Res. **B407**, 256 (2017).

How well does the chiral expansion converge in nuclear and neutron matter? F. Sammarruca, L. Coraggio, Jeremy W. Holt, N. Itaco, R. Machleidt, and L. E. Marcucci, The 8th International Workshop on Chiral Dynamics, CD201, Pisa, Italy, Proceedings of Science **CD15**, 026, (2017).

In-medium bottomonium production in heavy-ion collisions, Xiaojian Du, Min He, and Ralf Rapp, Quark Matter 2017, Chicago, IL, Nucl. Phys. **A967**, 904 (2017).

Internal charmonium evolution in the quark--gluon plasma, Baoyi Chen, Xiaojian Du, and Ralf Rapp, 8th International Conference on Hard and Electromagnetic Probes of High Energy Nuclear Collisions 2016, Wuhan, China, Nucl. Part. Phys. Proceedings **289-290**, 475 (2017).

Isoscalar E0, E1, and E2 strength in ^{44}Ca, J. Button, Y.-W. Lui, D.H. Youngblood, X. Chen, G. Bonasera, and S. Shlomo, Phys. Rev. C **96**, 054330 (2017).

Large longitudinal spin alignment of excited projectiles in intermediate energy inelastic scattering, D. E.M. Hoff, R.J. Charity, K.W. Brown, C.D. Pruitt, L.G. Sobotka, T.B. Webb, G. Potel, B. Roeder, and A. Saastamoinen, Phys. Rev. Lett. **119**, 232501 (2017).

Mean free path and shear viscosity in central ^{129}Xe+^{119}Sn collisions below 100 MeV/nucleon, H.L. Liu, Y.G. Ma, A. Bonasera, X.G. Deng, O. Lopez, and M. Veselsky, Phys. Rev. C **96**, 064604 (2017).

Measurement of D0 azimuthal anisotropy at midrapidity in Au+Au collisions at $\sqrt{s}$ = 200 GeV, L. Adamczyk *et al.*(STAR Collaboration), Phys. Rev. Lett. **118**, 212301 (2017).

Measurement of the cross section and longitudinal double-spin asymmetry for dijet production in polarized pp collisions at $\sqrt{s}$ = 200 GeV, L. Adamczyk *et al.* (STAR Collaboration), Phys. Rev. D **95**, 071103 (2017).

Measurements of jet quenching with semi-inclusive hadron+jet distributions in Au+Au collisions at $\sqrt{s_{NN}}$ = 200 GeV, L. Adamczyk *et al.* (STAR Collaboration), Phys. Rev. C **96**, 024905 (2017).

NeutronSTARS: A segmented neutron and charged particle detector for low-energy reaction studies, O.A. Akindele, R.J. Casperson, B.S. Wang, J.T. Burke, R.O. Hughes, S.E. Fisher, A. Saastamoinen, and E. B. Norman, Nucl. Instrum. Methods Phys. Res. **A872**, 112 (2017).

New accurate measurements of neutron emission probabilities for relevant fission products, J. Agramunt, J.L. Taín, F. Albiol, A. Algora, R. Caballero-Folch, F. Calvino, G. Cortes, I. Dillmann, T. Eronen, A.R. Garcia, E. Ganioglu, W. Gelletly, D. Gorelov, V. Guadilla, H. Hakala, A. Jokinen, A. Kankainen, A. Montaner, M. Marta, E. Mendoza, I. Moore, C. Nobs, S. Orrigo, H. Penttilä, M. Reponen, S. Rinta-Antila, A. Riego, B. Rubio, A. Saastamoinen, P. Salvador-Castiñeira, A. Tarifeño-Saldivia, A. Tolosa, and E. Valencia, ND 2016: International Conference on Nuclear Data for Science and Technology, Bruges, Belgium, Eur. Phys. J. Web of Conferences **146**, 01004 (2017).

Nuclear data sheets for A=158, N. Nica, Nucl. Data Sheets **141**, 1 (2017).

Nuclear force imprints revealed on the elastic scattering of protons with ^{10}C, A. Kumar, R. Kanungo, A. Calci, P. Navrátil, A. Sanetullaev, M. Alcorta, V. Bildstein, G. Christian, B. Davids, J. Dohet-Eraly, J. Fallis, A.T. Gallant, G. Hackman, B. Hadinia, G. Hupin, S. Ishimoto, R. Krücken, A.T. Laffoley, J. Lighthall, D. Miller, S. Quaglioni, J.S. Randhawa, E.T. Rand, A. Rojas, R. Roth, A. Shotter, J. Tanaka, I. Tanihata, and C. Unsworth, Phys. Rev. Lett. **118**, 262502 (2017).

Nuclear forensics methodology for reactor-type attribution of chemically separated plutonium, Jeremy M. Osborn, Evans D. Kitcher, Jonathan D. Burns, Charles M. Folden, III and Sunil S. Chirayath, Nucl. Technology **201**, 1 (2017).

Nuclear stopping and light charged particle emission in ^{12}C+^{12}C at 95 MeV/nucleon, G. Tian, R. Wada, Z. Chen, R. Han, W. Lin, X. Liu, P. Ren, F. Shi, F. Luo, Q. Sun, L. Song, and G.Q. Xiao, Phys. Rev. C **95**, 044613 (2017).

Observation of different isoscaling behavior between emitted fragments and residues, M. Youngs, A. B. McIntosh, K. Hagel, L. Heilborn, M. Huang, A. Jedele, Z. Kohley, L.W. May, E. McCleskey, A. Zarrella, and S.J. Yennello, Nucl. Phys. **A962**, 61 (2017).

Open heavy flavor transport in $\sqrt{s_{NN}}$=5.02 TeV Pb + Pb Collisions, Min He, Rainer J. Fries, and Ralf Rapp, 8th International Conference on Hard and Electromagnetic Probes of High Energy Nuclear Collisions 2016, Wuhan, China, Nucl. Part. Phys. Proceedings **289-290**, 475 (2017).

Partial restoration of chiral symmetry in hot and dense neutron matter, J.W. Holt and Keighley E. Rockcliffe, *Quarks, Nuclei and Stars : Memorial Volume Dedicated to Gerald E Brown*, World Scientific, p. 105 (2017).

Pigmy resonances, transfer, and separable potentials, C.A. Bertulani, A.S. Kadyrov, A. Kruppa, T.V. Nhan Hao, A.M. Mukhamedzhanov, and Shubhchintak, in: Exotic Nuclei and Nuclear/Particle Astrophysics (VI). Physics with small accelerators: Proceedings of Carpathian Summer School of Physics 2016 (CSSP16), Sinaia, Romania, AIP Conference Proceedings **1852**, 020004 (2017).

Precise measurement of α_K and α_T for the 109.3-keV M4 transition in ^{125}Te: Test of internal-conversion theory, N. Nica, J.C. Hardy, V.E. Iacob, T.A. Werke, C.M. Folden, III, K. Ofodile and M.B. Trzhaskovskaya, Phys. Rev. C **95**, 064301 (2017).

Radiative capture reactions via indirect methods, A.M. Mukhamedzhanov and G.V. Rogachev, Phys. Rev. C **96**, 045811 (2017).

Range of plasma ions in cold cluster gases near the critical point, G. Zhang, H.J. Quevedo, A. Bonasera, M. Donovan, G. Dyer, E. Gaul, G.L. Guardo, M. Gulino, M. La Cognata, D. Lattuada, S. Palmerini, R.G. Pizzone, S. Romano, H. Smith, O. Trippella, A. Anzalone, C. Spitaleri, and T. Ditmire, Phys. Lett. A **381**, 1682 (2017).

Repulsive three-body force and channel-coupling effects via ^{12}C+^{12}C scattering at 100 AMeV, W.W. Qu, G.L. Zhang, S. Terashima, T. Furumoto, Y. Ayyad, Z.Q. Chen, C.L. Guo, A. Inoue, X.Y. Le, H.J. Ong, D.Y. Pang, H. Sakaguchi, Y. Sakuragi, B.H. Sun, A. Tamii, I. Tanihata, T.F. Wang, R. Wada, and Y. Yamamoto, Phys. Rev. C **95**, 044616 (2017).

Shape coexistence in the odd-odd nucleus ^{98}Y: The role of the $g_{9/2}$ neutron extruder, W. Urban, M. Czerwiński, J. Kurpeta, T. Rzaca-Urban, J. Wiśniewski, T. Materna, Ł.W. Iskra, A.G. Smith, I. Ahmad, A. Blanc, H. Faust, U. Köster, M. Jentschel, P. Mutti, T. Soldner, G.S. Simpson, J.A. Pinston, G. de France, C. A. Ur, V.-V. Elomaa, T. Eronen, J. Hakala, A. Jokinen, A. Kankainen, I.D. Moore, J. Rissanen, A. Saastamoinen, J. Szerypo, C. Weber, and J. Äystö, Phys. Rev. C **96**, 044333 (2017).

Structure of ^{10}N in ^{9}C+p resonance scattering, J. Hooker, G.V. Rogachev, V.Z. Goldberg, E. Koshchiy, B.T. Roeder, H. Jayatissa, C. Hunt, C. Magana, S. Upadhyayula, E. Uberseder, and A. Saastamoinen, Phys. Lett. B **769**, 62 (2017).

Structure of ^{20}Ne states in resonance ^{16}O+α elastic scattering, D.K. Nauruzbayev, V.Z. Goldberg, A.K. Nurmukhanbetova, M.S. Golovkov, A. Volya, G.V. Rogachev, and R.E. Tribble, Phys. Rev. C **96**, 014322 (2017).

Structure of neutron star crusts from new Skyrme effective interactions constrained by chiral effective field theory, Yeunhwan Lim and Jeremy W. Holt, Phys. Rev. C **95**, 065805 (2017).

Sub-barrier fusion of weakly bound ^{6}Li with ^{58}Ni, E.F. Aguilera, E. Martinez-Quiroz, P. Amador-Valenzuela, D. Lizcano, A. García-Flores, J.J. Kolata, A. Roberts, G.V. Rogachev, G.F. Peaslee, V. Guimaraes, F.D. Becchetti, A. Villano, M. Ojaruega, Y. Chen, H. Jiang, M. Febbraro, P.A. DeYoung, and T.L. Belyaeva, Phys. Rev. C **96**, 024616 (2017).

Subthreshold resonances and resonances in the R-matrix method for binary reactions and in the Trojan horse method, A.M. Mukhamedzhanov, Shubhchintak, and C.A. Bertulani, Phys. Rev. C **96**, 024623 (2017).

Sum-fit method of analysis of nuclear decay spectra affected by extending dead-time, V. Horvat and J. C. Hardy, Nucl.Instrum. Methods Phys. Res. **A868**, 53 (2017).

Symmetry energy and experimentally observed cold fragments in intermediate heavy-ion collisions, Su-Ya-La-Tu Zhang, Mei-Rong Huang, R. Wada, Xing-Quan Liu, Wei-Ping Lin, and Jian-Song Wang, Chinese Phys. C **41**, 044001 (2017).

Test of internal-conversion theory with a measurement in ^{111}Cd, N. Nica, J.C. Hardy, V.E. Iacob, T.A. Werke, C.M. Folden, III, L. Pineda, and M.B. Trzhaskovskaya, International Conference on Nuclear Data for Science and Technology (ND 2016), Bruges, Belgium, Eur. Phys. J. Web Conf. **146,** 10004 (2017).

The Cyclotron Institute at Texas A&M University, Gregory Christian, Charles M. Folden, III, John Hardy, Yiu-Wing Lui, Donald May, Dan Melconian, Joseph Natowitz, Ralf Rapp, Grigory Rogachev, Robert Tribble, and Sherry Yennello, Nucl. Phys. News **27**, 5 (2017).

The electric conductivity of a pion gas, J. Atchison and R. Rapp, Hot Quarks 2016 South Padre Island, TX, J. Phys. Conference Series **832**, 012057 (2017).

The hyperion particle-γ detector array, R.O. Hughes, J.T. Burke, R.J. Casperson, S. Ota, S. Fisher, J. Parker, C.W. Beausang, M. Dag, P. Humby, J. Koglin, E. McCleskey, A.B. McIntosh, A. Saastamoinen, A. S. Tamashiro, E. Wilson, and T.C. Wu, Nucl. Instrum. Methods Phys. Res. **A856**, 47 (2017).

The partial truncated icosahedron phoswich detector array: A light charged particle array for pionic fusion measurements, A. Zarrella, L. Galvan, L. Heilborn, A. Jedele, A.B. McIntosh, A. Rodriguez Manso, M. Youngs and S.J. Yennello, Conference on the Application of Accelerators in Research and Industry, CAARI 2016, Ft. Worth, TX, USA, Phys. Procedia **90**, 463 (2017).

Theoretical perspective on quarkonia from SPS via RHIC to LHC, R. Rapp and X. Du, Quark Matter 2017, Chicago, IL, Nucl. Phys. **A967**, 216 (2017).

Three-nucleon interaction in heavy-ion collisions at intermediate energies, R. Wada, Phys. Rev. C **96**, 031601(R) (2017).

Three-particle correlations in a multiphase transport model, Yifeng Sun and Che Ming Ko, Phys. Lett. B **769**, 219 (2017).

Spinodal instabilities of baryon-rich quark matter in heavy ion collisions, F. Li and C.M. Ko, Phys. Rev. C **95**, 055203 (2017).

Elliptic flow of light nuclei, X.J. Yin, C.M. Ko, Y. Sun, and L.L. Zhu, Phys. Rev. C **95**, 054913 (2017).

Medium effects on pion production in heavy ion collisions, Z. Zhang and C.M. Ko, Phys. Rev. C **95**, 064904 (2017).

Chemical freeze-out in relativistic heavy ion collisions, J. Xu and C.M. Ko, Phys. Lett. B **772**, 290 (2017).

Lambda hyperon polarization in relativistic heavy ion collisions from a chiral kinetic approach, Y. Sun and C.M. Ko, Phys. Rev. C **96**, 024906: 1-6 (2017).

Probing QCD critical fluctuation from light nuclei production, K.J. Sun, L.W. Chen, C.M. Ko, and Z. Xu, Phys. Lett. B **774**, 103 (2017).

Nuclear dipole polarizability from mean-field modeling constrained by chiral effective field theory, Z. Zhang, Y. Lim, J.W. Holt, and C.M. Ko, Phys. Lett. B **777**, 73 (2018).

Effects of energy conservation on equilibrium properties of hot asymmetric nuclear matter, Z. Zhang and C.M. Ko, Phys. Rev. C **97**, 014610 (2018).

Hypertriton production in relativistic heavy ion collisions, Z. Zhang and C.M. Ko, Phys. Lett. B **780**, 191 (2018).

Comparison of heavy-ion transport simulations: collision integral in a box, Y.X. Zhang, Y.J. Wong, M. Colonna, P. Danilewicz, A. Ono, B. Tsang, H. Walter, J. Xu, L.W. Chen, D. Cozma, Z.Q. Feng, S.D. Gupta, N. Ikeno, C.M. Ko, B.A. Li, Q.F. Li, Z.X. Li, S. Mallik, Y. Nara, T. Ogawa, A. Ohnishi, D. Oliinychenko, K. Papa, H. Peterson, J. Su, T. Song, J. Weil, N. Wang, F.S. Zhang, and Z. Zhang, , Phys. Rev. C **97**, 034625 (2018).

Theoretical perspective on strangeness production, C.M. Ko, Eur. Phys. J. Web of Conferences **171**, 03002 (2018).

White paper on nuclear astrophysics and low energy nuclear physics Part 1: Nuclear astrophysics, Almudena Arcones, Dan W. Bardayan, Timothy C. Beers, Lee A. Bernstein, Jeffrey C. Blackmon, Bronson Messer, B. Alex Brown, Edward F. Brown, Carl R. Brune, Art E. Champagne, Alessandro Chieffi, Aaron J. Couture, Pawel Danielewicz, Roland Diehl, Mounib El-Eid, Jutta E. Escher, Brian D. Fields, Carla Fröhlich, Falk Herwig, William Raphael Hix, Christian Iliadis, William G. Lynch, Gail C. McLaughlin, Bradley S. Meyer, Anthony Mezzacappa, Filomena Nunes, Brian W. O'Shea, Madappa Prakash, Boris Pritychenko, Sanjay Reddy, Ernst Rehm, Grigory Rogachev, Robert E. Rutledge, Hendrik Schatz, Michael S. Smith, Ingrid H. Stairs, Andrew W. Steiner, Tod E. Strohmayer, F. X. Timmes, Dean M. Townsley, Michael Wiescher, Remco G.T. Zegers, and Michael Zingale, Prog. Part. Nucl. Phys. **94**, 1 (2017).

White paper on nuclear astrophysics and low-energy nuclear physics, Part 2: Low-energy nuclear physics, Joe Carlson, Michael P. Carpenter, Richard Casten, Charlotte Elster, Paul Fallon, Alexandra Gade, Carl Gross, Gaute Hagen, Anna C. Hayes, Douglas W. Higinbotham, Calvin R. Howell, Charles J. Horowitz, Kate L. Jones, Filip G. Kondev, Suzanne Lapi, Augusto Macchiavelli, Elizabeth A. McCutchen, Joe Natowitz, Witold Nazarewicz, Thomas Papenbrock, Sanjay Reddy, Mark A. Riley, Martin J. Savage, Guy Savard, Bradley M. Sherrill, Lee G. Sobotka, Mark A. Stoyer, M. Betty Tsang, Kai Vetter, Ingo Wiedenhöver, Alan H. Wuosmaa and Sherry Yennello, Prog. Part. Nucl. Phys. **94**, 68 (2017).

Photoneutron cross-section measurements in the ^{209}Bi (γ,xn) reaction with a new method of direct neutron-multiplicity sorting, I. Gheorghe, H. Utsunomiya, S. Katayama, D. Filipescu, S. Belyshev, K. Stopani, V. Orlin, V. Varlamov, T. Shima, S. Amano, S. Miyamoto, Y.-W. Lui, T. Kawano, and S. Goriely Phys. Rev. C **96**, 044604 (2017).

SECTION VI

APPENDIX

50 years of research at the Cyclotron Institute, **J.B. Natowitz**, **Invited Seminar**, 50 Years of Beam Seminar Series, Cyclotron Institute, Texas A&M University, College Station, Texas (December 2017).

50 years of research at the Cyclotron Institute, **D.H. Youngblood**, **Invited Seminar**, 50 Years of Beam Seminar Series, Cyclotron Institute, Texas A&M University, College Station, Texas (December 2017).

Precise test of internal-conversion theory: α_K measurements for transitions in nine nuclei spanning $45 \leq Z \leq 78$ **J.C. Hardy**, **Invited talk**, *ICRM2017, the* 21st International Conference on Radionuclide Metrology, Buenos Aires, Argentina (May 2017).

The current evaluation of $|V_{ud}|$ and the top-row test of CKM matrix unitarity **J.C. Hardy**, **Invited talk**, Solvay workshop on Beyond the Standard Model with Neutrinos and Nuclear Physics, Brussels, Belgium (November 2017).

The current evaluation of $|V_{ud}|$ and the role played by radiative corrections, **J.C. Hardy**, **Invited talk**, the Workshop on the Electroweak Box, Amherst Center for Fundamental Physics, Amherst, Massachusetts (September 2017).

Testing CVC and CKM unitarity via superallowed nuclear beta decay, **J.C. Hardy**, **Invited talk**, the XXXV Mazurian Lakes Conference on Physics, Piaski, Poland (September 2017).

Testing the Standard Model with superallowed nuclear beta decay, **J.C. Hardy**, **Invited talk**, 50 years of beam symposium, Texas A&M University, College Station, Texas (November 2017).

Superallowed beta decay of ^{26}Si: A sensitive test of isospin symmetry-breaking corrections, **Miguel Bencomo**, the International conference on Advances in Radioactive Isotope Science (ARIS), Keystone, Colorado (May 2017).

Progress report of precision internal conversion-coefficient measurements with transitions in ^{127}Te, ^{125}Te and ^{103}Rh, **N. Nica**, the 22nd Technical Meeting of the NSDD network, Lawrence Berkeley Nuclear Laboratory, Berkeley, California (May 2017).

Progress report of precision internal conversion-coefficient measurements with transition in ^{103}Rh, **N. Nica**, the US National Nuclear Data Week 2017, NDAC meeting, Brookhaven National Laboratory, Upton, New York (October 2017).

Study of astrophysical alpha + Ne reaction using alpha transfer with TIARA and MDM spectrometer, **Shuya Ota**, the 2017 Fall Meeting of the APS Division of Nuclear Physics, Pittsburgh, Pennsylvania (October 2017).

Constraining the astrophysical ^{23}Mg(p,γ)^{24}Al reaction rate using the ^{23}Na(d,p)^{24}Na reaction, **Eames Bennett**, the 2017 Fall Meeting of the APS Division of Nuclear Physics, Pittsburgh, Pennsylvania (October 2017).

Spin and forward physics with STAR, **C.A. Gagliardi**, **Invited talk**, (for the STAR Collaboration), Workshop Forward Phys. High-Energy Scatt. Zero Degrees 2017, Nagoya, Japan (September 2017).

Probing the origin of the proton spin at STAR, **C.A. Gagliardi**, **Invited talk**, (for the STAR Collaboration), 6th Int. Conf. New Front. Phys., Kolymbari, Crete, Greece (August 2017).

Neutron star core-crust boundaries from mean field model constrained by χEFT, **Yeunhwan Lim**, 2017 International Collaboration of Nuclear Theory (ICNT), Michigan State University, East Lansing, Michigan (April 2017).

Quasiparticle interaction in nuclear matter from chiral effective field theory, **Jeremy W. Holt**, **Invited talk**, ECT* Workshop: Landau Fermi liquid theory in nuclear and many-body systems, Trento, Italy (May 2017).

Toward supernova equations of state from chiral effective field theory, **Jeremy W. Holt**, **Invited Talk**, Microphysics in Computational Relativistic Astrophysics 2017 (MICRA2017), Michigan State University, East Lansing, Michigan (July 2017).

Hot and dense neutron-rich matter from chiral effective field theory, **Jeremy W. Holt**, **Invited Seminar**, Institute for Nuclear and Particle Physics seminar, Ohio University, Athens, Ohio (November 2017).

Hot and dense neutron-rich matter from chiral effective field theory, **Jeremy W. Holt**, **Invited Seminar**, Beihang University, Beijing, China (March 2018).

Structure of unbound 10-N and 9-He, **G. Rogachev**, 3rd International Conference on Advances in Rare Isotope Science, ARIS2017, Keystone, Colorado (June 2017).

Overview of ARUNA facilities, **G. Rogachev**, **Invited Plenary Talk**, Low Energy community meeting, Argonne National Laboratory, Argonne, Illinois (August 2017).

Alpha-cluster structure populated in the resonance reactions induced by rare beams, **V.Z. Goldberg**, **Invited Talk**, Int. Conf. Nucler Physics in Astrophysics VIII (NPA8), Catania, Italy (June 2017).

Alpha-capture reaction rates for 22-Ne(alpha,n) via sub-Coulomb alpha-transfer, **Heshani Jayatissa**, Gordon Research Seminar on Nuclear Chemistry (GRS), New London, New Hampshire (June 2017).

Probing the cluster structure in 10-Be using resonant 6-He+alpha scattering, **Sriteja Upadhyayula**, Gordon Research Conference on Nuclear Chemistry, New London, New Hampshire (June 2017).

The study of the 22-Ne(alpha,n)25-Mg reaction rate via indirect sub-coulomb alpha-transfer techniques, **Heshani Jayatissa**, The 9th European Summer School on Nuclear Astrophysics, Santa Tecla, Catania, Italy (September 2017).

Commissioning of the new Texas Active Target Detector (TexAT), **J. Hooker**, The 9th European Summer School on Experimental Nuclear Astrophysics, Santa Tecla, Sicily, Italy (September 2017).

Search for the 6+ state of 10-Be, **Sriteja Upadhyayula**, The 9th European Summer School on Experimental Nuclear Astrophysics, Santa Tecla, Sicily, Italy (September 2017).

Studying light exotic nuclei through isobaric analogues, **Curtis Hunt**, the 2017 Fall Meeting of the APS Division of Nuclear Physics, Pittsburgh, Pennsylvania (October 2017).

Alpha-capture reaction rates for 22-Ne(alpha,n) via sub-Coulomb alpha-transfer and its effect on final abundances of s-process isotopes, **Heshani Jayatissa**, the 2017 Fall Meeting of the APS Division of Nuclear Physics, Pittsburgh, Pennsylvania (October 2017).

Structure of 10-N via 9-C+p resonance scattering, **J. Hooker**, the 2017 Fall Meeting of the APS Division of Nuclear Physics, Pittsburgh, Pennsylvania (October 2017).

T=5 states in 48-Ca, **Sriteja Upadhyayula**, the 2017 Fall Meeting of the APS Division of Nuclear Physics, Pittsburgh, Pennsylvania (October 2017).

New studies at new ACCULINNA mass separator, **V.Z. Goldberg**, **Invited Seminar**, Joint Institute for Nuclear Research, Dubna, Russian Federation (July 2017).

New approach to study resonance (alpha,n) reactions, **V.Z. Goldberg**, **Invited Seminar**, Nazyrbayev University, Astana, Kazakhstan (July 2017).

Resonance reactions of 21st century, **V.Z. Goldberg**, **Invited Talk**, the 39th Symposium on Nuclear Physics, Morelos Mexico (January 2018).

Design and commissioning of Texas Active Target (TexAT) detector system, **G. Rogachev**, **Invited Talk**, Workshop on Active Targets and Time Projection Chambers for High-intensity and Heavy-ion Beams in Nuclear Physics, Santiago de Compostela, Spain (January 2018).

From nucleon-nucleon interaction to stars and physics beyond the standard model, **G. Rogachev**, **Invited Colloquium**, Texas A&M University at Commerce, Commerce, Texas (January 2018).

Recent jet measurements in heavy-ion collisions at STAR in a nutshell, **Nihar Sahoo**, **Invited talk**, RHIC & AGS Users' Meeting 2017, Upton, New York (June 2017).

Towards the full reconstruction of neutral-triggered recoil jets in Au+Au Collisions, **Derek Anderson**, the Texas Heavy-Ion & Spin physics symposium, Houston, Texas (November 2017).

Hot vs. cold nuclear matter suppression of the J/Psi, **Yanfang Liu**, the Texas Heavy-Ion & Spin physics symposium, Houston, Texas (November 2017).

Short-range correlations effect on the single proton $3s_{1/2}$ wave function in ^{206}Pb, **S. Shlomo**, **Invited Talk**, I. Talmi, M.R. Anders, and G. Bonasera, the 12th International Spring Seminar on Nuclear Physics, Current Problems and Prospects for Nuclear Structure, Sant'Angelo d'Ischia, Napoli, Italy (May 2017).

Fundamentally cool physics with trapped atoms and ions. **D. Melconian**, **Invited Talk**, Tel Aviv University, Tel Aviv, Israel (Apr 2017).

Nuclear β decay: using the atomic nucleus to probe symmetries of the weak interaction, **D. Melconian**, **Invited Talk**, Joint APS/AAPT/SPS meeting, Tarleton University, Stephenville, Texas (March 2018).

Using trapped atoms and ions for fundamentally cool physics, **D. Melconian**, Talk for students of the Research Experience for Undergraduates (REU) program, Cyclotron Institute, Texas A&M, College Station, Texas (July 2017).

Stellar secrets: earth bound insights into elements through heavy-ion reactions, **S.J. Yennello**, **Invited Talk**, University of Dallas, Irving, Texas (October 2017).

NZ equlibration in Fermi-energy heavy ion collisions: what can we learn about the EOS? **S.J. Yennello**, **Invited Talk**, 7th International Symposium on Nuclear Symmetry Energy (NUSYM17), Ganil, Caen, France (September 2017).

Studying the stars here on earth: how the equation of state of nuclear matter impacts the formation of the elements, **S.J. Yennello**, **Invited Talk**, ACS-DNCT summer school, San Jose State University, San Jose, California (June 2017).

Imagine a universe with 85% down quarks: mentoring for inclusive excellence in nuclear science, **S.J. Yennello**, **Invited Talk**, the 2017 Fall Meeting of the APS Division of Nuclear Physics, Pittsburgh, Pennsylvania (October 2017).

Effective negotiation, **S.J. Yennello**, **Invited Talk**, Women in Astronomy, Austin, Texas (June 2017).

Toward inclusive excellence in nuclear science, **S.J. Yennello**, **Invited Talk**, NSCL, Michigan State Univeristy, East Lansing, Michigan (January 2018).

Effective negotiation, **S.J. Yennello**, **Invited Talk**, Michigan State University, East Lansing, Michigan (January 2018).

Equilibration chronometry, **Alan McIntosh**, **Invited Talk**, Department of Physics and Center for the Exploration of Energy and Matter, Indiana University, Bloomington, Indiana (January 2018).

Equilibration chronometry probes neutron-proton equilibration with sub-zeptosecond time resolution, **Alan McIntosh**, **Invited Talk**, GANIL Seminar Series, GANIL, Caen, France (September 2017).

Detailed investigation of neutron-proton migration using equilibration chronometry, **Alan McIntosh**, **Invited Talk**, 7th International Symposium on the Nuclear Symmetry Energy (NuSym17), GANIL, Caen, France (September 2017).

Detailed investigation of neutron-proton migration using equilibration chronometry, **Alan McIntosh**, 50 Years of Beam Symposium, Cyclotron Institute, Texas A&M University, College Station, Texas (November 2017).

Equilibration Chronometry, **Andrea Jedele**, the 2017 Fall Meeting of the APS Division of Nuclear Physics, Pittsburgh, Pennsylvania (October 2017).

Heavy element synthesis using multi-nucleon transfer reactions between heavy nuclei, **Kris Hagel**, 50 Years of Beam Symposium, Cyclotron Institute, Texas A&M University, College Station, Texas (November 2017).

Exploring clustering in alpha-conjugate nuclei using the thick target inverse kinematic technique for multiple alpha emission, **M. Barbui**, 50 Years of Beam Symposium, Cyclotron Institute, Texas A&M University, College Station, Texas (November 2017).

On the way to studying nihonium chemistry, **E.E. Tereshatov**, **Invited Talk**, 50 Years of Beam Symposium, College Station, Texas (November 15, 2017).

Chemistry at the Bottom of the Periodic Table, **C.M. Folden III**, **Invited Talk**, Texas A&M University Department of Chemistry Seminar, College Station, Texas, (October 2017).

Optimization of indium and thallium separation with liquid-liquid extraction technique for a future study of nihonium chemistry, **M.F. Volia**, 9th Workshop on the Chemistry on the Heaviest Elements, Ascona, Switzerland (October 2017).

Research and lab engagement at Texas A&M University, nuclear science and security consortium, **C.M. Folden III**, September Workshop and Advisory Board Meeting, Berkeley, California (September 2017).

Extraction of Nh homologs using "designer" molecules, **C.M. Folden III**, **Invited Talk**, 16th h Workshop on a Recoil Separator for Superheavy Element Chemistry, Darmstadt, Germany (September 2017).

Heavy element chemistry research at Texas A&M University, **C.M. Folden III**, **Invited Talk**, 254th American Chemical Society National Meeting, Washington, District of Columbia (August 2017).

New chemical media for superheavy element study, **E.E. Tereshatov**, 254th American Chemical Society National Meeting, Washington, District of Columbia (August 2017).

Introduction to superheavy elements, **C.M. Folden III**, **Invited Talk**, Exotic Beam Summer School 2017, Argonne National Laboratory, Argonne, Illinois (July 2017).

Experimental and computational assessment of fission product residue in Pu from low-burnup thermal reactor fuel and inverse analysis for nuclear forensics, **C.M. Folden III**, (with Sunil S. Chirayath), Interagency Technical Nuclear Forensics Program Review, Oak Ridge, Tennessee (July 2017).

Influence of fission on the prospects for discovering the next new element, **C.M. Folden III**, **Invited Talk**, Advances in Radioactive Isotope Science 2017, Keystone, Colorado (May 2017).

Application of mass spectrometry in nuclear forensics for interdicted plutonium source attribution, **C.M. Folden III**, (with Sunil S. Chirayath), Geology Department Seminar, College Station, Texas (May 2017).

Liquid phase chemistry study of indium and thallium for a future investigation of nihonium, **M.F. Volia**, 253rd American Chemical Society National Meeting, San Francisco, California (April 2017).

Survival of Excited Nuclei Produced in Warm Fusion Reactions, **C.M. Folden III**, **Invited Talk**, 253rd American Chemical Society National Meeting, San Francisco, California (April 2017).

Jet Fragmentation via shower parton recombination, **C.M. Ko**, **Invited Talk**, Workshop on Precision Spectroscopy of QGP Properties with Jets and Heavy Quarks, Seattle, Washington (May 2017).

Chiral transport model study of chiral magnetic and vortical effects, **C.M. Ko**, **Invited Talk**, Symposium on the Intersection of Electro, Chromo, and Hydro-Dynamics in Nuclear Physics, Minneapolis, Minnesota (June 2017).

Pion properties in dense neutron-rich matter, **C.M. Ko**, **Invited Talk**, Huzhou-CUSTIPEN Workshop on Spectroscopy and Reactions of Exotic Nuclei, Huzhou, Zhejiang, China (July 2017).

Theoretical perspective on strangeness production, **C.M. Ko**, **Invited Talk**, 17th International Conference on Strangeness in Quark Matter, Ultrecht, Netherlands, (July 2017).

Lambda polarization in the chiral kinetic approach, **C.M. Ko**, **Invited Talk**, The 12th Workshop on QCD Phase Transition and Relativistic Heavy-Ion Collisions, Xián, Hebei, China (July 2017).

Reflections on AMPT, **C.M. Ko**, **Invited Talk**, Workshop on AMPT for Relativistic Heavy Ion Collisions, Chengdu, Sichuan, China, (July 24 - 27, 2017).

Chiral magnetic and vortical Effects in heavy ion collisions, **C.M. Ko**, **Invited Talk**, Workshop on Phases of Quantum Chromodynamics (QCD) and Beam Energy Scan Program with Heavy Ion Collisions, Shanghai, China (August 2017).

Pion production in transport model, **C.M. Ko**, **Invited Talk**, 7th International Symposium on Nuclear Symmetry Energy, Caen, France (September 4 - 7, 2017).

Light nuclei production in relativistic heavy ion production, **C.M. Ko**, **Invited Talk**, 2nd EMMI Workshop on Anti-Matter, Hyper-Matter and Exotic Production at the LHC, Turin, Italy (November 2017).

Chiral magnetic effects in HICs, **Y. Sun**, Texas Heavy-Ion and Spin Physics Symposium, Houston, Texas (November 2017).

50 years of theoretical nuclear physics research at the Cyclotron Institute, **C.M. Ko**, **Invited Seminar**, 50 Years of Beam Seminar Series, Cyclotron Institute, Texas A&M University, College Station, Texas (December 2017).

Using lasers for nuclear physics: measuring cross-sections in (non) equilibrium plasmas, **A. Bonasera**, **Invited Talk**, 4th Workshop on New Aspects and Perspectives in Nuclear Physics, Hellenic Institute of Nuclear Physics, Ioannina, Greece (May 2017).

Nuclear physics using lasers, **A. Bonasera**, **Invited Talk**, International School on Nuclear Astrophysics, Santa Tecla, Italy (September 2017).

Bose-Einsten condensation, fermionic quenching and Efimov states from heavy ion collisions, **A. Bonasera**, **Invited Colloquium**, Tongliao University, Tongliao, Inner Mongolia, China (October 2017).

Analysis of experiments performed at SG-II (up) with 8(+1) Lasers, **A. Bonasera**, **Invited Colloquium**, Shanghai Institute of Applied Physics (SINAP), Chinese Academy of Sciences, Shanghai, China (January 2018).

Jet hadronization in vacuum and in the medium, **R.J. Fries**, INT Program on Precision Spectroscopy of QGP Properties with Jets and Heavy Quarks, Institute of Nuclear Theory, University of Washington, Seattle, Washington (May 2017).

Hadronization, **R.J. Fries**, INT Program on Precision Spectroscopy of QGP Properties with Jets and Heavy Quarks, Institute of Nuclear Theory, University of Washington, Seattle, Washington (May 2017).

Let There Be Light, **R.J. Fries**, **Invited Talk**, Symposium on Light, Color and Dense Matter, University of Minnesota, Minneapolis, Minnesota (June 2017).

Angular momentum and early time gluon fields, **R.J. Fries**, 4th Int. Conference on the Initial Stages in High-Energy Nuclear Collisions 2017, Polish Academy of Arts and Sciences, Cracow, Poland (September 2017).

Nuclear matter in extreme conditions, **R.J. Fries**, **Invited Colloquium**, Texas A&M University, Texas College Station, Texas (September 2017).

A hybrid hadronization model, **R.J. Fries**, **Invited Seminar**, Central China Normal University, Wuhan, China (October 2017).

A hybrid hadronization Model, **R.J. Fries**, **Invited Talk**, JETSCAPE Workshop 2018, Lawrence Berkeley National Laboratory, Berkeley, California (January 2018).

Vector mesons and chiral restoration in hadronic matter, **R. Rapp**, **Invited Talk**, ECT* workshop on Space- and Timelike Electromagnetic Baryonic Transitions, ECT*, Trento, Italy (May 2017).

Enlightening insights into hot and dense matter, **R. Rapp**, **Invited Talk**, Symposium on the Intersections of Electro-, Chromo- and Hydrodynamics in Nuclear Physics, University of Minnesota, Minneapolis, Minnesota (June 2017).

Microscopic description of heavy-flavor diffusion in QCD matter, **R. Rapp**, **Invited Talk**, Institute for Nuclear Theory (INT) program on "Precision Spectroscopy of Quark-Gluon Plasma with Jets and Heavy Quarks", Institute for Nuclear Theory, Seattle, Washington (May 2017).

Heavy-flavor theory for heavy-ion collisions, **R. Rapp**, **Invited Talk**, RHIC and AGS Annual Users' Meeting, Brookhaven National Laboratory, Upton, New York (June 2017).

Nonperturbative approach to equation of state and collective modes of the QGP, **R. Rapp**, XLVII International Symposium on Multiparticle Dynamics (ISMD 2017), Tlaxcala, Mexico (September 2017).

Heavy-flavor probes of quark-gluon plasma: objectives and opportunities, **R. Rapp**, **Invited Opening Talk**, Workshop on Heavy-Flavor Production in High-Energy Collisions, Lawrence Berkeley National Laboratory, Berkeley, Calfornia (October 2017).

Quarkonium transport theory in heavy-ion collisions, **X. Du**, Texas Heavy-Ion and Spin Physics Symposium, Rice University, Houston, Texas (November 2017).

Nonperturbative apporach to thermal, spectral and transport properties of QGP, **S. Liu**, Texas Heavy-Ion and Spin Physics Symposium, Rice University, Houston, Texas (November 2017).

Potential of heavy-flavor particles to probe strong-interaction matter, **R. Rapp**, **Invited Talk**, Santa Fe Jets and Heavy-Flavor Workshop, Santa Fe, New Mexico (January 2018).

Bottomonium production in heavy-ion collisions, **X. Du,** Santa Fe Jets and Heavy-Flavor Workshop, Santa Fe, New Mexico (January 2018).

Quantum many-body theory for heavy-quark transport, **S. Liu**, Santa Fe Jets and Heavy-Flavor Workshop", Santa Fe, New Mexico (January 2018).

Quarkonia at high-luminosity LHC: Can we determine the in-Medium QCD force?, **R. Rapp**, **Invited video Presentation** (from College Station), General WG-5 Heavy-Ion Meeting, CERN, Geneva, Switzerland (March 2018).

Bottomonium production at RHIC and the LHC, **X. Du**, **Invited High-Energy Physics Seminar**, University of Illinois at Chicago, Chicago, Illinois (July 2017).

Heavy-quarkonium production in heavy-ion collisions, **X. Du**, **Invited Nuclear Theory Seminar**, University of Science and Technology, Hefei, Anhui, China (December 2017).

Quarkonium production at RHIC and the LHC, **X. Du**, **Invited Nuclear Theory Seminar**, Nanjing University, Nanjing, China (December 2017).

Bottomonium and charmonium production in heavy-ion collisions, **X. Du**, **Invited Nuclear Theory Seminar**, Institute of Modern Physics, Chinese Academy of Sciences, Lanzhou, China (December 2017).

RESEARCH PERSONNEL AND ENGINEERING STAFF

April 1, 2017 - March 31, 2018

Faculty and Research Group Leaders

Bonasera, Aldo Senior Scientist
Christian, Gregory Assist. Prof. of Physics
Fries, Rainer Assoc. Professor of Physics
Folden, III, Charles M. Assoc. Prof. of Chemistry
Gagliardi, Carl A. Professor of Physics
Hardy, John C. Professor of Physics, Ralph and Marsha
    Schilling Chair in Physics
Holt, Jeremy Assist. Professor of Physics
Ko, Che Ming Professor of Physics
Kwiatkowski, Ania Assist. Professor of Physics – To
    8/15/2017
Melconian, Dan Assoc. Professor of Physics
Mioduszewski, Saskia Assoc. Prof. of Physics
Natowitz, J. B. Professor of Chemistry – Retired
Rapp, Ralf Professor of Physics
Rogachev, Grigory Professor of Physics
Shlomo, Shalom Senior Scientist
Tribble, Robert E. Professor of Physics (20%)
Yennello, Sherry J. Professor of Chemistry, Bright
    Chair, Director
Youngblood, Dave H. Professor of Physics - Retired
Zhanov, Akram M. Senior Scientist

Research Staff

Ahn, Sunghoon – From 8/1/2017
Arje, Juha
Barbui, Marina Assist. Research Scientist
Chubaryan, Grigor Research Scientist
Clark, Henry Accelerator Physicist (50%)
Goldberg, Vladilen Research Scientist – Retired
    1/15/2018
Hagel, John C. Research Scientist (50%)
Horvat, Vladimir Research Scientist (50%)
Iacob, Victor Research Scientist
Koshchiy, Yevgen Assist. Research Scientist
Lui, Yiu-Wing Research Scientist
McIntosh, Alan Assist. Res. Scientist
Nica, Ninel Associate Research Scientist
Rodrigues, Marcia Dias Assist. Res. Scientist – From
    10/30/17
Saastamoinen, Antti (50%)
Shidling, Praveen Assist. Research Scientist
Tereshatov, Evgeny Assist. Research Scientist

Wada, Roichi (40%)
Wuenschel-Horn, Sara – To 7/14/2017

Accelerator Physics and Radiation Line Staff

Brinkley, Joseph Research Associate
Chen, Lixin Research Associate
Clark, Henry Accelerator Physicist (50%)
Vladimir Horvat, Research Scientist (50%)
Hyman, Bruce Research Associate
Kim, George Accelerator Physicist
May, Don Accelerator Physicist
Roeder, Brian Accelerator Physicist
Saastamoinen, Antti (50%)
Tabacaru, Gabriel Accelerator Physicist

Computer Systems Staff

Burch, Jr. Robert Lead Microcomputer/LAN
    Administrator
Hagel, John C. Research Scientist (50%)

Engineering Staff

Olsen, Robert Senior Mechanical Engineer

Postdoctoral Research Associates

Gauthier, Jerome
Kirakosyan, Vahan– From 10/23/17
Holhinen, Veli Sakari – From 6/16/17
Lim, Yeunhwan
Lin, Ting – From 1/10/18
Ota, Shuya
Park, Hyo-In
Rodriguez Manso, Alis
Sahoo, Nihar
Sun, Yifeng – From 1/1/18
Wakhle, Aditya – From 10/1/17
Werke, Tyler – To 4/30/17
Zhang, Zhen

STUDENTS

April 1, 2017 - March 31, 2018

Graduate Students

Aboud, Eric – From 9/5/17
Anderson, Derek
Atchison, Joseph
Bencomo, Miguel
Bennett, Eames
Bonasera, Giacomo
Chyzh, Roman
Dede, Stefania – From 9/1/16
Du, Xiaojian
Fleming, Alex
Glennon, Kevin
Heilborn, Lauren
Henderson, Lawrence
Hooker, Josh
Hunt, Curtis
Jayatissa, Heshani
Jedele, Andrea
Liu, Shuai
Liu, Yanfang
Magana, Cordero - To 6/7/17
Nasser, Morgan – From 9/12/17
Ozmetin, Asim - From 9/11/17
Patti, John – To 7/12/16
Rose, Steven
Sarver, Issac
Schroeder, Benjamin – From 5/30/17
Scriven, Dustin – From 9/17/17
Shin, Eunkyoung –From 1/20/18
Spiridon, Alexandra – To 12/15/17
Sun, Yifeng – To 12/31/17
Upadhyayula, Sriteja
Volia, Merinda
Wang, Kang – From 11/1/17
Whitehead, Taylor – From 5/1/17
Xu, Zhaojie
Yang, Zidong
Zarrella, Andrew

Undergraduates and Student Technicians

Baley, Colton – From 1/29/18
Bellesio, Andrew
Forbe, Haley
Gerlt, Stephen – To 5/26/17
Jeanis, Ian – From 1/18/18
Kircher, Philip – From 2/23/18
Lawrence, Christine – To 12/31/17
Leeper, Kathrine– To 6/30/17
Muzak, Mateo
O'Dwyer, Rory – From 9/5/17
Pajouhafsar, Yasmin – To 12/31/17
Pybus, Jackson
Salas, Elysia – From 9/11/17
Tamez, Celeste – From 2/20/18
Tepe,Victoria

ORGANIZATIONAL CHART - CYCLOTRON INSTITUTE

DIRECTOR
Yennello

Operations Chief
Abegglen

Computer Systems
Hagel
Burch

Administration/ Accounting
Jeske

Anderson
Barton
Gallegos
Skrabanek
Student Worker

SEE Line Proj. Manager
Clark

Brinkley
Chen
Chubaryan
Horvat
Hyman
Roeder
Tabacaru

Sr. Mechanical Engineer
Olsen

Designer II
Molitor

Machine Shop Supervisor
Whiteley

Hanhart
Peters
Raines

Electrical Shop/Accelerator Tech.
Bailey
Carmona
Cowden
Eisenmann
Foxworth
Gathings
Junek
LaPoint
Miles
Panus
Peeler
Potter
Russell
Schmidt
Sherman
Vickers
Yendrey

Building Maint.
Adams
Mynar
Student Worker

Senior Accelerator Physicist
May

Accelerator Physicists
Kim
Clark
Roeder
Tabacaru

Research Group Leaders

Research Scientists

Research Associates

Graduate Students

**STUDENTS WHO RECEIVED GRADUATE DEGREES
FROM THESIS WORK CONDUCTED
AT
THE CYCLOTRON INSTITUTE**

April 1, 2017 – March 31, 2018

Name	Year	Thesis Title	Advisor	Present Position
Sidharth Somanathan	2016	*Relativistic viscous hydrodynamics for nuclear collisions and applications to thermalizing color glass*	R.J. Fries	N.A.
Yifeng Sun	2017	*Chiral magnetic and vertical effects in relativistic heavy ion collision*	Che-Ming Ko	Post Doc. Cyclotron Institute, Texas A&M University, College Station, Texas
Alexandra Elena Spiridon	2017	*A determination of the 27Si(p,g) reaction rate using its mirror and its importance in x-ray burst nucleosynthesis*	R.E. Tribble	N.A.

2017

April 4	Kenneth R. Hogstrom, PhD, Professor Emeritus, Dept. of Physics and Astronomy, Louisiana State University, Dept. of Radiation Physics, The University of Texas M D, Anderson Cancer Center, Senior Medical Physics Advisor, Mary Bird Perkins Cancer Center	*Advancing Electron Beam Radiation Therapy through Physics Research – 50 Years of Beam Seminar series*
April 12	Dr. Daniel Lascar, TRIUMF Vancouver, British Columbia, Canada	*Recent Work with the TITAN System and EMMA Trap: An Introduction*
April 21	Dr. Bao-An Li, Regents' Professor, Department of Physics and Astronomy, Texas A&M University – Commerce, Commerce, Texas	*Probing High – Density Symmetry Energy with Heavy – Ion Reactions - 50 Years of Beam Seminar series*
April 25	Dr. Peter Petreczky, Nuclear Theory Group, Brookhaven National Laboratory, Upton, New York	*Super Computing the Matter at Extremes: From Hardrons to Quarks*
May 2	Danelle M. Tanner, PhD, Distinguished Member of the Technical Staff at Sandia National Laboratories, Albuquerque, New Mexico	*33 Years of Interesting Projects – 50 Years of Beam Seminar Series*
May 9	Dr. Tony Ahn, National Superconducting Cyclotron Laboratory, Michigan State University, East Lansing, Michigan	*Nuclear Reaction Cross Section Measurements to Study the Abundance Pattern of Metal Poor Halo Stars*
May 11	Dr. Alexander Yakushev, Deputy Head of SHE Chemistry, GSI, Darmstadt, Germany	*Gas Phase Chemistry of Flerovium and $Sg(CO)_6$*
May 12	Dr. Arturo Menchaca-Rocha, National Autonomous University of Mexico (UNAM), Mexico City, Mexico	*Scintillation Studies Initiated at TAMU 30 Years Ago – 50 Years of Beam Seminar Series*

May 15	Dr. María-Ester Brandan, Physics Institute, National Autonomous University of Mexico (UNAM), Mexico City, Mexico	*A Remarkable Property of (Some) Thermoluminescent Dosemeters: A Single Irradiation Gives Dose and Beam Quality Information – 50 Years of Beam Seminar Series*
May 17	Dr. Christoph E. Düllmann, GSI HelmHoltz Institute Mainz and Johannes Gutenberg University Mainz, Germany	*Physics Experiments with the Heaviest Elements: from TASCA at GSI, over ISOL at JAEA, to the Th-229 "Nuclear Clock" Isomer*
May 18	Professor Michael Block, GSI HelmHoltz Institute Mainz and Johannes Gutenberg University Mainz, Germany	*Nobelium Laser Spectroscopy*
June 6	Dr. Xiaodong Tang, Institute of Modern Physics, Chinese Academy of Sciences, Lanzhou, China	*Nuclear Astrophysics at Institute of Modern Physics (IMP) – 50 Years of Beam Seminar Series*
June 15	Dr. Akram Zhanov, Cyclotron Institute, Texas A&M Univeristy, College Station, Texas	*Astrophysical Radiative Capture Processes via Indirect Method: $^{12}C(\alpha,\gamma)^{16}O$*
June 27	Dr. Jeff Allen Winger, Department of Physics and Astronomy, Mississippi State University, Mississippi	*35 Years of β-Decay Spectroscopy – 50 Years of Beam Seminar Series*
June 15	Dr. Akram Zhanov, Cyclotron Institute, Texas A&M Univeristy, College Station, Texas	*Astrophysical Radiative Capture Processes via Indirect Method: $^{12}C(\alpha,\gamma)^{16}O$*
July 11	Dr. Peter L. Gonthier, Physics Department, Hope College, Holland, Michigan	*Millisecond Pulsars and the Galactic Center Excess – 50 Years of Beam Seminar Series*
July 18	Dr. Douglas Rowland, Center for Molecular and Genomic Imaging (CMGI), University of California - Davis, Davis, Calfornia	*Mice to Mars: A Journey in Research – 50 Years of Beam Seminar Series*
July 25	Dr. Xingbo Zhao, Institute of Modern Physics, Chinese Academy of Sciences, Lanzhou, China	*Frontiers on ab Intio Approach to Nuclear Physics in Super-Computing Era – 50 Years of Beam Seminar Series*
August 22	Professor George A. Souliotis, National and Kapodistrian University of Athens, Athens, Greece	*Systematics Studies of Proton-Induced Spallation Reactions*

October 13	Dr. Peter Geltenbort, The Institute Laue Langevin (ILL), Grenoble, France	*The Ultracold Neutron Physics Program at the ILL*
October 30	Dr. Péter Lévai, Director General MTA Wigner Research Center for Physics, Hungarian Academy of Sciences, Budapest, Hungary	*Attoworld under Fire – 50 Years of Beam Seminar Series*
November 3	Dr. O.B. Tarasov, National Superconducting Cyclotron Laboratory, Michigan State University, East Lansing, Michigan	*Exploration of the ^{60}Ca Region*
November 28	Professor Paolo Napolitani, IPN-Orsay, CNRS, University of Paris-Sud and University of Paris-aclay, Paris, France	*Violent Fluctuations in Fluids of Neutrons and Protons Explain How Atomic Nuclei Disintegrate*
December 1	Dr. Che-Ming Ko, Cyclotron Institute and Department of Physics and Astronomy, Texas A&M University, College Station, Texas	*50 Years of Theoretical Nuclear Physics Research at the Cyclotron Institute – 50 Years of beam Seminar Series*
December 4	Dr. Joseph B. Natowitz, Cyclotron Institute, Texas A&M University, College Station, Texas	*WTWT (Whatever They Want to Talk!) – 50 Years of Beam Seminar Series*
December 4	Dr. Dave H. Youngblood, Cyclotron Institute, Texas A&M University, College Station, Texas	*WTWT (Whatever They Want to Talk!) – 50 Years of Beam Seminar Series*

2018

January 22	Dr. Carlos Bertulani, Department of Physics and Astronomy, Texas A&M Commerce, Commerce, Texas	*Cosmological Lithium Problems*
February 20	Dr. Michael Forbes, Department of Physics and Astronomy, Washington State University, Pullman, Washington	*Fermi Superfluids: From Cold Atoms to Neutron Stars and Back*
February 27	Dr. Oded Haber, Weizmann Institute, of Science, Rehovot, Israel	*New Frontiers in Ion Beam Trapping*
March 2	Dr. Vladilen Goldberg, Cyclotron Institute, Texas A&M University, College Station, Texas	*A Life Filled with Physics: Over 50 Years of Fun*

| March 6 | Dr. Justin Frantz, Department of Physics, Ohio University, Athens Ohio | *Studying Quark Gluon Plasma in Intermediate to Small Collision Volumes via Particle Correlations* |
| March 20 | Dr. Michael Famiano, Department of Physics, Western Michigan University, Kalamazoo, Michigan | *Relativistic Electron-Positron Plasma Screening in Astrophysical Environments* |

50 yrs of Beam Symposium Schedule

All scientific sessions will take place at the Hawking Auditorium in the lower level of the Mitchell Institute for Fundamental Physics & Astronomy. For those who indicated their interest in a tour of the Institute, we will be offering them during the poster session Wednesday evening.

If you have any questions, please email us, or call us at +1(979)845-1411.

You may download a pdf of the abstracts for the oral presentations here.

Wednesday morning — Registration (8:00 am–9:00 am)

8:00 am	Registration outside Hawking Auditorium	
8:50 am	Sherry Yennello	Welcome address

Wednesday morning — Nuclear Equation of State (9:00 am–12:35 pm)
Chair: Remco Zegers

9:00 am	Robert Charity	Exotic nuclei, equation of state, and other reaction studies at the TAMU cyclotron
9:45 am	Bao-An Li	The role of isospin and symmetry energy in heavy-ion collisions at Fermi energies
10:10 am	Roy Wada	Primary reconstruction of IMF and symmetry energy
10:35 pm	Alan McIntosh	Equilibrium chronometry: resolving the migration of nucleons on a sub-zeptosecond timescale
11:00 am	20 min break	
11:20 am	Kris Hagel	Heavy element synthesis using multi-nucleon transfer reactions between heavy nuclei
11:45 am	Evgeny Tereshatov	On the way to studying Nihonium chemistry
12:10 pm	Anatoli Afanasjev	Super- and hyper-heavy nuclei in covariant density functional theory
12:35 pm	85 min lunch	

Wednesday afternoon — Nuclear Astrophysics (2:00 pm–5:35 pm)

Chair: Robert Charity

2:00 pm	Remco Zegers	Giant resonances and nuclear astrophysics at the Texas A&M Cyclotron Institute
2:45 pm	Michael Wiescher	Nucleosynthesis in first stars, the on-set of chemical evolution
3:10 pm	Giuseppe Gabriele Rapisarda	Trojan horse measurement at the Cyclotron Institute with RIBs: the $^{18}F(p,\alpha)^{15}O$ reaction
3:35 pm	20 min break	
3:55 pm	Chris Wrede	Beta decays of the neutron-deficient chlorine isotopes
4:20 pm	Livius Trache	Nuclear astrophysics with rare ion beams from MARS
4:45 pm	Ani Aprahamian	Neutron-rich nuclei and the sensitivities to the r-process
5:10 pm	William Newton	Nuclear pasta: inhomogeneous neutron-rich matter in neutron stars and astrophysical implications
5:35 pm	25 min break	

Wednesday evening — Poster session (6:00 pm–8:00pm)

We will be offering tours of the Cyclotron Institute at this time as well; if you haven't already signed up, please let us know to expect you by registering here.

6:00 pm	Hors d'oeuvres and wine/beer will be served	
	Avinash Agarwal	Low energy fusion incompleteness in heavy ion induced reactions
	Miguel Bencomo	Superallowed β decay of 26Si: Sensitive test for isospin symmetry-breaking corrections
	Eames Bennett	Constraining the astrophysical 23Mg(p,γ)24Al reaction rate using the 23Na(d,p)24Na reaction
	Megan Bennett	Development of a $^{235,236}Np$ tracer via $^{236}U(d,xn)$ pathway
	Giacomo Bonasera	Theoretical Predictions of Giant Resonances in 94Mo
	XiGuang Cao	Exotic α emission from α conjugate nuclei collisions
	Sahila Chopra	Role of non-coplanar degree-of-freedom in heavy-ion reactions
	Xiaojian Du	Bottomonium Production in Heavy-Ion Collisions
	Kevin Glennon	Separating Irradiated Uranium Fuel to Measure Isotope Ratios Essential for Attribution
	Joshua Hooker	Structure of ^{10}N via ^{9}C+p Resonance Scattering
	Curtis Hunt	Studying light exotic nuclei through isobaric analogue states
	Peter Jacobs	QCD Matter: status and prospects
	Heshani Jayatissa	Probing the effect of the 22Ne(alpha,n) reaction rate on the s-process isotope abundances using sub-Coulomb alpha-transfer techniques
	Manpreet Kaur	Comparative analysis of fragment production in the decay of A=80 compound systems at low and intermediate energies

Mandeep Kaur	Neck length parameter of dynamical cluster decay model and entrance channel mass asymmetry
Suresh Kumar	High spin states and polarization asymmetry measurements in transitional strontium isotopes near the N=50 shell closure
Shuai Liu	T-MATRIX APPROACH TO QUARK-GLUON PLASMA
Daniel Nagasawa	Chemical Abundance Measurements of Ultra-Faint Dwarf Galaxies Discovered by the Dark Energy Survey
Ninel Nica	Precise Measurement of alpha_k for the 39.76-keV E3 Transition in 103Rh:A Further Test of Internal Conversion Theory
Shuya Ota	Study of astrophysical alpha + 22Ne reaction using alpha transfer with TIARA and MDM spectrometer
Alis Rodriguez Manso	"Neutron-proton equilibration chronometry in dynamically deformed nuclear systems"
Steven Rose	A Novel Semi-Analytic Color Glass Event Generator
Benjamin Schroeder	Commissioning TAMUTRAP: The World's Largest Penning Trap
FNU Shubhchintak	Primordial $d(\alpha, \gamma)^6Li$ reaction and second lithium puzzle
Mandira Sinha	The effect of breakup on elastic and fusion reactions involving loosely bound nuclei
Sriteja Upadhyayula	Probing the cluster structure in 10Be using resonant 6He + alpha scattering
Merinda Volia	Solvent extraction of indium and thalium into betainium based ionic liquid and DL-menthol based deep eutectic solvent
Zhidong Yang	Extract shear viscosity of hot hadron gas with a viscous blast wave model

Thursday morning — Nuclear Structure (9:00 am–12:35 pm)

Chair: Bradley Sherrill

9:00 am	Kai Hebeler	Status and future perspectives in ab initio nuclear structure theory
9:45 am	Jiansong Wang	Recent experimental studies at RIBLL1
10:10 am	Carlos Bertulani	Quasi-free scattering with radioactive beams
10:35 am	20 min break	
10:55 am	Valdir Guimaraes	Elastic scattering of the halo nucleus ^8B on ^{12}C, ^{27}Al, ^{58}Ni and ^{208}Pb targets
11:20 am	Marina Barbui	Exploring clustering in alpha-conjugate nuclei using the thick target inverse kinematic technique for multiple alpha emission
11:45 pm	Zhiqiang Chen	Study of three-body forces and fragmentation in nuclear reactions
12:10 pm	110 min lunch	

Thursday afternoon — Applications of Cyclotron-based Nuclear Science (2:00 pm–3:35 pm)

Chair: Henry Clark

2:00 pm	Kenneth LaBel	Why NASA and the space electronics community cares about cyclotrons
2:35 pm	Gregory Allen	A trip down the beamline – a behind the scenes look at single-event effects testing at the Texas A&M Cyclotron
3:10 pm	Carlos Gonzalez Lepera	Production of metal radioisotopes for positron emission tomography (PET)
3:35 pm	15 min break	

Thursday afternoon — Historical Talks by former Directors (3:50 pm–6:00 pm)

Chair: Sherry Yennello

3:50 pm	Dave Youngblood	The beginning
4:00 pm	Whit McFarlin	The construction and operation of the 88" cyclotron
4:30 pm	Dave Youngblood	From the 88" cyclotron to the K500 superconducting cyclotron 1971 to 1991
5:00 pm	Joseph Natowitz	The golden years: 1991 to 2002
5:30 pm	Robert Tribble	A step back to move ahead: the Cyclotron Institute from 2003 to 2014

Thursday evening — Conference Banquet (7:00 pm)

7:00 pm	Banquet and talk by the Cyclotron Institute director, Sherry Yennello, at the Hildebrand Equine Complex (click here to sign up if you haven't already). There is plenty of parking for participants with vehicles (click here for the location). For those who do not have a car, we will be providing a shuttle bus to and from the banquet.

Friday morning — Fundamental Symmetries I (9:00 am–11:00 am)

Chair: Nicholas Scielzo

9:00 am	John Hardy	Testing the standard model with superallowed $0^+ \rightarrow 0^+$ beta decay
9:45 am	Yang Sun	Systematical shell-model study towards understanding of isospin-symmetry breaking in nuclei
10:10 am	Willem van Oers	Measurement of the weak charge of the proton
10:35 am	Alejandro Garcia	Searches for chirality-flipping interactions in ^{6}He
10:35 am	30 min break	

Friday morning — Recognition Session and BBQ (11:30 am–1:45 pm)

11:30 am	Special session to recognize successes in the past 50 yrs, followed by a BBQ lunch (provided; click here to sign up if you haven't already).

Friday afternoon — Fundamental Symmetries II (1:45 pm–2:35 pm)

Chair: Dan Melconian

1:45 pm	Maxime Brodeur	Precision measurements of mirror transitions at the University of Notre Dame
2:10 pm	Nicholas Scielzo	Improving beta-decay studies for fundamental science and applications
2:35 pm	10 min break	

Friday afternoon — High-energy Nuclear Physics (2:45 pm–5:30 pm)

Chair: Charles Gale

2:45 pm	Peter Jacobs	QCD Matter: status and prospects
3:30 pm	Michael Murray	Phase transitions in small systems
3:55 pm	20 min break	
4:15 pm	Roy Lacey	Indications for a critical end point in the phase diagram for hot and dense nuclear matter
4:40 pm	Yu-Gang Ma	Research progress on anti-matter in relativistic heavy-ion collisions
5:05 pm	Jun Xu	Investigating the RHIC-BES physics based on an extended AMPT model with mean-field potentials

Closing remarks (5:30 pm–5:35 pm)

ĀĪM | TEXAS A&M
UNIVERSITY

Last modified: November 15 2017

A Great "Breakthrough Into Excellence" for Texas Science

In 1964, Texas Governor John B. Connally personally visited the Texas A&M University campus to deliver the good news to then-Texas A&M President James Earl Rudder '32 that a $6 million "atom smasher" would be built at Texas A&M, thanks to a unique public-private partnership involving the Atomic Energy Commission, the state of Texas and the Welch Foundation.

"This is one of the most significant announcements to be made this year and perhaps for some time," Connally told *The Houston Post* at the time regarding the new cyclotron, the fourth to be located on a university campus and the largest in the South. "It is the biggest thing of its kind east of Berkeley, California."

On December 4, 1967, Nobel Prize winners Glenn T. Seaborg and Willard F. Libby helped dedicate the Texas A&M Cyclotron Institute — three days after it had achieved its first external cyclotron-accelerated particle beam, thanks to a 400-ton, 2,000-kilowatt magnet whose power was equivalent to one-fifth of the output of the Texas A&M Power Plant. Twenty years later, that K150 cyclotron was joined by a K500, currently one of the world's five largest superconducting cyclotrons.

Thank you for joining us today to revisit the Texas A&M Cyclotron Institute's rich legacy as we commemorate 50 years of beam and conclude a three-day symposium dedicated to Texas A&M's past, present, and future of exploring the nuclear frontier. #TAMUleads #BeFearless

Texas A&M University Cyclotron Institute
50 YEARS OF BEAM: Exploring the Nuclear Frontier

Recognition Event
November 17, 2017

Presiding	Dr. Sherry J. Yennello, *Director* Cyclotron Institute, Texas A&M University
Welcome	Mr. Michael K. Young, *President* Texas A&M University
Recognition of Founding Partners	Mr. Norbert Dittrich, *President* The Welch Foundation
	The Honorable John Raney '69 *State Representative, District 14* Texas House of Representatives
	Dr. Timothy J. Hallman *Associate Director of Science for Nuclear Physics* United States Department of Energy
Remarks	Col. John O. "Jack" Teague '59 United States Air Force (retired)
	Dr. Karen Butler-Purry, *Interim Vice President for Research* Texas A&M University
Closing	Dr. Yennello

Department of Energy
Washington, DC 20585

October 6, 2017

Professor Sherry Yennello
Director
Cyclotron Institute
Texas A&M University
College Station, Texas 77843-3366

Dear Professor Yennello:

I am writing to express my sincere congratulations to you and your colleagues during a milestone year marking two momentous achievements: the 50th anniversary of the Texas A&M University's K150 cyclotron's first external beam as well as the 30th anniversary of Texas A&M's K500 superconducting cyclotron's first internal beam.

Fifty years ago, the Atomic Energy Commission partnered with the State of Texas and the Welch Foundation to fund the construction of a K150 cyclotron in College Station. It is gratifying that this first cyclotron—coupled with its successor built 20 years later and a myriad of additional experimental equipment—continues to serve as the workhorse for a three-fold program in discovery science, workforce development, and radiation effects testing.

Thanks to the inspired leadership and stewardship you and your colleagues have provided during the past half-century, the Texas A&M University Cyclotron Institute has progressed from that early small laboratory into a Department of Energy Center of Excellence for Nuclear Physics, of which only five exist in the United States. The accomplishments are too numerous to count, from groundbreaking discoveries and technological achievements, to an entire generation of talented nuclear scientists, many of whom are among today's top leaders in nuclear science across the nation and globe.

I wish you every success in building upon an impressive legacy in transformative research, cutting-edge accelerator-based education, and innovative service to the

state, nation, and world, as I join in celebrating your proud past, present, and future in exploring the nuclear frontier.

Sincerely,

Timothy J. Hallman
Associate Director of the Office of Science
for Nuclear Physics